Universidad Autónoma de Madrid
Facultad de Ciencias

Departamento de Química

Estudios de primeros principios en YAG ($Y_3Al_5O_{12}$) dopado con Ce

Codopaje, defectos *antisite* y transiciones $4f$-$5d$ en Ce^{3+}

Memoria

psesentada por

ANA BELÉN MUÑOZ GARCÍA

para optar al Grado de

Doctor en Química

MADRID, MARZO 2011

Universidad Autónoma de Madrid
Facultad de Ciencias

Departamento de Química

First-principles studies on Ce-doped YAG ($Y_3Al_5O_{12}$)

Codoping, antisite defects and Ce^{3+} $4f$-$5d$ transitions

Dissertation

reported by

ANA BELÉN MUÑOZ GARCÍA

Applying for the Degree of

Doctor en Química

MADRID, MARZO 2011

A mi madre,

porque de ella he aprendido
las cosas más valiosas de la vida.

Te quiero mucho.

" When it comes to atoms,
language can be used only
as in poetry."

N. Bohr

"... Y qué le voy a hacer si yo
nací en el Mediterráneo ..."

J.M. Serrat

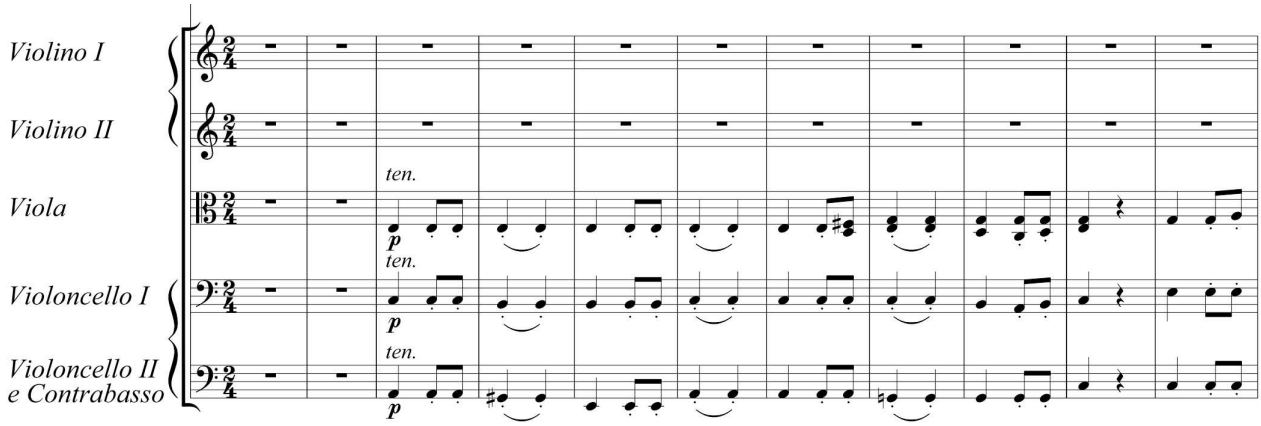

Ludwig van Beethoven,
Symphony No. 7 in A Major,
2^{nd} mov. Allegretto

Acknowledgments

Este trabajo no hubiera sido posible si muchas personas no hubieran estado a mi lado y no hubieran alimentado de un modo u otro mi curiosidad por el mundo desde que tengo uso de razón. En esta página quería simbólicamente dar las gracias a todas ellas y dedicar especialmente algunas palabras a gente importante que me ha acompañado en este último período durante esta tesis.

En primer lugar quiero dar las gracias a Luis y a Zoila, porque me han dado la oportunidad única de trabajar en su grupo y de aprender de ellos y me han apoyado a través de muchos cambios a todos los niveles durante estos años. Para mí ha sido un verdadero honor trabajar con vosotros, ojala todo el mundo tuviese vuestra pasión por el trabajo y sobre todo por la vida. Muchísimas gracias!

A Jose Luis, por esa manía que tiene de hacer el mundo mejor por donde pasa... Millones de gracias por todo el tiempo que has dedicado a que esto saliera bien. Te (os) espero allende los mares. Y aupa Atleti!

Gracias a mis padres Felisa y Nicasio, por su cariño, su esfuerzo sobrehumano y su paciencia. Nunca me habeis pedido nada y lo habeis dado todo para que yo pudiera cumplir mi sueño de estudiar. Gracias por darme la libertad de decidir, gracias por ayudarme a levantarme cuando después me he caído y gracias por alegraros conmigo cuando después ha salido bien. Todo esto es gracias a vosotros. Estoy muy orgullosa de ser vuestra hija.

Gracias a mis 2+2 hermanos Carmela, Alejandro, Jose y Maribel, por estar a mi lado contra viento y marea a lo largo de ese siempre inacabado proceso de hacerse mayor y hacerme vivir un montón de cosas especiales. Os quiero.

A mis cuatro fantásticos Jorge, Noelia, Silvia y Javier; espero que me perdoneis por no haber sido la tia perfecta... que sepais que estoy orgullosisima de ser "la tita Ana"!

Estoy realmente agradecida al Prof. Emilio Artacho, porque me dió la primera oportunidad de trabajar y vivir en el extranjero, con todo lo que eso significa, y, con gran paciencia y dedicación, me dio un empujón grandísimo en un momento tan delicado como son los comienzos de una tesis.

I would like to express my sincere gratitude to Prof. Emily A. Carter, who has placed confidence on me from the very beginning and whose expertise, understanding, vision, dedication, interaction with students and attitude in life are absolutely inspiring and encourage me to improve my graduate skills. Thanks for this great opportunity!

A la gente de la UAM. A Goar, porque cuando él estaba más agusto que un arbusto, yo estaba más feliz que una perdiz. Fdo: Anetta Franklin. A Fernando y Belén porque aunque coicidimos poco tiempo, fue una experiencia estupenda. Fernando, gracias por tu apoyo logístico via chat. A mis compis de doctorado Pablito, Josito y Ane, porque me dieron un abrazo fuerte aquel frío febrero y siempre me han recibido con los brazos abiertos aunque no les haya dedicado tanto tiempo como merecían. Gracias de corazón, chicos.

A mi prima Rosi, porque siempre tiene espacio para mí en los lugares mágicos que crea a su paso. Lombriceando que es gerundio.

A mi familia de Hinojosas y en especial a mi tia Cristina porque mis raíces están en ese lugar de la Mancha de cuyo nombre sí quiero acordarme. Un besote muy fuerte a mis otros primos y pseudoprimos de Getafe.

A Fede y Carolina, porque aunque estais lejos, estais muy muy cerca y seríais de las primeras personas que me llevaría a una isla desierta.

A Dani porque, efectivamente, There Is A Light That Never Goes Out.

A los miembros de ECDCP (aka ECDC12), por hacerme empezar toooodos los dias con una sonrisa; en especial a David, porque es tan mentiroso que dice que puede ser malo. Por cierto, cual me dijiste que era el teléfono del diablo?

A Ali porque desde el principio de la carrera me ha estado mandando paquetes de energía positiva. Y ya sabes, que tiemblen los pollos del lugar!

A Eduardo Anglada porque siempre ha mandado águilas a rescatarme cuando se ponía feo el camino a Mordor.

A Mercedes, mi profesora de química del instituto Aldebarán. Espero que de algún modo u otro te llegue esta tesis y estés contenta.

I would like to thank my workmates in Cambridge Lydia and Liliana, and Pete (jazz!).

Also, thanks to the Fellowship of the Dagger; Kostas, Bess, Elena, Losilla, Johannes, Becky, Mivsam and Remedios. Grande ESQC09, grande Sicilia.

A tutto il mondo che a Princeton mi ha fatto sentire a casa, specialmente a Andrea, Atti, Geppino, Germa', Marina e Michelle...grazie! Mi mancate ragazzi.

Y a Michele, por el auténtico auténtico *poema de los dones*. QLS.

Como dice la canción: "...gracias a la vida, que me ha dado tanto..."

Ana Belén Muñoz-García
Marzo 2011

Preface

This thesis applies for the European PhD degree. Then, the present manuscript should contain some parts written in two languages of the European Union. My choice for the main body of the document is English. Moreover, selected parts are written also in Spanish. These sections in Spanish, which appear in *italic* letters in the general index, are:

- The general introduction of the thesis.
- Conclusions of every chapter devoted to results.
- The general conclusions.

Thanks,

Ana Belén Muñoz-García

Contents

Chapter 1

General introduction

1.1 Lanthanides and Luminescence

Ancient civilizations already used technologies that involved the various branches of chemistry. Examples include: extracting metals, making ceramics and jewelry, fermenting cereals, grapes and milk, extracting drugs from plants and making pigments for cosmetics and painting.

Alchemy, an amalgam of some chemical techniques and philosophical speculations, failed in explaining the nature of matter, but many experiments performed and results recorded set the stage for modern chemistry. The first clear separation between chemistry and alchemy was made by R. Boyle in his book *The Skeptical Chemist* (1661). Chemistry became an independent science when A. Lavoisier developed his law of conservation of mass, since it demanded a rigorous and quantitative treatment of matter. The concept of *element* appeared for the first time in Lavoisier's *Traité elementaire de Chimie*(1789) and, in only one century, the discovery of new elements had been increasing. Their classification in the periodic table by D. Mendeleev and L. Meyer ($\sim$ 1870) was then a great breakthrough in understanding the internal chemical properties [1].

The lanthanide story begins with the discovery of a new unknown mineral in a quarry in the village of Ytterby, near Stockholm, in 1787. The material was studied by the Swedish chemist Johan Gadolin, who announced in 1794 that it contained a new compound that he called *ytterbia*, honoring the village. Half a century later, three different fractions were separated from *ytterbia*: *yttria*, *terbia* and *erbia*. These fractions turned out to be complicated mixtures as well. As seen on chart 1.1, the discovery of the whole series of lanthanides took all XIXth century long, because of the difficulty on separating the individual species. Moreover, in most cases the lanthanides were detected as a part of compounds, such as oxides, and only decades after, the pure materials were extracted. These difficulties are a result of them having very similar chemical properties. Their dominant valence state is +3 and they show only small differences in complex formation and solubility. The existence of only fourteen lanthanide elements was interpreted by Bohr as a gradual filling of an 32-electrons shell, corresponding to an extension of the 18-electrons one (s, p and d) by addition of seven orbitals from the $4f$ shell [2].

Year	Element	Origin or meaning of the name
1803	Cerium	Ceres was the Roman god of corn, and the first asteroid, discovered in 1801
1839	Lanthanum	An ancient Greek word for meaning "to lurk", because lanthanum was "lurking" undetected in a Cerium mineral
1843	Erbium	The village of Ytterby
1843	Terbium	The village of Ytterby
1878	Holmium	Holmia is the Latin name for Stockholm, where it was discovered
1878	Ytterbium	The village of Ytterby
1879	Samarium	The mineral Samarskite (where the metal was first found) was named after Russian engineer Vasili Samarsky-Bykhovets (1803-1870)
1879	Thulium	Thule is the Greek name for the far northern region of Europe that includes Scandinavia, where the mineral was discovered
1880	Gadolinium	From the mineral Gadolinite, which was named after chemist Johan Gadolin
1885	Praseodymium	Meaning "lime-green-didymium" since it was discovered in the form of green compounds separated out from didymium (once tought to be an element itself)
1885	Neodymium	"New didymium"
1886	Dysprosium	Meaning "difficult to get", referring to how difficult it was to separate the element from holmium oxide
1901	Europium	Named from the continent of Europe
1907	Lutetium	Lutetia, the Latin name for Paris, where it was discovered
1938	Promethium	Prometheus, the Greek god who brought fire to humankind

Figure 1.1: Year of discovery and origin of the name of the lanthanide series. From Ref. [2].

Going from La^{3+} to Lu^{3+} the $4f$ orbitals are filled with electrons. These electrons have little interaction with the chemical environment of the ion, as the $4f$ orbitals are shielded from it by the electrons in the $5s$ and $5p$ shells, which are lower in energy, but spatially located outside the $4f$ orbitals. This explains the similarity in chemical properties of all lanthanide ions mentioned above. The small differences between them are due to the decrease in size when increasing atomic number (the "lanthanide contraction") [3, 4].

Luminescence is present long since in human thoughts as well. The ancients admired and were afraid of phenomena such as aurora borealis, lightning, luminous animals (e.g. fireflies and worms) or stones. The discovery of the Bolognian stone by shoemaker and alchemist V. Cascariolo in 1603 was the first of multiple milestones in the long process which led to the understanding of the phenomena linked to light emission. In 1888, the german physicist E. Wiedemann coined the word *luminescence* for characterizing the light emission not conditioned by a rise in temperature [5].

All luminescence is the result of a competition between radiative and non-radiative pathways in the relaxation of an electronically excited species. Luminescence present when lanthanide ions are incorporated into certain host materials (glasses, crystals and

powders) is not an exception. The vaste number of electronic energy levels due to the f electrons gives rise to a rich variety of radiative and non-radiative relaxation processes in lanthanide excited ions. Thus, usually, the absorbed and emitted light have different colors (wavelengths). The emissive properties of a lanthanide ion are governed by the facility with which its excited states can be populated and the non-radiative deactivation paths minimized. Moreover, these processes are enhanced or quenched depending on the host, presenting each type of combination host/lanthanide ion its strengths and weaknesses for the construction of luminescent materials.

The shielding of the $4f$ orbitals by the filled $5s^2 5p^6$ sub-shells results in special spectroscopic properties with parity-forbidden $4f \rightarrow 4f$ absorptions having very low molar absorption coefficients and characteristic narrow-line emission, mostly in the visible and near infrared ranges. These narrow bands present in free lanthanide ions suffer from slight splittings when they are inside crystals as impurities due to the crystal field. These energies and transitions involving the $4f$ configurations of lanthanides give raise to narrow absorption and emission bands and have been widely studied and characterized using various theoretical models. However, the $4f \rightarrow 5d$ transitions have been studied to a lesser extent. They present wide UV and VUV bands, difficult to study and interpret experimentally. The broadness of these bands comes from the coupling of the electron in the d orbital with crystal phonons, because $5d$ orbitals are much more extended than the much more internal $4f$ ones. Thus, whereas the f electrons are only weakly affected by ligand field, d electrons are exposed to covalent interactions with the crystal and ligand field theory is not enough to identify and assign electronic states, far beyond a rough characterization as $f \rightarrow d$ transitions. Some empirical models appear aiming the prediction of trends for these transitions in terms of structural and electronic data. One of these models regarding $4f \rightarrow 5d$ transitions is the one set out by Judd [6] and Morrison [7]. In this model, the $4f \rightarrow 5d$ transition of a lanthanide Ln^{3+} in a crystal in comparison to such transition in the free-ion depends on the Ln^{3+}-L distance, being L the ligands of the first coordination shell, which is usually not known. This model has been used by Bettinelli and Moncorgé to show a linear dependence of the lowest $4f \rightarrow 5d$ transitions in lanthanides with respect to such transition of Ce^{3+} in different crystals [8]. Dorembos uses this scheme in the study of various Ce^{3+}-, Pr^{3+}-, Nd^{3+}-, Sm^{3+}- and Eu^{3+}-doped crystals [9, 10, 11, 12, 13]. Then, in order to achieve a better understanding of lanthanide luminescence, the detailed description of the local geometries around lanthanides appears as a challenging scenario.

The application of *ab initio* quantum chemistry methods to the study of these systems has been attempted only by a comparative small number of researchers, bearing in mind the huge number of *ab initio* calculations devoted to other systems. This is because the large number of lower-lying electronic states and the complicated interactions to be treated simultaneously (including relativistic effects) make a rationalization of the electronic structure rather difficult. However, the success of embedded cluster *ab initio* calculations in rationalization of luminescences of lanthanides in ionic solids [14, 15, 16, 17, 18], make this technique a good candidate for the study of the mentioned structure-luminescence

relationship in these compounds.

Increasing interest for lanthanide luminescence is stimulated by the continuously expanding need for luminescent materials meeting the stringent requirements of telecommunication, lighting, electroluminescent devices, bio-analytical sensors and bio-imaging set-ups [19]. The materials studied in this work are within the technological frame of solid-state lighting (SSL). SSL refers to a type of lighting that uses semiconductor light-emitting diodes (LEDs), organic light-emitting diodes (OLEDs), or polymer light-emitting diodes (PLEDs) as sources of illumination rather than electrical filaments, plasma or gas. The term "solid-state" refers commonly to light emitted by solid-state electroluminescence, as opposed to incandescent bulbs (which use thermal radiation) or fluorescent tubes. Compared to incandescent lighting, SSL creates visible light with reduced heat generation or parasitic energy dissipation. Most common "white" LEDs convert blue light from a solid-state device to an (approximate) white light spectrum using photoluminescence, the same principle used in conventional fluorescent tubes. SSL devices, apart from having a small mass, present greater resistance to shock and vibration compared to glass bulbs and filament wires. They also eliminate filament evaporation, increasing the life span of the illumination device. Thus, there is a remarkable energetic saving associated to SSL devices (around 29 % in USA, $\sim$ 125.000 million USD from 2005 to 2025) and they are, besides, environmentally friendly. Solid-state lighting is currently used in traffic and vehicle lights, street and parking lot lights, and remote controls. The use of this kind on lighting is on the increase and a complete substitution of conventional lighting is foreseen for 2025 [20].

1.2 Motivation of this work: Luminescence of Ce:YAG

Yttrium aluminum garnet ($Y_3Al_5O_{12}$, YAG) is an optical material of the utmost importance. The mechanical, thermal and optical properties of this synthetic garnet have made it a practical choice for a wide range of applications, not only pure but also containing traces of other elements. YAG for a period was used in jewelry as a diamond and other gemstone simulator. Colored variants and their doping elements include: green (chromium), blue (cobalt), red (manganese), yellow (titanium) and purple (neodymium) [21]. Moreover, when YAG is doped (and codoped) with rare-earth elements, its range of technical applications increases, being lasers and phosphors two fields with increasingly interest in YAG-based materials design.

In the group of *lasers*, we can find, among others, the well known Nd:YAG [22](one of the most common types of laser; emits light in the infrared and is used in different fields, from eye surgery to military devices [23, 24]), Nd,Cr:YAG, Er:YAG, Yb:YAG, Nd,Ce:YAG, Ho,Cr,Tm:YAG and Tm:YAG [25]. Regarding *phosphors*, examples are Dy:YAG and Sm:YAG (thermal-sensitive phosphors used in temperature measurements) [26] and Tb:YAG (used in cathode ray tubes, emitting at yellow-green color) [27].

Cerium(III)-doped YAG (Ce:YAG), the material of interest in this work, is a luminescent material with a rich history and a wide variety of applications. Blasse and Brill

reported for the first time Ce:YAG as a material with a high luminescence efficiency, short luminescence lifetime and relatively long (visible) wavelengths, ideal for its use as a phosphor in cathodic ray tubes. Later, they reported spectroscopic details such as the first four $4f \rightarrow 5d$ excitation bands, emission bands and the Stokes shift [28]. Ce:YAG is also used in some mercury-vapor lamps often together with Eu-doped yttrium phosphate-vanadate and, since it has virtually no afterglow when is excited by electrons, it is suitable for use in photomultipliers.

However, the use of interest in this work is within the SSL context since, at present, Ce:YAG is the most used blue-to-yellow converter in white light-emitting diodes. This conversion is associated to the Ce^{3+} local states in the point defect. Used as a coating on a high-brightness blue InGaN diode, Ce:YAG converts part of the blue light into yellow, which then appears as white (Fig.1.2) [29].

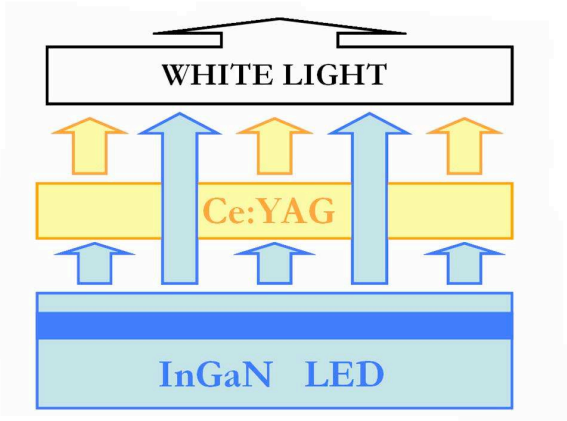

Figure 1.2: Scheme of Ce:YAG acting as yellow phosphor in SSL devices.

Such an arrangement gives an overall energy efficiency approaching that of fluorescent lamps but better efficiencies are need in the rapidly expanding market of SSL, as well as a better coverage of the full spectrum and an improved thermal quenching behavior [30]. Actually, controlling the color of white light SSL devices is considered one of the important issues governing the success of these technologies [31]. In this context, codoping appears as one of the methods used for the color control [32, 33, 34, 35, 36], not only because the known ability of codopants as co-activators [34] but also as wavelength shifters [37, 38, 39, 40].

1.3 Targets of this thesis and outline of the manuscript

At the very beginning of this thesis, we faced two different issues related to Ce:YAG luminescence.

On the one hand, previous embedded-cluster calculations on the structure and absorption/luminescence on Ce:YAG performed in our group [41] matched profiles of absorption

and emission spectra but failed in an equally good description of the experimental Stokes shift (the energy difference between the absorption and emission maxima) and pointed out the importance of local atomistic structures in the ground state and the excited states for light absorption and luminescence in YAG-related materials. Recent measurements give a smaller Ce:YAG Stokes shift [42]. Even if it is closer to the calculated one in Ref. [41], the underestimation of the value in such calculation is still important. In this context, we thought of the possibility of a more realistic description of YAG as Ce^{3+} host, taking into account the intrinsic antisite defects that appear in YAG during syntheses [43], because they are known to change the luminescence patterns of YAG and bulk Ce:YAG [44, 45, 46].

On the other hand, in the context of codoping and color control of Ce:YAG in SSL devices, it was known that La^{3+} and Gd^{3+} shift the first $5d \rightarrow 4f$ yellow absorption of Ce:YAG to longer wavelengths (red shift), whereas Ga^{3+} and In^{3+} shift this absorption to shorter wavelengths (blue shift). However, no much was known about the $4f \rightarrow 5d$ absorptions and, moreover, no much was known about the relationship between the structure of local defects and the red/blue shift induced by codoping beyond empirical rules linking a larger size of codopants with a red shift (if the larger atom takes an Y^{3+} place) or to a blue shift (if the larger atom takes a Al^{3+} place) [32, 39, 40].

A common starting point to tackle both problems was to find reliable and affordable methods to describe the parent solid YAG and, increasingly, different levels of complexity of defects. The first level is the presence of single defects in YAG, whether they are antisite defects or cations as Ce^{3+}, La^{3+} or Ga^{3+}. We call them *single defects* in this work, even if each antisite defect contains a pair of exchanged cations itself. The next step would include our defect of interest, Ce^{3+} in YAG plus antisite defects or codoping cations as modifiers of its structure, electronic structure and, finally, luminescence. These cells containing Ce^{3+} plus another cation or antisite defect(s) are called *double defects* in this work.

As a matter of nomenclature, Ce:YAG label refers to YAG cells containing one Ce atom per unit cell in this work. Cells containing single La or Ga defects are called La:YAG and Ga:YAG respectively. As we will see later, Ce and La in YAG can only occupy a Y site, whereas Ga, which substitutes an Al atom, can be placed in a pseudotetrahedral or in a pseudooctahedral site. Then, Ga_{tet}:YAG and Ga_{oct}:YAG labels are used specifically in this work when we refer to YAG materials containing Ga in tetrahedral or octahedral environment respectively. YAG materials containing one antisite defect or two antisite defects per unit cell are called 1AD:YAG and 2AD:YAG respectively. Regarding double defects, we use the labels Ce,La:YAG, Ce,Ga_{tet}:YAG and Ce,Ga_{oct}:YAG for corresponding Ce_Y codoped materials. The general label Ce,ADs:YAG is given all this work long to YAG cells containing Ce_Y plus antisite defects. More specifically, if we consider Ce_Y plus one antisite defect per unit cell, we use the Ce,1AD:YAG label and if we consider Ce_Y plus two antisite defects per unit cell, we use the Ce,2AD:YAG label.

At this point, we should keep in mind that our structural and spectroscopic problems fit different theoretical approaches, and we should fulfill a reliable structural study of our materials as macroscopic entities taking into account also the atomistic structures that

would give rise to the spectroscopic properties, which will be studied at much more local level.

Thus, this manuscript is structured as follows:

A first part contains a methodological context for the methods used in our calculations. Chapter 2 offers a brief overview of methods used in quantum chemistry, emphasizing the aspects of calculations in solids, and our specific choices for the problem of Ce:YAG. After this methodological introduction, Chapters 3 and 4 cover the methods used in this work for the obtaining of structural properties and for spectra calculations respectively. Chapter 3 is devoted to basic aspects of density functional theory (DFT) and to peculiarities of the periodic boundary conditions density functional theory (PBC-DFT) program used in this work for structural aspects. Chapter 4 outlines the embedded cluster approach used to differentiate the impurity from the rest of the crystal, followed by a description of the level of theory that accurately describes the multiconfigurational nature and the electronic structure of the impurity (complete active space self-consistent field (CASSCF)/complete active space 2^{nd} order perturbation theory (CASPT2) methods).

The second part contains our results on the studied systems. We can consider the description of Ce:YAG luminescence under the effects of codoping or antisite defects the ultimate target of this work. However, the problem of luminescence of Ce:YAG upon codoping or antisite defects influence is not but the tip of the iceberg of a complex problem involving many ingredients.

First of all, an accurate and reliable description of the host YAG is needed, because it is the parent solid present, one way or another, in all our calculations. Thus, we present in Chapter 5 an extended study of both structural and electronic properties of pure and perfect bulk YAG, crosschecked with calculations on other solids containing Y, Al and O, confirming that pseudopotentials and basis sets specifically generated for these calculations are reliable enough.

The natural step beyond the study of pure and perfect YAG is the separated study of individual defects, to set up our references for following calculations including double defects. In this way, Chapters 6 and 7 are devoted to atomistic descriptions of Ce/La/Ga-doped YAG and ADs:YAG respectively, regarding their structures and electronic structures. All these *previous* steps are indeed interesting by themselves because of the scarce data available of these systems.

Once the structural study of individual defects is completed, we present in Chapter 8 the two main targets of this work, the study of Ce:YAG luminescence affected, on one hand, by codoping cations and, on the other hand, by antisite defects. We pay attention in this chapter to the methodology followed from structure calculations (focused on distortions around Ce_Y) to spectra analyses (in terms of different levels of distortion), which aims to highlight the structural-spectroscopic interplay in these materials. Moreover, we present Ce:YAG (no antisite defects, no codoping atoms) calculated $4f$ and $5d$ energy levels as our reference for further comparisons with the "double defects" materials. Moreover, we compare this spectrum with Ce:YAG spectrum previously calculated in our group also under the *ab initio* model potential (AIMP) approach but using cluster

structures arising from wavefunction-based methods and including spin-orbit effects [41].

After this introductory chapter, detailed studies on Ce,La:YAG and Ce,Ga:YAG are presented in Chapters 9 and 10 respectively. For these codoped Ce:YAG materials, we perform a PBC-DFT study of stability of the different possible cells that can be made with the two defects and structure and electronic structure of the most stable ones. These distorted Ce and surroundings structures are used in further CASSCF/CASPT2 embedded-cluster calculations to obtain the corresponding absorption spectra. The red/blue shifts found with respect to Ce:YAG, in agreement with experimental results, are analyzed in terms of the influence of distortions and electronic effects of the codoping atoms to the components of the $4f \rightarrow 5d$ transition.

Chapter 11 firstly includes the stability, structural and electronic structure analysis of Ce,1AD:YAG and Ce,2AD:YAG materials. We also present information on the shifts induced by the presence of antisite defects in Ce:YAG absorption spectra following the same analytical scheme performed for codoped Ce:YAG. Moreover, this chapter presents our results on the calculated Stokes shift of Ce,1AD:YAG and Ce,2AD:YAG materials.

After a section containing specific conclusions, data tables are included at the end of each chapter devoted to results.

Chapter 12 lists the main general conclusions obtained in this work.

To end, we also include two appendices containing additional information: Appendix A includes some additional work carried out in this period not belonging to the Ce:YAG luminescence issue. Appendix B encloses the scientific publications originated during this work.

1.4 *Lantánidos y luminiscencia*

Las civilizaciones antiguas ya usaban técnicas que involucraban diferentes ramas de la química, como por ejemplo la extracción de metales, fabricación de cerámica y joyería, la fermentación de cereales, uvas y leche, la extracción de fármacos de plantas o la preparación de pigmentos de uso en cosmética y pintura.

La naturaleza de la materia no pudo ser descrita correctamente desde el punto del conglomerado de técnicas químicas y especulaciones filosóficas en que se sustentaba la alquimia, pero muchos experimentos realizados y resultados obtenidos por los alquimistas sentaron las bases de la química moderna. La primera separación clara entre alquimia y química aparece en el libro *El químico escéptico* de R. Boyle, en 1661. La química se convirtió en una ciencia independiente cuando A. Lavoisier desarrolló su ley de conservación de la masa, puesto que ésta requería un tratamiento más riguroso y cuantitativo de la materia. El concepto de *elemento* apareció por primera vez en el *Tratado de química elemental* de Lavoisier (1789) y, en tan sólo un siglo, el número de nuevos elementos había incrementado. La clasificación de todos estos elementos en una tabla periódica realizada por D. Mendeleev y L. Meyer ($\sim$ 1870) fue un gran paso adelante en el proceso de comprensión de las propiedades químicas internas [1].

La historia de los lantánidos comienza con el descubrimiento de un nuevo material en una cantera de la villa de Ytterby, cerca de Estocolmo, en 1787. El material fue estudiado por el químico sueco Johan Gadolin, que anunció en 1794 que contenía un nuevo compuesto al que llamó *ytterbia* en honor a la villa. Medio siglo después, se aislaron tres fracciones diferentes del material *ytterbia*: *yttria*, *terbia* and *erbia*, que resultaron ser también complicadas mezclas. El cuadro 1.3 muestra cómo el descubrimiento de toda la serie lantánida llevó todo el siglo XIX, debido a la dificultad en separar las especies. Además, en la mayoría de los casos, los lantánidos eran detectados formando parte de compuestos, e.g. óxidos, y solo décadas después pudieron ser aislados los materiales puros. Estas dificultades se deben a que todos ellos presentan propiedades químicas muy parecidas. Su estado de oxidación es mayormente $+3$ y solo presentan pequeñas diferencias en formación de complejos y solubilidad. La existencia de sólo catorce lantánidos fue interpretada por Bohr a través del llenado gradual de una capa de 32 electrones, correspondiente a una extensión de la habitual de 18 electrones (s, p y d) con siete orbitales de carácter $4f$ [2].

Avanzando en la serie lantánida desde La^{3+} hasta Lu^{3+}, los orbitales $4f$ se van llenando con electrones. Estos electrones tienen muy poca interacción con el entorno químico del ión correspondiente, puesto que los orbitales $4f$ están protegidos por las capas $5s$ y $5p$, que tienen menor energía pero están localizadas espacialmente más lejanas al núcleo. Esto explica la similitud antes mencionada en cuanto a propiedades químicas. Las pequeñas diferencias entre ellos son debidas a la disminucion de tamaño experimentada a medida que aumenta el número atómico (fenómeno conocido como "contracción lantánida" [3, 4]).

El concepto de luminiscencia está presente el el pensamiento humano también desde tiempos remotos. Los hombres de la antigüedad admiraban y temían fenómenos como la aurora boreal, los relámpagos, animales luminosos (por ejemplo luciérnagas y gusanos)

Año	Elemento	Origen o significado del nombre
1803	Cerio	Ceres era la diosa romana de la cosecha, y el primer asteriode, descubierto en 1801
1839	Lantano	Antigua palabra griega que significaba “esconderse”, porque el La estaba “escondido” antes de detectarlo en minerales de Ce
1843	Erbio	De la villa de Ytterby
1843	Terbio	De la villa de Ytterby
1878	Holmio	Holmia era el nombre en latín de Estocolmo, donde fue descubierto
1878	Ytterbio	De la villa de Ytterby
1879	Samario	El mineral Samarsquita (donde el metal fue primeramente encontrado) tomó el nombre del ingeniero ruso Vasili Samarsky-Bykhovets (1803-1870)
1879	Tulio	Thule es el nombre giego de la región del norte de Europa que incluye Escandinavia, donde el mineral fue descubierto
1880	Gadolinio	Del mineral Gadolinita, llamado así por el químico Johan Gadolin
1885	Praseodimio	Significa “didimio verde” puesto que fue descubierto como un compuesto verde separable del didimio (que se creía que era un elemento en sí mismo)
1885	Neodimio	“Nuevo didimio”
1886	Disprosio	Significa “difícil de obtener”, referido a la dificultad de separarlo del óxido de osmio
1901	Europio	Llamado así por el continente Europa
1907	Lutecio	Por Lutecia, el nombre en latín de Paris, donde fue descubierto
1938	Prometio	Por Prometeo, el dios griego que trajo el fuego a la humanidad

Figura 1.3: Año de descubrimiento y origen del nombre de los elementos de la serie lantánida. Extraído de Ref. [2].

y piedras. El descubrimiento de la *piedra Boloñesa* por el zapatero y alquimista V. Cascariolo en 1603 fue el primero de múltiples hitos en el largo proceso que condujo a la racionalización de los fenómenos relacionados con la emision de luz. En 1888, el físico alemán E. Wiedermann acuñó el término *luminiscencia* para caracterizar los fenómenos de emisión de luz no condicionados por un aumento de temperatura [5].

Toda luminuscencia es el resultado de la competición entre procesos radiativos y no radiativos en la relajación de especies electrónicas excitadas. La luminiscencia que presentan los iones lantánidos cuando se introducen en matrices sólidas (vidrios, cristales y polvos) no es una excepción. El gran número de niveles de energía debido a los electrones f da lugar a una gran variedad de procesos radiativos y no radiativos de los iones lantánidos excitados. Por tanto, normalmente, la luz absorbida y emitida tienen diferente color (longitud de onda). Las propiedades emisivas de un ión lantánido estan gobernadas por la facilidad con que sus estados excitados pueden ser poblados y por la minimización de aquellos caminos de desactivación de tipo no radiativo. Además, estos procesos se potencian o se mitigan dependiendo del cristal, presentando cada combinacion de ion lantánido y sólido sus puntos fuertes y débiles en la construcción de materiales luminiscentes.

El apantallamiento debido a las capas llenas $5s^2 5p^6$ sufrido por los orbitales $4f$ da lugar a propiedades espectroscópicas especiales, con absorciones $4f \rightarrow 4f$ de paridad prohibida

de bajos coeficientes de absorción molar y características líneas de emisión estrechas, mayormente en el rango visible e infrarrojo próximo. Estas estrechas bandas que presentan los iones lantánidos libres experimentan ligeros desdoblamientos cuando dichos iones son introducidos como impurezas en cristeles debido al campo ligando. Estas energías y transiciones que involucran los estados $4f$ de los lantánidos dan lugar a estrechas bandas de absorción y emisión que han sido ampliamente estudiadas y caracterizadas mediante varias técnicas. Sin embargo, las transiciones $4f \rightarrow 5d$ han sido objeto de estudio en mucha menor medida. Estas transiciones presentan bandas anchas en el UV y VUV, difíciles de estudiar y de interpretar experimentalmente. La anchura de estas bandas surge del acoplamiento del electrón el el orbital $5d$ con los fonones del cristal, ya que los orbitales $5d$ son mucho más externos que los orbitales $4f$. Asi, mientras los electrones f se ven afectados sólo ligeramente por el campo ligando, los electrones d están expuestos a interacciones covalentes con el cristal, siendo la teoría del campo ligando insuficiente para identificar y asignar estados electrónicos más allá de una aproximada caracterización como transiciones $f \rightarrow d$. Algunos modelos empíricos aparecen con el objetivo de predecir tendencias para esas transiciones en términos de datos estructurales y electrónicos. Uno de esos modelos en lo que se refiere a transiciones $4f \rightarrow 5d$ es el modelo establecido por Judd [6] y Morrison [7]. En este modelo, la transición $4f \rightarrow 5d$ de un lantánido Ln^{3+} en un cristal en comparación con dicha transición en el ión libre depende de la distancia Ln^{3+}-L, siendo L los ligandos de la primera esfera de coordinación, que normalmente se desconoce. Este modelo ha sido usado por Bettinelly y Moncorgé para mostrar una dependencia lineal de la primera transición $4f \rightarrow 5d$ en lantánidos con respecto a la primera transición $4f \rightarrow 5d$ de Ce^{3+} en distintos cristales [8]. Dorembos usa este esquema en el estudio de varios cristales dopados con Ce^{3+}, Pr^{3+}, Nd^{3+}, Sm^{3+} y Eu^{3+} [9, 10, 11, 12, 13]. Por tanto, con objeto de entender su luminiscencia de los, la detallada descripción de las geometrias locales alrededor de los lantánidos, aparece como un desafiante objetivo.

Muy pocos investigadores han aplicado métodos *ab initio* de la química cuántica a estos problemas, en comparación con el enorme número de cálculos *ab initio* realizados en otros sistemas. Esto es debido que el gran número de estados electrónicos y las complicadas interacciones que hay que tratar simultaneamente (incluidos efectos relativistas), hacen de la racionalización de la estructura electónica de lantánidos en cristales una ardua tarea. Sin embargo, el éxito de métodos *ab initio* dentro de la aproximación de *cluster* embebido [14, 15, 16, 17, 18], hacen que esta técnica sea una buena candidata para el estudio de la mencionada relación entre estructura y luminiscencia en estos compuestos.

El interés creciente por la luminiscencia de lantánidos se ve estimulado por la creciente necesidad de materiales luminiscentes que cumplan las severas exigencias dentro de los campos de las telecomunicaciones, iluminación, dispositivos electroluminiscentes o de los sensores bioanalíticos [19]. Los materiales estudiados en este trabajo estan dentro del marco tecnológico del SSL (siglas en inglés de *Solid-State lighting*, iluminación en estado sólido). SSL se refiere a un tipo de iluminación que usa diodos semiconductores emisores de luz (LEDs), diodos orgánicos emisores de luz (OLEDs) o diodos poliméricos emisores de luz (PLEDs) como fuentes de iluminación, en lugar de filamentos eléctricos, plasma

o gas. El término "estado sólido" se refiere comunmente a la luz emitida por un sólido luminiscente, en oposición a las bombillas incandescentes (que usan radiación térmica) y a los tubos fluorescentes. Comparados con la iluminación incandescente, los dispositivos SSL crean luz visible con reducidas pérdidas de calor parásitas. Los dispositivos SSL más comunes son los LEDs denominados "blancos", pues convierten luz azul proveniente de un dispositivo en estado sólido en (aproximada) luz blanca por medio de fotoluminscencia, el mismo principio usado en tubos fluorescentes convencionales. Los dispositivos SSL, además de poseer una reducida masa, presentan gran resistencia al choque y a la vibración comparados con las bombillas de vidrio y los filamentos de alambre. La evaporación del filamento también es eliminada en sistemas SSL, de modo que aumenta la vida útil del dispositivo. Asi, hay un notable ahorro energético asociado a los dispositivos SSL (alrededor de un 29% en EEUU, $\sim$ 125 millones de dólares desde 2005 hasta 2025) y, además, son respetuosos con el medio ambiente. La iluminación en estado sólido se usa actualmente en luces de tráfico y vehículos, iluminación de aparcamientos y controles remotos. El uso de este tipo de iluminación va en aumento y se prevee sustituya a la iluminación convencional hacia 2025 [20].

1.5 *Motivación de este trabajo: luminiscencia de Ce:YAG*

El granate de yttrio y aluminio ($Y_3Al_5O_{12}$, YAG) es un material óptico de suma importancia. Las propiedades mecánicas, térmicas y ópticas de este granate sintético lo han convertido en un material con un amplio rango de aplicaciones, no solo en su forma pura, sino tambien cuando contiene trazas de otros elementos. Durante un tiempo, se utilizó en joyería simulando diamantes y otras piedras preciosas. Algunas variantes coloreadas del YAG con sus elementos dopantes son: verde (cromo), azul (cobalto), rojo (manganeso), amarillo (titanio) y violeta (neodimio) [21]. Además, cuando el YAG es dopado (y codopado) con tierras raras, su rango de aplicaciones tecnológicas aumenta, siendo en el campo de los láseres y de los materiales fosoforescentes donde se concentra el mayor interés en el diseño de materiales basados en YAG.

Dentro del grupo de los *láseres* podemos encontrar, entre otros, el conocido Nd:YAG [22] (un tipo de láser muy común que emite luz en el inrfrarrojo y se usa en diferentes campos, desde cirugía oftalmológica a instrumentación militar[23, 24]), Nd,Cr:YAG, Er:YAG, Yb:YAG, Nd,Ce:YAG, Ho,Cr,Tm:YAG y Tm:YAG [25]. Algunos ejemplos de materiales fosoforescentes son Dy:YAG and Sm:YAG (materiales fosforescentes termosensibles usados en medidas de temperatura) [26] y Tb:YAG (usado en tubos de rayos catódicos y que emite en el verde-amarillo) [27].

El YAG dopado con Ce^{3+} (Ce:YAG), que es el material de interés en este trabajo, es un material luminiscente con una rica historia y una gran variedad de aplicaciones. Blasse y Bril dieron cuenta por primera vez de la alta eficiencia luminiscente del Ce:YAG, de su bajo tiempo de vida en estados excitados y su relativamente alta (visible) longitud de onda,

condiciones ideales para su uso en tubos de rayos catódicos. Posteriormente, comunicaron detalles espectroscópicos del material, tales como las cuatro primeras bandas de excitación $4f \rightarrow 5d$, las bandas de emisión y el desplazamiento de Stokes. El Ce:YAG también se utiliza en lámparas de mercurio-vapor a menudo junto a fosfato-vanadato de yttrio, y, puesto que presenta cortos tiempos de emisión desde estados electrónicos excitados, es adecuado su uso en fotomultiplicadores.

Sin embargo, el uso con interés en este trabajo es en el marco de la SSL puesto que, en este momento, Ce:YAG es el más usado conversor de luz azul a amarillo en LEDs de luz blanca. Esta conversión de luz está asociada a estados locales del Ce^{3+} en el defecto puntual. Usado como material de revestimiento en diodos de luz azul de InGaN, Ce:YAG convierte parte de la luz azul en amarilla, de modo que la luz emitida total aparece blanca(Fig. 1.4) [29].

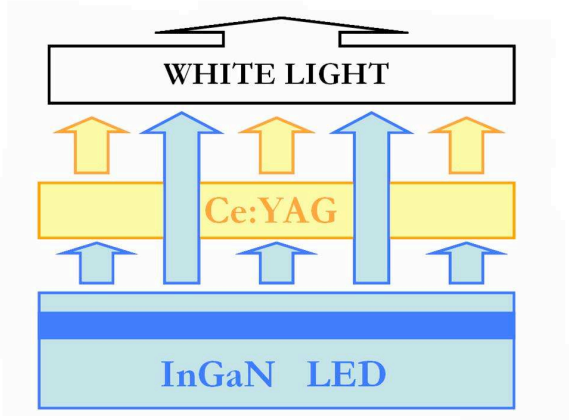

Figura 1.4: Esquema de Ce:YAG como convertidor de luz azul-amarillo en un dispositivo SSL.

Esta disposición ofrece una eficiencia energética similar a la de las lámparas fluorescentes pero es necesario mejorar la eficiencia, la cobertura del espectro y el comportamiento respecto a desactivaciones de emisión dependientes de temperatura (*thermal quenching*) de cara a satisfacer las necesidades crecientes del mercado de SSL [30]. De hecho, el control del color de un dispositivo SSL es una de las cuestiones más importantes en el éxito de estas tecnologías [31]. En este contexto, el codopaje aparece como uno de los métodos usados para el control del color [32, 33, 34, 35, 36], no solo por la habilidad de los codopantes como coactivantes [34], sino también por los desplazamientos de longitud de onda que provocan [37, 38, 39, 40].

1.6 *Objetivos de esta tesis y estructura del manuscrito*

Al inicio de este trabajo, nos enfrentamos a dos temas diferentes relacionados con la luminiscencia del Ce:YAG.

Por un lado, cálculos previos realiazdos en nuestro grupo utilzando el método de *cluster* embebido [41] consiguen reproducir adecuadamente los perfiles de los espectros de absorción y emisión pero no describen correctamente el desplazamiento Stokes (diferencia de energia entre los máximos de absoción y emisión) experimental, poniendo de manifiesto la importancia de las estructuras locales de los estados fundamental y excitados a nivel atómico en la absorción y luminiscencia de estos materiales. Medidas recientes dan cuenta de un desplazamiento Stokes más pequeño [42], más cercano al valor calculado en la Ref. [41]. Aun así, dicho cáculo subestima notablemente este valor. En este contexto, pensamos en la posibilidad de realizar una descripción más realista del YAG como matriz para el Ce^{3+}, teniendo en cuenta los defectos intrínsecos de tipo *antisite* que aparecen en el YAG durante la síntesis [43] y que se sabe modifican los patrones de luminiscencia de YAG y de Ce:YAG [44, 45, 46].

Por otro lado, en el contexto del codopaje y el control del color en dispositivos SSL que contienen Ce:YAG, se conoce que los iones Gd^{3+} y La^{3+} desplazan la primera absorción $4f \rightarrow 5d$ a mayores longitudes de onda (desplazamiento al rojo), mientras que los iones Ga^{3+} y In^{3+} desplazan esa absorción a menores longitudes de onda (desplazamiento al azul). Sin embargo, poco se sabía sobre las absorciones $4f \rightarrow 5d$ y, además, poco se sabía sobre la relación entre la estructura local de los defectos y los desplazamientos al rojo/azul inducidos por codopaje, más allá de reglas empíricas que relacionan el codopaje con iones grandes a un desplazamiento al rojo (si éstos sustituyen a un Y^{3+} de la red) o al azul (si sustituyen a un Al^{3+} de la red) [32, 39, 40].

Un necesario primer punto en común para abordar ambos problemas era encontrar métodos fiables y asquibles para describir al sólido matriz YAG y, progresivamente ir incorporando defectos que presentan niveles de complejidad creciente. El primer nivel es la presencia de defectos simples en YAG, sean defectos *antisite* o cationes como Ce^{3+}, La^{3+} o Ga^{3+}. Llamamos a todos ellos defectos simples en este trabajo, pese a que cada defecto *antisite* ya contiene dos cationes con posiciones intercambiadas. El siguiente paso es el tratamiento del defecto de interés en este trabajo, Ce^{3+} en YAG junto a defectos *antisite* o cationes en cuanto modifican su estructura, estructura electrónica y, finalmente, luminiscencia. Estas celdas de YAG conteniendo Ce^{3+} más otro catión o *antisite*(s) se llaman defectos dobles a lo largo de este trabajo.

En cuanto a nomenclatura, en este trabajo usamos la etiqueta Ce:YAG para referirnos a celdas de YAG conteniendo un átomo de Ce por celda unidad. Las celdas que contienen defectos simples de La y Ga se llaman La:YAG y Ga:YAG en este trabajo, respectivamente. Como veremos despues, Ce y La ocupan ambos posiciones originales de Y en la celda de YAG. Sin embargo, Ga, que sustituye a un átomo de Al, puede por tanto colocarse en una posición pseudotetraédrica y pseudooctaédrica. Así, la etiquetas Ga_{tet}:YAG y Ga_{oct}:YAG se usan en este trabajo para los materiales que contienen Ga en entorno pseudotetraédrico y pseudooctaédrico respectivamente. Los materiales que contienen uno o dos defectos *antisite* se llaman 1AD:YAG y 2AD:YAG en este manuscrito, respectivamente. Respecto a los defectos dobles, usamos las etiquetas Ce,La:YAG, Ce,Ga_{oct}:YAG y Ce,Ga_{tet}:YAG para los corresponientes materiales codopados. La etiqueta general Ce,ADs:YAG se usa

para denominar celdas que contienen Ce_Y y *antisite* defects. Específiamente, usamos Ce,1AD:YAG para nombrar al material que contiene un átomo de Ce y un defecto *antisite* por celda y y Ce,2AD:YAG para el material con un átomo de Ce y dos defectos *antisite*.

En este punto, debemos tener en cuenta que nuestros problemas estructural y espectroscópico se ajustan a diferentes enfoques teóricos, y debemos realizar un análisis estructural fiable de nuestros materiales como entidades macroscópicas teniendo en cuenta también las estrucuras a nivel atómico que dan lugar a las propiedades espectroscópicas, estudiadas a nivel mucho más local.

Asi, este manuscrito está orgenizado del modo siguiente:

Una primera parte comprende el contexto metodológico de las técnicas usadas en nuestros cálculos. El capítulo 2 ofrece un breve repaso a los métodos usados en la química cuántica, enfatizando los aspectos propios de cálculos en sólidos y nuestras elecciones metodológicas concretas para el estudio del Ce:YAG. Depués de esta introducción metodológica, los capítulos 3 y 4 abarcan los métodos usados en este trabajo para la obtención de propiedades estructurales y espectroscópicas respectivamente. En el capítulo 3 están recogidos los aspectos básicos de la teoría del funcional de la densidad (DFT) y a particularidades del programa usado en este trabajo, que utiliza condiciones de contorno periódicas (PBC) en el contexto de la DFT (PBC-DFT). El capítulo 4 da una idea general del método de *cluster* embebido utilizado para diferenciar la impureza del resto del cristal de YAG, seguido de una descripción del nivel de teoría que describe adecuadamente la naturaleza multiconfiguracional y la estructura electrónica de la impureza (método del campo autoconsistente de espacio activo completo (CASSCF)/ método de perturbaciones de segundo orden de espacio activo completo (CASPT2)).

La segunda parte contiene los resultados obtenidos en nuestros distintos sistemas. Podemos considerar la descripción de la luminiscencia de Ce:YAG bajo los efectos de iones codopantes o defectos *antisite* el objetivo último de esta tesis. Sin embargo, este problema final de la luminiscencia de Ce:YAG afectada por codopantes o defectos antisite, no es sino la punta del iceberg de un problema complejo que contiene muchos ingredientes.

Primeramente, se necesita una descripción precisa y fiable del YAG puro y perfecto porque es el sólido matriz, presente, de un modo u otro, en todos nuestros cálculos. Así, presentamos en el capítulo 5 nuestros resultados en el estudio de las propiedades estructurales y de estructura electrónica del YAG puro y perfecto en su forma *bulk*, cotejado con cálculos realizados en otros sólidos que contienen Y, Al y O y que confirman la suficiente fiabilidad de los pseudopotenciales y los conjuntos de base generados específicamente para este trabajo.

El paso natural tras el estudio del YAG puro y perfecto es el estudio separado de los defectos individuales, con objeto de establecer una referencia para los subsiguientes cálculos incluyendo dobles defectos. Así, los capítulos 6 y 7 contienen el estudio a nivel atómico del YAG dopado con Ce, La o Ga y del YAG conteniendo defectos *antisite* respectivamente. Todos estos pasos "previos" son interesantes *per se*, debido a la escasa informacion disponible sobre estos sistemas.

Una vez que el estudio individual de los defectos individuales está completado, pre-

sentamos en el capítulo 8 los dos principales objetivos de este trabajo: el estudio de la luminiscencia de Ce:YAG afectada, por un lado, por la presencia de codopantes y, por otro, por la presencia de defectos *antisite*. En este capítulo, prestamos antencion a la descripción de la metodología empleada desde el cálculo estrucutural (focalizado en las distorsiones en el entorno del Ce_Y) hasta el análisis espectroscópico (en términos de diferentes niveles de distorsión, lo cual tiene por objetivo poner en relieve la relación entre estructura y espectroscopía en estos materiales). Además, presentamos los niveles energéticos $4f$ y $5d$ calculados par el Ce:YAG (sin codopantes y sin defectos *antisite*) como referencia para futuras comparaciones con materiales con dobles defectos. Además, comparamos este espectro con el espectro de Ce:YAG previamente calculado en nuestro grupo, tambien bajo la aproximacion de potenciales modelo *ab initio*(AIMP), pero que usa coordenadas de *cluster* calculadas con métodos de función de onda y que incluye efectos espín-órbita [41].

Después de este capítulo introductorio, los resultados del estudio detallado de los materiales Ce,La:YAG y Ce,Ga:YAG están recogidos en los capítulos 9 y 10 respectivamente. En estos materiales codopados, usamos un método PBC-DFT para estudiar la estabilidad de los diferentes pares de defectos que se pueden presentar en la red seguido de un estudio estructural y de estructura electrónica de los más estables en cada caso. Las estructuras locales distorsionadas alrededor de Ce obtenidas de ese modo, se utilizan en cálculos de *cluster* embebido de tipo CASSCF/CASPT2 para obtener los correspondientes espectros de absorción. Los despalzamientos al rojo/azul encontrados, en acuerdo con los resultados experimentales, se analizan en términos de la influencia de las distorsiones y los efectos electrónicos de los átomos codopantes sobre los componentes de la transición $4f \rightarrow 5d$.

El capítulo 11 incluye el análisis de estabilidad, estructura y estructura electrónica realizado en Ce,1AD:YAG y Ce,2AD:YAG. Presentamos información sobre los shifts inducidos por los defectos *antisite* sobre el espectro de absorción siguiendo el mismo esquema de análisis realizado para el Ce:YAG codopado. Además, este capítulo contiene los resultados de un estudio preliminar sobre el desplazamiento Stokes de Ce,1AD:YAG.

Tras una sección dedicada a conclusiones específicas, las tablas de datos se incluyen al final de cada capítulo dedicado a resultados.

El capítulo 12 contiene una lista con los resultados generales más importantes obtenidos a lo largo de esta tesis.

Para finalizar, incluimos dos apéndices con información adicional: el apéndice A contiene el trabajo adicional realizado fuera del contexto de la luminiscencia del Ce:YAG y en el apéndice B se incluyen las publicaciones científicas originadas a lo largo de este trabajo.

Part I

METHODOLOGY

Chapter 2

Methodological background

Scientists have been dealing with the description of the chemical and physical properties of matter long since. Twenty centuries after the Greek term *atom* as an indivisible object, throughout the discovery of the electron in 1897 and the first modern models of the atom as a positively charged nucleus neutralized by negatively charged electrons (Thomson and his student's Rutherford improvement, 1910), scientist established a model of the atom consisting of a Z number of electrons orbiting around a $+Ze$ charged nucleus. However, a huge number of experimental observations were incompatible with this *orbiting* electrons, due to, according to the electromagnetic theory, they should decay, radiating energy and collapsing onto the nucleus. This kind of incompatibility led to the idea that matter at this atomic scale does not obey the laws of classical mechanics and electromagnetism, but a different set of laws, called *quantum mechanics* (Bohr, 1913 [47]). To solve the problem of electron radiation, Bohr postulated the existence of certain orbits with specific energies and radii for which the electron would not radiate. The promotion of an electron from one of these orbits to another could only take place through the absorption of emission of a *quantum* of energy. In only two decades, this ideas grew up over a new mathematical language and were largely developed. Schrödinger equation, published in 1926 [48], was soon applied to multi-electronic atoms and polyatomic systems, both molecules (Heitler and London, 1927 [49]) and solids (Bloch, 1928 [50]).

The impossibility of solving the Schrödinger equation exactly for systems with more than two particles incited the scientific community to adopt a large number of (physically meaningful) approximations and implement them in methods of increasing complexity. Along the past decades, more accurate methods have been appearing targeting the wide variety of many-body problems and the development of more efficient and accurate tools is an open researching field itself.

There is no a universal method to solve the many-body problem whatever its nature is. Then, the first step when facing a many-body problem is a careful choice of the calculation method taking into account the nature of our system, the properties of interest and the computational resources available. This chapter is aimed to present an overview of the basis of the most used quantum-mechanical approaches, forming the backdrop to our specific choices for the problem under study: luminescence of Ce-doped yttrium aluminum

garnet (Ce:YAG).

It is divided in six sections. After a brief introduction on the Schrödinger equation and the Born-Oppenheimer approximation (Section 2.1), the cornerstone method in quantum chemistry is presented: the Hartree-Fock approach (Section 2.2). Beyond, some methods appear in order to deal with electronic *correlation* absent in HF; they are presented in Section 2.3. The quality of a calculation depends not only on the accuracy of the method of choice but also on the quality of the basis set used to represent our system. Thus, a brief overview on basis sets is present in Section 2.4. Yttrium aluminum garnet, an ionic solid, is a main component of all our calculations. Thus, the general lines of study of problems in solid state are presented in Section 2.5. Finally, our methodological choices in the study of luminescence of Ce:YAG are outlined in Section 2.6.

2.1 The time-independent Schrödinger equation and the Born-Oppenheimer approximation

In general terms, the matter in stationary states is able to be described according to the picture of interacting particles (nuclei and electrons), sometimes under the influence of an external potential, through the time-independent non relativistic Schrödinger eigenvalue equation :

$$\widehat{H}\Psi = E_{tot}\Psi \tag{2.1}$$

where both the Hamiltonian operator $\widehat{H}$ and the wavefunction Ψ depend on both the whole set of nuclear coordinates $\vec{R}_I$ and the whole set of electronic coordinates $\vec{x}_i$, being included in $\vec{x}_i$ electron positions $\vec{r}_i$ and spins s_i.

Formally, we can write the Hamiltonian operator of a system with M nuclei and N electrons in the following general way (atomic units):

$$\begin{aligned}\widehat{H} = &-\sum_{I=1}^{M}\frac{1}{2M_I}\bigtriangledown_I^2 - \sum_{i=1}^{N}\frac{1}{2}\bigtriangledown_i^2 + \frac{1}{2}\sum_{I=1}^{M}\sum_{J\neq I}^{M}\frac{Z_I Z_J}{|\vec{R}_I - \vec{R}_J|} \\ &+ \frac{1}{2}\sum_{i=1}^{N}\sum_{j\neq i}^{N}\frac{1}{|\vec{r}_i - \vec{r}_j|} - \sum_{I=1}^{M}\sum_{i=1}^{N}\frac{Z_I}{|\vec{R}_I - \vec{r}_i|}\end{aligned} \tag{2.2}$$

The two first terms of the above Hamiltonian are the kinetic energy of the nuclei ($\widehat{T}_N$) and of the electrons ($\widehat{T}_e$) respectively, the third term is the nuclear-nuclear repulsion (V_{NN}) , the fourth one is the (V_{ee}) electron-electron interaction and the last one is the electron-nuclear interaction (V_{Ne}). V_{Ne} is also often termed as external potential V_{ext} since this potential comes from a “external" source to the electron. Then, the external potential is not necessary limited to the nuclear field but may include external magnetic or electric fields, etc... The general scheme above is valid even when this potential is replaced by a pseudopotential, which takes into account effects of the *core* electrons as well. This Hamiltonian neglects realativistic effects, in particular the spin-orbit interaction between the

magnetic moment arising from the electron orbiting around the nucleus and the magnetic moment of the electron. For simplicity, we use the non-relativistic Hamiltonian all along this chapter. However, we include scalar relativistic effects in our calculations; details will be described later.

In practice, equation 2.1 is indeed almost impossible to cover in a full quantum mechanical framework, due to the two-body nature of the repulsive coulombic interactions. Exact analytic solutions are only available for hydrogenoid atoms or for the H_2^+ molecule and exact numerical solutions are available only for very few atoms and small molecules [51]. A major approximation is then adopted: the *Born-Oppenheimer* separation of nuclear and electronic degrees of freedom. As a first observation, nuclei are heavier than electrons (even the lightest atom, H, is about 2000 times heavier than an electron). Then, we can have a picture of electrons moving faster than nuclei, in average, if energy would equally be distributed among them. Born and Oppenheimer (BO), showed in 1927 [52] that to a very good approximation the nuclei in a molecule are stationary with respect to the electrons and then, the latter are moving in the field of the instantaneous fixed nuclei. Thus, if the nuclei are fixed in space and do not move, their kinetic energy $\widehat{T}_N$ is taken as zero and the potential energy due to the internuclear repulsion is a constant. Actually, the nuclei are not stationary, but show vibrations of small amplitude around equilibrium positions. Due to this nuclear movement, a certain non-adiabatic coupling between electronic states appears trough a non-zero $\widehat{T}_N$ term. This coupling is only small if these electronic states are well separated in energy, which is normally the case. However, the BO approximation breaks down when two or more electronic states are near degeneracy, e.g. in Jahn Teller and Renner-Teller distortions [53, 54], conical intersections of different potential surfaces [55] or electron-phonon coupling in metals [56].

In cases where the BO approximation holds, the unknown total wavefunction Ψ, depending on both nuclear and electronic coordinates ($\Psi(\vec{R},\vec{r})$) can be approximately written as:

$$\Psi(\vec{R},\vec{r}) = \Psi_n(\vec{R})\Psi_e(\vec{r},\vec{R}) \tag{2.3}$$

In the product above, $\Psi_n(\vec{R})$ is the nuclear wavefunction and does not depend on the electronic coordinates, whereas $\Psi_e(\vec{r},\vec{R})$ is the electronic wavefunction, depending on both electronic and nuclear coordinates. Strictly speaking, the Born-Oppenheimer approximation involves to take $\vec{\nabla}_{\vec{R}}\Psi_e$=0, that is, the variation of the electronic wavefunction with the nuclei positions is null. The main consequence is that, in the electronic wavefunction $\Psi_e(\vec{r},\vec{R})$, the nuclear coordinates $\vec{R}$ are no longer variables but parameters, which will be denoted as $\Psi_e(\vec{r};\mathbf{R})$ from now on.

The complete Hamiltonian $\widehat{H}$ can be then expressed as

$$\hat{H} = \hat{T}_N + \hat{H}_e \tag{2.4}$$

where

$$\hat{H}_e = \hat{T}_e + V_{ee} + V_{Ne} + V_{NN} \tag{2.5}$$

is the electronic Hamiltonian operator. The term $\widehat{V}_{NN}$ is a constant number for each position of the nuclei, that is, for each set of parameters $\mathbf{R}$, and acts shifting the eigenvalues

by some constant amount.

The electronic Hamiltonian only acts on the electronic part of the wavefunction $\Psi_e(\vec{r}, \mathbf{R})$ and the following electronic Schrödinger equation has to be solved:

$$\hat{H}_e \Psi_e(\vec{r}; \mathbf{R}) = E_e(\mathbf{R}) \Psi_e(\vec{r}; \mathbf{R}) \tag{2.6}$$

Equation 2.6 is solved for each set of nuclear coordinates $\vec{R}_I$, that is, for each nuclear configuration, finding an electronic wavefunction $\Psi_e(\vec{r}; \mathbf{R})$ and a electronic energy E_e, which also depends parametrically on the nuclear coordinates $\mathbf{R}$. These eigenvalues $E_e(\mathbf{R})$ are used to build the nuclear potential energy surfaces.

If we now introduce the product wavefunction (Eq 2.3) in the global time-independent Schrödinger equation 2.1, considering the total Hamiltonian 2.2

$$\begin{aligned} \widehat{H} \Psi_n(\vec{R}) \Psi_e(\vec{r}, \vec{R}) &= E_{tot} \Psi_n(\vec{R}) \Psi_e(\vec{r}, \vec{R}) \\ (\hat{T}_e + V_{ee} + V_{Ne} + V_{NN} + \hat{T}_N) \Psi_n(\vec{R}) \Psi_e(\vec{r}, \vec{R}) &= E_{tot} \Psi_n(\vec{R}) \Psi_e(\vec{r}, \vec{R}) \end{aligned} \tag{2.7}$$

and take into account the electronic Schrödinger equation 2.6 and we adopt the approximation

$$\hat{T}_N \Psi_e(\vec{r}, \vec{R}) = 0 \tag{2.8}$$

then we obtain the nuclear Schrödinger equation

$$(\hat{T}_N + E_e) \Psi_n(\vec{R}) = E_{tot} \Psi_n(\vec{R}) \tag{2.9}$$

2.1.1 The electronic problem

In order to solve the electronic Schrödinger equation 2.6, it is necessary first to build the electronic Hamiltonian for the target system, and then find its eigenfunctions and corresponding eigenvalues. Once the wavefunctions are determined, all properties of interest can be obtained as expectation values of the proper operator.

Unfortunately, no strategy for solving Schrödinger equation exactly is known, becoming essential both efficient development and implementation of mathematical methods able to provide approximate solutions to such eigenvalue equations. Two fundamental methods are widely used in this context: the variational method and perturbation theory.

The variational principle states as follows: *"The energy computed for a trial well behaved wavefunction Ψ_{trial} is always greater than or equal to the true energy of the ground state Ψ_0 "*.

$$\langle \Psi_{trial} \mid \widehat{H}_e \mid \Psi_{trial} \rangle = E_{trial} \geq E_0 = \langle \Psi_0 \mid \widehat{H}_e \mid \Psi_0 \rangle \tag{2.10}$$

Then, the procedure for finding the ground state energy and wavefunction starts from minimizing the energy related to each one of the N-electron trial wavefunctions with respect to some adjustable parameters α called *variational parameters* :

$$E_0 = \min_\alpha E(\Psi) = \min_\alpha \langle \Psi \mid \widehat{H}_e \mid \Psi \rangle \tag{2.11}$$

To implement this method one needs to know the Hamiltonian $\widehat{H}_e$ whose energy levels are sought and one needs to construct a trial wavefunction belonging to a subset of acceptable (continuous everywhere and quadratic integrable) wavefunctions, which is different depending on the algebraic approach chosen to solve the electronic problem.

In perturbation theory approaches, the Schrödinger equation is modeled by means of a perturbed Hamiltonian $\hat{H}$ sum of a reference Hamiltonian $\hat{H}_0$ and a time independent perturbation $\hat{P}$

$$\hat{H}_e = \hat{H}_0 + \hat{P} \tag{2.12}$$

where the energy levels and wavefunctions of the reference Hamiltonian $\hat{H}_0$ can be easily found in principle. The success of this approach depends strongly on how well the model $\hat{H}_0$ represents the true problem, i.e. how small is the perturbation $\hat{P}$.

Compared to perturbation theory, the variational method can be more robust in situations where it is hard to determine a good unperturbed Hamiltonian and it is used in Hartree-Fock and some post-Hartree-Fock methods (such as CI and multiconfigurational methods). On the other hand, in cases where there is a good unperturbed Hamiltonian, perturbation theory can be more efficient than the variational method.

At this point, it is necessary to find a subset of acceptable wavefunctions in our way of approximation to the solutions of the Schrödinger equation.

The simplest approach to a many-electron wavefunction Ψ_e is based on a simple product of one-electron wavefunctions (or Hartree product; $\Psi_H = \varphi_1(\vec{x}_1)\varphi_2(\vec{x}_2)\ldots\varphi_N(\vec{x}_N)$). However, it is not acceptable as a trial wavefunction for fermions since it assigns a particular one-electron function to a particular electron and violates the fact that electrons are indistinguishable. Moreover, it does not fulfill the Pauli exclusion principle (a Hartree product is not antisymmetric with respect to the interchange of the coordinates of any two electrons).

Antisymmetry in the wavefunction can be achieved using a Slater determinant (SD). Fock and Slater, based on the original work of Hartree [57], proposed in 1930 an antisymmetrical many-electron wavefunction in the form of a Slater determinant [58, 59]:

$$\Psi_{HF}(\vec{x}_1, \vec{x}_2 ... \vec{x}_n) = \frac{1}{\sqrt{N!}} \begin{vmatrix} \varphi_1(\vec{x}_1) & \varphi_2(\vec{x}_1) & \ldots & \varphi_N(\vec{x}_1) \\ \varphi_1(\vec{x}_2) & \varphi_2(\vec{x}_2) & \ldots & \varphi_N(\vec{x}_2) \\ \vdots & \vdots & \ddots & \vdots \\ \varphi_1(\vec{x}_N) & \varphi_2(\vec{x}_N) & \ldots & \varphi_N(\vec{x}_N) \end{vmatrix} \tag{2.13}$$

where the one-electron functions $\varphi_i(\vec{x}_j)$ are called *spin orbitals*, and are composed of a spatial orbital $\phi_i(\vec{r})$ and a spin component α or β

$$\varphi(\vec{x}) = \phi(\vec{r})\sigma(s); \qquad \sigma = \alpha, \beta \tag{2.14}$$

The spin functions have the property that they are orthonormal ($< \alpha \mid \alpha >=< \beta \mid \beta >= 1$ and ($< \alpha \mid \beta >=< \beta \mid \alpha >= 0$) and for computational convenience, the spin orbitals are chosen orthogonal themselves ($\int \varphi_i^*(\vec{x})\varphi_j(\vec{x})\vec{dx} =< \varphi_i \mid \varphi_j >= \delta_{i,j}$).

If a single SD is considered to construct the trial wavefunction, and the variational principle is applied, we arrive to the first method to solve the many-electron Schrödinger

equation in an *ab initio* fashion (i.e. without resorting to empirical data): the Hartree-Fock method.

2.2 Hartree-Fock approximation

The historical background of all the quantum chemical calculations lies on the Hartree-Fock (HF) approach and even density functional theory (chapter 3), a quite different theory regarding the physical point of view, contains many concepts intimately related to the Hartree-Fock ones.

In order to solve the time-independent Schrödinger equation for a multi-electronic atom or molecule (as described in the Born Oppenheimer approximation and under the variational approach), Hartree-Fock theory approach applies the variational principle to a trial wavefunction constructed with a single Slater determinant in order to find the one with the lowest energy. The only flexibility here comes from spin orbitals, and then $\{\varphi_i\}$ are varied under orthonormality constraints. The consequence of the choice of a single Slater determinant is that each electron is subject to the average influence of the other electrons, i.e. HF is a mean field theory.

The Hartree-Fock energy is the expected value for the Hamiltonian using the above single Slater determinant (2.13):

$$E_{HF} =< \Psi_{HF} \mid \hat{H} \mid \Psi_{HF} >= \sum_{i}^{N}(i \mid \hat{h} \mid j) + \frac{1}{2}\sum_{i}^{N}\sum_{j}^{N}(ii \mid jj) - (ij \mid ji) \tag{2.15}$$

where

$$(i \mid \hat{h} \mid j) = \int \varphi_i^*(\vec{x}_1)\Big\{ -\frac{1}{2}\nabla_1^2 - \sum_{I}^{M}\frac{Z_I}{\mid \vec{R}_I - \vec{r}_1 \mid}\Big\}\varphi_i(\vec{x}_1)d\vec{x}_1 \tag{2.16}$$

is the *monoelectronic* contribution to the energy from kinetic and electron-nucleus attraction, and

$$(ii \mid jj) = \int\int \mid \varphi_i(\vec{x}_1) \mid^2 \frac{1}{\mid \vec{r}_1 - \vec{r}_2 \mid} \mid \varphi_j(\vec{x}_2) \mid^2 d\vec{x}_1 d\vec{x}_2 \tag{2.17}$$

$$(ij \mid ji) = \int\int \varphi_i^*(\vec{x}_1)\varphi_j(\vec{x}_1)\frac{1}{\mid \vec{r}_1 - \vec{r}_2 \mid}\varphi_j^*(\vec{x}_2)\varphi_i(\vec{x}_2)d\vec{x}_1 d\vec{x}_2 \tag{2.18}$$

are the so-called *Coulomb* and *exchange* integrals and are two-electron contributions to the energy.

In the double summation of the expression 2.15 for the Hartree-Fock energy, the term $i = j$ is allowed. It means that the term $+\frac{1}{2}\sum_i^N\sum_j^N(ii \mid jj)$ describes a Coulomb interaction of the charge distribution of an electron with itself. As a consequence, even if there is computed the energy of a one-electron system with no repulsion energy between electrons, the result is incorrectly non-zero. This is called *self-interaction* and has no physical sense. However, the exchange term $-\frac{1}{2}\sum_i^N\sum_j^N(ij \mid ji)$ solves it, since for $i = j$, the Coulomb and exchange integrals are identical and both reduce to

$$\int\int \mid \varphi_i(\vec{x}_1) \mid^2 \frac{1}{\mid \vec{r}_1 - \vec{r}_2 \mid} \mid \varphi_i(\vec{x}_2) \mid^2 d\vec{x}_1 d\vec{x}_2$$

They enter with opposite signs in the equation and the self-interaction is canceled. This problem is solved in the Hartree-Fock approach but it is a major obstacle in density functional theory (DFT). It will be shown in Chapter 3 that, due to the approximate character of the DFT exchange term, obtained in an independent way than the repulsion term, the self-interaction is not canceled and there is an intrinsic error associated to it.

Since E_{HF} depends on the spin orbitals, the variational freedom is in the choice of a set of them which gives the lowest value for E_{HF}. *Lagrange multipliers* ε_i are then introduced to minimize E_{HF} fulfilling orthonormality constraints for φ_i. That results in the Hartree-Fock equations

$$\hat{f}(1)\varphi_i(1) = \varepsilon_i\varphi_i(1), \qquad i = 1, 2 \dots N \tag{2.19}$$

These N equations are eigenvalue-like equations where the Lagrangian multipliers are the eigenvalues of the one-electron Fock operator $\hat{f}$

$$\hat{f}(1) = -\frac{1}{2}\nabla_1^2 - \sum_I^M \frac{Z_I}{\mid \vec{r}_1 - \vec{R}_I \mid} + \hat{V}_{HF}(1) \tag{2.20}$$

The first two terms are the kinetic energy and the potential energy due to the electron-nucleus attraction and $\hat{V}_{HF}$ is the *Hartree-Fock potential*, which is an average repulsive potential experienced by the $i-th$ electron due to the remaining $N-1$ ones. Thus, the two-electron repulsion scalar operator $\frac{1}{|\vec{r}_i - \vec{r}_j|}$ is replaced by this simple one-electron operator $\hat{V}_{HF}$. $\hat{V}_{HF}$ has the following two components:

$$\hat{V}_{HF}(\vec{x}_1) = \sum_j^N (\hat{J}_j(\vec{x}_1) - \hat{K}_j(\vec{x}_1)) \tag{2.21}$$

- The *Coulomb operator* $\hat{J}$ is defined as

$$\hat{J}_j(\vec{x}_1) = \hat{J}_j(\vec{r}_1) = \int \mid \varphi_j(\vec{x}_2) \mid^2 \frac{1}{\mid \vec{r}_1 - \vec{r}_2 \mid} \vec{dx}_2 = \int \mid \phi_j(\vec{r}_2) \mid^2 \frac{1}{\mid \vec{r}_1 - \vec{r}_2 \mid} \vec{dr}_2 \tag{2.22}$$

  and represents the potential that an electron with position and spin $\vec{x}_1$ experiences due to the average charge distribution of another electron in spin orbital $\varphi_j(\vec{x}_1)$, integrated over all the space and spin coordinates. Since the result of application of $\hat{J}$ on a spin orbital depends only on the value of the spin orbital at position $\vec{r}_1$, this operator and the corresponding potential are called *local*.

- The *Exchange operator* $\hat{K}$ has no classical interpretation and can only be defined through its effect when operating on a spin orbital:

$$\hat{K}_j(\vec{x}_1)\varphi_i(\vec{x}_1) = \int \varphi_j^*(\vec{x}_2) \frac{1}{\mid \vec{r}_1 - \vec{r}_2 \mid} \varphi_i(\vec{x}_2) \vec{dx}_2 \varphi_j(\vec{x}_1) \tag{2.23}$$

  This operator leads to the exchange of the variables in the two spin orbitals. The result of operating with $\hat{K}$ on $\varphi_i(\vec{x}_1)$ depends on the value of φ_i in all the points of the space since now φ_i is related to $(\vec{x}_2)$ as the variable over which is integrated. Consequently, this operator and the corresponding potential are called *non local* or *integral*.

These definitions lead to the fact that the expectation values for $\hat{J}$ and $\hat{K}$ are the exchange and coulomb integrals given in eqs. 2.17 and 2.18. Introducing a basis set transforms the Hartree-Fock equations 2.19 into the Roothaan-Hall equations.

The Koopmans' theorem In 1933, Koopmans [60] provided a physical meaning to the orbitals energies from eq. 2.19, stating that the orbital energy ε_i obtained from Hartree-Foch theory is the ionization energy (with opposite sign) associated to removing an electron from that particular orbital φ_i

$$\varepsilon_i = E_N - E^i_{N-1} = -IE(i) \tag{2.24}$$

This statement is valid within the *frozen orbital* approach, where the φ_i are constant in both states before and after removing the electron.

The Roothaan-Hall equations Monoelectronic orbitals can be represented by means of a basis set. Many possibilities have been explored since the early times of quantum mechanics, based on the general characteristics of the electronic problem and on the particular features of the studied problem.

The first step is expanding the one-electron wavefunctions in a generic basis set described by the orbitals $|\phi_\mu\rangle$. Then, the Hartree-Fock (or Kohn-Sham orbitals, see Chapter 3) φ are written as a linear combination of these basis orbitals:

$$\varphi_j(\vec{r}) = \sum_{\mu=1}^{M} c_{j\mu}\phi_\mu(\vec{r}) \tag{2.25}$$

This sum runs over all the basis functions up to the *size* (M) while $c_{j\mu}$ are the expansion coefficients of the of the wavefunction j.

In these tems, equation 2.19 becomes a generalized linear eigenvalues problem:

$$\mathbb{F}\mathbb{C} = \Lambda\mathbb{S}\mathbb{C} \tag{2.26}$$

with

$$\mathbb{F}_{\alpha\beta} = \langle\phi_\alpha|\widehat{F}|\phi_\beta\rangle; \qquad \widehat{F} = -\frac{\hbar^2}{2m}\nabla^2 + V_{ext}(r) + \sum_{j=1}^{N}(\widehat{J}_j - \widehat{K}_j) \tag{2.27}$$

the overlap matrix elements given by

$$\mathbb{S}_{\alpha\beta} = \langle\phi_\alpha|\phi_\beta\rangle \tag{2.28}$$

and Λ a diagonal matrix with $\Lambda_i = \varepsilon_i$.

In the Kohn-Sham case, the one-electron effective Hamiltonian operator involved in these equations is

$$\widehat{h}_{KS} = -\frac{1}{2}\nabla^2 + V_{ext}(r) + \int \frac{\rho(\vec{r}_2)}{r_{12}}\vec{dr}_2 + E_{XC}[\rho] \tag{2.29}$$

All those equations were derived independently by Roothaan and Hall in the 50s, and are consequently called *Roothaan-Hall* equations [61].

Restricted and unrestricted Hartree-Fock If the system under study has an even number of electrons (*closed shell* system), the condition of having two electrons in each spatial orbital (one with α and one with β spin) is normally imposed. Then, a unique set of spatial orbitals is used, being each one doubly occupied. Wave functions generated in this way (SD 2.13) define the *restricted Hartree-Fock* (RHF) approach. For *open shell* systems, where the number of electrons of each spin are not equal, *unrestricted HartreeÚFock* (UHF) theory uses different sets of orbitals for the α and β electrons. This is known as the *different orbitals for different spins* (DODS) method. The result is a pair of coupled Roothaan equations, known as the Pople Nesbet equations [62]:

$$\begin{aligned} \mathbb{F}^{\alpha}\mathbb{C} &= \Lambda^{\alpha}\mathbb{S}\mathbb{C}^{\alpha} \\ \mathbb{F}^{\beta}\mathbb{C} &= \Lambda^{\beta}\mathbb{S}\mathbb{C}^{\beta} \end{aligned} \tag{2.30}$$

$\mathbb{F}^{\alpha}$ and $\mathbb{F}^{\beta}$ are the Fock matrices for the α and β sets of orbitals, and $\mathbb{C}^{\alpha}$ and $\mathbb{C}^{\beta}$ are the matrices of coefficients for the α and β orbitals, $\mathbb{S}$ is the overlap matrix of the basis functions, and Λ^{α} and Λ^{β} are the diagonal matrices of orbital energies for the α and β orbitals . The pair of equations are coupled because the Fock matrix elements for one spin contains coefficients of both spins due to the orbital has to be optimized in the average field of all other electrons. The UHF method has one drawback: a single Slater determinant with different orbitals for different spins is not a satisfactory eigenfunction of the total spin operator $\hat{S}^2$ and the ground state can be contaminated with excited states. Anyway, UHF method is widely used, not only in Hartree-Fock theory but also in post-Hartree-Fock methods.

In density functional theory, the analogous terms to RHF and UHF are *non-spin polarized* and *spin polarized*. In order to extend the Kohn Sham equations (Section 3.2.2) to systems with different number of α and β electrons, the electronic density has to be decomposed in two independent densities $\rho = \rho_{\alpha} + \rho_{\beta}$, being each of these densities constructed with different Kohn Sham spin orbitals. In the non-spin polarized case, $\rho_{\alpha} = \rho_{\beta}$ and, in the spin polarized case, $\rho_{\alpha} \neq \rho_{\beta}$.

The SCF method The Fock operator depends on the spin orbitals through the Hartree-Fock potential. Since those spin orbitals are the very solutions of the eigenvalue problem to be solved (Eq. 2.19), it becomes not a standard eigenvalue problem but a *pseudo*-eigenvalue problem and must be treated iteratively. The technique used is the so-called *self-consistent field* (SCF) procedure. It starts with the calculation of all one- and two-electron integrals, followed by construction of a set of orbitals with a 'guess' set of coefficients, used to solve the Roothan-Hall or Pople-Nesbet equations. The resulting set of orbitals is then used in the next iteration and so on until the input and output orbitals differ by less than a predetermined threshold.

2.3 Correlation

The main limitation of the Hartree-Fock approximation is that the correct many-body wavefunction is not always well represented by a single Slater determinant. In one hand, there are many other possibly antisymmetric wavefunctions that cannot be written in that way. On the other hand, since the Fock operator is an effective one-electron operator, the Hartree-Fock equations describe a system of N non-interacting particles moving in the field of the average effective potential V_{HF}. In other words, the probability of finding an electron in a region of space does not depend on the position of the other electrons. However, this is not the real picture of the system: each electron suffers from repulsion due to the presence of other electrons, that is, the probability of finding an electron in a region of space depends on the positions of the other electrons. This phenomenon is called *correlation* and it is only reflected in an average way in HF approach. Correlation is usually described in terms of the electron-electron pair distribution (or pair correlation function) $g(\vec{r}_1, \vec{r}_2)$, defined as

$$g(\vec{r}_1, \vec{r}_2) = \frac{\rho_2(\vec{r}_1, \vec{r}_2)}{n} \tag{2.31}$$

where $\rho_2(\vec{r}_1, \vec{r}_2)$ is the pair density (see definition in Section 3.1) and n is the average density of particles. Thus, $g(\vec{r}_1, \vec{r}_2)$ represents the probability of finding an electron at $\vec{r}_2$ given that there is another electron at $\vec{r}_1$. The presence of the first electron discourages the other electron from approaching it because of Coulomb repulsion. Then, $g(\vec{r}_1, \vec{r}_2)$ goes from zero at $\mid \vec{r}_1 \mid = \mid \vec{r}_2 \mid$ to one at infinite distance.

In the completely uncorrelated case, $\rho_2(\vec{r}_1, \vec{r}_2)$ can be written in terms of two independent monoelectronic densities, i.e. $\rho_2(\vec{r}_1, \vec{r}_2) = \rho_1(\vec{r}_1)\rho_1(\vec{r}_2)$. This is the HF case. Actually, in HF there is a small exchange contribution ($\rho_2(\vec{r}_1, \vec{r}_2) = \rho_1(\vec{r}_1)\rho_1(\vec{r}_2)(1 + C_{ex})$) but we can consider that electrons are uncorrelated. On the contrary, the pair density for correlated systems have the following form: $\rho_2(\vec{r}_1, \vec{r}_2) = \rho_1(\vec{r}_1)\rho_1(\vec{r}_2)(1 + C_{ex} + C_{corr})$. The correlation term C_{corr} has an impact on the energy of the system. Then, the definition of correlation in terms of energy, within the *ab initio* framework, was given by Lödwin [63]: *The correlation energy of a given state with respect to a specific Hamiltonian is the difference between the exact eigenvalue of the Hamiltonian and its expected value in the Hartree-Fock approximation.*

$$E_{corr} = E_{exact} - E_{HF} \qquad \text{using the same Hamiltonian for both terms} \tag{2.32}$$

From this definition, E_{corr} is negative, since E_{exact} is lower than E_{HF}, according to the variational principle. Another distinction is done between *dynamic* and *static* correlation. The correlation energy directly related to the $\frac{1}{|\vec{r}_1 - \vec{r}_2|}$ term is called *dynamical* electron correlation because it is related to the "instantaneous" movements of the individual electrons and is known to be a short range effect. This kind of correlation depends both on position and momentum of the electrons, i.e the closer and slower electrons are moving, the higher is the correlation between them. There is another contribution to the correlation energy called *non dynamical* (or *static*) correlation. It is related to the fact that many systems

cannot be described across all the nuclear configurations just in terms of one electronic configuration. It becomes important where different configurations are really close in energy if not degenerated. The static part is associated with electrons avoiding each other in a more "permanent" manner and, then, when *dynamic* correlation is included, it is mandatory to include *non dynamic* correlation as well. Actually, there is no a clear way of separating both kinds of correlation, and such division should be understood as a useful tool to describe the global picture of electronic correlation.

Anyway, the HF wavefunction contains most of the total energy (about 99%), and thus is likely to be a good starting point for more elaborated calculations.

In order to include correlation in quantum mechanical calculations, there are two main lines of *ab initio* approaches arising from two different physical perspectives of the electronic problem: methods where the wavefunction plays a central role, as in HF, and density functional theory, where the electronic density is the fundamental variable.

In the context of quantum-mechanical calculations in molecules, both lines are widely used, depending much the choice on the particular system and properties of interest. However, DFT is the main theory in periodic boundary conditions calculations.

2.3.1 Wavefunction-based methods

Wavefunction-based (or post-Hartree-Fock) methods appear to introduce approximately electron correlation in electronic structure calculations via explicit modeling of the wavefunction. Some of the post-Hartree-Fock methods apply the variational principle to a improved wavefunction beyond the single Slater determinant used in HF. A second group of methods arise from perturbation theory. Moreover, coupled pair theories attempt to introduce electron correlation between pairs of electrons.

2.3.1.1 Correlation from variational principle

Configuration Interaction (CI) In principle, any antisymmetric wavefunction can be written as a linear combination of an infinite number of Slater determinants, although this is surely not so practical. A better strategy is to include a small number of determinants but with a huge contribution on energy. Lett's consider a general multideterminantal wavefunction for an N-electron system as a linear combination of a finite number (ND) of Slater determinants:

$$\Psi(x_1...x_N) = C_0\Psi_{HF}(x_1...x_N) + \sum_{i=1}^{ND} C_i\Psi_i(x_1...x_N) \tag{2.33}$$

where Φ_{HF} is the ground state solution of the Hartree-Fock methods, with N electrons occupying the N spin orbitals lowest in energy $\{\varphi_i(\vec{r}), i = 1...N\}$, and Ψ_i are other determinants corresponding to *excited configurations*.

In order to build these excited determinants, we can consider all the possibilities of promoting one electron from any occupied HF state to any unoccupied state. These are called *single (S) excitations*. In the same way, determinants in which two electrons

have been promoted to unoccupied states are called *double (D) excitations*, *triple (T) excitations* when promoting three electrons, *quadruple (Q) excitations* when promoting four, and so on. It is obvious that the number of possible different determinants is indeed huge, and grows quickly as soon as the number of electrons increases.

The simplest multi-determinantal method consists of expressing the wavefunction in terms of *single (S)*, *double (D)*, *triple (T)*, (and so on) excited determinants and, leaving them untouched, finding the expansion coefficients $\{C_i\}$ that make the energy minimal, with the normalization constraint $\sum_i C_i^2 = 1$

$$\Psi_{CI} = C_0\Psi_{HF} + \sum_{i\in S} C_i^S\Psi_i^S + \sum_{i\in D} C_i^D\Psi_i^D + \sum_{i\in T} C_i^T\Psi_i^T + \dots \tag{2.34}$$

The physical meaning of a wavefunction built in that way lies in the fact that each determinant of the expansion represents an idealized configuration (in the sense of contributing to the real electronic distribution). If every possible determinant were included in this expansion, then every possible idealized electronic state of the system would be taken into account in the wavefunction (called *full CI* wavefunction). Correlation is retrieved here from contributions to the energy arising from Hamiltonian matrix elements between different Slater determinants. The most common CI approximate methods are those in which the expansion is truncated at various levels of excitation, e.g. CISD (truncating at doubles excitations) or CISDT (truncating at triples). Normally the highest level of truncation is CISDTQ, truncating at quadruple excitations, which appears to be near to a full CI. Anyway, these methods are very expensive; CISD scales as M^6 (where M is the basis set size) and CISDQT scales as M^{10} [64].

Multi-configuration self-consistent field (MCSCF) and complete active space self-consistent field (CASSCF) The limitation of building the determinants of the CI expansion with fixed HF one-electron eigenstates can be improved by allowing both the determinants and the expansion coefficients to be variationally optimized. This kind of method receives the name of *multi-configuration self-consistent field* (MCSCF). Basically, this procedure allows for the one-electron orbitals to be partially occupied instead of forcing double occupancy. This is important when two or more electronic configurations of a system are close in energy and have different occupancy. The problem here is not *how many* configurations should be chosen for the optimization procedure, but *how* to choose them. There are no general recipes in that way, and election should be done depending on the problem under consideration. A strong approach about that is the *complete active space self-consistent field method* (CASSCF). The selection is done by dividing the one-electron orbitals into *active* and *inactive* spaces. Orbitals in the inactive space are those which are expected to be negligible on static correlation effects. They are variationally optimized, but their occupation is fixed to two electrons per orbital. Orbitals in the active space are used to construct all possible configurations by allowing excitations to the lowest unoccupied orbitals. Then, the active space includes not only the selected highest occupied (i.e. valence) orbitals but also the lowest unoccupied ones. The active

space orbitals, as well as their occupations, are variationally determined. It can be seen as a full CI calculation in a restricted configurational space [65, 66].

Explicitly correlated methods Using the wavefunction ansatz proposed by Hylleraas in 1929 [67], explicitly correlated methods try to include the correlation explicitly into the trial wavefunction without modifying the Hamiltonian. They These methods are called, in general, *R12* methods, since they use explicit dependences on the interelectronic distance $r_{12} = |\vec{r}_1 - \vec{r}_2|$ (e.g. presence of a cusp condition). Then, appropriate correlation functions $\gamma(\{r_{ij}\})$ are included in the wavefunction

$$\Psi_{R12} = \gamma(\{r_{ij}\})\Psi_M \tag{2.35}$$

leading to a fast convergence not only with $M = CI$ wavefunctions, but also with M =Møller Plesset or coupled cluster ones. The shape of $\gamma(\{r_{ij}\})$ and the parameters involved on it are chosen via Monte Carlo simulations and variational optimization in terms of energy. Although explicitly correlated methods are potentially more accurate then the usual one-electron orbital approaches, algorithms are cumbersome and difficult to implement. Moreover, many of them are only applicable to systems with few electrons, and, as a result, they have not reached yet the efficiency required to become a standard tool.

Quantum Monte Carlo simulations Monte Carlo methods is the generic name given to a large family of techniques used to solve mathematical problems by generating suitable random numbers and observing which of these numbers do obey some property or properties of interest. The method is useful for obtaining numerical solutions of problems with too many degrees of freedom to be solved analytically. The most common application of the Monte Carlo method is Monte Carlo integration. It is used to obtain the value of a multidimensional integral of a function by random evaluation in some points of the whole variable space and then estimating the integral by statistical averaging. In the limit of an infinite number of sampling points, the calculated value is equal to such value obtained by analytical integration. However, for the randomly-chosen finite number of points, the result is given as a average value with an associated deviation. This statistical uncertainty can be diminished by increasing the number of points and, thus, the calculation time.

Since the square of the wavefunction associated to a given set of particles represents a probability function, Quantum Monte Carlo (QMC) simulations are used to calculate the energy of such system using Monte Carlo integration methods [68]. The trial wavefunction in the QMC approach can be constructed by multiplying a HF wavefunction by a correlating Jastrow factor **J**, which contains functionals modeling the nuclear-electron and electron-electron cusps conditions. With this factor, the particle-particle correlation can be treated explicitly, but the many-body integral becomes inseparable, so Monte Carlo integration is the only way to evaluate it efficiently.

2.3.1.2 Correlation from perturbation theory

Møller-Plesset (MP) The MP theory is a special application of Rayleigh Schrödinger (RS-PT) perturbation theory, where a small perturbation $\hat{P} = \lambda\hat{V}$ is added to an unperturbed operator ($\hat{H} = \hat{H}_0 + \lambda\hat{V}$). In MP theory [69], the zeroth-order wave function is an exact eigenfunction of the Fock operator, which thus serves as unperturbed operator. The perturbation is then the correlation potential. Both the perturbed wavefunctions and perturbed energies can be expressed as power series of the strength of the perturbation λ. The correlation potential does not affect the energy at first order. Then, the first non-vanishing perturbation correction beyond the Hartree Fock treatment is the second-order energy. Second (MP2), third (MP3) and fourth (MP4) order Møller Plesset calculations are standard levels used in calculating small systems and are implemented in many computational chemistry codes. Higher level MP calculations, generally only MP5, are possible in some codes. However, they are rarely used because of their cost. Moreover, systematic studies of MP perturbation theory have shown that it is not necessarily a convergent theory at high orders. Besides, various important molecular properties calculated at MP3 and MP4 level are no better than their MP2 analogous, even for small molecules.

Complete active space with second-order perturbation theory(CASPT2) We can find an special implementation of the MP2 perturbative approach in the context of CASSCF reference wavefunctions. In the CASPT2 method, a multiconfigurational wavefunction, generated from a CASSCF calculation, is used as the zeroth-order wave function in a perturbation approach to the correlation problem. Then, the perturbative treatment is applied for any reference state constructed as a full CI wave function in some orbital subspace [70, 71]. Details of this approach can be found in Section 4.2.3.1.

2.3.1.3 Correlation from coupled pair theories

Coupled Cluster (CC) Electron correlation is primarily a two-body effect. This is because, if a third electron is taken into account, it would tend to be apart from the other electron considered before with its same spin (Pauli principle). Then, correlation between electrons with the same spin (Fermi correlation) can be considered small. This is also true for more-electron situations. However, there can be an interaction between groups of two correlated electrons, giving a kind of four body correlation. We can extend this idea to three pairs of interacting electrons giving rise to six-body correlation terms and so on. These pair-product correlations correspond to the disconnected clusters terms in a wavefunction. Derived by Čižek and Paldus in the late 60's [72, 73] and exploited by Bartlett in the 80's [74, 75], it is known as *coupled clusters* (CC) method. In this method, the wavefunction (constructed by a perturbation expansion with an infinite number of terms of a certain class) is written as

$$\Psi_{CC} = e^{\hat{T}}\Psi_0 \tag{2.36}$$

where Ψ_0 is the HF wavefunction and $\hat{T} = \hat{T}_1 + \hat{T}_2 + \ldots + \hat{T}_N$ is an operator acting on the HF wavefunction. A $\hat{T}_i$ operator generates linear combinations of i-excitations of the HF wavefunction. The coefficients of each i-excited Slater determinant in the linear combination are the unknowns in this approach. That implies that the Schrödinger equation for the ground state

$$\hat{H} \mid e^{\hat{T}}\Psi_0\rangle = E_{CC} \mid e^{\hat{T}}\Psi_0\rangle \tag{2.37}$$

cannot be solved in a variational way. However, the main advantage of CC methods over CI methods, although both expand the wavefunction in unexcited plus excited components, is related to the *size-consistency error* when truncation at some level is applied. A method is called *size-consistent* if it gives the energy of a collection of n-widely separated fragments as the sum of the energies of each fragment n. Full CI, as to be expected from a formally exact theory is size-consistent. Unfortunately, truncated CI does not have this property, whereas CC is a size-consistent method by construction.

2.3.2 Density Functional Theory

Parallel to the approaches mentioned so far, where the wavefunction plays a central role, density functional theory (DFT) appears as a method with the electronic density as the cornerstone variable [76, 77]. Within the framework of Kohn-Sham DFT, the intractable many-body problem of interacting electrons under the influence of a static external potential is reduced to a tractable problem of non-interacting electrons moving in an effective potential. The effective potential includes the external potential and the effects of the Coulomb interactions between the electrons, i.e., the exchange and correlation interaction. Some basics on this theory are in Chapter 3. It will be shown that DFT, due to the second Hohenberg-Kohn theorem, is a ground state theory and it is not transferable to excited states. Time dependent density functional theory (TDDFT) [78] appears as a extension of DFT to deal with them. It is based in the unique mapping between the time dependent external potential of a system and its time dependent density (Runge-Gross theorem). The most popular application of TDDFT is in the calculation of the energies of excited states of isolated systems and, less commonly, solids.

2.4 Basis Sets

Expanding an unknown function in a set of known functions is not an approximation if the basis has an infinite number of elements, i.e. the basis is complete. However, this is impossible to achieve in practice and then some basis functions are selected. In principle, the smaller the basis set size, the worse is the representation of the wavefunction. However, a small basis set size is desired in terms of diminishing the computational effort. Then, it is necessary to select the best single basis functions of in the sense that the better each one does represent the unknown function, the fewer number of basis is needed for a determinate level of accuracy.

The most common approach is to expand the one-electron wavefunctions (or molecular orbitals, MOs) in terms of atomic orbitals (AOs)(Eq. 2.25). This scheme, introduced by Mulliken [79], is called *linear combination of atomic orbitals* (LCAO). AOs are centered on the atomic nuclei and, since the molecular electronic distribution is largely dominated by atomic distributions, a natural choice is to optimize the basis functions to reproduce AOs and then, export them to molecular system or condensed phases. The starting point is to solve the atomic problem, that is, to find the one-electron eigenstates in the effective Coulomb-like field. In spherical coordinates, the one-electron Schrödinger equation reads:

$$\left[-\frac{1}{2}\left(\frac{1}{r^2}\frac{\partial}{\partial r}\left(r^2\frac{\partial}{\partial r}\right)-\frac{\widehat{L}^2}{r^2}\right)+V_{eff}(r)\right]\phi_\alpha(r)=E_\alpha\phi_\alpha(r) \tag{2.38}$$

where $\widehat{L}$ is the angular momentum operator. Since for a central field $\widehat{L}^2$ and $\widehat{L}_z$ commute with the Hamiltonian, the AOs ϕ_α factorize into a radial and an angular part:

$$\phi_\alpha(\vec{r})=\phi_{nlm}(\vec{r})=\chi_{nl}(r)Y_{lm}(\theta,\varphi) \tag{2.39}$$

An atomic basis function must contain at least one single basis function per occupied or partially occupied atomic orbital of the atom considered. This is called *single-ζ* (SZ) basis set and it is accurate for isolated atoms, but some flexibility on the angular and on the radial part should be included to represent the effects when electrons participate in chemical bonding. Flexibility on the radial is improved by adding an additional set of basis functions per atomic orbital, in the so-called *multiple-ζ* (DZ, TZ, QZ...). Flexibility in the angular part is improved by adding polarization (P) functions of different angular momenta. Perturbation theory indicates that the most important contribution to the angular deformation arises from functions of $l\pm1$ character. Moreover, for states that are significantly different from the fundamental atomic one (e.g. anions, excites states, zones far from nuclei ...), some functions representing spread orbitals (diffuse functions, (+)) are often added. A common approach is to select analytical expressions for basis functions in Eq. 2.39. Slater type (STOs) and Gaussian type basis functions (GTOs) are the most common analytical basis sets used in electronic structure calculations, even if they are not in general solutions of the atomic Schrödinger equations. STOs have the general form $\phi_{\zeta,n,l,m}(r,\theta,\varphi)=NY_{l,m}(\theta,\varphi)r^{n-1}e^{-\zeta r}$, where N is a normalization constant and $Y_{l,m}$ the spherical harmonics. The use of STOs is restricted in practice to atoms and diatomic systems, due to the calculations of tri- and tetra-centric integrals cannot be performed analytically but numerically. An alternative to STOs are Gaussian type orbitals GTOs which general expression is $\phi_{\zeta,n,l,m}(r,\theta,\varphi)=NY_{l,m}(\theta,\varphi)r^{2n-2-l}e^{-\zeta r^2}$ in polar coordinates and $\phi_{\zeta,n,l,m}(x,y,z)=Nx^{l_x}y^{l_y}z^{l_z}e^{-\zeta r^2}$ in cartesian coordinates. The sum $l_x+l_y+l_z$ determines the type of orbital (e.g. a sum $l_x+l_y+l_z=1$ corresponds to a *p*-type orbital). GTOs have the enormous advantage of allowing an analytical calculation of all the integrals. This is possible because of the product of two GTOs centered in two different points of space, A and B, can be reduced to a linear combination of GTOs centered in any point belonging to the segment that links such points A and B. Then, the integrals are reduced

to two-center integrals at most. This is the main reason why these basis sets are widely used for molecular calculations, in spite of their disadvantages. The first consideration of molecular integrals over GTOs was proposed by Boys in 1950 [80] and systematized by Huzinaga [81, 82]. Much work has been done since then to speed up the evaluation of the integrals. Different from the r exponential dependence on STOs, the r^2 exponential dependence on GTOs leads to a failure when describing the function near the nucleus. This in an undesirable feature, since the interactions electron-nucleus are important in this zone. Furthermore, the behavior at long distances is not very good either, because of the fast decay of the function with distance. Thus, more GTOs are needed in order to achieve the same accuracy obtained with STOs. To improve the behavior near the nucleus using GTOs avoiding the use of a large number of them, contracted Gaussian functions (CGTOs) are used. In the CGTOs scheme, a set of Gaussians is used to generate a linear combination (called *contracted* GTOS (CGTOs), $G^{CGTO}(r) = \sum_{i=1}^{k} a_i G^{PGTO}(r)$) where both the coefficients a_i and the exponents are optimized to reproduce the atomic ground state orbitals at the desired level of theory. There are two different schemes of contraction: segmented contraction (PGTOS are only present in one CGTO) and general contraction (all the basis functions are linear combinations of all the PGTOs of the same symmetry).

Basis described above are aimed at modeling atomic orbitals subsequently used in linear combinations to describe molecular orbitals. However, in extended systems (as unit cells with periodic boundary conditions), it is common the use of analytical basis extended on the whole system rather than localized in the nuclei. These are the plane waves basis sets (PWs). In general, the representation of an arbitrary orbital of a infinite system in terms of a PW basis set would require an infinite basis set. However, the imposition of periodic boundary conditions limits the representation to a only one Brillouin zone coming from the unit cell repeated in space (see below Section 2.5). PWs have the general form $\phi_{\vec{G}}(\vec{r}) = \frac{1}{\sqrt{\Omega}} e^{i\vec{G}\vec{r}}$, with the reciprocal lattice vectors $\vec{G}$ lying always outside the first Brillouin Zone except for $\vec{G} = 0$. That means that PWs are not linked to the atomic nuclei but extended over the whole system, representing all the regions with the same accuracy. Plane waves are solutions of the one-electron effective Schrödinger equation in the presence of a constant external potential, as approximately is in the interstitial regions in condensed phases. Closer to the atomic nuclei, however, the potential is far from constant and, hence, the wavefunction solution of the Schrödinger equation is not a single PW anymore but a linear combination of PWs. That means that, in principle, infinite number of planewaves ($\vec{G}$) are need to represent a wavefunction. In practice, the expansion is truncated including only those PWs with kinetic energy lower than some cutoff E_{cut} and calculations must be converged respect to this value. The size of a PWs basis set depends on the size of the periodic cell, not in the system described within it and then it is more advantageous for systems with large number of atoms, where GTOs basis set size would increase linearly. PWs are primarily used to describe periodic systems but they can also be used for molecules within the supercell approach, where a molecule is placed in a large unit cell and periodic boundary conditions are artificially introduced in a way that images of neighboring cells do not interact.

However, both in atomic-like and periodic calculations, it is not always trivial to find analytical functions to represent then accurately enough. Then, sometimes AOs are represented numerically directly in a grid, as they come out from atomic calculations. The main problem of these so-called numerical basis sets is that the Hamiltonian and the overlap matrix elements have to be computed numerically. This is computationally expensive, specially due to the necessity of three- and four-center Coulomb integrals. This extra cost can be reduced decreasing the basis size by tailoring properly the basis functions under the constraint that they should be strictly zero beyond some localization radius [83].

2.5 Electronic structure calculations in solid state

Due to the periodic character of systems belonging to the solid state, they present different technical requirements with respect to molecular systems in the study of the electronic structure and properties. The translational symmetry of the cell make the structural properties (geometrical parameters, elastic constants, compressibility coefficients ...) non local in character, but arising from the electronic structure of the ground state of the crystal as a periodic macroscopic entity. These properties can be modeled using periodic boundary conditions (PBC) approaches from calculations on the one unit cell replicated in the space.

However, when the crystal losses the periodicity due to a punctual imperfection or impurity, some properties (e.g. spectroscopic properties) associated to electronic states of the defect do appear. They only depend on the defect and the defect-neighborhood interaction, at a local level. Nevertheless, the study of such local properties may be treated within the embedded cluster approach, where a few atoms or *cluster* (responsible of the properties of interest) are studied using the same quantum-mechanical techniques used for molecules under the influence of the external potential generated by a representation of the rest of the crystal.

2.5.1 Periodic boundary conditions methods

Condensed phases such as solids, liquids, amorphous, surfaces, wires, etc., are macroscopic objects constituted by a huge number of atoms, typically of the order of Avogadro's number. In crystalline solids, a small number of atoms (a basis) is replicated periodically *ad infinitum* along one, two or three dimensions in the space. There are many possible choices for the basis but the one containing the whole symmetry of the system is called *Wigner-Seitz* cell and, together with the primitive lattice vectors $\{\vec{a}_i\}$ ($i = 1, 2, 3$ in 3D), contains all the information to reproduce the infinite crystalline structure [84]. The set of points in space corresponding to integer combinations of the primitive vectors $\vec{a} = c_1\vec{a}_1 + c_2\vec{a}_2 + c_3\vec{a}_3$ receives the name of *Bravais lattice*. In that way, a given Bravais lattice vector $\vec{a}$ connects two equivalent points of two different unit cells.

An infinite number of atoms involves an infinite number of electrons; take all them into account is out of question. Fortunately, Bloch's theorem [50] connects the properties of the electrons in a periodic system with those of electrons in the unit cell.

Bloch's theorem The wavefunction of an electron in a external periodic potential $V(\vec{r}) = V(\vec{r}+\vec{a})$ can be written as the product of a function with the same periodicity of the potential and a purely imaginary phase factor arising from the translational symmetry:

$$\psi_{\vec{k}}(\vec{r}) = e^{i\vec{k}\vec{r}}u_{\vec{k}}(\vec{r}); \qquad u_{\vec{k}}(\vec{r}) = u_{\vec{k}}(\vec{r}+\vec{a}) \tag{2.40}$$

The wavefunction evaluated at the related point mentioned above adopts the form

$$\psi_{\vec{k}}(\vec{r}+\vec{a}) = e^{i\vec{k}\vec{a}}\psi_{\vec{k}}(\vec{r}) \tag{2.41}$$

and the probability density $\mid \psi_{\vec{k}}(\vec{r}) \mid^2$ is exactly the same in the two points because the complex square of the purely imaginary phase factor is unity.

The Brillouin zone From expression 2.41, it can be seen that there is a particular class of vectors $\vec{k}$ such that $e^{i\vec{k}\vec{a}} = 1$ and thus the wavefunction is in phase in all the periodic replicas of the unit cell. These such $\vec{k}$ vectors are enough to represent the unit cell in the *reciprocal space* as the Bravais lattice vectors $\{\vec{a}\}$ do in real space. Primitive lattice vectors can be defined not only in real space ($\{\vec{a}_i\}$) but also in reciprocal space. They are denoted as $\{\vec{b}_i\}$ and are defined by the relation $\{\vec{b}_i\}\{\vec{a}_i\} = 2\pi\delta_{ij}$. They can be calculated through

$$\vec{b}_1 = 2\pi\frac{\vec{a}_2 \times \vec{a}_3}{\Omega} \qquad \vec{b}_2 = 2\pi\frac{\vec{a}_3 \times \vec{a}_1}{\Omega} \qquad \vec{b}_3 = 2\pi\frac{\vec{a}_1 \times \vec{a}_2}{\Omega} \tag{2.42}$$

where $\Omega = \vec{a}_1 \cdot (\vec{a}_2 \times \vec{a}_3)$ is the volume of the unit cell. The cell defined by the three reciprocal lattice primitive vectors, whose volume is $\Omega_{BZ} = \vec{b}_1 \cdot (\vec{b}_2 \times \vec{b}_3)$, receives the name of *first Brillouin zone* or sometimes only *Brillouin zone* (BZ).

For many properties, such as the counting of electrons in bands, total energies, etc., it is essential to sum over the states belonging to the BZ (labeled with the wavevector $\vec{k}$), since, while the eigenfunctions that obey periodic boundary conditions are repeated in a large crystal of an arbitrary number of cells, there is *exactly only one* value of $\vec{k}$ for all these cells. Thus, to find a property of the crystal expressed "per unit cell", the sum is over values of $\vec{k}$ divided by the number of them N_k. Then, the average value $\bar{f}_i$ of a function $f_i(\vec{k})$ becomes

$$\bar{f}_i = \frac{1}{\Omega_{BZ}}\int_{BZ} f_i(\vec{k})d\vec{k} \tag{2.43}$$

Of course, there are infinite $\vec{k}$ in the BZ but, in practice, a finite number of k-points is selected (Brillouin zone sampling). The selection of these points is not arbitrary and are sought for efficiency in the integration. The general method proposed by Monkhorst and Pack [85] is the most widely used method, since it provides an equally spaced k-points

set. These are constructed according to:

$$\vec{k}_{MP} \equiv \sum_{i=1}^{3} \frac{2n_i - N_i - 1}{2N_i} \vec{b}_i; \qquad n_i = 1, 2 \ldots N_i \tag{2.44}$$

where N_i is the total number of points in the i direction, and determines the finesses of the grid. This set does not include the Γ point ($\vec{k} = \vec{0}$) nor other points in the limits of the BZ leading to a decreasing in the number of inequivalent points used and, therefore, a decreasing in the computational effort. The average integrals become

$$\bar{f}_i = \sum_{\vec{k}}^{\vec{k}_{MP}} w_{\vec{k}} f_i(\vec{k}) \tag{2.45}$$

where $w_{\vec{k}}$ is the weight assigned to each k-point according to its generation algorithm.

Basis sets in periodic systems In the study of periodic systems such as solids, it has to be ensured that Bloch's theorem is verified, in the sense that the combination of basis orbitals that represents a solution of the Schrödinger equation verifies the translational periodicity of the unit cell. In that case, the expansion of the one-electron wavefunction in the basis set is modified, leading to:

$$\varphi_j^{(\vec{k})}(\vec{r}) = e^{i\vec{k}\vec{r}} \sum_{\alpha=1}^{M} c_{j\alpha}^{(\vec{k})} \phi_\alpha(\vec{r}) = \sum_{\alpha=1}^{M} c_{j\alpha}^{(\vec{k})} \phi_\alpha^{(\vec{k})}(\vec{r}) \tag{2.46}$$

where $\vec{k}$ indicates a wavevector in the Brillouin zone and $\phi_\alpha^{(\vec{k})}(\vec{r}) = e^{i\vec{k}\vec{r}}\phi_\alpha(\vec{r})$. This representation is adequate for basis functions $\phi_\alpha(\vec{r})$ that *already* fulfill periodic boundary conditions, but for another kind of basis, care must be taken and a expression compatible with Bloch's theorem must be found. An example is the expression for atom-centered basis sets:

$$\varphi_j^{(\vec{k})}(\vec{r}) = \sum_{\alpha=1}^{M} c_{j\alpha}^{(\vec{k})} \left(\frac{1}{\sqrt{\Omega}} \sum_{\vec{T}} e^{i\vec{k}\vec{T}} \phi_\alpha(\vec{r} - \vec{T}) \right) \tag{2.47}$$

where the expression in parentheses corresponds to the Periodic Boundary Conditions (PBC) adapted basis functions, with a sum running all over the possible translations $\vec{T}$ of the cell in the space ($\vec{T} = n_1\vec{a}_1 + n_2\vec{a}_2 + n_3\vec{a}_3$; $\vec{a}_i$ are the lattice vectors). With this definition, Bloch' s theorem $\phi_j^{(\vec{k})}(\vec{r} + \vec{a}) = e^{i\vec{k}\vec{a}}\phi_j^{(\vec{k})}(\vec{r})$ is verified.

The general eigenvalue equation 2.27 is still valid, but now there is an equation *for each k-point in the Brillouin zone*.

$$\sum_{\beta=1}^{M} (\mathbb{H}_{\alpha\beta}^{(\vec{k})} - E_j^{(\vec{k})} \mathbb{S}_{\alpha\beta}^{(\vec{k})}) c_{j\beta}^{(\vec{k})} = 0 \tag{2.48}$$

The external potential is periodic as well, with the periodicity of the lattice. Thus, the Hamiltonian reads:

$$\widehat{H} = -\frac{1}{2}\nabla^2 + V_{ext}(\vec{r} - \vec{R}) + \int \frac{\rho(\vec{r}_2)}{\mid \vec{r}_1 - \vec{r}_2 \mid} \vec{dr}_2 + E_{XC}[\rho] \tag{2.49}$$

Electronic structure in solids: methods Since planewaves are eigenvalues of the one-electron effective Schrödinger equation in the presence of a constant external potential, they are used in many techniques for electronic structure calculations in solid state. Sometimes they are used together with ultrasoft pseudopotentials (US-PP) or in the projected augmented waves (PAW) approach and the independent-particle electronic problem is solved within the DFT theory. Ultrasoft pseudopotentials [86] attain smoother pseudowavefunctions than norm-conserving pseudopotentials by relaxing the norm-conserving constraint. That allows the use of much less number of planewaves but are less transferable than harder pseudopotentials that describe accurately the behavior of the wavefunction near the ion. Unlike pseudopotentials, which keep only the valence pseudowavefunction, the PAW formulation [87] keeps the full wavefunction for each electron. Since there is a component that retains the nodal structure inside the core region, they tend to be harder that US-PP.

Other methods resort to augmented planewaves functions (APW method, Slater [88]) in the context of the muffin-tin approximation. It considers non-overlapping spheres centered on atomic positions. Within these spheres, the potential is spherically symmetric whereas outside the sphere the potential is smooth. Wavefunctions (the augmented plane waves) are constructed by matching solutions of the radial Schrödinger equation within each sphere with plane-wave solutions in the interstitial region, and linear combinations of these wavefunctions are then determined by the variational method. Many modern methods of electronic structure in solids use this approximation: e.g. the linear muffin-tin orbital method (LMTO) [89] and various Green's function methods, as the one of Korringa, Kohn and Rostoker (KKR) [90, 91].

Contrasting with PWs extended basis sets, the concept of locality can be introduced in solid state calculations via using LCAO as basis sets. The tight-binding model, developed by Koster and Slater [92], describes the electronic states starting from the limit of orbitals belonging to isolated and weakly interacting atoms. Core orbitals, which scarcely overlap, can be obtained from atomic Hamiltonians. However, in order to describe valence orbitals, one must include a semiempirical correction term taking into account part of the periodic potential of the crystal.

LCAO of STOs, GTOs or numerical atomic orbitals are also widely used in full *ab initio* solid state calculations within DFT. These calculations, implemented in highly developed codes, can be very efficient and accurate and, since these orbitals are localized, they provide the basis for the new *order-N* methods. However, they require specification of the basis sets and, then, certain generality is lost with respect to PW-based methods.

2.5.2 Embedded cluster methods

Historically, the first *cluster* approach was performed by Sugano and Shulman [93]. In order to study some magnetic and spectroscopic properties, they proposed a restriction on the resolution on the Roothan-Hall equations only for a set of atoms, that is, the cluster. However, they ignored all cluster-lattice interactions, which turned out to be important

soon.

In parallel, *building-block* techniques appeared, where a large system is divided in interacting subsystems [94]. This approach leads to a set of coupled equations, each one representing a given subsystem under the influence of the rest of them. These equations are solved iteratively till convergence on the electronic density and the solution of the whole system is obtained. However, within this scheme, it is also possible to solve iteratively only a given set of equations related to a given subsystem/s, keeping the rest frozen and obtaining properties of interest only for such subsystem. An intermediate position is the most adequate in the embedding cluster approach: the cluster of interest and some atoms of the vicinity are included in the LCAO expansion and enter in the iterative procedures, whereas the rest remains frozen. The representation of some neighboring atoms attenuates the sharp division cluster-environment.

In solid state, a first approximation to the embedded cluster approach, known as perturbed cluster [95], performs separated calculations for the cluster and the host crystal and the density matrix of the cluster is corrected in terms of the density of states of the crystal.

In ionic solids, the cluster-environment interaction can be represented by an electrostatic (Madelung) potential generated by the charge points array surrounding the crystal. However, the bare Madelung potential gives wrong values for some cluster structural and spectroscopic properties [18].

The *ab initio* model potential method (AIMP) (used in this work and detailed in Section 4.1) describes accurately the cluster-environment interactions. It is based in the former work performed by Huzinaga and McWeeny in molecules. They adopt the building block approach for a large system, concentrating the computational effort in a certain subsystem. Moreover, they propose a total wavefunction constructed in terms of group functions fulfilling special orthogonality conditions. This wavefunction is treated variationally within each group and the resulting set of equations are solved iteratively. Barandiaran and Seijo [96] pointed out that the picture of valence electrons of a impurity in an ionic solid giving rise to some local properties was comparable to the picture of molecular valence electrons treated by Huzinaga and McWeeny. Then, they developed the AIMP method, where the cluster is selected such as it contains the group of atoms responsible of the properties under study, the crystal appears as a frozen environment acting on the cluster and neighboring atoms to the cluster are taken into account in the wavefunction construction. Moreover the cluster-environment is represented by model potentials, implemented in the computational codes used to solve the equations iteratively.

2.6 The problem of Ce:YAG: Our methodological choices

In this work, we attempt to rationalize the interplay between structure and luminescence in Ce:YAG, by studying the La and Ga codoped Ce:YAG and Ce:YAG with antisite defects. Then, this study comprises two consecutive stages: the structural study of the

materials mentioned above and the study of their spectroscopic features arising from those previously obtained structures.

Thus, the problem of luminescence of Ce:YAG, as presented in this work, has two main aims presenting quite different methodological requirements. In both of them, we have to decide a) how to model the solid and b) which level of theory we need for the specific problem. Wherever calculations involve Ce^{3+}, we also have to decide which relativistic effects are relevant for our properties of interest and then, include them in our calculations.

Firstly, we tackle the study of the structure of the host YAG pure and perfect in its ground state and the complex structural distortions produced by defects and impurities. Moreover, we study the different electronic structures of the different cells. That means that in all cases our calculations are performed in a YAG unit cell of 160 atoms. Then, we need a method able to deal with a large number of electrons in a periodic cell, taking accurately into account the electronic correlation of all of them. Thus, DFT methods appear as good candidates for our particular case since this theory fulfills these requirements at a good value for quality and computational effort. Due to the periodicity of the lattice and, since the considered concentration of defects is low enough to consider non-interacting defects between adjacent cells, we use the PBC approach.

Thus, Chapter 3 describes briefly the DFT general features, common for molecules and solids, and briefly outlines the specific technical aspects used by the periodic boundary conditions program chosen for this purpose, the SIESTA code [97]. This program uses numerical atomic orbitals as basis sets and Troullier-Martins pseudopotentials. Both basis sets and pseudopotentials used in this work have been generated specifically for our calculations. Thus, we have generated basis sets with DZP quality and pseudopotentials including scalar relativistic effects wherever appropriate. In all those calculations involving Ce (an open-shell atom) we perform spin-polarized calculations.

The second step comprises the calculation of the shifts induced by codoping on the Ce^{3+} absorption spectra and the calculation of the Stokes shift of Ce:YAG with and without antisite defects. These spectroscopic features of Ce:YAG arise from local properties of Ce^{3+} and surroundings under the influence of the host. Then, it sounds reasonable to study these properties within the the embedded cluster approach, specifically using the AIMP method, which accurately takes into account the cluster-environment interactions and has been successfully used before in the study of luminescence of lanthanides in ionic solids [98, 18, 99, 41, 100]. In order to decide the level of theory, we have to take into account that spectroscopic calculations involve both ground states and excited states. Thus, we need a theory able to describe properly the wavefunction of both states, giving accurate values for the energetic transitions. Then, multiconfigurational methods are needed. Among them, we have chosen the state-average CASSCF method to take into account bonding interactions and static electronic correlation, and multi-state CASPT2 approach has been chosen to include dynamic correlation effects.

Chapter 4 outlines the embedded cluster (AIMP method) [96] and the multiconfigurational methods of choice. We have performed these calculations using the MOLCAS package [101]. Experimentally, two emission peaks associated to Ce $4f$ manifold spin-

orbit splitting are observed. Also $5d$ manifold presents spin-orbit splitting to a different extent. Then, spin-free calculations are not adequate to obtain the highest accuracy in the absolute values of the $4f \rightarrow 5d$ transitions. However, the comparison between transitions aimed in this work is meaningful within the spin-orbit-free approach, since Ce chemical environment is so similar that the same splitting is expected for all the cells studied. Moreover, we can predict the effect of the spin-orbit coupling in our results from calculations on the emission spectra of Ce:YAG performed previously in our group using the same (relativistic) AIMP embedding cluster scheme and basis sets and including spin-orbit effects [41]. Thus, we have adopted the approach of including scalar relativistic effects in the ECPs (AIMPs) used in our calculations. Using the same embedded cluster approach, the only differences between our calculations and calculations on Ref. [41] are the cluster geometries and the YAG unit cell coordinates used to build the AIMP embedding. In this work, both come from previous PBC-DFT calculations and in Ref. [41] only the geometry of the cluster is optimized at the CASPT2 level, whereas YAG host is constructed from experimental values. Since the optical spectrum of Ce:YAG arises from electronic transitions localized in the impurity and surroundings, we use both the $(CeO_8)^{13-}$ (also used in Ref. [41]) and $(CeO_8Al_2O_4)^{15-}$ clusters in all our calculations. The choice of the latter responds to the tight relationship observed in this work between the CeO_8 moiety and the two AlO_2 moieties connected to it along a given axis.

Chapter 3

Structure of defects: Periodic boundary conditions density functional theory calculations (PBC-DFT)

Developed much later than the wavefunction-based methods, the density functional theory (DFT) represents an alternative to such methods for introducing the effects of electron correlation into the Schrödinger equation in an *ab initio* way. A question sometimes raised up is whether DFT should be regarded as an special kind of *ab initio* method. The main disadvantage against this point of view is that, as it will be shown in this chapter, the correct mathematical form of the exact DFT functional is not known, in contrast to the conventional *ab initio* theories, where the correct mathematical form of the fundamental (Schrödinger) equation is known. Moreover, since there is no way to systematically improve the unknown functional, DFT results are compared both with experiments and high-level *ab initio* calculations. Anyway, the possibility of finding the exact functional makes it *ab initio* in spirit.

DFT is based on the full electronic density as the fundamental variable of the many-body problem instead of the system wavefunction. Unlike the wavefunction (which is not an observable), the electronic density is measurable, e.g. by X-Ray diffraction or electron diffraction. Besides, the density has another property that makes DFT a suitable alternative to wavefunction methods: it is a function of position only. That is, no matter how big the molecule may be, it remains always a function of three variables (x, y, z) only, while the wavefunction of an N-electron system depends on $4N$ variables: three spatial and one spin coordinates *for each electron*. To the chemists, the main advantage of DFT is that, once chosen the most appropriate set of ingredients (DFT exchange-correlation flavor, basis set, pseudopotentials if needed) one can often obtain results of about the quality of MP2 calculations in about the same time needed for a HF calculation.

Nevertheless, DFT presents some disadvantages. On the one hand, it is a formally exact theory but at the practical level, one has to resort to some approximated functionals

and there is no systematic way to improve a result once a functional has been chosen. On the other hand, calculations with DFT functionals always contain a certain self-interaction error associated to the approximated character of the exchange term.

For our final purposes, the preliminary step before studying luminescence of Ce:YAG under the influence of codopants or antisite defects is the obtaining of detailed local structures around Ce_Y. Moreover, we are interested in the global distortions that the defect or defects print in the cell, since they offer a picture of the real solid containing defects instead of considering it a perfect lattice farther than impurity surroundings. Besides, we want to analyze the changes that YAG electronic structure undergoes when the cell contains antisite defects and/or impurities. Thus, our calculations involve a large number of electrons so that DFT is a useful tool to obtain reliable structures in our large system and, implemented in the context of periodic boundary conditions, allows us to obtain properties derivated from the whole solid, e.g. the eigenvalue gap.

In this work, DFT presents the problem of being a ground state theory and, thus, structures obtained in this way can be only used in calculations of absorption spectra. Moreover, the difference in energies between occupied and virtual states are not comparable to absorption energies.

In this chapter, some physical concepts related to the electronic density are included in Section 3.1. The basics on DFT theory, the Hohenberg-Kohn and the Kohn Sham equations are outlined in Section 3.2. The LDA and PBE exchange correlation functionals are presented in Section 3.3, after a brief introduction ion the homogeneous electronic gas as the parent model for exchange correlation functionals. In Section 3.4 we outline the DFT approaches targeting an improvement of the self-interaction error present in standard DFT: the DFT+U and hybrid methods. Finally, we briefly describe in chapter 3.5 some of the particularities of the periodic boundary conditions-DFT code used in this work, the SIESTA program.

3.1 Preliminary concepts

The idea of calculating atomic and molecular properties from the electron density arose independently from calculations made by Enrico Fermi and Paul Dirac in the 1920s on an ideal electron gas (work well-known nowadays as the Fermi-Dirac statistics [102, 103]). They gave a prescription of the energy of an electronic system in terms of electronic density, even so their unrealistic model of a positive nucleus surrounded by an uniform electron gas failed completely when going far from atoms to molecules. In their model, the only dependence of the energy on the electronic variables was through the electronic density. In that sense it is said that the energy is a *functional* of the density. If a *function* is, roughly speaking, a rule that transforms a number into another number, a *functional* is a rule that transforms a function into a number. In that way, the function $\rho(x, y, z)$ is transformed into the energy, a number. In other words, a functional is a function of another definite function.

Some properties and concepts related to the electron density must be discussed in

order to understand the density functional theory and its goals. A remarkable position is given to the *pair density*, since it contains all the information about exchange and correlation effects in atoms and molecules.

The Electron Density The probability interpretation of the wavefunction leads to the definition of the electron density $\rho(\vec{r})$ as the multiple integral over the spin coordinates of all electrons and over all but one spatial variables

$$\rho(\vec{r}_1) = \int \rho(\vec{x}_1) ds_1 = N \int \dots \int \mid \Psi(\vec{x}_1, \vec{x}_2 ... \vec{x}_N) \mid^2 ds_1 \vec{dx}_2 \dots \vec{dx}_N \tag{3.1}$$

$\rho(\vec{r})$ determines the probability of finding any of the N electrons within the volume element $\vec{dr}_1$ independently of where the others are placed. Thus, is a probability per volume unit and, then, its units are volume^{-1}. $\rho(\vec{r})$ is a function of only three spatial variables whatever the considered system is Since electrons are indistinguishable, the probability of finding any electron at position $\vec{r}$ is N times the probability for a single electron. $\rho(\vec{r})$ vanishes at infinity for molecules ($\rho(\vec{r} \rightarrow \infty) = 0$) and integrates to the total number of electrons ($\int \rho(\vec{r}) \vec{dr} = N$)

The Pair Density It is an extension of the concept of electron density $\rho(\vec{r})$ and answers the question of how likely is it to find not one but two electrons with spins σ_1 and σ_2 *simultaneously* in the volume elements $\vec{dr}_1$ and $\vec{dr}_2$ while the remaining $N-2$ electrons have arbitrary positions and spins. Then, the *pair density* $\rho_2(\vec{x}_1, \vec{x}_2)$ is defined as

$$\rho_2(\vec{x}_1, \vec{x}_2) = N(N-1) \int \dots \int \mid \Psi(\vec{x}_1, \vec{x}_2 ... \vec{x}_N) \mid^2 \vec{dx}_3 \dots \vec{dx}_n \tag{3.2}$$

Like the density, the pair density is also positive. Here it is shown the normalization proposed by McWeeny to all the possible non-distinct pairs of electrons ($N(N-1)$), but can be normalized to all the distinct pairs ($1/2N(N-1)$) such Lödwin, Parr and Yang do.

It is necessary to introduce the concept of *reduced density matrix* γ_2 in order to show the effects both of antisymmetry of the wavefunction and Coulomb repulsion between electrons. It is defined as a generalization of $\rho_2(\vec{x}_1, \vec{x}_2)$

$$\begin{aligned} &\gamma_2(\vec{x}_1, \vec{x}_2; \vec{x}'_1, \vec{x}'_2) = \\ &= N(N-1) \int \dots \int \Psi(\vec{x}_1, \vec{x}_2, \vec{x}_3 ... \vec{x}_N) \Psi^*(\vec{x}'_1, \vec{x}'_2, \vec{x}_3 ... \vec{x}_N) \vec{dx}_3 \dots \vec{dx}_N \end{aligned} \tag{3.3}$$

where from $\rho_2(\vec{x}_1, \vec{x}_2)$ to $\gamma_2(\vec{x}_1, \vec{x}_2; \vec{x}'_1, \vec{x}'_2)$ are primed those variables not included in the integration. Then, two sets of independent variables, $(\vec{x}_1, \vec{x}_2)$ and $(\vec{x}'_1, \vec{x}'_2)$ define the value of $\gamma_2(\vec{x}_1, \vec{x}_2; \vec{x}'_1, \vec{x}'_2)$ and this is the reason for calling it a *matrix*.

In one hand, the interchange of the variables $\vec{x}_1$ and $\vec{x}_2$ (or $\vec{x}'_1$ and $\vec{x}'_2$) leads to the change of sign of $\gamma_2(\vec{x}_1, \vec{x}_2; \vec{x}'_1, \vec{x}'_2)$:

$$\gamma_2(\vec{x}_1, \vec{x}_2; \vec{x}'_1, \vec{x}'_2) = -\gamma_2(\vec{x}_2, \vec{x}_1; \vec{x}'_1, \vec{x}'_2)$$

The diagonal elements of this matrix, where $\vec{x}_1 = \vec{x}'_1$ show the pair density $\rho_2(\vec{x}_1, \vec{x}_1)$. If $\vec{x}_1 = \vec{x}_2$ (two electrons with the same spin within the same volume element) it is found that $\rho_2(\vec{x}_1, \vec{x}_1) = -\rho_2(\vec{x}_1, \vec{x}_1)$ and it can only be possible if $\rho_2(\vec{x}_1, \vec{x}_1) = 0$. That is, *the probability of finding an electron with the same spin in the same point in space is exactly zero.* Hence, it is shown that spin-like electrons do not move independently from each other. This kind of correlation is not related to Coulomb interactions but to Pauli principle and it is known as exchange or Fermi correlation. It is already included in the Hartree-Fock approach due to the antisymmetry of the Slater determinant.

On the other hand, the effect of Coulomb repulsion is independent of spin. The term $1/r_{12}$ prevents an electron from coming too close to another electron. This is known as Coulomb correlation, but often is called simply as electron correlation. It is not included in Hartree Fock approach.

It is convenient to separate the influence of the Fermi and Coulomb correlations on the pair density by separating it into two parts: the simple product of the independent densities and the remainder, brought about by Fermi and Coulomb effects:

$$\rho_2(\vec{x}_1, \vec{x}_2) = \rho(\vec{x}_1)\rho(\vec{x}_2)[1 + f(\vec{x}_1; \vec{x}_2)] \tag{3.4}$$

where $f(\vec{x}_1; \vec{x}_2)$ is called *correlation factor* and gives us $f(\vec{x}_1; \vec{x}_2) = 0$ for the completely uncorrelated case.

At this point, another term is necessary to be defined: the *conditional probability* $\Omega(\vec{x}_2; \vec{x}_1)$, which is the probability of finding an electron at position 2 (both spin and spatial coordinates included) if there is a previous electron placed at position 1:

$$\Omega(\vec{x}_2; \vec{x}_1) = \frac{\rho_2(\vec{x}_1, \vec{x}_2)}{\rho(\vec{x}_1)} \tag{3.5}$$

This conditional density integrates to $N - 1$ electrons, since it contains all the electrons except the reference one. The difference between $\Omega(\vec{x}_2; \vec{x}_1)$ and the uncorrelated probability $\rho(\vec{x}_2)$ of finding an electron at $\vec{x}_2$ describes the change in the conditional probability caused by the correction for self-interaction, exchange and Coulomb correlation, compared to the uncorrelated situation:

$$h_{XC}(\vec{x}_1; \vec{x}_2) = \Omega(\vec{x}_2; \vec{x}_1) - \rho(\vec{x}_2) = \frac{\rho_2(\vec{x}_1, \vec{x}_2)}{\rho(\vec{x}_1)} - \rho(\vec{x}_2) = \rho(\vec{x}_2) f(\vec{x}_1; \vec{x}_2) \tag{3.6}$$

This difference is called *exchange-correlation hole* since correlation usually leads to a depletion of the electron density at $\vec{x}_2$ in comparison with the independent particle

situation. Thus, it usually has negative sign and, moreover, since $\Omega(\vec{x}_2;\vec{x}_1)$ integrates to $N-1$ and the independent density integrates to N, the exchange-correlation hole $h_{XC}(\vec{x}_1;\vec{x}_2)$ integrates exactly to -1, that is, the exchange-correlation hole contains the charge of one electron:

$$\int h_{XC}(\vec{x}_1;\vec{x}_2)d\vec{x}_2 = -1 \tag{3.7}$$

Fermi and Coulomb holes The potential energy due to the electrostatic repulsion of the electron E_{ee} and corresponding to the expectation value of the operator $\hat{V}_{ee}$, can be written in terms of the pair density, once integrated over the spin-coordinates, becoming then spin-independent pair density $\rho_2(\vec{r}_1,\vec{r}_2)$

$$E_{ee} = \langle \hat{V}_{ee} \rangle = \langle \Psi \mid \sum_i^N \sum_{j>i}^N \frac{1}{r_{ij}} \mid \Psi \rangle = \frac{1}{2}\int\int \frac{\rho_2(\vec{r}_1,\vec{r}_2)}{r_{12}} d\vec{r}_1 d\vec{r}_2 \tag{3.8}$$

Then, using $\rho_2(\vec{r}_1,\vec{r}_2) = \rho(\vec{r}_1)\rho(\vec{r}_2) + \rho(\vec{r}_1)h_{XC}(\vec{r}_1;\vec{r}_2)$ the above energy can be split into two contributions:

$$E_{ee} = \frac{1}{2}\int\int \frac{\rho(\vec{r}_1)\rho(\vec{r}_2)}{r_{12}} d\vec{r}_1 d\vec{r}_2 + \frac{1}{2}\int\int \frac{\rho(\vec{r}_1)h_{XC}(\vec{r}_1;\vec{r}_2)}{r_{12}} d\vec{r}_1 d\vec{r}_2 \tag{3.9}$$

The first term is $J[\rho]$, the classical electrostatic energy of a charge distribution with itself, containing the unphysical self-interaction. The second term is the energy of interaction between the charge density and the charge distribution of the exchange-correlation hole. It includes correction for the self-interaction as well as all contributions of quantum mechanical correlation effects. In that way, the hole functions are so useful for discussing exchange and correlation effects. The more is known about the characteristics of the exchange correlation hole h_{XC} and the better the approximate h_{XC} used in calculations, the more accurate results are expected.

The exchange-correlation hole h_{XC} can formally be split into the *Fermi hole* $h_X^{\sigma_1=\sigma_2}(\vec{r}_1,\vec{r}_2)$ and the *Coulomb hole* $h_C^{\sigma_1=\sigma_2}(\vec{r}_1,\vec{r}_2)$

$$h_{XC}(\vec{r}_1;\vec{r}_2) = h_X^{\sigma_1=\sigma_2}(\vec{r}_1,\vec{r}_2) + h_C^{\sigma_1=\sigma_2}(\vec{r}_1,\vec{r}_2) \tag{3.10}$$

Just to mention here that, even if the formal separation above is convenient, only the total hole h_{XC} has physical meaning.

- **The Fermi hole**
  The Fermi hole arises from the Pauli principle (antisymmetry of the wavefunction) and dominates by far the Coulomb hole. It integrates, as the total hole does, to -1

$$\int h_X(\vec{r}_1;\vec{r}_2)d\vec{r}_2 = -1 \tag{3.11}$$

and it is negative everywhere. If applying Eq. 3.6 only for the exchange case, it becomes

$$h_X(\vec{r}_1;\vec{r}_2) = \rho(\vec{r}_2) f_X(\vec{r}_1;\vec{r}_2) \tag{3.12}$$

In that way, its shape is determined both by the Fermi correlation factor f_X and by the density at point $\vec{r}_2$ and then, it is not expected to be spherically symmetric and usually is largest around the reference electron.

- **The Coulomb hole**
  If both the total and exchange holes integrate to -1, the Coulomb hole integrates to zero

$$\int h_C(\vec{r}_1;\vec{r}_2)\vec{dr}_2 = 0 \tag{3.13}$$

That is, the integral over space contains no charge. Since the Coulomb hole is negative and largest at the position of the reference electron (due to its origin in $1/r_{12}$ interactions) and it integrates to zero, it has positive values in some regions far away from that reference electron.

3.2 Basics of DFT

3.2.1 The Hohenberg-Kohn theorems

In 1964, Hohenberg and Kohn [76] formulated and proved a theorem that put on solid mathematical grounds the intuitive former Fermi and Dirac's ideas. It is divided in two parts:

The first Hohenberg-Kohn theorem : ***The external potential is univocally determined by the ground state electronic density, besides a trivial additive constant.***

Corollary: With the external potential, the Hamiltonian is fully determined, except for a constant shift of the energy, and then, the many-body wavefunctions for *all* states (ground and excited) are determined. Therefore all the properties of the system are completely determined given only the ground state density.

Given that $\rho(\vec{r})$ determines the total number of electrons of the system ($\int \rho(\vec{r})\vec{dr} = N$) and establishes $V_{ext}(\vec{r})$, it is concluded that $\rho(\vec{r})$ determines the Hamiltonian, the wavefunction of the ground state and, by extension, the expectation value of any observable of the ground state (the energy among them). Thus, there is a direct relation between the density and the wavefunction through the external potential.

$$\rho(\vec{r}) \rightarrow V_{ext}(\vec{r}) \rightarrow \widehat{H} \rightarrow \Phi \tag{3.14}$$

$$\rho(\vec{r}) \Leftrightarrow \Phi \tag{3.15}$$

It is important to point out that this first Hohenberg-Kohn theorem is only valid for non degenerated ground states and always when $\rho(r)$ is N-representable (it means both $\rho(r) \geq 0$ and $\int \rho(r)dr = N$) and v-representable (it means there is an external potential from which density $\rho(r)$ can be derived). There are many reasonable trial functions that cannot be derived from a potential. For the cases where this theorem is valid, we have:

$$E[\rho] = T[\rho] + E_{Ne}[\rho] + E_{ee}[\rho] \tag{3.16}$$

where $T[\rho]$ and $E_{ee}[\rho]$ do no depend on the external potential and are included within the Hohenberg-Kohn functional $F_{HK}[\rho]$

$$F_{HK}[\rho] = T[\rho] + E_{ee}[\rho] = \langle \Phi[\rho] | \widehat{T} + \widehat{V}_{ee} | \Phi[\rho] \rangle \tag{3.17}$$

Then,

$$E[\rho] = \int \rho(\vec{r}) V_{Ne}(\vec{r}) \vec{dr} + F_{HK}[\rho] \tag{3.18}$$

This functional $F_{HK}[\rho]$ is the big unknown in density functional theory. Known exactly, the Schrödinger equation would be solved exactly as well. Since it does not depend on the external potential (V_{ext} or V_{Ne}), it is an universal functional, that is, does not depend on the system we are working with. Thus, it is applied equally to atoms as to big molecules. The main problem is the explicit form of both $T[\rho]$ and $E_{ee}[\rho]$ is completely unknown.

From the latter, at least the classical Coulomb part can be extracted:

$$E_{ee}[\rho] = \frac{1}{2} \int \int \frac{\rho(\vec{r}_1)\rho(\vec{r}_2)}{r_{12}} \vec{dr}_1 \vec{dr}_2 + E_{ncl} = J[\rho] + E_{ncl}[\rho] \tag{3.19}$$

where $E_{ncl}[\rho]$ is the non-classical contribution to the electron-electron interaction containing all the effects of self-interaction, exchange and Coulomb correlation. Finding explicit expressions for the yet unknown functionals $T[\rho]$ and $E_{ncl}[\rho]$ is the major challenge in DFT.

Up to this point, the Hamiltonian operator of the system (which characterizes *all* the states of the system) is just determined by the ground state density through the external potential. Thus, all properties for all states, ground *and* exited, are formally determined by the ground state density. However, DFT is usually a ground state theory as a consequence of the second Hohenberg-Kohn theorem. On the other hand, the ground state density contains information about positions and charges of the nuclei allowing the mapping from density to external potential; then, densities of excited states cannot be used.

The second Hohenberg-Kohn theorem ***The electron density of a non-degenerate ground state can be calculated, exactly in theory, determining the density that minimizes the energy of the ground state.***

Corollary: The functional $E[\rho]$ is enough to determine the ground state energy and density. In general, excited states must be determined by other means.

This second theorem is providing the variational principle for $E[\rho]$:

$$E_0 \leq E[\tilde{\rho}(\vec{r})] = T[\tilde{\rho}(\vec{r})] + E_{Ne}[\tilde{\rho}(\vec{r})] + E_{ee}[\tilde{\rho}(\vec{r})] \tag{3.20}$$

where $\tilde{\rho}(\vec{r})$ is a N-representable and v-representable arbitrarily chosen trial density. If the first Hohenberg-Kohn theorem is applied both to the trial and the exact densities, it takes to the conclusion that each one of the two densities defines a different Hamiltonian and therefore a different wavefunction.

$$\tilde{\rho}(\vec{r}) \rightarrow \tilde{V}_{ext}(\vec{r}) \rightarrow \tilde{\widehat{H}} \rightarrow \tilde{\Phi} \qquad \text{Trial density} \tag{3.21}$$

$$\rho(\vec{r}) \rightarrow V_{ext}(\vec{r}) \rightarrow \widehat{H} \rightarrow \Phi \qquad \text{Exact density} \tag{3.22}$$

If we calculate now the energy for the trial density with the exact Hamiltonian, according to the variational principle, we are left with:

$$E[\tilde{\rho}(\vec{r})] = \langle \tilde{\Phi} | \widehat{H} | \tilde{\Phi} \rangle \geq \langle \Phi | \widehat{H} | \Phi \rangle = E_0 \tag{3.23}$$

where E_0 is the exact energy of the considered ground state. Thus, the variational principle is defined within the DFT framework, assuring that any trial density results in a greater energy or equal to the exact energy of the ground state. Therefore, to obtain the exact density of the ground state, it is necessary to find the density that minimizes the energy

$$\left[\frac{\delta E(\rho)}{\delta \rho} \right] = 0 \tag{3.24}$$

To sum up:

- All the properties of a system defined by an external potential V_{ext} are determined by the ground state density.
- In particular, the ground state energy is associated with a density ρ is available through the functional $\int \rho(\vec{r}) V_{Ne} \vec{dr} + F_{HK}[\rho]$.
- This functional attains its minimal value only if the input density is the ground state density: $\tilde{\rho}(\vec{r}) = \rho_0(\vec{r})$

The applicability of this variational recipe is limited to the ground state energy since the property that E_0 is the lowest possible energy of the system is explicitly used. Hence, this strategy is not transferable to the problem of excited states.

Limitations of the Hohenberg-Kohn theorems The Hohenberg-Kohn theorems are the bedrocks of the modern DFT but they are only proofs of the unique mapping between the ground state density and the ground state energy; they do not provide any guidance at all how the functional that delivers the ground state energy should be built. Moreover, in any real application of DFT, it is necessary to use an approximation for

the functional $F[\rho]$ since the true functional is not available. However, the variational principle used in the second Hohenberg-Kohn theorem applies to the exact functional only. Then, the use of approximations leads to unpleasant consequences. First, many wavefunction-based theories (as Hartree-Fock) are strictly variational and the expectation value $E = \langle \tilde{\Psi} \mid \hat{H} \mid \tilde{\Psi} \rangle$ is an indicator of the quality of the trial wavefunction (the lower E is, the better the approximation of $\tilde{\Psi}$ to Ψ). In DFT, the energy value obtained from a trial functional has no meaning in that respect. Second, it is possible to obtain energies lower than the exact ones since the approximation of $F[\rho]$ leads to an approximation to the Hamiltonian while not paying attention to the wavefunction and the variational principle does not hold anymore.

3.2.2 The Kohn-Sham approach

The equation showing the relationship between the energy and the electronic density and, therefore, the equation to be solved is

$$E[\rho] = \int \rho(\vec{r}) V_{ext}(\vec{r}) \vec{dr} + F_{HK}[\rho] \tag{3.25}$$

$$F_{HK}[\rho] = \langle \Phi[\rho] | \widehat{T} + \widehat{V}_{ee} | \Phi[\rho] \rangle = T[\rho(\vec{r})] + J[\rho(\vec{r})] + E_{ncl}[\rho(\vec{r})] \tag{3.26}$$

where only $J[\rho(\vec{r})]$ is known. Kohn and Sham proposed a general approach to deal with this problem, introducing one electron orbitals. It starts from the observation that a system of non-interacting electrons is exactly described by an antisymmetric wavefunction of the Slater determinant type, made of one-electron non-interacting orbitals [104]. Thus, it is possible to build a *non-interacting reference system* with a Hamiltonian in which an effective, local potential $V_s(\vec{r})$ that does not contain any electron-electron interaction is introduced:

$$\widehat{H}_s = -\frac{1}{2} \sum_i^N \nabla_i^2 + \sum_i^N V_s(\vec{r}_i) \tag{3.27}$$

The ground state wavefunction of this system is represented by an Slater determinant, as in Hartree-Fock theory:

$$\Theta_s(\vec{x}_1, \vec{x}_2 ... \vec{x}_n) = \frac{1}{\sqrt{N!}} \begin{vmatrix} \psi_1(\vec{x}_1) & \psi_2(\vec{x}_1) & \dots & \psi_N(\vec{x}_1) \\ \psi_1(\vec{x}_2) & \psi_2(\vec{x}_2) & \dots & \psi_N(\vec{x}_2) \\ \vdots & \vdots & \ddots & \vdots \\ \psi_1(\vec{x}_N) & \psi_2(\vec{x}_N) & \dots & \psi_N(\vec{x}_N) \end{vmatrix}$$

where the spin orbitals are determined by:

$$\hat{f}^{KS} \psi_i = \varepsilon_i \psi_i; \qquad \hat{f}^{KS} = -\frac{1}{2} \nabla^2 + V_s \tag{3.28}$$

These are the Kohn-Sham (KS) orbitals and the density can be expressed in terms of them:

$$\rho_s(\vec{r}) = \sum_i^N \int \mid \psi_i(\vec{x}_i) \mid^2 ds_i \tag{3.29}$$

Regarding the physical meaning of these orbitals, the DFT counterpart to the Koopman's theorem relates the first ionization energy and electron affinity to the HOMO and LUMO energies. This would be an exact statement in the formalism of DFT, the use of approximate exchange-correlation potentials makes the calculated energies approximated. A proof of this theorem usually employs Janak's theorem: that the derivative of the total DFT energy E with respect to the occupation of a given orbital n_i is equal to the corresponding orbital energy ($\frac{\partial E}{\partial n_i} = \varepsilon_i$).

The Kohn and Sham next and central idea lies in the connection between this artificial system and the real one: The potential V_s has to be chosen such that the density resulting from those non-interacting orbitals $\{\psi_i\}$ is exactly the same as the density of the real system of interacting electrons

$$\rho_s(\vec{r}) = \rho_0(\vec{r}) \tag{3.30}$$

The Kohn-Sham equations The kinetic energy of the reference system can be calculated with the expression for the exact kinetic energy of a system of non-interacting electrons as

$$T_s = -\frac{1}{2}\sum_{i=1}^{N}\langle\psi_i|\nabla^2|\psi_i\rangle \tag{3.31}$$

Of course this non-interacting kinetic energy is not equal to the true kinetic energy of the interacting system, even if the systems have the same density. Kohn and Sham accounted for it introducing the following separation on $F[\rho]$:

$$F[\rho(\vec{r})] = T_s[\rho(\vec{r})] + J[\rho(\vec{r})] + E_{XC}[\rho(\vec{r})] \tag{3.32}$$

where E_{XC}, the so-called *exchange-correlation energy* is defined as:

$$E_{XC}[\rho] = (T[\rho] - T_s[\rho]) + (E_{ee}[\rho] - J[\rho]) = T_c[\rho] + E_{ncl}[\rho] \tag{3.33}$$

where T_c is the part of kinetic energy not covered by T_s and is added to the non classical electrostatic contributions. In that way, E_{XC} contains everything unknown.

Now, to solve the problem of defining V_s such that it provides a Slater determinant with the same density as the real system, the energy of the real interacting system has to be written in terms of E_{XC}, the only term without explicit form:

$$E[\rho(\vec{r})] = T_s[\rho(\vec{r})] + J[\rho(\vec{r})] + E_{XC}[\rho(\vec{r})] + E_{Ne}[\rho(\vec{r})] \tag{3.34}$$

$$= T_s[\rho(\vec{r})] + \frac{1}{2}\int\int\frac{\rho(\vec{r}_1)\rho(\vec{r}_2)}{\mid\vec{r}_1 - \vec{r}_2\mid}\vec{dr}_1\vec{dr}_2 + E_{XC}[\rho(\vec{r})] + \int V_{Ne}\rho(\vec{r})\vec{dr} \tag{3.35}$$

$$= -\frac{1}{2}\sum_{i=1}^{N}\langle\psi_i|\nabla^2|\psi_i\rangle + \frac{1}{2}\sum_{i}^{N}\sum_{j}^{N}\int\int\mid\psi_i(\vec{r}_1)\mid^2\frac{1}{\mid\vec{r}_1 - \vec{r}_2\mid}\mid\psi_j(\vec{r}_2)\mid^2\vec{dr}_1\vec{dr}_2$$

$$+ E_{XC}[\rho(\vec{r})] - \sum_{i}^{N}\int\sum_{I}^{M}\frac{Z_I}{\mid\vec{r}_1 - \vec{R}_I\mid}\mid\psi_i(\vec{r}_1)\mid^2\vec{dr}_1 \tag{3.36}$$

And, similarly to the Hartree-Fock approximation, the variational principle is applied to that energy:

$$\left[-\frac{1}{2}\nabla^2 + \left[\int \frac{\rho(\vec{r}_2)}{\mid \vec{r}_1 - \vec{r}_2 \mid} d\vec{r}_2 + V_{XC}(\vec{r}_1) - \sum_I^M \frac{Z_I}{\mid \vec{r}_1 - \vec{R}_I \mid} \right] \right] \psi_i$$
$$= \left[-\frac{1}{2}\nabla^2 + V_{eff}(\vec{r}_1) \right] \psi_i = \varepsilon_i \psi_i \tag{3.37}$$

Where V_{eff} is identical to V_s and it is related with the potential due to the exchange-correlation energy V_{XC} through

$$V_s = V_{eff} = \int \frac{\rho(\vec{r}_2)}{\mid \vec{r}_1 - \vec{r}_2 \mid} d\vec{r}_2 + V_{XC}(\vec{r}_1) - \sum_I^M \frac{Z_I}{\mid \vec{r}_1 - \vec{R}_I \mid} \tag{3.38}$$

Once are known the various contributions of the equation above, V_s is determined and eq 3.37 can be solved, finding the orbitals and the ground state density and energy. Since V_{eff} depends on the density and thus on the orbitals though the Coulomb term, just like Hartree- Fock equations, the Kohn-Sham ones have to be solved iteratively.

Since it is not known how E_{XC} is expressed, the explicit form of its corresponding potential V_{XC} is not known and it is defined as

$$V_{XC} = \frac{\delta E_{XC}}{\delta \rho} \tag{3.39}$$

If the exact forms of E_{XC} and V_{XC} were known, the Kohn-Sham strategy would lead to the exact energy. The approximation does not lie on the method itself, but in the choice of the form of the unknown E_{XC} and corresponding V_{XC}. The central goal on DFT is therefore finding the best possible approximations to these two quantities.

3.3 Exchange and correlation in DFT

As said above, DFT provides a practical approach to solve the electronic ground state problem by mapping the many-body problem onto a self-consistent one-electron problem. Therefore, given an external potential, it is possible to find the electronic density, the ground state energy, and any desired ground state property, e.g. equilibrium geometry, vibrational frequencies and normal modes, elastic moduli, dielectric constant, transport properties, etc. The remaining problem is how to devise a reliable and practical approximation of the exchange-correlation functional E_{XC}. In that way, the quality of the DFT approach depends only on the accuracy of the chosen approximation to E_{XC}. Before analyzing the different flavors and trends on E_{XC}, let us point out again that, in opposition to wavefunction methods, there is no way to improve the result once chosen a functional, since the explicit form of the real one is completely unknown. The search for better functionals relies on physical and mathematical intuition and has a strong “trial and error" component as well. Within the physical constraints, the better the functional

describes the exchange-correlation hole, the better the functional accounts for the non-classical effects. However, functionals fulfilling these conditions are not necessarily better than functionals that do not and most of the successful ones violates them. Then, it is important then to choose a functional that suits the particular problem and, actually, many of the new functionals developed are based in previous series of empirical data.

In this work, we have used two of the most widely employed approaches on the exchange-correlation problem within DFT: the *local density* and the *generalized gradient* approximations. They are presented below, and, since all these functionals have their roots in the homogeneous electronic gas model, it is presented as a reference.

3.3.1 The homogeneous electronic gas

A starting point is the picture of a neutral system made of an homogeneous electronic gas moving on a positive background, which is a simplified model for metallic systems and presents the simplest treatment of correlated electrons. In that way, it has been widely studied in detail. This model considers both the number of electrons N and the volume of the system V are considered to approach infinity, while the electron density, i.e $\rho = N/V$, remains finite and attains a constant value. The exchange energy density (energy per particle, ε) for this system is exactly given by Dirac's equation:

$$\varepsilon_X^D = -\frac{3}{4}\left(\frac{3}{\pi}\right)^{1/3}\rho^{1/3} = -\frac{0.458}{r_s}\text{a.u.} \tag{3.40}$$

with $r_s = \left(\frac{3}{4}\pi\rho\right)^{1/3}$ as the mean interelectronic distance expressed in atomic units. For the correlation term, an explicit expression is not known, but excellent approximations are available as well. The most accurate one is based on the Monte Carlo simulations of Ceperley and Alder (1980) [105] and its parametrization by Perdew and Zunger (1981) [106].

$$\varepsilon_C^{PZ} = \begin{cases} A\ln r_s + B + Cr_s\ln r_s + Dr_s & \text{if } r_s \leq 1 \\ \gamma/(1+\beta_1\sqrt{r_s}+\beta_2 r_s) & \text{if } r_s > 1 \end{cases} \tag{3.41}$$

The use of the homogeneous electron gas as a reference may not seem a particular good idea for molecular systems, since their electronic densities are far from uniform. The fact that most of the available approximations are derived from the homogeneous electron gas may be one of the reasons of the initial reluctant attitude of the computational chemistry community in order to adopt DFT.

3.3.2 Local density approximation (LDA) and local spin density approximation (LSDA)

The local density approximation was proposed in the seminal paper by Kohn and Sham in 1965 but its philosophy was already present in Thomas-Fermi-Dirac theory. The main idea is to consider a general inhomogeneous electronic system as *locally homogeneous*, and then using the above exchange correlation functional corresponding to the homogeneous

electron gas, which is known to an excellent accuracy. The exchange-correlation energy can be written as

$$E_{XC}^{LDA}[\rho] = \int \rho(r)\varepsilon_{XC}^{LDA}[\rho(r)]dr \tag{3.42}$$

with $\varepsilon_{XC}^{LDA}[\rho] = \varepsilon_{X}^{LDA}[\rho] + \varepsilon_{C}^{LDA}[\rho]$ and both $\varepsilon_{X}^{LDA}[\rho]$ and $\varepsilon_{C}^{LDA}[\rho]$ given by the above expressions 3.40 and 3.41. Other approaches, using different analytic forms for $\varepsilon_{C}^{LDA}[\rho]$ than expression 3.41 have generated several LDAs including: Vosko-Wilk-Nusair (VWN) [107], Cole-Perdew (CP) [108] and Perdew-Wang (PW92) [109].

Inserting Eq. 3.40 into Eq. 3.42, the $\rho^{\frac{4}{3}}$ dependence of the exchange energy is shown.

In order to extend Kohn-Sham theory to spin-polarized system, the electronic density is considered as composed by two independent spin densities $\rho = \rho\uparrow + \rho\downarrow$. Each one of theses densities is constructed with the Kohn-Sham spin orbitals, which satisfy the self-consistent Kohn-Sham equations. No information about the individual spin densities is required except in cases where the external potential contains spin-dependent parts, such as an external magnetic fields. In the former situations, functionals that explicitly depend on the α and β spin densities are employed for open shell systems.

Then, the extension of the local density approximation LDA to those systems where density is split into $\rho\uparrow$ and $\rho\downarrow$ is possible. This is called local spin density approximation (LSDA) and basically consists of replacing the exchange-correlation energy density with a spin-polarized expression:

$$\begin{aligned} E_{XC}^{LSDA}[\rho\uparrow(r), \rho\downarrow(r)] &= \int [\rho\uparrow(r) + \rho\downarrow(r)]\varepsilon_{XC}^{h}[\rho\uparrow(r), \rho\downarrow(r)]dr \\ &= \int \rho(r)\varepsilon_{XC}^{h}[\rho(r), \zeta(r)]dr \end{aligned} \tag{3.43}$$

The common practice in LSDA is to interpolate between the fully-polarized ε_{XC}^{P} and unpolarized ε_{XC}^{U} exchange-correlation energy densities using some interpolation function f that depends on the magnetization density ζ:

$$\varepsilon_{XC}^{h}[\rho(r), \zeta(r)] = f(\zeta)\varepsilon_{XC}^{U}[\rho] + [1 - f(\zeta)]\varepsilon_{XC}^{P}[\rho] \quad ; \tag{3.44}$$

$$\zeta = \frac{\rho\uparrow(r) - \rho\downarrow(r)}{\rho\uparrow(r) + \rho\downarrow(r)} = \frac{\rho\uparrow(r) - \rho\downarrow(r)}{\rho(r)} \tag{3.45}$$

3.3.3 Generalized gradient approximation (GGA)

In order to address inhomogeneities in the electronic density, the next exploited approach introduced them in a semi-local way, by expanding $E_{XC}[\rho]$ as a series in terms of the density and its gradients. This approach is known as *gradient expansion* and, its implementation easiness together with the improvement of cancellation of self-interaction respect to LDA, turned it into a catalyst for the adoption of DFT within the community of computational chemists.

In general, the exchange and correlation energy can be written in the following form:

$$E_{XC}[\rho] = \int \rho(r)\varepsilon_{XC}[\rho(r)]F[\rho(r), \nabla\rho(r), \nabla^2\rho(r), \ldots]dr \tag{3.46}$$

where F is an enhancement factor that modifies the LSDA expression according to the variation of the density in the neighboring points of a considered one. In that way, gradient corrections constitute a semi-local approach and it will hardly deal with non-local effects at longer ranges.

When GGA is used to solve real problems, it does not lead to the desired systematic accuracy and often performs worse than LDA. The reason for this failure is that the exchange-correlation hole associated with a GGA functional has lost many of the properties which the LDA hole has in order to retain all the relevant contributions up to the desired order, such as normalization condition, the negativity of the exchange density, self-interaction cancellation, etc. Then, since it is not the physics but the results obtained which dictate the choices of the mathematical constructions, a large number of different flavors with the gradient expansion have been proposed, leading to the *generalized gradient approximations* (GGAs).

3.3.3.1 Langreth-Mehl

The first GGA functional proposed in the literature (1981) [110] corrects both the ε_X^{LDA} and the ε_C^{RPA} (RPA from Random Phase Approximation [111, 112]) including $|\nabla\rho(r)|^2$

$$\varepsilon_X = \varepsilon_X^{LDA} - a\frac{|\nabla\rho(r)|^2}{\rho(r)^{4/3}}\Big(\frac{7}{9} + 18f^2\Big) \tag{3.47}$$

$$\varepsilon_C = \varepsilon_C^{RPA} + a\frac{|\nabla\rho(r)|^2}{\rho(r)^{4/3}}\Big(2e^{-F} + 18f^2\Big) \tag{3.48}$$

where $F = b|\nabla\rho(r)|/\rho(r)^(7/6)$, $b = (9\pi)^{1/6}f$, $a = \pi/(16(3\pi^2)^{4/3})$ and $f = 0.15$, being the latter introduced to fit the ground state energies and ionization energies of various atoms (He, Be, Ne, Mg, Ar).

3.3.3.2 BLYP

The exchange-correlation energy functional can be split into two negative quantities:

$$E_{XC} = E_X + E_C \tag{3.49}$$

and, since $\mid E_X \mid > \mid E_C \mid$, the gradient corrections are more effective when applied to the exchange energy functional E_X. In 1988, Becke proposed an exchange functional where the ε_X^{LDA} was modified in such a way that the parameters were fitted to experimental molecular data [113].

$$\varepsilon_X = \varepsilon_X^{LDA}\Big(1 - \frac{\beta}{2^{1/3}A_x}\frac{x^2}{1 + 6\beta x\sinh^{-1}(x)}\Big) \tag{3.50}$$

for $x = 2^{1/3} \mid \nabla\rho(r) \mid /\rho(r)^{4/3}$, $A_x = (3/4)(3/\pi)^{1/3}$ and the parameter $\beta = 0.0042$ chosen according to the exact Hartree-Fock exchange energy of noble gases.

This was complemented by a correlation functional by Lee, Yang and Parr, not derived from LDA but from other closed shell system of the Colle-Salvetti expression for the electronic correlation in Helium, giving rise to the widely used BLYP functional [114].

$$\varepsilon_C = -\frac{a}{1+d\rho^{-1/3}}\Big\{\rho + b\rho^{-2/3}\Big[C_F\rho^{5/3} - 2t_w + \frac{1}{9}\Big(t_w + \frac{1}{2}\nabla^2\rho\Big)\Big]e^{-c\rho^{-1/3}}\Big\} \tag{3.51}$$

where

$$t_w = \frac{1}{8}\Big(\frac{|\nabla\rho|^2}{\rho} - \nabla^2\rho\Big) \tag{3.52}$$

is known as Weizsacker kinetic energy density and $C_F = 3/10(3\Pi^2)^{2/3}$, $a = 0.04918$, $b = 0.132$, $c = 0.2533$ and $d = 0.349$.

3.3.3.3 PBE

Perdew, Burke and Erzenhof (PBE), in 1996, proposed an exchange and correlation functional that satisfies as many formal properties and limits as possible, sacrificing only those deemed to be energetically less important [115]. In this functional, the enhancement factor over the local exchange F depends on the density, the magnetization density (for spin-dependent cases), and the dimensionless *density gradient* $s = |\nabla\rho(r)\ |\ /\rho^{\frac{4}{3}}$. From the theoretical point of view, the PBE functional is very satisfactory because it verifies many of the exact conditions of the exchange correlation hole and it does not contain any fitting parameter to experimental data, while its quality is equivalent or even better then BLYP. The exchange part is written as the enhancement factor multiplied by the LDA functional:

$$\varepsilon_x^{PBE} = \varepsilon_x^{LDA}F(s); \qquad F(s) = 1 + \kappa - \frac{\kappa}{1+\mu s^2/\kappa} \tag{3.53}$$

where $\mu = 0.21951$ and $\kappa = 0.804$ are parameters arising for the conditions (e.g. the Lieb-Oxford condition [116]) imposed to fulfill the formal properties. Other authors have proposed the same form but with values of μ and κ fitted empirically to a database of atomization energies.

The correlation energy assumes the form:

$$E_C = \int \rho(r)[\varepsilon_C^{LDA}(\rho,\zeta) + H[\rho,\zeta,t]]dr; \tag{3.54}$$

$$H[\rho,\zeta,t] = (e^2/a_0)\gamma\phi^3\ln\Big\{1 + \frac{\beta}{\gamma}t^2\Big[\frac{1+At^2}{1+At^2+A^2t^4}\Big]\Big\}; \tag{3.55}$$

$$A = \frac{\beta}{\gamma}[e^{-\varepsilon_C^{LDA}/(\gamma\phi^3e^2/a_0)} - 1]^{-1}; \qquad t = \frac{|\nabla\rho(r)\ |}{(2\phi k_s\rho)} \tag{3.56}$$

where k_s is the Thomas-Fermi screening wavenumber, $\phi = \phi(\zeta)$ is a spin-scaling factor and $\beta = 0.066725$ and $\gamma = 0.031091$ also arising by construction. A revision of PBE, RPBE appears to provide an improved description of adsorption and hydrogen-bonded systems [117].

3.4 Self-interaction in DFT: DFT+U and hybrids HF-DFT methods

As mentioned before the exchange term neutralizes the undesired portion of $J[\rho]$ by construction in the Hartree-Fock approach (sec. 2.2). However, in DFT, due to the approximate character of the exchange term, which is obtained in an independent way that the repulsion term, the self-interaction is not canceled and there is an intrinsic error associated to it. In fact, no exchange-correlation functional is self-interaction free.

3.4.1 The DFT + U approach

The problem of self-interaction is particularly notorious in transition-metal oxides and rare-earth metal compounds, because of their characteristic well-localized d and f orbitals. This localization leads to strong on-site electronic correlations, such that if one electron is occupying a state localized in a particular site, placing a second electron in the same site is penalized with an additional energy U. This idea was originally proposed at the level of empirical Hamiltonians by Hubbard in 1965. Currently, Hubbard phenomenological approach has been combined with DFT calculations, by supplementing the LDA or GGA with a Hubbard-type on-site repulsion term U [118, 119]:

$$E_{DFT+U} = E_{DFT} - \frac{1}{2}UN(N-1) + \frac{1}{2}U\sum_{i\neq j} f_i f_j \qquad f_i = \text{orbital occupancies} \qquad (3.57)$$

In practice, the on-site interaction energy is evaluated with a parametrized Hamiltonian. The parameters that modify this Hamiltonian are designated as U_{Il} and J_{Il} and correspond, respectively, to the average Coulomb and exchange interactions between electrons of the same angular momentum (l) that are localized on the same atom (I). Then U_{Il} and J_{Il} must be chosen properly in order to perform an accurate enough DFT+U calculation. They can be selected empirically by browsing some different values in order to reproduce know properties of the system under study [120] but this approach cannot be applied whenever there is a lack of experimental data available. However, it is possible to evaluate U_{Il} and J_{Il} from *ab initio* procedures, which lead to a DFT+U theory not only explicative but also predictive [121, 122]. In this approach, interactions between electrons in states localized on the same atomic center are considered in a HF-like manner (due to the self-interaction free character of HF theory), while the remaining interactions are treated with DFT. The method takes advantage of the relationship between U_{Il} and J_{Il} and the Coulomb and exchange integrals evaluated in the basis of the UHF molecular orbitals of localized states of the system. These integrals are evaluated by means of embedded cluster models that represent the material of interest with modest and affordable size and reproduce the true interactions between the localized electrons in the real material. U_{Il} and J_{Il} values obtained in this way are used as constants for the material and do not depend on the exchange correlation flavor used.

3.4.2 Hybrid HF-KS approaches

Another alternative approach to remove the improper self-interaction term using the advantages of Hartree-Fock theory is the use of *hybrid*(HF-DFT) exchange correlation functionals [123]. They involve a pure DFT correlation term and a mixed HF-DFT exchange term:

$$E_{XC}^{hyb} = \alpha E_C^{DFT} + \alpha E_X^{HF} + (1-\alpha) E_X^{DFT} \tag{3.58}$$

where the coefficient α is chosen to assume a specific fractional value or is fitted to some properties of a molecular database. The value $\alpha = 0.25$ (25% of the exact HF exchange) is known to be a good compromise value for matching many features of semiconductors and some insulators, such as bandgaps, structural and optical properties.

3.5 SIESTA code features

We use for our structural calculations the *spanish initiative for electronic simulation with thousand of atoms* (SIESTA) program [97]. It implements the PBC conditions within the DFT framework.

The wavefunction under periodic boundary conditions should have the same periodicity as the unit cell besides a phase factor related to the wave vector $\vec{k}$ (Eq. 2.41). Constructed the electronic density as the square of the wavefunction, the phase factor cancels and the density has the same periodicity of the unit cell, i.e. $\rho_{\vec{k}}(\vec{r}+\vec{L}) = \rho_{\vec{k}}(\vec{r})$ for any linear combination of lattice vectors L. In PBC-DFT, one has to solve a set of coupled Kohn-Sham equations, one for each k-point included in the Brillouin zone sampling.

Starting from Born-Oppenheimer approximation, the SIESTA project is based on DFT and can use different flavors of exchange-correlation functionals, including spin-polarization, collinear or non-collinear effects. The core electrons are replaced by norm-conserving pseudopotentials factorized in the Kleinman-Bylander form [124], including scalar relativistic effects and non-lineal partial core corrections. The one particle problem is solved using linear combination of numerical atomic orbitals, including multiple-zeta and polarization. Forces on the atoms and the stress tensor are obtained from the Hellmann-Feynman theorem [125].

The DFT equations are solved using the self-consistent field SCF procedure. For a Hamiltonian, the one-particle Schrödinger equation is solved yielding the energy and the density matrix for the ground state. This is performed either via diagonalization (cube-scaling) or with an $\mathcal{O}$(N) algorithm.

Once the density matrix is obtained, the SCF procedure continues with the calculation of a new Hamiltonian matrix. The calculation of the Hamiltonian matrix elements has an $\mathcal{O}$(N) scaling provided that the range of overlap between the basis orbitals is finite. To achieve that, basis orbitals with strictly vanish beyond a cutoff radius are used. This approach is different from the usual one of using decaying orbitals and neglecting matrix elements trough some criterion.

Since we have constructed our own pseudopotentials and basis sets for the calculations performed all along this work, we present here a brief introduction about pseudopotential theory and the main particular features of pseudopotentials implemented in SIESTA, as well as a description of the method used for generating the basis sets. Moreover, the structure of the SIESTA Hamiltonian and the expression of the total energy are outlined, followed by some remarks about the density of states as obtained in this work. Finally, we present the basics on the Mulliken population analysis, performed also by SIESTA and present for YAG and related crystals in Section 5.3.2.

3.5.1 Pseudopotentials

A common procedure among chemists is to separate the whole set of electrons of a given system into core and valence electrons. The physical reason is that only valence electrons are actively involved in the chemical bonding that leads to molecules and crystals, whereas the core ones are inactive in terms of chemical bonding. Thus, these *frozen* core electrons can be considered as one ingredient more in the total effect that the environment produces on the wavefunctions and energies associated to the valence electrons, together with those from atomic nuclei and external fields. This particular effect of the core electrons is represented in terms of Effective Core Potentials (ECPs). These ECP methods are widely used in in *ab initio* calculations not only because of the associated reduction in the computational cost but also because of the intrinsic correction of the basis set superposition error (BSSE) coming in a major extent from deficiencies in the atomic basis describing the core electrons. There are two families of ECP methods: on the one hand, those relying on the Philips-Kleinman equation, which produce nodeless valence pseudo-orbitals and are known as *pseudopotential* methods and, on the other hand, those based on Huzinaga-Cantu equation, which lead to valence orbitals with the same nodal structure as the all-electron orbitals and are known as *model potential* methods. In this work, both kinds of ECPs are present: pseudopotentials in the structural DFT calculations and model potentials, in the *ab initio* model potential approach (AIMP) of our spectroscopic calculations. We describe here the common roots of both methods before focusing on pseudopotential issues, to which this section is devoted.

The many-electron nonrelativistic Hamiltonian of a given molecule with $N_c + N_v$ electrons (subindex c and v read for *core* and *valence* respectively) can be expressed as:

$$\hat{H}(1, \dots N_c, N_c+1, \dots N_c+N_v) \equiv$$

$$\sum_{i=1}^{N_c+N_v} \left\{ -\frac{1}{2}\hat{\nabla}_i^2 - \sum_{\mu} \frac{Z_\mu}{|\vec{r}_i - \vec{R}_\mu|} \right\} + \sum_{i>j}^{N_c+N_v} \frac{1}{r_{ij}} + \sum_{\mu>\nu} \frac{Z_\mu Z_\nu}{|\vec{R}_\mu - \vec{R}_\nu|} \tag{3.59}$$

Assuming, for simplicity, a closed-shell HF calculation, the orbitals are solution of the following one-electron pseudoeigenvalue equation:

$$\hat{F} \mid \psi_a\rangle = \epsilon_a \mid \psi_a\rangle$$

$$\left\{ -\frac{1}{2}\hat{\nabla}_i^2 - \sum_\mu \frac{Z_\mu}{|\vec{r}_i - \vec{R}_\mu|} + \sum_c (2\hat{J}_c - \hat{K}_c) + \sum_v (2\hat{J}_v - \hat{K}_v) \right\} \mid \psi_a\rangle = \epsilon_a \mid \psi_a\rangle \quad (3.60)$$

where the monoelectronic Fock operator is in braces and includes the local Coulomb operator $\hat{J}$ and the non local change operator $\hat{K}$. The solutions $\mid \psi_a\rangle$ are both occupied and virtual orbitals. Only the occupied orbitals contribute to the Fock operator. Thus, they can be divided into core orbitals $\mid \psi_c\rangle$ and valence orbitals $\mid \psi_v\rangle$. If we choose $\mid \psi_c\rangle$ such as they are atomic core orbitals with zero overlap, the molecular core Coulomb and exchange operators arise as a sum of atomic core operators. Then, we can substitute the terms that depend on the core in Eq. 3.60 by $-\frac{Z_\mu^{eff}}{|\vec{r}_i - \vec{R}_\mu|} + V_\mu^{ECP}$, (where $\hat{V}_\mu^{ECP}$ is an effective core potential for the μ atom and $Z_\mu^{eff} = Z_\mu - N_\mu^{core}$, being N_μ^{core} the number of core electrons of atom μ) and we arrive to

$$\left\{ -\frac{1}{2}\hat{\nabla}_i^2 - \sum_\mu \frac{Z_\mu^{eff}}{|\vec{r} - \vec{R}_\mu|} + \sum_\mu \hat{V}_\mu^{ECP} + \sum_v (2\hat{J}'_v - \hat{K}'_v) \right\} \mid \psi'_v\rangle = \epsilon'_v \mid \psi'_v\rangle \quad (3.61)$$

This equation is common for both pseudopotential and model potential methods and it importance lies in the fact that the only solutions that are occupied orbitals are the valence molecular orbitals. Thus, the basis set does not have to represent the core orbitals and can be smaller than the basis set used in regular all-electron calculations (Eq. 3.60). In Eq. 3.61, the $\hat{V}_\mu^{ECP}$ are fixed and are not made self-consistent. As a consequence of this, both energies and valence orbitals are approximate (we use prime symbols to express that). The valence Coulomb and exchange operators are built in terms of such approximated valence orbitals.

What makes a difference between pseudopotential and model potential methods is the atomic effective core potential operator $\hat{V}_\mu^{ECP}$ of Eq. 3.61, that have implications in the corresponding valence basis sets. From now on, we focus on pseudopotentials. Particularities of model potentials can be found in Section 4.1.

Unlike within a planewaves framework, the use of pseudopotentials is not strictly necessary with atomic basis sets, but their use in SIESTA allows to get rid of the core electrons and for the expansion of a smooth pseudocharge density on a uniform spatial grid. SIESTA program uses norm-conserving pseudopotentials in semilocal form (a different radial potential for each angular momentum, optionally generated relativistically) from a data file generated by the user in her own. It is used the Troullier-Martins parametrization and the transformation from semilocal to fully-non local form is performed by means of the Kleinman-Bylander procedure. Just to remark here that, strictly speaking, SIESTA *reads* the semi-local pseudopotentials but does not generate them automatically. They need to be generated carefully by the user itself. In the present work, all the semi-local pseudopotentials were obtained with the program ATOM [126].

3.5.1.1 Pseudopotential theory

The origin of the modern pseudopotential approach can be found in the paper of Phillips and Kleinman (1959) [127], who defined a smooth valence pseudowavefunction $\tilde{\psi}_v$, called

pseudoorbital, as a linear combination of the core ψ_c and the true valence wavefunctions ψ_v in the following way:

$$\mid \tilde{\psi_v}\rangle = \alpha_v \mid \psi_v\rangle + \sum_c \alpha_c \psi_c; \qquad \alpha_c = \langle \psi_c \mid \tilde{\psi_v}\rangle \neq 0 \tag{3.62}$$

$\tilde{\psi_v}$ is not orthogonalized to the core states ψ_c.

If we apply the one-electron Fock operator $\hat{F}$ to the pseudoorbital $\tilde{\psi_v}$, i.e. $\widehat{F} \mid \tilde{\psi_v}\rangle = \varepsilon_v \mid \tilde{\psi_v}\rangle$, use the expression 3.62 and rearrange, we arrive to

$$\widehat{F}_{PS} \mid \tilde{\psi_v}\rangle \equiv \left[\widehat{F} + \sum_c (\varepsilon_v - \varepsilon_c) \mid \psi_c\rangle\langle\psi_c \mid \right] \mid \tilde{\psi_v}\rangle = \varepsilon_v \mid \tilde{\psi_v}\rangle \tag{3.63}$$

which is the Phillips-Kleinman equation. By construction, ψ_c and ψ_v are degenerated solutions of this equation. $\widehat{F}$ is the Fock operator of Eq. 3.60. If we express in detail $\widehat{F}_{PS}$ of the above equation, we have the following molecular expression

$$\left[-\frac{1}{2}\hat{\nabla}_i^2 - \sum_\mu \frac{Z_\mu^{eff}}{|\vec{r} - \vec{R}_\mu|} + \sum_\mu \left[\frac{N_\mu^{core}}{|\vec{r} - \vec{R}_\mu|} + \sum_c (2\hat{J}_c - \hat{K}_c) + \sum_c (\varepsilon_v - \varepsilon_c) \mid \psi_c\rangle\langle\psi_c \mid \right] + \sum_v (2\hat{J}_v - \hat{K}_v)\right] \tag{3.64}$$

For one atom μ, we obtain

$$\left[-\frac{1}{2}\hat{\nabla}_i^2 - \frac{Z_\mu^{eff}}{r} + \left[\frac{N_\mu^{core}}{r} + \sum_c (2\hat{J}_c - \hat{K}_c) + \sum_c (\varepsilon_v - \varepsilon_c) \mid \psi_c\rangle\langle\psi_c \mid \right] + \sum_v (2\hat{J}_v - \hat{K}_v)\right] \tag{3.65}$$

where c and v subindex read for core and valence atomic orbitals. The term in small square brackets is the atomic *pseudopotential* $\widehat{V}_\mu^{PP}$ and then we can write

$$\left[-\frac{1}{2}\hat{\nabla}_i^2 - \frac{Z_\mu^{eff}}{r} + \widehat{V}_\mu^{PP} + \sum_v (2\tilde{J}_v - \tilde{K}_v)\right] \mid \tilde{\psi_v}\rangle = \varepsilon_v \mid \tilde{\psi_v}\rangle \tag{3.66}$$

At this point, there is a enormous freedom in how pseudopotentials can be constructed. Many pseudopotentials currently used in electronic structure calculations follow the original idea of Philips and Kleimnan and are generated by inversion of Eq. 3.66. However, there are a widely used family of pseudopotentials that does not emerge from the "inversion of the equation" method. Those are the so-called *energy adjusted* pseudopotentials. Different from Phillips and Kleinman's idea of adopting a pseudoorbital and producing a pseudopotential which gives the same orbital energy ε_v, the parameters of the pseudopotentials are fitted to total energy differences [128, 129].

The "inversion of the equation" method is outlined in the following, since SIESTA program uses pseudopotentials produced in that way. A major consequence of the pseudopotential generation procedure that inverts the equation 3.66, is that obtained pseudopotentials act differently on wavefunctions of different angular momentum. The most general form of a pseudopotential $\widehat{V}_\mu^{PP}$ for a given atom μ is then:

$$\widehat{V}_\mu^{PP} = \widehat{V}_\mu^{PP} = \sum_{l=0}^{\infty} \sum_{m=-l}^{l} V_l^{PP}(r) \mid lm\rangle\langle lm \mid = \sum_{l=0}^{\infty} V_l^{PP}(r) \widehat{P}_l \tag{3.67}$$

where $V_l^{PP}(r)$ is the pseudopotential corresponding to the angular component l and the operator $\widehat{P}_l = \sum_{m=-l}^{l} \mid lm\rangle\langle lm \mid$ is a projection operator onto the l-th angular momentum subspace. The meaning of the last expression is the following: when $\widehat{V}^{PP}(r)$ acts on the electronic wavefunction, the projection operator $\widehat{P}_l$ selects the different angular components of the wavefunction, which are then multiplied by the corresponding pseudopotential $V_l^{PP}(r)$. Next, the contributions of all the angular momenta are added up to form the total pseudopotential contribution to the Hamiltonian matrix elements that enter equation 3.66. As said before, those are *non-local* pseudopotentials, because they act differently on the various angular components of the wavefunction. In practice, $V_l^{PP}(r)$ is a local operator in the radial coordinate. Therefore, a better name for these kind of expression is *semi-local* or *angular-dependent* pseudopotentials.

It is observed that all the $V_l^{PP}(r)$ are almost identical for a l larger than a l_{max}. Therefore, for values of $l > l_{max}$, $V_l^{PP}(r) \simeq V_{l_{max}}^{PP}(r)$ and the sum can adopt the following form:

$$\widehat{V}^{PP} = V_{l_{max}}^{PP}(r) + \sum_{l=0}^{l_{max}-1} \left[V_l^{PP}(r) - V_{l_{max}}^{PP}(r)\right] \widehat{P}_l = V_{l_{max}}^{PP}(r) + \sum_{l=0}^{l_{max}-1} \Delta V_l^{PP}(r)\widehat{P}_l \quad (3.68)$$

where the first term is purely local and the second one is semilocal, with a nonlocal angular part $\widehat{P}_l$ and a local radial part. The choice of the local component is rather arbitrary and it basically should be able to represent reasonably all the angular components that are not corrected by a non-local component.

Once the pseudopotential is generated, there are to ways of check its results in the required environment: against experimental results and against all-electron calculations. The second one may be the best for testing the bare quality of the pseudopotential, since the effect of pseudization is not masked by the approximation of exchange and correlation. It may happen that functional error and pseudopotential error compensate each other and a very good agreement with experiments is obtained, at least for some properties, while other properties may not be well reproduced.

3.5.1.2 Construction of pseudopotentials

Many of the pseudopotentials currently used are generated from all-electron atomic calculations. In the 70s, empirical pseudopotentials were performed by fitting experimental energy bands, but they lacked a crucial property: *transferability*, that is, the possibility of using a pseudopotential constructed for some specific environment in the same atomic specie but in a different environment. The first non-empirical (*ab initio*) approach was developed by Philips and Kleinman and a lot of possibilities have come afterwards.

The construction of a pseudopotential follows an inverse procedure:

1. The following all-electron radial equation is solved for a given atomic configuration(reference configuration), given that the all electron wavefunction $\mid \psi^{AE}\rangle$ can be factorized in $\mid \psi^{AE}\rangle = \phi_l^{AE}(r)Y_{lm}(\hat{r})$.

$$\Big\{ -\frac{1}{2}\frac{d^2}{dr^2} + \frac{l(l+1)}{2r^2} - \frac{Z}{r} + \int \frac{\rho(\vec{r}_2)}{r_{12}}\vec{dr}_2 + E_{XC}[\rho]\Big\} r\phi_l^{AE}(r) = \varepsilon_l r\phi_l^{AE}(r) \quad (3.69)$$

2. Once the all electron wavefunctions and eigenvalues are found, we construct a pseudowavefunction $|\tilde{\psi}_v\rangle$ that can also be factorized in a radial part, $\phi_l^{PP}(r)$, and spherical harmonics and fulfills the following conditions:

   (a) The radial part of the valence pseudowavefunctions generated from the pseudopotential should contain no nodes. This is due to wiggles associates with nodes are undesirable for a smooth wavefunction.

   (b) The valence all-electron and pseudopotential eigenvalues must be equal: $\varepsilon_l^{PP} = \varepsilon_l^{AE}$

   (c) The normalized atomic radial pseudowavefunction with angular momentum l is equal to the normalized radial all electron wavefunction beyond a chosen *cutoff radius* r_c: $\phi_l^{PP}(r) = \phi_l^{AE}(r)$ for $r > r_c$

   (d) The charge enclosed within r_c for both wavefunctions must be equal: $\int_0^{r_c} r^2[\phi_l^{PP}(\varepsilon, r_c)]^2 r^2 dr = \int_0^{r_c} r^2[\phi_l^{AE}(\varepsilon, r_c)]^2 r^2 dr$ (*norm-conservation*).

   (e) The logarithmic derivatives of the all-electron and pseudowavefunctions agree at r_c.

   (f) The first energy derivative of the logarithmic derivatives of the all-electron and pseudowavefunctions agree at r_c, and therefore for any $r > r_c$.

3. Once found a pseudowavefunction under some desirable conditions, the pseudopotential is obtained by inverting equation 3.66 for that pseudowavefunction.

The conservation of charge (point d) insures both that the total charge in the core region is correct and that the pseudoorbital is equal to the true orbital outside r_c, an important region where bonding occurs. The equality on the logaritmic derivatives of the $\phi_l^{PP}(r) = \phi_l^{PP}(r)$ wavefunctions (points e and f) is imposed to improve the tranferabilty of the constructed pseudopotential, since a small change in the eigenvalue due to changes in the external potential (the environment) produces only a second order change in the logarithmic derivative. Therefore, the equality of the logarithmic derivatives of AE and PS wavefunctions is not only valid for the eigenvalue ε_l used in its construction but also approximately in a range of eigenvalues around ε_l. In this case, the pseudopotential can be exported to other environments, thus becomes transferable . Just to remark that the norm-conservation guarantees that the pseudopotential is useful within a range of ε but not for every range of ε. It means, if the energy ranges are completely different due to quite different external conditions such those for the pseudopotential was constructed (i.e, a molecule under high pressure ...), transferability is not possible at all.

An important factor in pseudopotential generation is how to choose the electronic configuration of the isolated atom (the *reference* configuration) so that the pseudopotential remains useful in molecular systems or condensed phases. Even if the choice of the reference configuration were arbitrary, it should be irrelevant in principle, provided that the pseudopotential has good transferability properties. In practice this is often the case, but it must be carefully checked by comparing the pseudowavefunction and eigenvalues

for electronic configurations different from the one used to fit the pseudopotential. These *test* configurations should be similar to those present in the system of study. The obvious first choice for the reference configuration is the ground state configuration of the isolated atom. However, states of angular momenta that are unoccupied in the neutral atom hybridize with the occupied states when atoms are not isolated anymore become partially occupied. Therefore is necessary to include these angular momenta as non-local components of the pseudopotential.

Troullier Martins pseudopotentials A widely used method, included in SIESTA code, of generating norm-conserving pseudopotentials is the Troullier and Martins parametrization [126]. It consists of considering the following analytical form of the wavefunction inside the r_c:

$$\phi_l^{TM}(r) = r^l \exp(p(r)) \qquad \text{with} \tag{3.70}$$

$$p(r) = c_0 + c_2 r^2 + c_4 r^4 + c_6 r^6 + c_8 r^8 + c_{10} r^{10} + c_{12} r^{12} \tag{3.71}$$

The absence of odd terms is related with a higher level of smoothness achieved with only even terms. The coefficients c_{2n} are determined by norm conservation of the charge within the r_c, continuity of the pseudowavefunction and its four first derivatives at r_c zero curvature of the screened pseudopotential at the origin.

3.5.1.3 Unscreening in DFT

Once a different pseudowavefunction for each l is obtained with the desired properties, the radial equation is inverted to find the potential $V_l^{PP}(r)$ of which $\phi_l^{PP}(r)$ is a solution with energy ε_l. In DFT, pseudopotential that enters in the inversion of the equation procedure involves all the terms that are not related to kinetic energy in Eq. 3.60 and then includes coulombic and exchange valence interactions plus correlation interactions (the latter not present in HF). So, this is called a screened pseudopotential. Since the energy ε_l is fixed (usually as the value of the all-electron calculation), the final expression for the screened pseudopotential for each l, $V_{(scr)l}^{PP}(r)$, is:

$$V_{(scr)l}^{PP}(r) = \varepsilon_l - \frac{1}{2}\Big[\frac{l(l+1)}{2r^2} - \frac{\frac{d^2}{dr^2}\phi_l^{PP}(r)}{\phi_l^{PP}(r)}\Big] \tag{3.72}$$

From this equation we can see that this inversion can only be done if the nodeless condition is imposed and the pseudowavefunction has continuous first and second derivatives.

Finally, it is necessary to unscreen the above screened pseudopotential, in which the screening from the valence electrons depends strongly on the environment where they are placed, in order to obtain the bare ion pseudopotential, transferable to different environments. This ionic pseudopotential is obtained by subtracting the Hartree and the exchange-correlation potential from the screened potential:

$$V_l^{PP}(r) = V_{(scr)l}^{PP}(r) - V_H(\rho_v, r) - V_{XC}(\rho_v, r) \tag{3.73}$$

Both the exchange-correlation and the Hartree term are calculated *only* for the valence electrons. It is important here to remark that the exchange-correlation functional used in the construction of the pseudopotential ($V_{XC} \equiv V_{XC}^{LDA,GGA...}$) must be the same as the one used in the target calculation.

3.5.1.4 Non linear core corrections

If there is a significant overlap between the core and the valence charge densities, the unscreening process in the construction of the pseudopotential leads to an error because, while the Hartree energy is a linear function of the density, the exchange-correlation potential and energy are not. This is particularly important in systems with very few valence electrons (e.g alkali metals) and in transition metals as well, since d valence band overlaps spatially with the core s and p states. Then, the exchange-correlation energy cannot be written as $E_{XC}[\rho_{core}] + E_{XC}[\rho_{valence}]$. A solution, avoiding including semi-core states explicitly into the valence, was proposed by Louie in 1982 [130] and is called *non linear core corrections* (NLCC). It has the following steps:

- The unescreening expression is replaced by

$$V_l^{PP}(r) = V_{(scr)l}^{PP}(r) - V_H(\rho_v, r) - \tilde{V}_{XC}(\rho_v, \rho_c, r) \qquad \text{with} \tag{3.74}$$

$$\tilde{V}_{XC}(\rho_v, \rho_c, r) = V_{XC}(\rho_v, r) + [V_{XC}([\rho_v + \rho_c], r) - V_{XC}(\rho_v, r)] \tag{3.75}$$

  The exchange-correlation contribution is computed for the full electronic charge beyond a radius r_{cc}, usually chosen within the overlap zone between core and valence densities, where ρ_c is usually from 1 to 2 times ρ_v. The term in square brackets is a core correction that increases significantly the transferability of the pseudopotential.

- Since ρ_c is not a smooth function, it is replaced by

$$\rho_c = \frac{A \sin Br}{r} \qquad \text{for} \qquad r < r_{cc} \tag{3.76}$$

  for LDA calculations or

$$\rho_c = r^2 exp(a + br^2 + cr^4) \qquad \text{for} \qquad r < r_{cc} \tag{3.77}$$

  for GGA calculations, where the parameters A, B, a, b and c are determined by the continuity condition for ρ_c and its first derivative at r_{cc}.

3.5.1.5 Relativistic corrections

When heavy atoms are present, the core electrons in the deepest shells have such high energy that they have to be treated relativistically. Therefore, the kinetic operator in Schrödinger equation must be replaced by Dirac expression, which is invariant under Lorentz transformation [131, 132]. The solutions have well-defined total angular momentum ($\widehat{J}$) (made of orbital ($\widehat{L}$) and spin ($\widehat{S}$)components) and parity ($\widehat{P}$). Since the electron

spin is always 1/2, the composition of these two angular momenta can only give rise to two values of the quantum number j for each l: $j = l \pm 1/2$.

For a given value of j and parity, radial Dirac equation for one electron in a central field can be written as a pair of coupled differential equations on the auxiliary functions G and F, named *major* and *minor* wavefunction components:

$$F_k(r) = -\frac{1}{\alpha(\varepsilon - V)}\Big(\frac{d}{dr} + \frac{k}{r}\Big)G_k(r) \tag{3.78}$$

$$G_k(r) = -\frac{\alpha}{2m_0 + \alpha^2(\varepsilon - V)}\Big(\frac{d}{dr} - \frac{k}{r}\Big)F_k(r) \tag{3.79}$$

with

$$k_j = \begin{cases} l & \text{for } j = l - 1/2 \\ -(l+1) & \text{for } j = l + 1/2 \end{cases} \tag{3.80}$$

and

$$G(r) = rg(r) \qquad F(r) = rf(r) \tag{3.81}$$

with $g(r)$ and $f(r)$ being the radial contributions of the two *large* and *small* components of Dirac four spinors respectively. The norm of the wavefunction is given by $\int(\mid F \mid^2 + \mid G \mid^2)dr$. The index n refers to the principal quantum number and $\alpha = 1/137.04$ is the fine structure constant. The electronic density is calculated by means of the sum of the squares of the four components of Dirac wavefunction; the two first ones give the most of the electron density and this is the reason to call them *large*, whereas the other two give a small contribution to the density and are called *small*.

The *minor* and *major* wavefunction components are strongly mixed only in the core region but the Dirac equation for the valence electrons can be replaced by a Schrödinger-like equation in the *major* component

$$\left(-\frac{1}{2}\frac{d^2}{dr^2} + \frac{k_j(k_j+1)}{2r^2} + V_{rel}^{PP}(r) \right) F_{n,j}(r) = \varepsilon_{n,j} F_{n,j}(r) \tag{3.82}$$

This expression is used as a starting point to generate relativistic pseudopotential and pseudowavefunctions. The radial Schrödinger equation is solved for the chosen atomic configuration with $G_{n,j}$ instead of ϕ_l^{AE}.

Bachelet and Schlüter [133] present a $V_{rel}^{PP}(r)$ with scalar relativistic effects expressed as an average pseudopotential of the $l+1/2$ and the $l-1/2$ configurations, whereas Cowan and Griffin [134] (see Section 4.1.3) add the mass-velocity and the Darwin terms from the Pauli equation for one-electron atoms to the usual non-relativistic $V^{PP}(r)$. In the Bachelet approach, the spin-orbit term is proportional to the difference on the pseudopotentials with $l + 1/2$ and $l - 1/2$. Wood and Boring [135] add spin-orbit effects to the Cowan-Griffin relativistic Hamiltonian by means of an extra term added to the mass-velocity and Darwin ones (also see Section 4.1.3).

3.5.1.6 Kleinman-Bylander separation

The semilocal form of pseudopotentials suffers from the disadvantage that it is computationally very expensive to use since the number of matrix elements which need to be calculated scales as the square of the number of basis functions. The most common solution for this problem, is to use the *Kleinman-Bylander* separable form [124], where the semi-local term of the pseudopotential (the term $\sum_{l=0}^{l_{max}-1}\left[V_l^{PP}(r)-V_{l_{max}}^{PP}(r)\right]\widehat{P}_l$ in Eq. 3.68 is replaced by:

$$\widehat{V}^{KB}=\sum_{l=0}^{l_{max}^{KB}}\sum_{m=-l}^{l}\sum_{n=1}^{N_l^{KB}}\mid\chi_{nml}^{KB}\rangle\nu_{ln}^{KB}\langle\chi_{nml}^{KB}\mid \tag{3.83}$$

where $\chi_{nml}^{KB}=\chi_{ln}^{KB}(r)Y^{lm}$ are the *Kleinman-Bylander projectors*, with $\chi_{ln}^{KB}(r)=[V_l(r)-V_l^{local}]\varphi_{ln}(r)$ and $\nu_{ln}^{KB}=\langle\varphi_{ln}\mid[V_l(r)-V_l^{local}]\mid\varphi_{ln}\rangle$. The φ_{ln} functions are obtained using the orthogonalization Blochl's scheme [136]:

$$\varphi_{ln}=\phi_{ln}(r)-\sum_{n'=1}^{n-1}\varphi_{ln'}(r)\frac{\langle\varphi_{ln'}(r)\mid[V_l(r)-V_l^{local}]\mid\phi^{ln}(r)\rangle}{\langle\varphi_{ln'}(r)\mid[V_l(r)-V_l^{local}]\mid\varphi_{ln'}(r)\rangle} \tag{3.84}$$

from the functions $\phi_{ln}(r)$, eigenfunctions of the screened semilocal pseudopotential $V_l(r)$ at energy ε^{nl}

$$\Big[-\frac{1}{2r}\frac{d^2}{dr^2}r+\frac{l(l+1)}{2r^2}+V_l(r)+V_H(r)+V_{XC}\Big]\phi_{ln}(r)=\varepsilon_{nl}\phi_{ln}(r) \tag{3.85}$$

where V_{XC} and V_H are the exchange-correlation and Hartree potentials for the pseudo-valence charge density.

The total operator $\widehat{V}^{PP}=\widehat{V}^{local}+\widehat{V}^{KB}$ acts on the reference state in an identical manner to the original semilocal operator but the number of matrix elements to be calculated scales only linearly with the number of basis functions.

Ghost states The so-called *ghost states* are an undesirable feature that sometimes appears when introducing the separable non-local form of the pseudopotential as unphysical states below in energy than the true ground state eigenvalue of a specific l. These are expected when V_l^{local} is too much attractive and the non-local term $[V_l(r)-V_l^{local}]$ is repulsive. All the pseudopotentials used in the present work are free from these states, since they were eliminated varying the cutoff radii of the problematic angular momentum.

3.5.2 Basis sets in SIESTA

The radial functions have different cutoff radii and, up to that radius, their shape is completely free and can be determined by the user in the input file. In practice, it is convenient to have an automatic procedure to generate good basis sets. SIESTA provides a default automatic procedure of generating basis sets, but, as it happens with pseudopotentials, some customized methods may be necessaries for some problems. Here, the optimization method of E. Anglada *et al.* [137] will be described, since it has been used in the calculations present in this work.

3.5.2.1 SIESTA default generation of numerical basis sets

A useful numerical basis set is generated when the basis functions are chosen as solutions of the atomic problem, but with the additional constraint that they become strictly zero beyond some localization radius [83]. This is the *fireball* basis set. The advantage is that overlap, kinetic, and nuclear attraction matrix elements are strictly zero for centers beyond a certain distance. This is the kind of approach adopted by the SIESTA self-consistent DFT code.

In addition, as SIESTA is a pseudopotential code, the basis functions are chosen to be solutions of the pseudoatomic problem, that is, where the Coulomb potential is replaced by a pseudopotential. Thus, SIESTA uses Pseudo Atomic Orbitals (PAOs), that represent very accurately the orbitals close to the origin, although their quality decays with the distance from the atomic sites.

For a minimal (single-ζ, SZ) basis set, the scheme of Sankey and Niklewsky [83] is used. The basis functions are eigenfunctions of a pseudo-atom confined within a spherical box:

$$\Big(-\frac{1}{2r}\frac{d^2}{dr^2}r + \frac{l(l+1)}{2r^2} + V_l(\vec{r})\Big)\phi_l(\vec{r}) = (\epsilon_l + \delta\epsilon_l)\phi_l(\vec{r}) \tag{3.86}$$

The first node ($\phi_l(\vec{r}) = 0$) is chosen for $r = r_c$ and a common $\delta\epsilon$ (called *energy shift*) is chosen for all the atoms and angular momenta, in order to provide a similar confinement effect in all the orbitals.

Double-ζ basis sets are built such that the double-ζ basis orbitals have the same tail as the single-ζ ones after a *split radius* r_s^l and their behavior is polynomial inside such r_s^l

$$\phi^l_{2\zeta}(\vec{r}) = \begin{cases} r^l(a_l - b_l r^2) & \text{for } r < r_s^l \\ \phi^l_{1\zeta} & \text{for } r \geq r_s^l \end{cases} \tag{3.87}$$

Once the double-ζ is thus defined, SIESTA uses $\phi^l_{1\zeta} - \phi^l_{2\zeta}$, since it is has zero value beyond the matching radius r_s^l, in order to reduce the number of non-zero matrix elements.

Polarization orbitals are also included in the SIESTA code, to account for the deformation induced by bond formation. They are introduced perturbing orbitals of a quantum number l with an small electric field in the z-direction. Due to selection rules, the resulting perturbed orbital has only $l+1$ components and, once normalized, they are added to the basis set.

DZP basis sets are the “default" basis in SIESTA, because they represent the best balance between converged results and computational cost.

3.5.2.2 Numerical atomic orbitals optimized variationally

In the context orbitals as described by Eq. 3.86, the confining potential, which may be different for each atomic orbital, depends on a series of parameters which determine the shape of the orbital. A *variational* basis optimization is done if these parameters are adjusted to minimize the energy of a prototype molecule or solid. Unfortunately, if the

cutoff radii are taken as variational parameters, the orbitals thus obtained have very long tails without significance within the solid state framework.

A procedure to compress such orbitals was developed by Anglada *et al.* [137] by means of a *fictitious pressure* that reduces the orbital range in a systematic way. A *fictitious enthalpy* $E+PV$ is minimized , where P is the above mentioned parameter with dimensions of pressure, E is the total energy of the system and $V = (4\pi/3)\sum_\mu r_{c\mu}^3$ is the volume of the basis orbitals ϕ_μ.

The above "enthalpy" is minimized with respect to those parameters related to the confining potential $V(\vec{r})$: r_i, V_0 and the cutoff radius r_c of each single-ζ basis orbital in

$$V(\vec{r}) = V_0(\vec{r})exp[-(r_c - r_i)/(r - r_i)]/(r_c - r) \tag{3.88}$$

This confining potential is added to the full screened non-local pseudopotential corresponding to the angular momentum of the orbital and the radial Schrödinger equation is solved.

The reference system for which $E + PV$ is minimize must be a molecule or solid containing the atoms present in the target system and with interactions as closer as possible as they have within it.

Since the derivatives of E with respect those parameters are not available, the *downhill-simplex* method is used and therefore there is no a unique minimum. Anyway, those parameters have no special physical meaning, and thus any local minimum is in principle acceptable.

The parameter P is taken as ~ 0.2 GPa, since this value reduces notably the computational effort but preserves the results with zero pressure compared to the PW ones.

In the present work, this basis set generation procedure has been used to generate basis sets for all the atoms present in YAG due to SIESTA lacks of a systematic procedure to generate orbital basis sets for semi-core states, such as those we have in yttrium atoms.

3.5.3 Electronic Hamiltonian

Once the non-local pseudopotential approximation is applied, the Kohn-Sham one electron Hamiltonian reads:

$$\widehat{H} = \widehat{T} + \sum_I \widehat{V}_I^{KB} + \sum_I V_I^{local}(\vec{r}) + V^H(\vec{r}) + V^{XC}(\vec{r}) \tag{3.89}$$

Since the local term of the pseudopotential has long range, it is screened in SIESTA with the potential V_I^{atom}, created by an atomic electron density ρ_I^{atom}, obtained when filling the atomic basis orbitals with appropriate valence atomic charges. The resulting *neutral atom* (NA) potential $V_I^{NA} \equiv V_I^{local} + V_I^{atom}$ is then zero beyond the the maximum cutoff radius of the I atom, since the atomic basis orbitals are zero as well beyond their cutoff radii. If $\delta\rho$ is defined as $\delta\rho = \rho(\vec{r}) - \rho^{atom} = \rho(\vec{r}) - \sum_I \rho_I^{atom}$ (where $\rho(\vec{r})$ is the self-consistent density) and δV^H is the potential generated by $\delta\rho$, the above Hamiltonian is rewritten as:

$$\widehat{H} = \widehat{T} + \sum_I V_I^{KB} + \sum_I \widehat{V}_I^{NA} + \delta V^H(\vec{r}) + V^{XC}(\vec{r}) \tag{3.90}$$

The matrix elements of the two first terms involve two-center integrals, while the remaining terms involve potentials. The former are calculated in reciprocal space and tabulated as a function of interatomic distance and the latter are calculated on a 3-D real space grid.

3.5.3.1 Two-center integrals

The overlap $\mathbb{S}$ matrix, the kinetic energy and non-local part of the pseudopotential are given by two-centre integrals and SIESTA calculates them in Fourier space.

Using the Fourier transform

$$\psi(\vec{k}) = \frac{1}{(2\pi)^{3/2}} \int \psi(\vec{r}) e^{-i\vec{k}\vec{r}} \tag{3.91}$$

the overlap integrals

$$\mathbb{S}(\vec{R}) \equiv \langle \psi_1 \mid \psi_2 \rangle = \int \psi_1^*(\vec{r}) \psi_2(\vec{r} - \vec{R}) d\vec{r} \tag{3.92}$$

can be expressed as

$$\mathbb{S}(\vec{k}) = \int \psi_1^*(\vec{k}) \psi_2(\vec{k}) e^{-i\vec{k}\vec{R}} d\vec{k} \tag{3.93}$$

That means that the Fourier transform of a convolution in the real space is a simple product in reciprocal space. In the above expressions, ψ can be an orbital basis function ϕ_{lmn} or a Kleinman-Bylander projector χ_{lmn}.

In SIESTA, these ψ functions are expanded in spherical harmonics

$$\psi(\vec{r}) = \sum_{l=0}^{l_{max}} \sum_{m=-l}^{+l} \psi_{lm}(r) Y_{lm}(\hat{r}); \qquad \psi_{lm}(r) = \int_0^{\pi} \sin\theta d\theta \int_0^{2\pi} d\psi Y_{lm}^*(\theta, \psi) \psi(r, \theta, \psi) \tag{3.94}$$

with $r = \mid \vec{r} \mid$ and $\hat{r} = \vec{r}/r$. Then, Eq. 5.13 is used to obtain an expression for $\psi(\vec{k})$, which is substituted in Eq. 5.15 to obtain

$$\mathbb{S}(\vec{R}) = \sum_{l=0}^{2l_{max}} \sum_{m=-l}^{+l} S_{lm}(R) Y_{lm}(\hat{R}) \tag{3.95}$$

where

$$S_{lm}(R) = \sum_{l_1,m_1} \sum_{l_2,m_2} G_{l_1,m_1,l_2,m_2,lm} S_{l_1,m_1,l_2,m_2,l}(R), \tag{3.96}$$

$R = \mid \vec{R} \mid$ and $\hat{R} = \vec{R}/R$

The Gaunt coefficients $G_{l_1,m_1,l_2,m_2,lm}$ only depend on spherical harmonics. Then, they are universal and can be calculated once and for all. The functions $S_{l_1,m_1,l_2,m_2,l}(R)$ depend on the ψ functions being integrated and on k^2. For each pair of ψ functions, they are calculated and stored in a radial grid R_i, up to the maximum distance $R_{max} = r_1^c + r_2^c$ at which ψ_1 and ψ_2 overlap. Their value at an arbitrary distance R is obtained by means of a spline interpolation.

Kinetic matrix elements $\mathbb{T}(\vec{R})$ are obtained in the same way and only an extra factor of k^2 must be added to the existing k^2 factor in the expression for $S_{l_1,m_1,l_2,m_2,l}(R)$ to obtain $T_{l_1,m_1,l_2,m_2,l}(R)$.

3.5.3.2 Grid integrals

The matrix elements for $\sum_I \widehat{V}_I^{NA}$, $\delta V^H(\vec{r})$ and $V^{XC}(\vec{r})$ are calculated on a real space grid which fineness is controlled by a *grid cutoff* E_{cut} that represents the maximum kinetic energy of the planewaves that can be represented in the grid without aliasing. The higher the E_{cut} is, the finer the grid is.

Once the fineness of the grid is determined, then, the three above terms can be represented. In one hand, the short-range pseudopotentials $V_I^{NA}(\vec{r})$ are tabulated as a function of the distance to atoms I and interpolated in any desired point. On the other hand, both $\delta V^H(\vec{r})$ and $V^{XC}(\vec{r})$ terms require the calculation of the electronic density on the grid:

If $\psi_i(\vec{r}) = \sum_{mu} \phi_{mu}(\vec{r}) c_{\mu i}$ are the Hamiltonian eigenstates expanded in the atomic basis set, then, the electronic density is calculated by means of :

$$\rho(\vec{r}) = \sum_{\mu\nu} \rho_{\mu\nu} \phi_\nu^*(\vec{r}) \phi_\mu(\vec{r}); \qquad \rho_{\mu\nu} = \sum_i c_{\mu i} n_i c_{i\nu}^* \tag{3.97}$$

Here n_i is the occupation of state ψ_i and, in this case, $\phi_\nu^* = \phi_\nu$ since SIESTA uses real basis orbitals.

Then, to calculate the density in any point of the grid, all the atomic basis orbitals belonging to all the atoms in that point are found (Eq. 2.39) and their radial part are interpolated from numerical tables. Then, the density is given by Eq. 3.97 .

Since there are a small number of non-zero basis orbitals at a given grid point, the calculation of the density can be performed in a $\mathcal{O}(N)$ way, once $\rho_{\mu\nu}$ is known. The calculation of the latter itself does not scale linearly with the system size and special $\mathcal{O}(N)$ techniques are required.

Once the valence density is available on the grid, the non-local core corrections is added if necessary (Section 3.5.1.4), interpolated from a radial grid as well, but without passing through the basis orbitals.

The XC potential $V^{XC}(\vec{r})$ is obtained then introducing $\rho(\vec{r})$ in the LDA and GGA expressions described on Chapter 3. The $\delta V^H(\vec{r})$ term is then obtained by solving the Poisson equation ($\nabla^2 V^H(\vec{r}) = -4\pi\rho(\vec{r})$) for $\delta\rho(\vec{r})$. The latter is calculated by subtracting from $\rho(\vec{r})$ the $\rho^{atom}(\vec{r})$ density, obtained as a sum of spherical atomic densities in each given grid point, also interpolated.

The total grid potential is then $V(\vec{r}) = V^{NA}(\vec{r}) + \delta V^H(\vec{r}) + V^{XC}(\vec{r})$.

Finally, at every grid point, $V(\vec{r})\phi_\mu(\vec{r})\phi_\nu(\vec{r})\triangle\vec{r}^3$ is calculated, for all pairs $\phi_\mu(\vec{r})\phi_\nu(\vec{r})$ non zero at that point and added to the Hamiltonian matrix element $H_{\mu\nu}$.

3.5.4 Total Energy

The total Kohn-Sham energy can be written as a sum of a band structure (BS) energy and some "double-count" correction terms. The band structure term is a sum of eigenvalues

$$E^{BS} = \sum_i n_i \langle \psi_i \mid \widehat{H} \mid \psi_i \rangle = \sum_{\mu\nu} H_{\mu\nu} \rho_{\mu\nu} \tag{3.98}$$

where ψ_i are occupied states, the eigenfunctions of the Hamiltonian at convergence. The correction terms are functionals of the density calculated as in 3.97. Then, the total Kohn-Sham energy can be written as:

$$E^{KS} = \sum_{\mu\nu} H_{\mu\nu}\rho_{\mu\nu} - \frac{1}{2}\int V^H(\vec{r})\rho(\vec{r})d^3r + \int(\epsilon^{XC}(\vec{r}) - V^{XC}(\vec{r}))\rho(\vec{r})d^3r + \sum_{I<J}\frac{Z_I Z_J}{R_{IJ}} \tag{3.99}$$

where Z_I and Z_J are the valence ion pseudoatomic charges and ϵ^{XC} is the exchange-correlation energy density. In the last term long-range interactions are avoided if it is written as:

$$\sum_{I<J}\frac{Z_I Z_J}{R_{IJ}} = \frac{1}{2}\sum_{IJ} U_{IJ}^{local}(R_{IJ})^a + \sum_{I<J}\delta U_{IJ}^{local}(R_{IJ})^b - \sum_I U_I^{local\ c} \tag{3.100}$$

where

a.
$$U_{IJ}^{local}(R_{IJ}) = \int V_I^{local}(\vec{r})\rho_J^{local}(\vec{r}-\vec{R})d^3r \tag{3.101}$$
is the electrostatic interaction between the diffuse ion charges in atoms I and J.

b.
$$\delta U_{IJ}^{local}(R_{IJ}) = \frac{Z_I Z_J}{R} - U_{IJ}^{local}(R) \tag{3.102}$$
is a small short-range interaction term to correct for a possible overlap between the ion charges if the core densities are very extended.

c.
$$U_I^{local} = \frac{1}{2}\int V_I^{local}(\vec{r})\rho_J^{local}(\vec{r})4\pi r^2 dr \tag{3.103}$$
is the fictitious self-interaction of an ion charge.

ρ_I^{local} above is constructed from the local part of the pseudopotential:

$$\rho_I^{local}(\vec{r}) = -\frac{1}{4\pi}\nabla^2 V_I^{local}(\vec{r}) \tag{3.104}$$

Analogously, defining a ρ_I^{NA} from $V_I^{NA}(\vec{r})$, ρ_I^{NA} can be written as $\rho_I^{NA} = \rho_I^{local} + \rho_I^{atom}$ and equation 3.99 can be rewritten on the following form, that is actually the total-energy equation used by SIESTA:

$$E^{KS} = \sum_{\mu\nu}(T_{\mu\nu} + V_{\mu\nu}^{KB})\rho_{\mu\nu} + \frac{1}{2}\sum_{IJ} U_{IJ}^{NA}(R_{IJ}) + \sum_{I<J}\delta U_{IJ}^{local}(R_{IJ}) - \sum_I U_I^{local} + \delta V^{NA}(\vec{r})\delta\rho(\vec{r})d^3r + \frac{1}{2}\int \delta V^H(\vec{r})\delta\rho(\vec{r})d^3r + \int(\epsilon^{XC}(\vec{r}) - V^{XC}(\vec{r}))\rho(\vec{r})d^3r \tag{3.105}$$

In this equation:

- $V^{NA} = \sum_I V_I^{NA}$ and $\delta\rho = \rho - \sum_I \rho_I^{atom}$
- $U_{IJ}^{NA} = \int V_I^{NA}(\vec{r})\rho_J^{NA}(\vec{r} - \vec{R})d^3r$, $T_{\mu\nu} = \langle\phi_\mu \mid -\frac{1}{2}\nabla^2 \mid \phi_\nu\rangle$ and $V_{\mu\nu}^{KB} = \sum_\alpha \langle\phi_\mu \mid \chi_\alpha\rangle\nu_\alpha^{KB}\langle\chi_\alpha \mid \phi_\nu\rangle$ are obtained by two-center integrals. (KB projector χ_α is that overlaps simultaneously with ϕ_μ and ϕ_μ).
- The last three terms are calculated using the real space grid

The advantage of equation 3.105 is not only to get rid off the long-range potentials, but also to minimize the errors associated to the real space grid, since the grid integrals involve $\delta\rho(\vec{r})$, much smaller than $\rho(\vec{r})$.

Electronic Temperature An *electronic temperature* T and/or a *chemical potential* μ can be introduced in order to either reproduce the physical conditions of the target system or to accelerate the selfconsistency iteration. Then, what is minimized is the free energy F, which includes the temperature T via the Mermin fucntional [138]:

$$F(\vec{R}_I, \psi_i(\vec{r}), n_i) = E^{KS}(\vec{R}_I, \psi_i(\vec{r}), n_i) - \mu\sum_i n_i - k_B T\sum_i((n_i)\log(n_i) + (1-n_i)\log(1-n_i)) \quad (3.106)$$

The occupation of the electronic states n_i can be performed using the usual Fermi-Dirac distribution

$$n_i = \frac{1}{1 + e^{\frac{\epsilon_i - \mu}{k_B T}}} \quad (3.107)$$

or the Methfessel-Paxton [139] one, a step function approximated by a hierarchy of increasingly accurate smooth approximations based on Hermite polynomials. In both cases, once a finite temperature has been chosen, the relevant energy is not E^{KS} but F and, in particular, the atomic forces are derivatives of F, not of E^{KS}.

3.5.5 Density of states and projected density of states

In solid state and condensed matter physics, density of states $g(E)dE$ (DOS) represents the number of one-electron states around the energy E, i.e. the number of states between the energies E and $E + dE$.

$$g(E) = \frac{1}{N_{\vec{k}}}\sum_i^{bands}\sum_{\vec{k}}\delta(E - E_i(\vec{k})) \quad (3.108)$$

DOS units are [states/eV cell]. In SIESTA, DOS is calculated from the list of eigenvalues by constructing a Gaussian function around each eigenvalue within the desired window of energy. The gaussians are broadened according to a peak width σ (in eV) arbitrarily

decided by the user and are represented in an energy window divided in a given number of points, choice of the user as well.

$$\delta(E - E_i(\vec{k})) = \frac{1}{\sigma\sqrt{\pi}} e^{-\frac{(E-E_i(\vec{k}))^2}{\sigma^2}} \tag{3.109}$$

The window of energy has to be defined according to the zero of energies. In SIESTA, the zero-energy level is taken as the average of the electrostatic potential generated by the deformation charge $\delta\rho(\vec{r})$, defined in Section 3.5.3.2. All the eigenvalues and the Fermi level ε_F refers to this zero. Actually, the position of the ε_F in the gap between the valence and the conduction bands is not physically meaningful.

If all atoms are equivalent, then the total density of states would be distributed equally per atom. However, if we have different atoms in the unit cell, we will have different distributions of the density of states, but when summed up they all add up to the total density of states. One way to distribute the total density of states locally is by distributing it per each basis state, which we know is associated with one particular atom. Then, we have the projected density of states $g_\mu(E)$ (PDOS) per orbital μ:

$$g_\mu(E) = \frac{1}{N_{\vec{k}}} \sum_{i}^{bands} \sum_{\vec{k}} \sum_{\nu} c^*_{\nu i}(\vec{k}) c_{\mu i}(\vec{k}) \delta_{\mu\nu}(\vec{k}) \delta(E - E_i(\vec{k})) \tag{3.110}$$

DOS and PDOS, according to this picture have the following normalization relationship:

$$g(E) = \sum_{\mu} g_\mu(E) \tag{3.111}$$

In this work, we have extracted the PDOS using the *fmpdos* processing tool of A. Postnikov (http://www.home.uni-osnabrueck.de/apostnik/download.html).

3.5.6 Mulliken population analysis

One of the most immediate property of a molecule of solid we can think about is its charge distribution. There is no an unique scheme to determine how many electrons are "attached" to a given atom, that is, there are different *population analyses* and is quite useful in many cases perform any of them, in order to have a general picture of the chemical bond. Due to its simplicity, Mulliken population analysis [140] has become one of the most used method to "count" electrons associated to an atom from calculations of computational chemistry, particularly those based on the linear combination of atomic orbitals (LCAO). Within this framework, a molecular orbital ψ_i, containing N_i electrons, can be expressed as linear combination of atomic orbitals $\phi_\mu(k)$ centered on atom k:

$$\psi_i = \sum_{k} \sum_{\mu} C_{\mu i}(k) \phi_\mu(k) \tag{3.112}$$

Mulliken approach is based in two main ideas:

- The electronic population is splitted into *atomic populations*, $N_i(k)$ and *overlap populations*, $N_i(kl)$.
- Overlap population between two atoms k=A and l=B , $N_i(AB)$, is divided in two *equal* parts, so that $N_i(AB)/2$ is assigned to each atom.

Then, if

$$n_i(A) = N_i \sum_{\mu} \sum_{\nu} C_{\mu i}(A) C_{\nu i}(A) \langle \phi_\mu(A) \mid \phi_\nu(A) \rangle \tag{3.113}$$

$$n_i(AB) = 2N_i \sum_{\mu} \sum_{\nu} C_{\mu i}(A) C_{\alpha i}(B) \langle \phi_\mu(A) \mid \phi_\alpha(B) \rangle \tag{3.114}$$

the population of the orbital ψ_i, i.e N_i, of atom A, will be the sum of the two above quantities (atomic and a half of the overlap corresponding to all the possible pairs of atoms A-B):

$$N_i(A) = n_i(A) + \frac{1}{2} \sum_{B} n_i(AB) \tag{3.115}$$

Then, the atomic total population N(A) of the atom A arise from the sum of N_i(A) over all the occupied molecular orbitals of the system:

$$N(A) = \sum_{i} N_i(A) \tag{3.116}$$

and the charge Q(A) of the center A (with atomic number Z(A)) is given by

$$Q(A) = Z(A) - N(A) \tag{3.117}$$

and the atomic overlap is given by the sum of the overlaps over all the molecular orbitals:

$$n(AB) = \sum_{i} n_i(AB) \tag{3.118}$$

Chapter 4

Spectroscopy of *f* elements in solids: Embedded cluster multiconfigurational calculations (AIMP-CASSCF/CASPT2)

In order to interpret properly the experimental energy levels found experimentally in ionic solids containing lanthanide ions, there have been a great improvement of the theory and methods used in spectroscopic analyses along the past decades [141, 142, 143, 144, 145].

$f \rightarrow d$ transitions have been studied by means of the Judd-Morrison model [6, 7]. According to this model, the $4f \rightarrow 5d$ transitions of a lanthanide in a crystal suffer an stabilization with respect to the free ions because of the interaction of the excited state and the dipole moment induced in the ligands. Such stabilization depends on two parameters, σ_2 and S, depending on the free ion and on the crystal respectively. The S parameter depends inversely on R_i^6, being R_i the distance between the lanthanide and the ligands of the first coordination shell. In this model, it is assumed that no relaxation of the crystal occurs when the impurity is introduced. Moreover, it considers a symmetric interaction between the electrons and the ligands, without taking into account crystal field effects.

Crystal Field Theory (CFT) [146], a monoelectronic approach, incorporates spectroscopic experimental information available to parametrized operators used to predict spectra of other similar systems. CFT interprets properly the $4f^n$ spectroscopies of lanthanides but the use in $4f^{n-1}5d^1$ configurations is limited, due to the scarce experimental data available to model the higher number of parameters needed. Besides, CFT does not give any structural information about the ion and surroundings.

Ab initio embedded cluster methods overcome the limitations of these semiempirical methods by representing precisely on one hand, the crystalline environment of the lanthanide and, on the other hand, the internal properties of a cluster made of the lanthanide ion and certain neighboring atoms, by including electronic correlation and relativistic effects. Structural parameters of ground and excited states, difficult to obtain experimentally, can be obtained for the considered cluster. Specifically, the *Ab Initio* Model

Potential Method (AIMP) takes into account the lattice effects and the core effects in a unified framework. Actually, all the monoelectronic potentials obtained by means of the technique of representation of operators typical of the AIMP method described below can be associated both to ECPs and *embedding* potentials. In both cases, those potentials are formally identical and the same calculation of one-electron integrals is required. The definition will depend only on whether the frozen electronic structure corresponds to atomic cores or to embedding hosts. Thus, the AIMP method is a powerful tool to study local properties of ionic solids with the same quantum chemical methods routinely used for molecules in gas phase.

In this chapter, the AIMP method is presented in Section 4.1, regarding its performance as an embedding cluster method and as effective core potential generation procedure for atoms. Later, an overview on the methods used to perform spectroscopic calculations within the embedding cluster approach are presented in Section 4.2.

4.1 The AIMP method

The starting point of the AIMP method, as of all the model potential methods, is the Huzinaga Cantu equation.

If we apply a variational treatment to a wavefunction of $N_c + N_v$ electrons (c reads for core and v for valence) of the form:

$$\Phi = |\psi^{\alpha}_{c_1}\psi^{\beta}_{c_1} \ldots \ \psi^{\alpha}_{c_{N_c/2}}\psi^{\beta}_{c_{N_c/2}}\psi^{\alpha}_{v_1}\psi^{\beta}_{v_1} \ldots \ \psi^{\alpha}_{v_{N_v/2}}\psi^{\beta}_{v_{N_v/2}}| \tag{4.1}$$

under the orthogonality conditions

$$\langle\psi_{ci}\psi_{cj}\rangle = \delta_{ij} \qquad \langle\psi_{ci}\psi_{vj}\rangle = 0 \qquad \langle\psi_{vi}\psi_{vj}\rangle = \delta_{ij} \tag{4.2}$$

by minimization of the total energy with the restriction that all the core orbitals ψ_c remain frozen and we choose the these frozen core orbitals to be eigenfunctions of the Fock operator $\hat{F}$ ($\hat{F} \mid \psi_c\rangle = \epsilon_c \mid \psi_c\rangle$), the following Huzinaga-Cantu equation [147, 148] is obtained:

$$\hat{F}^{HC} \mid \psi_v\rangle \equiv \left\{ \hat{F} + \sum_c (-2\epsilon_c) \mid \psi_c\rangle\langle\psi_c \mid \right\} \mid \psi_v\rangle = \epsilon_v \mid \psi_v\rangle \tag{4.3}$$

It is similar to Philips Kleinman one (3.63), except that there is a negative constant multiplying the projector operators of the core. This constant makes the negative energies of the core orbitals, ϵ_c, to be projected much over the valence orbitals energies, ϵ_v. Thus, the lowest lying solutions, that will be considered as occupied orbitals, are the valence orbitals themselves, not linear combinations. Such term $\sum_{c\in\mu}(-2\epsilon_c) \mid \psi_c\rangle\langle\psi_c \mid$ comes directly from the conditions of linear independence between core and valence wavefunctions imposed through 4.2 in the restricted variational treatment. They are called strong orthogonality conditions [149, 150, 151].

With the use of this equation, the necessity of the core orbitals to be represented by the basis sets is eliminated and the basis size can be much smaller than for an all-electron calculation but of the same size that in a pseudopotential calculation. However,since the nodal structure of the valence orbitals is retained, the length of the contracted functions should be higher than that of the basis set that represent the nodeless valence orbitals on a pseudopotential calculation.

In molecular Hartree-Fock calculations, the $\hat{F}^{HC}$ operator of Eq. 4.3 can be expressed as follows:

$$\left\{ -\frac{1}{2}\hat{\nabla}^2 - \sum_{\mu} \frac{Z_{\mu}^{eff}}{|\vec{r}-\vec{R}_{\mu}|} + \sum_{\mu} \left[-\frac{N_{\mu}^{core}}{|\vec{r}-\vec{R}_{\mu}|} + \sum_{c\in\mu}(2\hat{J}_c - \hat{K}_c) + \sum_{c\in\mu}(-2\epsilon_c) \mid \psi_c\rangle\langle\psi_c \mid \right] + \sum_{v}(2\hat{J}_v - \hat{K}_v) \right\} \quad (4.4)$$

where $Z_{\mu}^{eff} = Z_{\mu} - N_{\mu}^{core}$.

When we go to the atomic level, it reads

$$\left\{ -\frac{1}{2}\hat{\nabla}_i^2 - \frac{Z_{\mu}^{eff}}{r} + \left[\frac{N_{\mu}^{core}}{r} + \sum_{c}(2\hat{J}_c - \hat{K}_c) + \sum_{c}(-2\epsilon_c) \mid \varphi_c\rangle\langle\varphi_c \mid \right] + \sum_{v}(2\hat{J}_v - \hat{K}_v) \right\} \quad (4.5)$$

where the whole term in square brackets is substituted by an approximated term, the atomic model potential $\hat{V}_{\mu}^{MP}$.

$$\left\{ -\frac{1}{2}\hat{\nabla}_i^2 - \frac{Z_{\mu}^{eff}}{r} + \hat{V}_{\mu}^{MP} + \sum_{v}(2\hat{J}_v - \hat{K}_v) \right\} \quad (4.6)$$

The term substituted in equation 4.5 does not depend on the valence. Then, the model potential $\hat{V}_{\mu}^{MP}$ can be constructed only using the core orbitals and their energy.

In the AIMP method, the term in square brackets in expression 4.5 is substituted, one by one for each atom μ, for approximate representations of them that should mimic as much as possible the operators that they represent . The result is an *ab initio* model potential $\hat{V}_{\mu}^{MP}$ made of additive terms with their own physical meaning, which reads as follows in its non-realtivistic version:

$$\hat{V}_{\mu}^{AIMP} \rightarrow \hat{V}_{\mu}^{NR-AIMP} = \hat{V}_{Coul}^{\mu,MP} + \hat{V}_{Exch}^{\mu,MP} + \hat{P}_{core}^{\mu} \quad (4.7)$$

The AIMP method can be used to represent atomic cores (Section 4.1.2) in calculations on the valence electronic structure of a wide variety of molecules and clusters, which leads to important computational savings. This approach and its advantages can be extended to ionic solids, as seen on the following section.

4.1.1 *Embedding* AIMP

The concept of valence electrons under the influence of frozen cores can be compared to the concept of a group of atoms (cluster) under the influence of an embedding host. Then,

ECPs and embedding potentials can be obtained using a common strategy. In the AIMP method, that leads to the practical advantage that the one electron operators (addends in Eq. 4.7) representing the effects of an atomic core or of an embedding ion are identical. Then, the same molecular code can be used to perform ECP calculations and embedding cluster calculations since, once the embedding potential input data are included in the molecular package, it is possible to forget about the surrounding solid and focus in a standard *ab initio* calculation on the cluster.

The parallelism cluster/valence embedding/frozen core arises clearly in the context of the MacWeeny's Group-Function Theory (GFT).

4.1.1.1 The Group-Function Theory formulation

The Group-Function Theory was proposed by McWeeny [149, 150] in the contet of intermolecular interactions, to allow for the calculation of the electronic structure of a very large system which can be partitionated into weakly interacting electronic groups. The simplest wavefunction for the whole system, Ψ_k, is a generalized antisymmetric product wavefunction

$$\Psi_k = M_k \hat{A}[\Phi_r^R \Phi_s^S ...] \qquad (k = Rr, Ss, ...). \tag{4.8}$$

assuming that the whole system can be partitioned into electronic systems $R, S, ...$, whose electronic states, $r, s, ...$, are represented by the $\Phi_r^R, \Phi_s^S, ...$ antisymmetric group-functions of $N_R, N_S, ...$ electrons.

$\hat{A}$ is an antisymmetrizer ensuring that the total wavefunction is properly antisymmetric with respect to the exchange of electrons between groups. M_k is a normalization factor.

Each individual group-function can be a multiconfigurational expansion so it is possible to include electron correlation locally within each group. And, since $N_R, N_S, ...$ are constant numbers (the electron transfer between groups is not permitted), electron correlation between different groups should be negligible. Then, the definition of *weakly interacting groups* arises. This requirement must guide the partition of Ψ_k (Eq.4.8).

If we construct each group-function from different sets of orthogonal spinorbitals and, moreover, conditions of *strong orthogonality* are imposed among the group-functions

$$\int \Phi_r^R(\mathrm{x}_1, \mathrm{x}_i, \mathrm{x}_j, ...)^* \Phi_s^S(\mathrm{x}_1, \mathrm{x}_k, \mathrm{x}_l, ...) \mathrm{dx}_1 = 0 \qquad (R \neq S) \tag{4.9}$$

the energy associated to the total wave-function in Eq.4.8 can be expressed as

$$E = \sum_R H^R(rr) + \sum_{R<S} \left[J^{RS}(rr, ss) - K^{RS}(rr, ss) \right] \tag{4.10}$$

where

$$E_{eff}^R = H^R(rr) + \sum_{S(\neq R)} \left[J^{RS}(rr, ss) - K^{RS}(rr, ss) \right] \tag{4.11}$$

represent the energy of the R electron group under the interactions with the other electron groups and defines the concept of embedded R group energy in the GFT framework.

$H^R(rr)$ is formally identical to the electronic energy of the r electronic state of the isolated R group.

Standard molecular methods can be used to calculate the Φ_r^R embedded group-function and energy(Eq.4.11) if the usual one-electron Hamiltonian $\hat{h}^R = \sum_{i=1}^{N_R} \{-\frac{1}{2}\nabla_i^2 - \sum_\mu \frac{Z_\mu}{|\vec{r}_i - \vec{R}_\mu|}\}$ is modified in order to include the interactions with the remaining S electron groups:

$$\hat{h}^R_{eff} = \sum_{i=1}^{N_R} \{ -\frac{1}{2}\nabla_i^2 - \sum_\mu \frac{Z_\mu}{|\vec{r}_i - \vec{R}_\mu|} + \sum_{S(\neq R)} \left[\hat{J}^S(i) - \hat{K}^S(i,i')\right] \} \tag{4.12}$$

The operators $\hat{J}^S(i)$ and $\hat{K}^S(i,i')$ are the "Coulomb" and "exchange" operators for an electron in the effective field due to the electrons of group S [149, 150]. Then, they are embedding operators.

From this point, the GFT continues as a building-block formalism which leads to a final variational self-consistent calculation of Ψ_k, by solving the variational problem of one group at a time. For our problem of a large system presenting local properties coming from a specific group of atoms, let's say the R group, the GFT set the basis to concentrate the computational effort on such R group, freezing the remaining electron system, say the S group. Then, the relevant R group-function Φ_r^R can be described using multiconfigurational methods, whereas frozen monoconfigurational descriptions are used for the S group. In valence-only calculations, Φ_r^R is the valence molecular wavefunction and Φ_r^S are the core closed-shell atomic functions. In embedded cluster calculations, Φ_r^R is associated to the electronic states of the point defect cluster, whereas Φ_r^S are closed-shell frozen wavefunctions representing the surrounding ions of the crystal. Usually, the R region comprises the point defect under study and its first neighbors and the S region, the atoms beyond first-neighbors.

The two major practical difficulties encountered in the rigorous application of the GFT to both valence-only and embedding calculations are, on the one hand, that the application of the restricted variational principle to Ψ_k (Eq.4.8) using the effective operator $\hat{h}^R_{eff}$ (Eq.4.12) usually leads to variational collapse. On the other hand, even though $\hat{J}^S(i) - \hat{K}^S(i,i')$ is a one-electron operator, it requires the calculation of as many two-electron integrals as if the system is treated as a unity so there are no savings in this respect. The restricted variational formulation of Huzinaga [147, 148] and the techniques for the representation of the AIMP operators described in 4.1.2 allow to overcome these problems [96, 152].

4.1.1.2 Representation of the embedding operators

The GFT embedding operators (Eq.4.12) are substituted by AIMP representations. The procedure starts by rearrangement of the contributions of one embedding group S in Eq.4.12, ensuring that long- and short-range interactions are separated, which is very

convenient in solid state applications. The potential for the embedding group S reads:

$$\hat{V}^S = -\sum_{\nu \in S} \frac{Z_\nu}{|\vec{r}_i - \vec{R}_\nu|} + \hat{J}^S(i) - \hat{K}^S(i,i')$$
$$= V^S_{lr-Coul}(i) + V^S_{sr-Coul}(i) + \hat{V}^S_{exch}(i,i'), \tag{4.13}$$
$$V^S_{lr-Coul}(i) = -\sum_{\nu \in S} \frac{Z_\nu - N_\nu}{|\vec{r}_i - \vec{R}_\nu|}, \tag{4.14}$$
$$V^S_{sr-Coul}(i) = -\sum_{\nu \in S} \frac{N_\nu}{|\vec{r}_i - \vec{R}_\nu|} + \hat{J}^S(i), \tag{4.15}$$
$$\hat{V}^S_{exch}(i,i') = -\hat{K}^S(i,i'). \tag{4.16}$$

The electrostatic potentials have been grouped in a long-range Coulomb potential (Eq.4.14) and a short-range Coulomb potential (Eq.4.15). The long/short range can be assured by a suitable choice of the arbitrary N_ν in Eqs. 4.14 and 4.15, which usually corresponds to the number of electrons assigned to the nuclei ν of group S.

- Representation of the long-range Coulomb potential $V^S_{lr-Coul}(i)$. It is the corresponding point-charge potential and can be rigorously calculated.

- Representation of the short-range Coulomb potential $V^S_{sr-Coul}(i)$. It represents the deviations from a point charge. If the group S is atomic, as in our case, the following local representation is used[96]:

$$V^S_{sr-Coul}(i) \qquad \longrightarrow \qquad V^{S,MP}_{sr-Coul} = \frac{1}{r_i} \sum_k C^S_k exp(-\alpha^S_k r_i^2), \tag{4.17}$$

  where the $\{C^S_k, \alpha^S_k\}$ parameters are determined through least-squares fitting to the genuine short-range Coulomb operator of Eq.4.15 evaluated with the S-group function.

- Representation of the exchange potential $\hat{V}^S_{exch}(i,i')$ This nonlocal exchange potential (Eq.4.16) is substituted by its spectral representation on the primitive basis set used to describe the S group function:

$$\hat{V}^S_{exch}(i,i') \qquad \longrightarrow \qquad \hat{V}^{S,MP}_{exch} = \hat{\Omega}^S \hat{V}^S_{exch} \hat{\Omega}^S. \tag{4.18}$$

  where $\hat{\Omega}^S$ is the projection operator of the space defined by the non-orthogonal basis set $\{\mid \chi^S_i \rangle\}$ of primitive Gaussian-type functions of the S group, with metric $\underline{S}^S$ defined by $S^S_{ij} = \langle \chi^S_i \mid \chi^S_j \rangle$ and $\hat{\Omega}^S \equiv \sum_p \sum_q \mid \chi^S_p \rangle (\underline{S}^{S-1})_{pq} \langle \chi^S_q \mid$.

The AIMP representation of the GFT one-electron embedding operator $\hat{V}^S$ is therefore

$$\hat{V}^S \rightarrow V^S_{sr-Coul} + V^{S,MP}_{lr-Coul} + \hat{V}^{S,MP}_{Exch} \tag{4.19}$$

The only information needed to obtain the AIMP representation of the GFT operator $\hat{V}^S$ is the S group wavefunction itself Φ^S_s. However, to obtain such Φ^S_s and the cluster wavefunction Φ^R_r, it is necessary to consider the restricted variational treatment of Huzinaga in the GFT formalism [147, 148]

Huzinaga's restricted variational method If the embedding group wavefunction Φ_s^S is taken to be the ground state of the external ion and it is represented by a monoconfigurational wavefunction, the addition of the projection operator

$$\hat{P}^S = \sum_{c \in S} (-2\varepsilon_c^S) \mid \psi_c^S \rangle \langle \psi_c^S \mid \tag{4.20}$$

prevents from the variational collapse. It is constructed using the occupied orbital energies and functions of group S, ψ_c^S and ε_c^S respectively. It acts providing an efficient repulsive barrier to the occupation of the S-group orbitals.

4.1.1.3 YAG embedding potentials for Ce

In order to visualize the procedure described above, let us take as an example the solid under study in this work: Ce_Y:YAG. The first decision to be taken is how to partition the crystal electronic structure of Ce_Y:YAG into groups (Eq.4.8). A good choice must be based in the available experimental information about the local properties of this material. In Ce_Y:YAG, it is known that Ce^{3+} substitutes an Y^{3+} in the lattice, in one of the 24(c) eightfold coordinated positions of the YAG unit cell, which belongs to the $Ia3d$ space group. In Fig.4.1 (left) it is highlighted in green the $(CeO_8)^{13-}$ cluster embedded in the YAG unit cell. To clarify, Fig.4.1 (right) shows Ce^{3+} together with its eightfold first coordination shell (grey O^{2-}) and the cations of the second coordination shell (red Al^{3+}_{oct} , yellow Al^{3+}_{tet} and blue Y^{3+}). As we will see in detail in part II, because of the

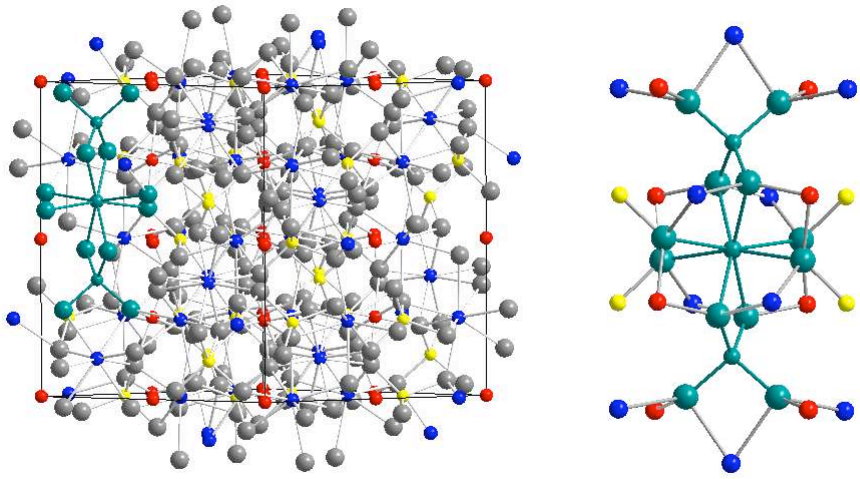

Figure 4.1: Left: $(CeO_8Al_2O_4)^{15-}$ cluster (highlighted in greeny blue) embedded in YAG. Right: $(CeO_8Al_2O_4)^{15-}$ (greeny blue) and its second neighbors Al_{oct} (red), Al_{tet} (yellow) and Y^{3+} (blue).

chemistry of Ce_Y:YAG, we have two possible suitable choices for group R, both of them centered in the impurity Ce^{3+}. Those are the clusters $(CeO_8)^{13-}$ and $(CeO_8Al_2O_4)^{15-}$.

This description is focused only on $(CeO_8Al_2O_4)^{15-}$, in order to illustrate as clear as possible the generation procedure of embedding AIMPs. Thus, the group function R, mainly responsible of the (spectroscopic) property under study is defined as $(CeO_8Al_2O_4)^{15-}$, whereas the group S ={Al^{3+}_{oct} ,Al^{3+}_{tet} ,Y^{3+} and O^{2-}} is only responsible of such properties in a lesser extent. In this work, we study the R group function at a CASSCF/CASPT2 level to calculate the $4f \rightarrow 5d$ absorption spectra of Ce^{3+} embedded in YAG.

At this point, obtaining the AIMP embedding operators demands the calculation of the embedding Φ^S_s group functions. With this purpose, self-consistent-embedded-ion calculations (SCEI) are performed on the perfect crystal: First, calculations on the single ions embedded in an initial representation of the host: Al^{3+}_{oct}:YAG, Al^{3+}_{tet}:YAG, Y^{3+}:YAG, O^{2-}:YAG, (being $R = Al^{3+}_{oct}$,Al^{3+}_{tet} ,Y^{3+} or O^{2-} respectively). Then, an iterative procedure is followed, in which the ground state wavefunction and energy of the ions are calculated at the Hartree-Fock level. The initial representation of the lattice can be a punctual charges model or a set of AIMPs previously generated in a different solid. AIn every case, the iterative procedure optimizes both wavefunction and energies at the HF level. Once Φ^S_s are available, the embedding AIMP operators are obtained automatically (Eqs.4.14, 4.17, 4.18 and 4.20).

The sum over external S group-functions (Eq.4.12) is infinite in the crystal and should be truncated. Since the only long-range term within the embedding operators is $\sum_{S(\neq R)} V^S_{lr-Coul}$, truncation guidelines should be extracted by analyzing it. A usual practice in embedded cluster calculations is to include all the terms of the AIMP operator in all ions surrounding the defect cluster up to second neighbors, at least. Beyond that, one can

- include all ions up to a long enough distance: the whole piece of crystal, arbitrarily centered in the defect, should preserve the shape of the unit cell, the distance from the center to the frontier ions should be high (e.g. 30 bohrs) and fractional charges should be assigned to the fronter ions following Evjen's method [153]. The truncation must not distort the potential energy surfaces of the cluster.

- integrate the Madelung potential directly [154]: only the sum of short-range potentials ($V^{S,MP}_{sr-Coul}$, $\hat{V}^{S,MP}_{exch}$, and $\hat{P}^S$) is actually truncated.

Results of both procedures are, in general, identical.

The partition of the crystal assumed in the AIMP embedded cluster method creates a *frontier* between the cluster group-function and the embedding group-functions. This feature should be analyzed under the methodological point of view. In our Ce:YAG example, the partition is associated to the assumption that correlation effects between the $(CeO_8Al_2O_4)^{15-}$ electrons and next cations can be neglected in the calculation of local properties. But it is also important to mention that the following interactions are included:

- short-range Coulomb interactions and exchange interactions between the $(CeO_8Al_2O_4)^{15-}$ and the cations group-functions.

- strong-orthogonality interactions, which do not allow for the occupation of environmental spin-orbitals in the $(CeO_8Al_2O_4)^{15-}$ configurational space.

The fulfillment of these quantum-mechanical features (direct consequence of the Pauli principle) gives the AIMP embedding method a practical advantage, since, because these interactions are present, some typical distortions of the calculated cluster properties related to a finite cluster size or frontier effects, do not occur in the AIMP context.

The AIMP embedding potential obtained in this way and used for YAG in this work was obtained by Gracia *et al.*(Ref. [41]).

Second-neighbor functions Huzinaga's restricted variational method constraint imposes orthogonality between cluster and crystal wavefunctions (strong-orthogonality, forced by Eq. 4.20). This orthogonality is improved with the flexibility of the cluster basis set.

Cluster molecular orbitals used to construct the multiconfigurational wavefunctions are expressed in terms of linear combination of atomic orbitals (LCAO). This approach is based on the locality of those electronic states responsible of local properties within the cluster region.

However, a source of error in these methods of finite cluster comes from delocalization features. Actually, even in those cases where the properties of the defect under study are localized, certain degree of delocalization should be included to ensure orthogonality between cluster(R) group-functions and orbitals of the rest of electronic groups on the surroundings. Thus, not-so-local LCAO are used for the cluster, where basis functions present components localized in other positions of the lattice. This adds extra flexibility, enforcing the strong orthogonality conditions. In this context, some basis functions in the neighborhood of the cluster limits are included [155], improving the LCAO expansion. These functions, called *orthogonality functions*, are strongly needed in cases where cluster vibrations are pointing the nearest neighbors positions to the cluster. In our case, the adjacent coordination shell is made of all the Al^{3+}_{oct}, Al^{3+}_{tet} and Y^{3+} cations connected to the oxygen atoms of the cluster.

4.1.2 *Core* AIMP

The whole *ab initio* model potential (AIMP) method to obtain core ECPs consist in two main steps: representation of core operators and optimization of the valence basis set.

4.1.2.1 Representation of core operators

Each term in Eq. 4.7 is obtained directly from those core orbitals and corresponding energies arising from a previous all electron restricted Hartree-Fock calculation of a certain atomic state (generally ground state).

- Coulomb potential $\hat{V}_{Coul}^{\mu,MP}$. The Coulomb operator $-\frac{N_\mu^{core}}{r} + 2\sum_{c\in\mu}\hat{J}_c$, local and spheric, is substituted by a local and radial model potential

$$-\frac{N_\mu^{core}}{r} + 2\sum_{c\in\mu}\hat{J}_c \rightarrow \hat{V}_{Coul}^{\mu,MP} \equiv \frac{1}{r}\sum_k C_k^\mu exp(-\alpha_k^\mu r^2) \tag{4.21}$$

whose exponents α_k^μ and coefficients C_k^μ are arbitrary numbers calculated by means of a least squares fitting under the constraint $\sum_k {C_k}^\mu = -N_\mu^{core}$. Those numbers are included to enforce proper asymptotic behaviors of $\hat{V}_{Coul}^{\mu,MP}$. This component represents the effect on one valence electron of the Coulomb repulsion exerted by the core electrons and the nuclear attraction eerted by the same number of protons.

- Exchange potential $\hat{V}_{Exch}^{\mu,MP}$. The atomic core exchange operator, $\hat{V}_{Exch}^{\mu} \equiv -\sum_{c\in\mu}\hat{K}_c$, non local operator, is substituted by its spectral representation in a space defined by a set of functions $\{\mid \chi_i^\mu\}\rangle$ (with metrics S^μ defined by $S_{ij}^\mu = \langle\chi_i^\mu \mid \chi_j^\mu\rangle$ and a projector operator $\hat{\Omega}^\mu \equiv \sum_p\sum_q \mid \chi_p^\mu\rangle(S^{\mu-1})_{pq}\langle\chi_q^\mu \mid)$,

$$\hat{V}_{Exch}^{\mu} \equiv -\sum_{c\in\mu}\hat{K}_c \rightarrow \hat{V}_{Exch}^{\mu,MP} \equiv \hat{\Omega}^\mu\hat{V}_{Exch}^{\mu}\hat{\Omega}^\mu = \sum_i\sum_j \mid \chi_i^\mu\rangle \mathbf{A}_{ij}^{E,\mu}\langle\chi_j^\mu \mid \tag{4.22}$$

where the matrix coefficients $A_{ij}^{E,\mu}$ are defined by

$$A_{ij}^{E,\mu} = \sum_p\sum_q (S^{\mu-1})_{ip}K_{pq}^\mu(S^{\mu-1})_{qj} \tag{4.23}$$

with $K_{pq}^\mu = \langle\chi_p^\mu \mid \hat{V}_{Exch}^\mu \mid \chi_q^\mu\rangle$.

Since $\hat{V}_{Exch}^\mu$ is a short-range operator, it can be properly represented by only a moderate number of primitive gaussians $\mid \chi_i^\mu\rangle$ centered on atom μ. This component represents the exchange interaction between the core electrons of atom μ and one valence electron.

- Projection operator $\hat{P}_{core}^\mu$. It is kept in its form

$$\hat{P}_{core}^\mu \equiv \sum_{c\in\mu}(-2\epsilon_c) \mid \psi_c\rangle\langle\psi_c \mid \tag{4.24}$$

and represents the repulsion effects on a valence electron that prevent it from collapsing into the core. It comes as a direct consequence of the so-defined strong orthogonality condition between valence and core wavefunction. The factor 2 has been suggested by Höjer y Chung [156].

4.1.2.2 Optimization of the valence basis set

Once the core *ab initio* model potential of an atom μ has been obtained, its valence basis set is optimized in atomic AIMP calculations with analogous procedure than for all-electron basis sets. With gaussian functions, the atomic valence orbitals read

$$\mid \psi_v^{'\mu}\rangle = \mid R_{nl}^{'\mu}(r)Y_{lm}^{'\mu}(\theta,\psi)\rangle \tag{4.25}$$

where r, θ and ψ refer to a framework centered on atom μ and the primes indicate that they are approximations to the all-electron valence orbitals. The radial functions are expanded in terms of an arbitrary number of radial primitive gaussian functions χ^{μ}_{il}

$$R'^{\mu}_{nl}(r) = \sum_i c_{ni:l}\chi^{\mu}_{il} = \sum_i c_{ni:l} r^l exp(-\zeta_{ni:l} r^2), \tag{4.26}$$

The exponents $\zeta_{ni:l}$ and the coefficients $c_{ni:l}$ are both optimized in valence only AIMP open-shell restricted Hartree-Fock atomic calculations.

4.1.3 Relativistic AIMP

So far, we have seen for the non-relativistic case that the AIMP approximation consists only in the adoption of a basic equation and the substitution of some operators by model potentials representations of them, one by one. This method can be applied to different relativistic formulations, as long as their respective valence-only equations are know and the operators that will be represented by model potentials are identified. In this section we describe the general features of the AIMP method based in the relativistic formulation of Cowan and Griffin [134] (CG-AIMP), used in this work, and its spin-orbit extension of Wood and Boring [135] (WB-AIMP).

4.1.3.1 Cowan-Griffin/Wood-Boring relativistic Hamiltonians

The method proposed by Cowan and Griffin [134] and Wood and Boring [135] reduces the computational effort associated to solve Dirac equations in the Hartree-Fock context with four-components spinorbitals. Starting from Dirac equation for hydrogenoid atoms, they proposed approximated scalar and spin-orbit Hamiltonians by addition of generalized expressions of the mass-velocity and Darwing operators from Pauli Hamiltonian [157].

They obtained the following approximated Hamiltonian for an electron in a central field:

$$\left\{ -\frac{d^2}{2dr^2} + \frac{l(l+1)}{2r^2} + \hat{V}(r) + \hat{V}_{mv,nl} + \hat{V}_{Dar,nl} \right\} G_{nl}(r) = \epsilon_{nl} G_{nl}(r) \tag{4.27}$$

where

$$\hat{V}_{mv,nl} = -\frac{\alpha^2}{4}(\epsilon_{nl} - V)^2 \tag{4.28}$$

$$\hat{V}_{Dar,nl} = -\frac{\alpha^2}{2[2 + \alpha^2(\epsilon_{nl} - V)]} \frac{dV}{dr} \left(\frac{1}{G_{nl}} \frac{dG_{nl}}{dr} - \frac{1}{r} \right) \tag{4.29}$$

Except for the two new relativistic operators ($\hat{V}_{mv,nl}$ and $\hat{V}_{Dar,nl}$), the equation above is completely analogous to the non-relativistic equation of the radial functions of an electron in a central field if $G_{nl}(r) = R_{nl}(r)/r$, being R_{nl} the radial part of the wavefunction ψ_{nlm}

of such electron. Thus, Cowan and Griffin added these two one-electron operators to the non-relativistic Fock operator $\hat{F}_{NR}$ for an atom:

$$\left(\hat{F}_{NR} + \hat{V}_{mv,nl} + \hat{V}_{Dar,nl}\right)\psi_{nlm} = \epsilon_{nl}\psi_{nlm} \tag{4.30}$$

This is a set of coupled equations that can be solved self-consistently by means of numerical procedures with special boundary conditions to avoid variational collapse and give rise to a set of non-orthogonal (quasi-orthogonal in practice) atomic orbitals (See Section aimp). Wood and Boring extended this line of approximation to treat spin-orbit coupling effects, using numerical orbitals from Eq. 4.30 to obtain the spin-orbit operators:

$$V_{SO,nl}\hat{\mathbf{l}}\hat{\mathbf{s}} = \frac{\alpha^2}{[2+\alpha^2(\epsilon_{nl}-V)]}\frac{1}{r}\frac{dV}{dr}\hat{\mathbf{l}}\hat{\mathbf{s}} \tag{4.31}$$

The above spin-orbit operators are used together with the one-electron contribution of the Cowan-Griffin Hamiltonian and can be used not only in self-consistent field two-components methods but also in spin-orbit configuration interaction (SO-CI) and perturbative methods.

We describe in the following subsections how these spin-free and spin-dependent relativistic components can be included in the AIMP Hamiltonian.

4.1.3.2 Cowan-Griffin AIMP

Since the new relativistic terms have short-range and atomic character, the molecular relativistic contribution can be safely approximated by addition of the atomic mass-velocity, Darwin and spin-orbit operators and those can be substituted by atomic model potentials [158]. Thus, the spin-free relativistic AIMP Hamiltonian based on Cowan-Griffin $\hat{H}^{CG-AIMP}$ reads :

$$\hat{V}_{\mu}^{AIMP} \rightarrow \hat{V}_{\mu}^{CG-AIMP} = V_{Coul}^{\mu,MP} + \hat{V}_{EMD}^{\mu,MP} + \hat{P}_{core}^{\mu} \tag{4.32}$$

where $V_{Coul}^{\mu,MP}$ is not but equivalent to 4.21 involving the atomic Cowan-Griffin orbitals instead of the non-relativistic ones. $\hat{V}_{EMD}^{\mu,MP}$ is the spectral representation of the core exchange operator, plus the Cowan-Griffin mass velocity and Darwin operators of the valence of atom μ:

$$\hat{V}_{EMD}^{\mu,MP} \equiv \hat{\Omega}^{\mu}\left(\hat{V}_{exch}^{\mu} + \hat{V}_{MV}^{\mu} + \hat{V}_{D}^{\mu}\right)\hat{\Omega}^{\mu} \tag{4.33}$$

where

$$\hat{V}_{MV}^{\mu} + \hat{V}_{D}^{\mu} = \sum_{nl}^{valence} \hat{O}_{l}^{\mu}\left(V_{MV,nl}^{\mu} + V_{D,nl}^{\mu}\right)\hat{O}_{l}^{\mu} \tag{4.34}$$

$V_{MV,nl}^{\mu}$ and $V_{D,nl}^{\mu}$ are potentials obtained in the atomic Cowan-Griffin-Hartree-Fock calculation and transferred without any modification. $\hat{O}_{l}^{\mu}$ is an angular projection operator defined on the basis of the spherical harmonics on atom μ:

$$\hat{O}_{l}^{\mu} = \sum_{m=-l}^{+l} \mid lm;\mu\rangle\langle lm;\mu \mid \tag{4.35}$$

which prevents the nl dependence mass-velocity and Darwin potentials of a given l from acting on orbitals with a different l, l'.

At this point we have defined the spin-free relativistic CG-AIMP Hamiltonian for any molecule in terms of elements coming from atomic Cowan-Griffin-Hartree-Fock calculations. This Hamiltonian presents the same symmetry properties as the non-relativistic one and, thus, can be used in the same kind of calculations: SCF, CASSCF, CI ...

4.1.3.3 Wood-Boring AIMP

The addition of the spin-orbit coupling effects to the spin-free relativistic effects already considered in the CG-AIMP molecular Hamiltonian is achieved with the spin-orbit relativistic AIMP Hamiltonian based on Wood-Boring, WB-AIMP:

$$\hat{V}_{\mu}^{AIMP} \rightarrow \hat{V}_{\mu}^{WB-AIMP} = V_{Coul}^{\mu,MP} + \hat{V}_{EMD}^{\mu,MP} + \hat{P}_{core}^{\mu} + \hat{h}_{SO}^{\mu,MP} \tag{4.36}$$

This Hamiltonian results from adding the monoelectronic spin-orbit operator $\hat{h}_{SO}^{\mu,MP}$ to the CG-AIMP Hamiltonian. This $\hat{h}_{SO}^{\mu,MP}$ is defined as follows:

$$\hat{h}_{SO}^{\mu,MP} \equiv \sum_{nl}^{valencia} V_{SO,nl}^{\mu,MP}(r)\hat{O}_l^{\mu}\hat{\mathbf{l}}^{\mu}\hat{\mathbf{s}}\hat{O}_l^{\mu} \tag{4.37}$$

where $\hat{\mathbf{l}}^{\mu}$ and $\hat{\mathbf{s}}$ are the angular momentum and spin operators respectively. $\hat{O}_l^{\mu}$ are the angular projection operators (used according to the Pitzer and Winter formula [159]) whose radial components are analytical functions obtained from a least-squares fit to the radial components of the Wood-Boring operator:

$$V_{SO,nl}^{\mu,MP}(r) = \lambda^{\mu}\sum_{k}\frac{B_{k;nl}^{\mu}exp(-\beta_{k;nl}^{\mu}r^2)}{r^2} \tag{4.38}$$

This spin-orbit WB-AIMP Hamiltonian is used in calculations at the CI level, e.g. in a basis of double-group symmetry-adapted functions, with molecular orbitals obtained in a spin-free relativistic HF or CASSCF calculation with the CG-AIMP Hamiltonian $\hat{H}^{CG-AIMP}$.

4.2 Multiconfigurational methods

Within the embedded cluster approximation described previously, the problem of luminescence of Ce:YAG can be studied with the same molecular quantum mechanical approaches used in gas phase calculations. Since we need to describe many states close in energy, we need to use methods that take into account the multiconfigurational nature of the wave function.

In this work, starting from a SCF calculation, the clusters $(CeO_8)^{13-}$ and $(CeO_8Al_2O_4)^{15-}$ have been studied at two levels of theory:

- Complete Active Space Self Consistent Field(CASSCF)
  Accounts for static correlation.

- Multiconfigurational 2^{nd} order Perturbation Theory (CASPT2)
  Accounts for dynamic correlation.

Both methods are described below after a brief introduction on multiconfigurational wavefunctions.

4.2.1 Multiconfigurational wavefunction and energy

In general, multiconfigurational calculations start with the expansion of the molecular orbitals in an atomic basis set. Then, the first computational step involves the calculation of the one- and two-electron integrals that will be used to build the Fock matrices. Such matrices give rise to the energy expression and its derivatives with respect to variational parameters.

4.2.1.1 Operators and matrix elements

To represent the quantum mechanical operators in the space generated by Slater determinants, it often used the second quantization formalism. This formalism involves two special operators: creation ($\hat{a}_i^\dagger$) and annihilation ($\hat{a}_i$) operators. Each creation operator is associated to one spin-orbital of the Slater determinant $\mid \phi_i\rangle$ in a way that, if $\hat{a}_i^\dagger$ acts on the Slater determinant and $\mid \phi_i\rangle$ is unoccupied, an electron in $\mid \phi_i\rangle$ is generated:

$$\hat{a}_i^\dagger \mid \phi_k \dots \ \phi_l\rangle = \mid \phi_i\phi_k \dots \ \phi_l\rangle \tag{4.39}$$

On the contrary, if $\mid \phi_i\rangle$ is already occupied, there is no action of $\hat{a}_i^\dagger$, to preserve the exclusion principle. The annihilation operator $\hat{a}_i$, adjoint of $\hat{a}_i^\dagger$, acts on the first occupied spin-orbital, removing an electron from it:

$$\hat{a}_i \mid \phi_i\phi_k \dots \ \phi_l\rangle = \mid \phi_k \dots \ \phi_l\rangle \tag{4.40}$$

Creation and annihilation operators fulfill the following anticommutative relations:

$$\begin{aligned} \{\hat{a}_i^\dagger, \hat{a}_j^\dagger\} &= 0 \\ \{\hat{a}_i, \hat{a}_j\} &= 0 \\ \{\hat{a}_i, \hat{a}_j^\dagger\} &= \delta_{ij} \end{aligned} \tag{4.41}$$

One-electron operators

Using the creation-annihilation operators $\hat{a}_i^\dagger$ and $\hat{a}_i$, a one-electron operator can be expressed as follows:

$$\hat{F} = \sum_i \sum_j F_{ij} \hat{a}_i^\dagger \hat{a}_j \tag{4.42}$$

where $F_{ij} = \int \phi_i^*(x)\hat{F}(x)\phi_j(x)dx$ is the matrix element of $\hat{F}$ in the spi-orbitals basis (both spatial and spin coordinates are included in x; $x = \{r, s\}$). In the second quantization formalism, if the operator $\hat{F}$ is independent of spin, an excitation operator $\hat{E}_{ij}$ can be defined as:

$$\hat{E}_{ij} = \hat{a}_{i\alpha}^\dagger \hat{a}_{j\alpha} + \hat{a}_{i\beta}^\dagger \hat{a}_{j\beta} \tag{4.43}$$

and $\hat{F}$ can be expressed in terms of $\hat{E}_{ij}$:

$$\hat{F} = \sum_i \sum_j F_{ij}\hat{E}_{ij} \tag{4.44}$$

where the sum is over orbitals and the integrals F_{ij} are defined in such orbital basis. A matrix element between two Slater determinants $\mid m\rangle$ and $\mid n\rangle$ can be expressed as follows:

$$\langle m \mid \hat{F} \mid n\rangle = \sum_i \sum_j F_{ij}\langle m \mid \hat{E}_{ij} \mid n\rangle = \sum_i \sum_j F_{ij} D_{ij}^{mn} \tag{4.45}$$

where $D_{ij}^{mn} = \langle m \mid \hat{E}_{ij} \mid n\rangle$ are the one-electron coupling coefficients and for Slater determinants can present the value -1, 0, 1 or 2. Diagonal elements are not but the occupation number of the i orbital if $m = n$. Otherwise are equal to zero. The reduced density matrix can be expressed in terms of these D_{ij}^{mn}. For a CI wavefunction such as $\mid \Psi\rangle = \sum_m c_m \mid m\rangle$;

$$D_{ij} = \langle \Psi \mid \hat{E}_{ij} \mid \Psi\rangle = \sum_m \sum_n c_m^* c_n D_{ij}^{mn} \tag{4.46}$$

Two-electron operators

In general, two-electron operators can be represented as

$$\hat{G} = \sum_i \sum_j \sum_k \sum_l g_{ijkl}\hat{a}_i^\dagger \hat{a}_k^\dagger \hat{a}_l \hat{a}_j \tag{4.47}$$

where

$$g_{ijkl} = \int \phi_i^*(x_1)\phi_k^*(x_2)\hat{G}(x_1, x_2)\phi_j(x_1)\phi_l(x_2)dx_1 dx_2 \tag{4.48}$$

The two-electron operator we are interested in is the inter electronic repulsion operator $\frac{1}{r_{12}}$. It is spin-independent and can be expressed as well in terms of excitation operators $\hat{E}_{ij}$:

$$\hat{G} = \sum_{i,j,k,l} g_{ijkl}(\hat{E}_{ij}\hat{E}_{kl} - \delta_{jk}\hat{E}_{il}) \tag{4.49}$$

where the sum is over molecular orbitals and the integral is defined as:

$$g_{ijkl} = \int \varphi_i^*(\mathbf{r}_1)\varphi_j(\mathbf{r}_1)\frac{1}{r_{12}}\varphi_k^*(\mathbf{r}_2)\varphi_l(\mathbf{r}_2)dV_1 dV_2 \tag{4.50}$$

The matrix elements between Slater determinants for this two-electron operator can be obtained by:

$$\langle m \mid \hat{G} \mid n \rangle = \sum_{i,j,k,l} G_{ijkl} P^{mn}_{ijkl} \tag{4.51}$$

where $P^{mn}_{ijkl} = \frac{1}{2}\langle m \mid (\hat{E}_{ij}\hat{E}_{kl} - \delta_{jk}\hat{E}_{il}) \mid n \rangle$ are the two-electron coupling coefficients. The second order reduced density matrix for the wavefunction $\mid \Psi \rangle = \sum_m c_m \mid m \rangle$ in terms of these P^{mn}_{ijkl} reads:

$$P_{ijkl} = \sum_{m,n} c^*_m c_n P^{mn}_{ijkl} \tag{4.52}$$

Hamiltonian

Using the above formalism, the Hamiltonian can be expressed in terms of the excitation operators $\hat{E}_{ij}$:

$$\hat{H} = \sum_{i,j} h_{ij}\hat{E}_{ij} + \frac{1}{2}\sum_{i,j,k,l} g_{ijkl}(\hat{E}_{ij}\hat{E}_{kl} - \delta_{jk}\hat{E}_{il}) \tag{4.53}$$

where h_{ij} is the one-electron integrals term, including kinetic energy and electron-nuclei attraction terms, and g_{ijkl} accounts for the electronic repulsion integrals defined in Eq.4.50. For a CI-type wavefunction, the energy as expectation value of the Hamiltonian (Eq.4.53) reads as follows:

$$E = \langle \Psi \mid \hat{H} \mid \Psi \rangle = \sum_{i,j} h_{ij} D_{ij} + \sum_{i,j,k,l} g_{ijkl} P_{ijkl} \tag{4.54}$$

This is the basic equation on multiconfigurational optimization methods. At this point, it should be stressed out that the information about the molecular orbitals, that is, the MO coefficients, is completely included in one- and two-electron integrals, whereas density matrices D y P contain the CI coefficients.

4.2.1.2 Exponential operators and orbital transformations

The variational parameters in Eq. 4.54 are the two sets of coefficients: MO and CI. Those variations are not but rotations of an orthonormal vectorial space. An example of this rotation is the unitary transformation (trough the unitary matrix $\boldsymbol{U}$, $\boldsymbol{U}^\dagger\,\boldsymbol{U} = 1$) of the original set of orbitals (row vector φ) in a new set of orbitals (φ'):

$$\varphi' = \varphi\, U \tag{4.55}$$

Spin orbitals are transformed adding the spin functions α or β to Eq.4.55. In this transformation, as well creation and annihilation operators do change, being the transformed operators

$$\hat{a}'_i = e^{-\hat{T}}\hat{a}_i e^{\hat{T}} \tag{4.56}$$

$$\hat{a}'^{\dagger}_i = e^{-\hat{T}}\hat{a}^{\dagger}_i e^{\hat{T}} \tag{4.57}$$

where $\hat{T}$ is an antihermitian operator:

$$\hat{T} = \sum_{i,j} T_{ij} \hat{a}_i^\dagger \hat{a}_j \tag{4.58}$$

that can be expressed in terms of excitation operators if an average over spin is done:

$$\hat{T} = \sum_{i,j} T_{ij} \hat{E}_{ij} \tag{4.59}$$

The corresponding representation matrix in any basis set is antihermitian and fulfills $T^\dagger$ = -T. Then, it is possible to identify the unitary matrix $U = e^{\text{-}T}$, since any unitary matrix can be expressed in terms of the exponential of an antihermitian matrix.

Once the transformation patterns of the creation-annihilation operators are known, we can express an arbitrary Slater determinant in the new basis in terms of determinants in the original basis. We just need to apply a creation-annihilation operator series to the vacuum state $\mid vac\rangle$ in order to generate the Slater determinant:

$$\begin{aligned} \mid m'\rangle &= \hat{a}_i'^\dagger \hat{a}_j'^\dagger \hat{a}_k'^\dagger \ldots \mid vac\rangle = e^{-\hat{T}} \hat{a}_i^\dagger e^{\hat{T}} e^{-\hat{T}} \hat{a}_j^\dagger e^{\hat{T}} \ldots \mid vac\rangle \\ &= e^{-\hat{T}} \hat{a}_i^\dagger \hat{a}_j^\dagger \hat{a}_k^\dagger \ldots \mid vac\rangle = e^{-\hat{T}} \mid m\rangle \end{aligned} \tag{4.60}$$

The equation above shows a important feature: an orbital transformation of a Slater determinant can be carried out just by applying the exponential operator $e^{-\hat{T}}$ on such Slater determinant. So far, we have considered transformations on the spin orbitals but, in practice, only the radial part (molecular orbitals) are transformed. The implication of this point in operator $\hat{T}$ are pointed out if spin orbitals are constructed by means of $\phi = (\varphi\alpha, \varphi\beta)$. Then, the T matrix can be expressed as a set of four submatrices, each one corresponding to the transformation between the two sets of spin orbitals:

$$T = \begin{pmatrix} T_{\alpha\alpha} & T_{\alpha\beta} \\ T_{\beta\alpha} & T_{\beta\beta} \end{pmatrix} \tag{4.61}$$

Each T_{ij} describes an unitary rotation of the molecular orbital by $U = e^{\text{-}T}$. And, since molecular orbitals are real, T matrix is real and antisymmetric ($T_{ij} = -T_{ji}$) and expression 4.58 can be re-written as follows:

$$\hat{T} = \sum_{i>j} T_{ij} (\hat{E}_{ij} - \hat{E}_{ji}) = \sum_{i>j} T_{ij} \hat{E}_{ij}^- \tag{4.62}$$

In conclusion, an orbital orthogonal rotation is described by the excitation operators $\hat{E}_{ij} - \hat{E}_{ji}$.

We can express the variational parameters of the CI expansion as the C_m coefficients in $\mid 0\rangle = \sum_m C_m \mid m\rangle$. The variational space can be chosen to be complementary to the MCSCF and it is defined in a set of states $\mid K\rangle$ expanded in the same basis set $\mid m\rangle$ ($\mid K\rangle = \sum_m C_m^K \mid m\rangle$). Then, each state $\mid K\rangle$ is linked to a variational parameter describing the contribution of such state to the variation of the multiconfigurational state

$\mid 0\rangle$. This variation can be described as a unitary rotation between the MCSCF state and the complementary space. This rotation is performed by an operator that can be built in the same way as the operator for orbital transformations was constructed. To that end, an antisymmetric replacement operator $\hat{S}$ is defined:

$$\hat{S} = \sum_{K \neq 0} S_{K0}(\mid K\rangle\langle 0 \mid - \mid 0\rangle\langle K \mid) \tag{4.63}$$

where S_{K0} are variational parameters and $S^{\dagger}$=-S. Thus, the corresponding unitary operator is not but $e^{\hat{S}}$ and a unitary transformation of $\mid 0\rangle$ is obtained by

$$\mid 0'\rangle = e^{\hat{S}} \mid 0\rangle \tag{4.64}$$

To sum up, rotation of orbitals and variation of CI coefficients are carried out by the $e^{\hat{T}}$ and $e^{\hat{S}}$ operators respectively. Thus, a variation of the multiconfigurational state MCSCF can be written as:

$$\mid 0'\rangle = e^{\hat{T}} e^{\hat{S}} \mid 0\rangle \tag{4.65}$$

The operators $e^{\hat{T}}$ and $e^{\hat{S}}$ do not commute and, then, the order in the expression above is not arbitrary. However, the final result does not depend on the order of intervention so this order is chosen such that one can get the simplest expressions. The energy is obtained as a function of the T and S rotational parameters:

$$E(T, S) = \langle 0 \mid e^{-\hat{S}} e^{-\hat{T}} \hat{H} e^{\hat{T}} e^{\hat{S}} \mid 0\rangle \tag{4.66}$$

where T and S must fulfill the stationary character of energy, that is :$\delta E/\delta T = 0$ and $\delta E/\delta S = 0$.

The Newton-Raphson method is the most used optimization procedure oriented to obtain the MCSCF function variational parameters. In this method, the energy is expanded in a Taylor series on such variational parameters, normally, up to second order.

4.2.2 CASSCF

Two main difficulties arise when we are facing a MCSCF calculation. The first one, present in monoconfigurational calculations as well, is the choice of a good enough basis set. Fortunately, some libraries with reliable basis sets of different levels of quality are available. The second one, present only in multiconfigurational methods, is the problem of the construction of the wavefunction. In MCSCF calculations, the general structure of the wavefunction must be defined *a priori* and only if the electronic structure is known, the guidelines of this procedure are reliable. In normal bonding cases (e.g. ground state calculations), this information, to a greater or lesser extent, is not too hard to obtain. However, in complex situations as transition or excited states are, can be so hard to decide *a priori* which are the relevant electronic configurations that should be included in the MCSCF function. This problem is tackled by the CASSCF method [160, 161, 162]; it

defines a set of quasi-degenerate active orbitals. Then, the CASSCF method starts from dividing the orbital space in three main blocks for each symmetry block, depending on their role in the wavefunction construction:

1. Inactive orbitals: Doubly occupied orbitals in all the configurations used to build the CASSCF function.

2. Active orbitals: Occupied by as many electrons as the total number of electrons minus twice the number of inactive orbitals. These are the *active electrons*.

3. Virtual orbitals: Unoccupied orbitals of the orbital space.

The CASSCF wavefunction is built as a linear combination of all the configurations in the N-electronic space and fulfills all the spatial and spin symmetry requirements, with doubly occupied inactive orbitals, which represent a *SCF electronic sea* that brings mobility to the active electrons.

Once the active/inactive orbitals have been chosen, the CASSCF wavefunction is completely defined. This conceptual simplicity brings computational simplifications as well in the computational procedures followed to obtain the optimized orbitals and the set of CI coefficients. The main technical disadvantage, by definition, arises from the size of the complete expansion within the active space. Weyl's formula measures this size, N_{CAS}, expressed as the dimension of the irreducible space of the associated unitary group $U(n)$, with n active orbitals, N active electrons and a total spin S:

$$N_{CAS} = \frac{2s+1}{n+1}\binom{n+1}{N/2-S}\binom{n+1}{N/2+S+1} \tag{4.67}$$

N_{CAS} rapidly increases with the size of the active space n, restricting such size in practice. Then, a good choice of the active space is essential. In this work, the active space consist of 13 orbitals (coming from Ce $4f$, $5d$ and $6s$ atomic orbitals) with one active electron (due to the Ce^{3+} nature of the lanthanide) so it is an affordable enough problem. However, analogous calculations carried out in our group with impurities belonging to the whole lanthanide series (Refs. [100, 163, 164]), present hundreds of thousands of configurations and a rigorous analysis becomes quite cumbersome.

CASSCF method is focused to obtain good zero-order approximations for the wavefunctions but it is not designed to account for dynamic correlation effects and, thus, CASSCF energies are not precise enough (dynamic correlation effects can contribute with 1-2 eV to the total energy). In spite of this, the CASSCF wavefunction is clearly a good starting point for second order wavefunction-based perturbative methods.

4.2.3 CASPT2

4.2.3.1 Perturbation theory

Perturbation theory begins by expressing the full Hamiltonian of the system as the sum of a reference Hamiltonian and a time independent perturbation

$$\hat{H} = \hat{H}_0 + \lambda\hat{H}_1 \tag{4.68}$$

where λ is a parameter measuring the strength of the perturbation. It is assumed that the exact solution of the Schrödinger equation for $\hat{H}_0$ is known:

$$\hat{H}_0 \mid \Psi_0\rangle = E_0 \mid \Psi_0\rangle$$

The full Schrödinger equation reads:

$$\hat{H} \mid \Psi\rangle = E \mid \Psi\rangle$$

and its eigenstates and eigenvalues can expressed in powers of the parameter λ as follows:

$$\begin{aligned} \Psi &= \Psi_0 + \lambda\Psi_1 + \lambda^2\Psi_2 + \dots \\ E &= E_0 + \lambda E_1 + \lambda^2 E_2 + \dots \end{aligned} \tag{4.69}$$

Introducing 4.68 and 4.69 in the full Schrödinger equation 4.69 and grouping terms with the same power of λ, it ends up with:

$$\begin{aligned} \hat{H}_0 \mid \Psi_0\rangle &= E_0 \mid \Psi_0\rangle \\ (\hat{H}_0 - E_0) \mid \Psi_1\rangle &= (E_1 - \hat{H}_1) \mid \Psi_0\rangle \\ (\hat{H}_0 - E_0) \mid \Psi_2\rangle &= (E_1 - \hat{H}_1) \mid \Psi_1\rangle + E_2 \mid \Psi_0\rangle \end{aligned} \tag{4.70}$$

Assuming that the total and the 0^{th}-order wavefunction are orthogonal, $\langle\Psi \mid \Psi_0\rangle = 1$, perturbed wavefunction are orthogonal as well to Ψ_0: $\langle\Psi_0 \mid \Psi_i\rangle = 1$. Using this property, the expression for the energy (up to 2^{nd} order) read:

$$\begin{aligned} E_0 &= \langle\Psi_0 \mid \hat{H}_0 \mid \Psi_0\rangle \\ E_1 &= \langle\Psi_0 \mid \hat{H}_1 \mid \Psi_0\rangle \\ E_2 &= \langle\Psi_0 \mid \hat{H}_1 \mid \Psi_1\rangle \end{aligned} \tag{4.71}$$

At this point, let's examine the 2^{nd}-order Møller-Plesset method MP2)[69], where Ψ_0 is a Hartee-Fock-like (monodeterminantal) reference wavefunction. The Hamiltonian whose eigenvector and eigenvalue are Ψ_0 and E_0 respectively can be built as follows:

$$\hat{H}_0 = \hat{P}_0\hat{F}\hat{P}_0 + \hat{P}_X\hat{F}\hat{P}_X \tag{4.72}$$

where $\hat{P}_0 =\mid \Psi_0\rangle\langle\Psi_0 \mid$ is a projection operator on the reference wavefunction, $\hat{P}_X$ is the projection operator on the remaining configurational space and $\hat{F}$ is the following sum of Fock operators:

$$\hat{F} = \sum_{p,q} f_{pq}\hat{E}_{pq} \tag{4.73}$$

To solve the 1^{st}-order equation, the 1^{st}-order wavefunction is expressed as a linear combination of all the configurations (Slater determinants) in the spin orbitals CI space, except the Hartree-Fock-like determinant:

$$\Psi_1 = \sum_{\mu} C_\mu\Phi_\mu \tag{4.74}$$

All these functions are eigenvalues of $\hat{H}_0$ with eigenvectors equal to the sum of the orbital energies of the occupied spin orbitals in a given determinant. Let's call such eigenvalues E_μ. If 4.74 is inserted into the 1^{st}-order equation of 4.70, we can obtain the coefficients of the 1^{st}-order expansion:

$$C_\mu = -\frac{\langle \Phi_\mu \mid \hat{H}_1 \mid \Psi_0 \rangle}{E_\mu - E_0} \tag{4.75}$$

$\langle \Phi_\mu \mid \hat{H}_1 \mid \Psi_0 \rangle$ accounts for the interaction of any configuration Φ_μ and the Hartree-Fock reference configuration Ψ_0; only the non-zero elements will be included in the 1^{st}-order expansion. Since Ψ_0 fulfills Brillouin's theorem, first excitations do not contribute so the 1^{st}-order wavefunction can be written as:

$$\Psi_1 = \sum_{i>j,a>b} C_{ijab} \Psi_{ij \to ab} \tag{4.76}$$

where i, j are occupied spin orbitals and a, b are virtual ones. The coefficients are given by:

$$C^{(1)}_{ijab} = -\frac{\langle \Psi_0 \mid \hat{H}_1 \mid \Phi_{ij \to ab} \rangle}{(\epsilon_a + \epsilon_b - \epsilon_i - \epsilon_j)} \tag{4.77}$$

and the 2^{nd}-order energy:

$$E_2 = -\frac{|\langle \Psi_0 \mid \hat{H}_1 \mid \Phi_{ij \to ab} \rangle|^2}{(\epsilon_a + \epsilon_b - \epsilon_i - \epsilon_j)} \tag{4.78}$$

This simple expression for the energy can be implemented in programming in a straightforward way.

4.2.3.2 Multiconfigurational extension of perturbation theory

In a multiconfigurational problem treated as CASPT2 level, the reference function Ψ_0 is a CASSCF wavefunction. The 0^{th}-order Hamiltonian is analogous to 4.72:

$$\hat{H}_0 = \hat{P}_0 \hat{F} \hat{P}_0 + \hat{P}_K \hat{F} \hat{P}_K + \hat{P}_{SD} \hat{F} \hat{P}_{SD} + \hat{P}_X \hat{F} \hat{P}_X \tag{4.79}$$

where the CI space has been divided into the following four subspaces:

1. V_0, space extended by the reference wavefunction: $\Psi_0 = \mid CASSCF\rangle = \mid 0\rangle$;
2. V_K, space orthogonal to Ψ_0 in the complementary CAS CI subspace: $\mid K\rangle$;
3. V_{SD}, space extended to all the simple and double excitations with respect to the CAS reference: $\mid pqrs\rangle = \hat{E}_{pq}\hat{E}_{rs} \mid \Psi_0\rangle$;
4. V_{TQ}, remaining CI space: $\mid X\rangle$.

According to the definition of 0^{th}-order Hamiltonian given in 4.79, only the configurations that interact with the CAS reference function are included in the 1^{st}-order wavefunction. All of them belong to the V_{SD} space. Then,

$$\begin{aligned} \mid \Psi_1\rangle &= \sum_{p,q,r,s} C_{pqrs} \mid pqrs\rangle \\ \mid pqrs\rangle &= \hat{E}_{pq}\hat{E}_{rs} \mid \Psi_0\rangle \end{aligned} \tag{4.80}$$

If all the four p, q, r, s subindex are active, the generated wavefunction would belong to the V_K space and do not interact with Ψ_0. Thus, among all the simple and double excitations generated by $\hat{E}_{pq}$ and $\hat{E}_{rs}$, there will be included in the wavefunction only those whose four indexes are not in the active space.

Orbitals are divided into four groups:

- Frozen: doubly occupied, they are not included in the correlation treatment and they do not appear explicitly.
- Inactives $(i, j, k, l...)$: doubly occupied in $\mid \Psi_0\rangle$.
- Actives $(t, u, v, x...)$: any occupation number between 0 and 2.
- Secondary $(a, b, c, d...)$: unoccupied in $\mid \Psi_0\rangle$.

All the set of functions needed to expand the 1^{st}-order wavefunction can be divided into eight groups, generated from excitation operators:

- Internal excitations, no secondary indexes:
  $A : \hat{E}_{ti}\hat{E}_{uv} \mid \Psi_0\rangle$
  $B : \hat{E}_{ti}\hat{E}_{uj} \mid \Psi_0\rangle$
- Semi-internal excitations, only one secondary index:
  $C : \hat{E}_{at}\hat{E}_{uv} \mid \Psi_0\rangle$
  $D : \hat{E}_{ai}\hat{E}_{tu} \mid \Psi_0\rangle$; $\hat{E}_{ti}\hat{E}_{au} \mid \Psi_0\rangle$
  $E : \hat{E}_{ti}\hat{E}_{aj} \mid \Psi_0\rangle$
- External excitations, two secondary indexes:
  $F : \hat{E}_{at}\hat{E}_{bu} \mid \Psi_0\rangle$
  $G : \hat{E}_{ai}\hat{E}_{bt} \mid \Psi_0\rangle$
  $H : \hat{E}_{ai}\hat{E}_{bj} \mid \Psi_0\rangle$

The fock operator of Eq.4.73 can be expressed as a sum of the diagonal and the non-diagonal terms:

$$\hat{F} = \hat{F}_D + \hat{F}_N \tag{4.81}$$

In the general expression

$$\hat{F} = \sum_{p,q} f_{pq}\hat{E}_{pq} \tag{4.82}$$

D is the one-particle density matrix and

$$f_{pq} = h_{pq} + \sum_{r,s} D_{rs}[\langle pr \mid qs\rangle - \frac{1}{2}\langle pq \mid rs\rangle] \tag{4.83}$$

$\hat{F}$ will be chosen to match its diagonal elements with the orbital energies of inactive and secondary orbitals (Koopman's theorem).

Moreover, the matrix f can be simplified taking into account that the CASSCF wavefunction is invariant with respect to rotations among the inactive, active and secondary orbitals. Three different subsets of orbitals should be chosen to make this matrix diagonal within each of them. Then, $\hat{F}$ can be expressed as:

$$\begin{aligned} \hat{F} &= \sum_i \epsilon_i \hat{E}_{ii} + \sum_t \epsilon_t \hat{E}_{tt} + \sum_a \epsilon_a \hat{E}_{aa} \\ &+ \sum_{i,t} f_{ti}[\hat{E}_{it} + \hat{E}_{ti}] + \sum_{i,a} f_{ai}[\hat{E}_{ia} + \hat{E}_{ai}] \\ &+ \sum_{t,a} f_{at}[\hat{E}_{ta} + \hat{E}_{at}] \end{aligned} \tag{4.84}$$

where $\epsilon_i = f_{ii}$ and i reads for inactive orbitals, t for active orbitals and a for external orbitals.

1^{st}-, 2^{nd}-, 3^{rd}- and 4^{th}-order density matrices of the CAS reference wavefunction are need to evaluate the complicated elements of F:

$$\langle pqrs \mid \hat{F} \mid p'q'r's'\rangle = \sum_{\alpha,\beta} f_{\alpha\beta}\langle \Psi_0 \mid \hat{E}_{sr}\hat{E}_{qp}\hat{E}_{\alpha\beta}\hat{E}_{p'q'}\hat{E}_{r's'} \mid \Psi_0\rangle \tag{4.85}$$

4^{th}-order matrices appear if both α and β are active.This part of $\hat{F}$ is diagonal ($\alpha = \beta$) and this makes the calculation simpler. Anyway, the computational effort associated to the calculation of these integrals is quite high, the bigger the active space the more demanding.

4.2.3.3 Intruder states and reference weight

If the 1^{st}-order wavefunction $\mid \Psi'\rangle = \mid \Psi_0\rangle + \mid \Psi_1\rangle$ is normalized to $\mid \Psi\rangle$ using

$$\begin{aligned} \langle \Psi' \mid \Psi'\rangle &= 1 + S_1 \\ S_1 &= \langle \Psi_1 \mid \Psi_1\rangle \end{aligned} \tag{4.86}$$

it can be expressed as

$$\mid \Psi\rangle = \sqrt{\omega} \mid \Psi_0\rangle + \sqrt{1-\omega} \mid 1\rangle \tag{4.87}$$

where $\mid 1\rangle$ is the normalized 1^{st}-order wavefunction and $\omega = 1/(1+S)$ is the so-called *reference weight* and represents the weight of the CAS reference function in $\mid \Psi\rangle$. This reference weight is used as a fast and simple quality criterion of reliability of the perturbative treatment. Ideally, the reference weight should be as close as possible to unity.

However, the numerical value of the reference weight depends on the number of correlated electrons. Then, the reference weight decreases as the system size increases. Low reference weights may indicate the presence of *intruder states* in the perturbative calculation. Those intruder states are those that have a 0^{th}-order energy close or even lower to the reference energy E_0 in the V_{SD} space and, then, are strongly interacting with Ψ_0.

4.2.3.4 MS-CASPT2

The Multistate CASPT2 method (MS-CASPT2) [165] represents an improvement of the CASPT2 method for perturbative treatments with several reference states because CASPT2 sometimes fails, e.g. when two electronic states are very close in energy and dynamic correlation does notably affect their mutual interaction. In CASPT2, as said above, the reference space V_0 is one-dimensional and it is not but the reference CASSCF state, eigenfunction of $\hat{H}_0$. The MS-CASPT2 method introduces two or more CASSCF states in a multidimensional reference space. An effective Hamiltonian is built in which all the diagonal elements correspond to CASPT2 energies and off-diagonal elements account for the 2^{nd}-order coupling in the dynamic correlation energy of the relevant states. In this way, all the states of a given symmetry can be treated simultaneously, including correlation effects of the CASSCF reference functions.

Part II

RESULTS

Chapter 5

Pure and perfect YAG

Garnets are materials widely studied by mineralogists and physicists, not only because natural garnets are hard materials with semiprecious properties, but also because the crystallographic structure of garnets has been expanded to synthetic crystals with applications in many fields [166].

In particular, yttrium aluminum garnet $Y_3Al_5O_{12}$ (YAG), is a synthetic material with adequate mechanical, thermal, and optical properties, which make it useful for a range of applications, such as thermal coating, optical lenses, widely used solid-state lasers and solid-state-lighting phosphors as Ce:YAG, the material of interest in this work [167, 168, 37].

Thus, in this work, a good description of YAG is a key factor in the further modeling of Ce:YAG luminescence because it is the host material present, in one way or another, in all our calculations.

The computational study of YAG at the atomistic level, apart from its role as host of our luminescent impurity, has a notorious interest by itself because the number of first-principles studies on this material is surprisingly small. Actually, despite the importance of this material due to its mechanical, thermal and optical properties and the large amount of experimental information about it [169, 170], *ab initio* quantum mechanical calculations were performed rarely due to the huge computational effort associated with the high number of atoms per unit cell and such complicated structure. So far, the periodic boundary conditions (PBC) first-principles calculations we are aware of are limited to the density functional theory (DFT) calculations within the local density approximation (LDA) of Xu and Ching [171], the Hartree-Fock (HF) calculations of Shelyapina *et al.* [172], and the tight-binding linearized muffin-tin orbital LDA (TB-LMTO-LDA) calculations of Pari *et al.* [173]. Xu and Ching [171] computed the electronic structure, the lattice constant and the bulk modulus, with a good agreement with experimental data; later, they made comparisons with and helped to interpret the electron energy loss near edge structure (EELNES) experiments [174]. However, they adopted the experimental relative atomic positions within the unit cell in their calculations and did not attempt the calculation of the YAG structure at the atomistic level. This task was not performed either in the more recent calculations of Pari *et al.* [173] and Shelyapina *et al.* [172], where even the lattice

constant was fixed to experimental values. We include in this work relaxation on both lattice vectors and internal positions for the first time to the best of our knowledge.

Thus, in this first step towards the study of Ce:YAG, we tackle the *ab initio* study of YAG at the atomistic level, necessary condition for the reliability of further calculations on materials containing defects, whose structures are hard to get from experiments alone and, nevertheless, are key factors governing the lasing and luminescence properties of YAG related materials, like Nd:YAG and Ce:YAG [37, 28], and the mechanism of Y segregation at the grain boundaries, directly related with the resistance to creep in high-temperature ceramic composites [175]. In this line, Freeman *et al.* [176] pointed out the crucial importance of the local environment of individual cations on the structure and energetics of garnet solid solutions.

We perform our study by means of periodic boundary conditions-density functional theory (PBC-DFT) techniques, used for atomistic structure predictions in other garnets like pyrope $Mg_3Al_2Si_3O_{12}$ at the HF level [177], and pyrope and grossular $Ca_3Al_2Si_3O_{12}$ [176].

In this chapter, we study *pure* and *perfect* YAG; *pure* in the sense that it does not contain any impurity (in Chapters 6, 9, 10 and 11 we treat YAG-based materials containing different atoms than Y, Al and O) and *perfect* in the sense that internal order of the $Ia\bar{3}d$ space group is preserved (in Chapters 7 and 11 we take into account the intrinsic antisite defects that appear in YAG during synthesis at high temperatures [43, 178], which have implications on luminescence of Ce:YAG [44, 46]).

The general garnet cubic unit cell contains eight formula units of $A_3B'_2B''_3O_{12}$, where A, B′ and B″ are cations in different symmetry sites. In YAG, A≡Y, B′ ≡Al in octahedral environment (Al_{oct}) and B′ ≡Al in tetrahedral environment (Al_{tet}). A unit cell of YAG contains eight times $Y_3Al_5O_{12}$, resulting on a 160 atom body-centered-cubic unit cell (80 atom primitive cell). It belongs to the $Ia\bar{3}d$ (230) space group, with Y in its 24(c) sites, Al_{oct} in the 16(a) sites, Al_{tet} occupying the 24(d) sites and the remaining 96 oxygen atoms in the (h) sites.

The structure, shown in Fig. 5.1, can be seen as a set of interconnected dodecahedrons centered on Y atoms, and both octahedrons and tetrahedrons centered on Al atoms, all of them sharing oxygens. Each oxygen is in fact a vertex of two dodecahedron, one octahedron and one tetrahedron, which means that each oxygen is linked to two Y, one Al_{oct} and one Al_{tet}.

A total description of this cell is done with the lattice constant a and the x, y and z internal parameters defining the h sites of oxygens atoms. We use as starting point for the present calculations the structure determined by Euler and Bruce by X-ray diffraction [179], with a lattice constant value of $a_0 = 12.000$ and $x = -0.0306$, $y = 0.0512$, $z = 0.1500$ as internal oxygen parameters.

Since all the structural calculations involving YAG have been performed within the DFT framework using the program SIESTA [97] and two main components in SIESTA calculations are pseudopotentials and numerical basis sets, we needed, at the very beginning, both of them for Al, Y and O atoms. This necessity extended to Ce, La and Ga when we moved ahead from YAG to doped YAG. Thus, we present in Section 5.1 a description of

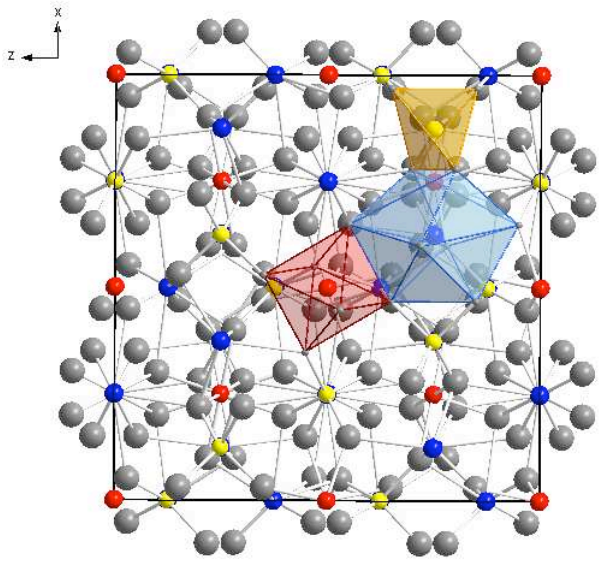

Figure 5.1: Unit cell of YAG. View along y axis. Y^{3+} ions (blue), Al^{3+}_{oct} (red), Al^{3+}_{tet} (yellow) and O^{2-} (grey) indicated.

both pseudopotentials and basis sets generated and used all along this work. Section 5.2 contains all our results concerning pure and perfect YAG and in Section 5.3 we present our results for crystals involving atoms present in YAG: yttrium aluminum perovskite ($YAlO_3$), alumina (Al_2O_3) and yttria (Y_2O_3), performed in parallel to those of YAG in order to check the performances of pseudopotentials and basis sets generated. Within this section, we include the computed Mulliken population analysis of these compounds in comparison with YAG and a set of calculated formation energies involving YAG and these species. Section 5.4 contains some conclusions extracted from this chapter. Finally, data tables are presented in Section 5.6.

5.1 Obtaining pseudopotentials and basis sets

At the starting point of this work, both pseudopotentials (of some DFT flavors, LDA and PBE among them) and basis sets (optimized for such pseudopotentials in different systems) of Al and O atoms were available in SIESTA pseudopotentials and basis sets database (http://www.icmab.es/siesta). However, Y pseudopotentials and Y basis sets were not available. These latter were impossible to generate by means of the SIESTA default procedure (see Section 3.5.2) because it cannot deal with the $4p$ semicore state present in the valence of Y atom. Thus, although the only mandatory requirement was obtaining Y pseudopotential and basis set, pseudopotentials and basis sets for Al and O were obtained simultaneously to those of Y (Section 5.1.1 and Section 5.1.2), in order to homogenize their source and errors. They were obtained for both LDA and GGA(PBE)

functionals in a parallel way and all the subsequent calculations in pure and perfect YAG were performed with both functionals. PBE results were in a better agreement with experimental data (see below, Section 5.2) and, then, we only used PBE for obtaining Ce, La and Ga pseudopotentials and basis sets.

5.1.1 Pseudopotentials generation

All the pseudopotentials used in the present work are norm-conserving Troullier-Martins pseudopotentials built with the ATOM program [126]. Reference configurations, cutoff radii for the different angular momentum channels and cutoff radius used to include non-lineal core corrections, where necessary, are shown in Table 5.1.

All the parameters in Table 5.1 have been chosen in a *trial and error* procedure in such a way that their corresponding pseudopotential fulfills the following criteria, according to Section 3.5.1.2:

- Fit as better as possible a table of energy differences between atomic calculations using the generated pseudopotential and all electron calculations for different configurations: the reference one used for pseudopotential generation and a few configurations different from the reference one (e.g. ionizations and excitations). The list of chosen configurations reads as follows:

  - Y: $Y^0(4p^6 5s^2 4d^1)$(ref), $Y^{3+}(4p^6 5s^0)$, $Y^{2+}(4ps^6 5s^1$ and $4ps^6 4d^1)$, $Y^+(4p^6 5s^2)$.
  - Al: $Al^0(3s^2 3p^1)$(ref), $Al^0(3s^2 3p^{0.5} 3d^{0.5})$, $Al^+(3s^2 3p^0)$, $Al^{2+}(3s^1 3p^0)$, $Al^{3+}(3s^0 3p^0)$.
  - O: O^0 $(2s^2 2p^4)$(ref), O^{2-} $(2s^2 2p^6)$, O^- $(2s^2 2p^5)$, O^0 $(2s^1 2p^5)$.
  - Ce: $Ce^{3+}(5s^2 5p^6 4f^1)$(ref), $Ce^{3+}(5s^2 5p^6 5d^1)$, $Ce^{4+}(5s^2 5p^6)$, $Ce^{3+}(5s^2 5p^6 4f^{0.5} 5d^{0.5})$.
  - La: $La^{3+}(5s^2 5p^6)$(ref), La^{2+} $(5s^2 5p^6 4f^1)$, $La^{2+}(5s^2 5p^6 5d^1)$, $La^0(5s^2 5p^6 5d^1 6s^2)$.
  - Ga: $Ga^0(4s^2 4p^1)$(ref), Ga^0 $(4s^2 4p^{0.5} 4d^{0.5})$, $Ga^+(4s^2 4p^0)$, $Ga^{2+}(4s^1 4p^0)$, $Ga^{3+}(4s^0 4p^0)$.

- Accurate matching of the logarithmic derivative of the related pseudowavefunction with respect to the all electron one.

- Do not present *ghosts states* (Section 3.5.1.6) once tested in a SIESTA trial calculation, that is, once factorized in their fully non local Kleinman-Bylander form.

Two remarks about the pseudopotential generation of the atoms present in this work must be pointed out here. First, whereas for Y, Al, O and Ga, the chosen reference configurations correspond to neutral atoms, the reference configurations for La and Ce are those corresponding to the trivalent cation (La^{3+}, Ce^{3+}). This is related to the fact that $5s$ orbitals are more external than $4f$ orbitals. Since $4f$ orbitals are included as valence orbitals, it is mandatory to include all the orbitals more external than the $4f$ shell in the valence. Then, the configuration of La and Ce neutral atom should include two channels with the same second quantum number, $5s$ and $6s$, together with the $5p$,

$5d$ and $4f$ orbitals in the valence, which leads to an error in the step of inversion of the radial Schrödinger equation of pseudopotential generation (Section 3.5.1.3).

This obstacle is avoided by ripping out the electrons of the $6s$ orbital (together with one electron of the $5d$ orbital, generating their usual 3+ valence state in the crystal) and, since they are empty, they don't have to be considered and the $5s$ shell can be included in the valence.

Second, just few words on the non-linear core corrections used for La pseudopotential. Despite the pseudopotential generated for La in this work responds to a GGA(PBE) DFT calculation, its non-linear core corrections are not those corresponding to the GGA scheme present on Section 3.5.1.4 but to the LDA scheme. This is due to pure technical reasons, since the GGA scheme introduced a too high semicore charge in the calculation and then, the *mesh cutoff* (fineness of the real grid) requirements were extremely high and no convergence was reached with reasonable mesh values.

5.1.2 Basis Sets generation

Y, Al and O The basis sets used in the present work were obtained using the optimization method described in Section 3.5.2.2. An optimization of the basis sets directly in the 160 atoms YAG unit cell is, unfortunately, unaffordable. Yttrium aluminum perovskite ($YAlO_3$), belonging to the *Pbnm* (62) space group, has the same kind of atoms involved in YAG and contains 30 atoms per unit cell; still too many for a basis set optimization. Then we used a much smaller cubic solid containing yttrium, aluminum and oxygen: the symmetrized perovskite $CeAlO_3$ (cubic, contains only 5 atoms per unit cell: a central Ce, corner-placed Al and edge-placed O [180]) substituting the central Cerium with an yttrium atom. This cubic $YAlO_3$ perovskite is represented in Fig. 5.2.

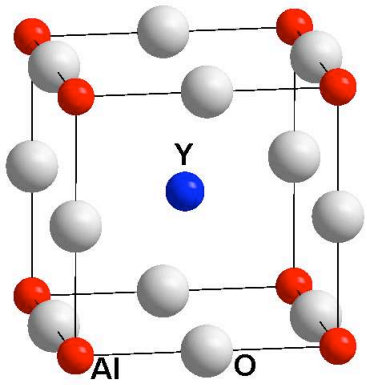

Figure 5.2: Scheme of the cubic $YAlO_3$ cell used to generate Y, Al and O basis sets.

Then, the lattice constant was approximately recalculated, using the proportionality between the radii of the trivalent cations. From the experimental lattice constant $a = 3.82$ Å of $CeAlO_3$, a smaller lattice constant of $a = 3.19$ Å was used for our cu-

bic $YAlO_3$, since cation Y^{3+} (ionic radius = 0.93 Å) is smaller than Ce^{3+} (ionic radius = 1.11 Å).

In order to obtain Y, Al and O basis sets simultaneously, the fictitious enthalpy $E + PV$ [137] of the above cubic solid is minimized, through a series of SIESTA calculations, using pseudopotentials obtained in the previous section. The parameters to be optimized, described also in Section 3.5.2.2, are: r_c of each single-ζ orbital, the matching radius r_s^l for the double-ζ (where appropriate), the value of the soft confining potential V_0 and the radius where it starts to act, r_i. The starting values of these parameters are, in principle, arbitrary, but, obviously, r_s^l and r_i must be smaller than r_c.

Since the basis generation procedure was not the SIESTA's default one, we were able to choose the basis orbitals for each atom. We use (the $'$ index reads for the double-ζ orbital):

- **Y**: $5s$ $5s'$ $4p$ $4p'$ $5p$ $4d$ $4d'$
- **Al**: $3s$ $3s'$ $3p$ $3p'$ $3d$
- **O**: $2s$ $2s'$ $2p$ $2p'$ $3d$

The parameters obtained for the orbitals above after minimization are reflected in Table 5.2 and such orbitals are showed on Fig. 5.3.

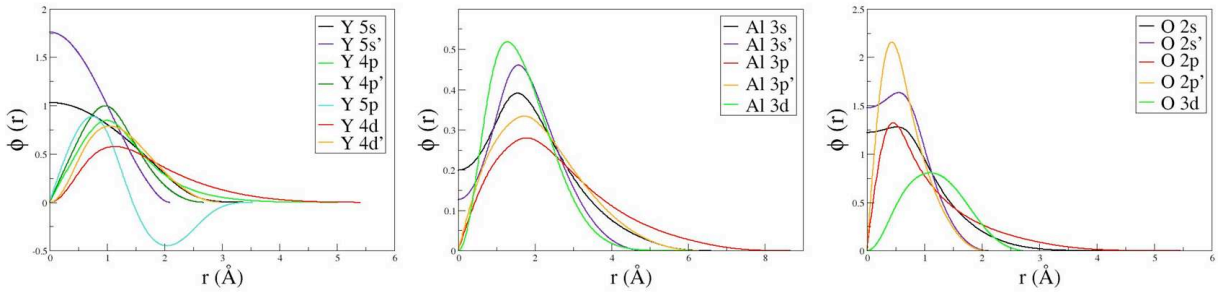

Figure 5.3: Radial part of Y (left), Al (center) and O (right) basis set orbitals.

Ce, La, Ga Once the basis sets for Y, Al and O were obtained, the basis set orbitals for La and Ce were obtained using the same cubic solid structure and the same minimization procedure, but substituting the central Y atom with La or Ce and fixing the basis sets parameters obtained for Al and O in the input file (Fig. 5.4, left and center). The lattice constant used for cubic $CeAlO_3$ was the experimental one (a = 3.82 Å) [180]. For cubic $LaAlO_3$, a lattice constant of a = 3.79 Å is used, according to the experimental value of the pseudocubic cell at P=0 [181]. For Ga basis set, one Al in the corner of the cubic solid was substituted with Ga, whereas Y and O basis sets were fixed (Fig. 5.4, right). The lattice constant of this cubic solid was recalculated in the same way as in the cubic $YAlO_3$, using the relationship between ionic radii of Ga^{3+} (0.62 Å) and Al^{3+} (0.50 Å), leading to a = 4.04 Å.

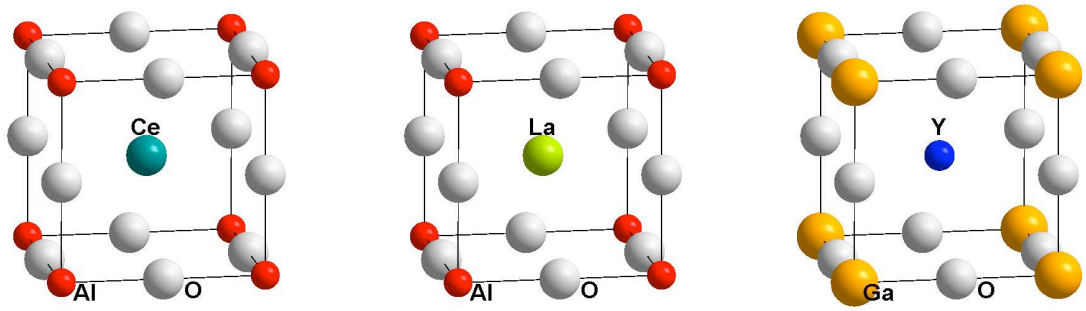

Figure 5.4: Scheme of the cubic cubic cell used to generate Ce (left), La (center)and Ga (right) basis sets.

Orbitals chosen for these atoms are:

- **La**: $5s$ $6s$ $6s'$ $5p$ $5p'$ $6p$ $5d$ $5d'$ $4f$
- **Ce**: $5s$ $6s$ $6s'$ $5p$ $5p'$ $6p$ $5d$ $5d'$ $4f$
- **Ga**: $4s$ $4s'$ $4p$ $4p'$ $4d$

The parameters obtained for the orbitals above after minimization are reflected in Table 5.2 and and such orbitals are showed on Fig. 5.5.

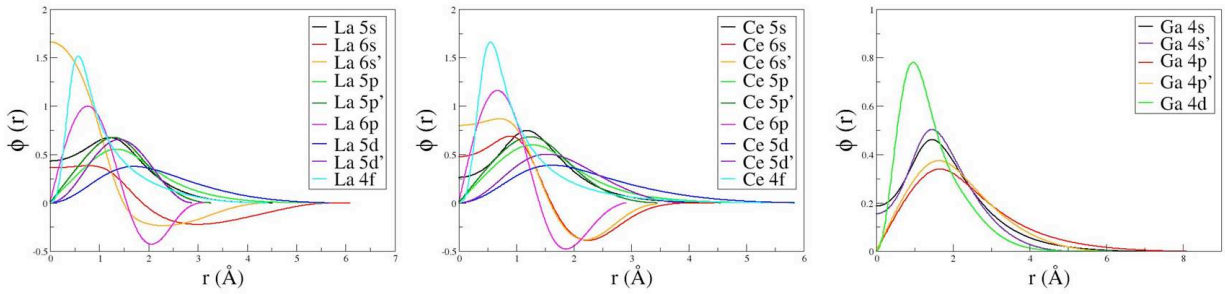

Figure 5.5: Radial part of Ce (left), La (center)and Ga (right) basis set orbitals.

5.2 Pure and perfect YAG

5.2.1 Total Energy

The total energy per unit cell of the YAG crystal is calculated for a set of values of lattice constant a both for PBE and LDA functionals, as shown in Fig. 5.6 (top). The positions of all the 160 atoms in the unit cell have been optimized without symmetry restrictions for each value of a, starting from the experimental parameters of Euler and Bruce [179] ($a_0 = 12.000$, $x = -0.0306$, $y = 0.0512$, $z = 0.1500$). Results show that the original symmetry of the crystal is kept, so that the cell at the minimum of the E *versus* a curve can be described with the structural data in Table 5.3 (YAG entry). We do obtain the same values of the equilibrium lattice constant a and internal parameters x, y, z in other calculations where both internal positions and lattice vectors are relaxed simultaneously.

Table 5.3 also includes the corresponding bulk moduli and the pressure derivatives obtained from a fitting of the Murnaghan isothermal equation of state [182] to the calculated energy and volume data.

Since agreement with experimental results (equilibrium lattice constant, internal parameters and bulk moduli) is better using PBE than LDA functional (see Table 5.3), LDA is ruled out for further calculations. With PBE, an equilibrium lattice constant of $a = 12.114$ Å is obtained, less than 1% higher than the experimental value [179]. It is within the same range of deviation than the LDA calculation of Ref. [171].

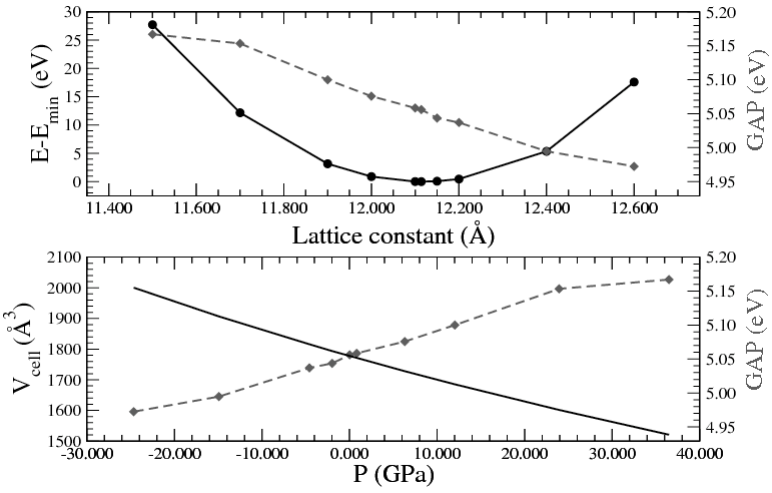

Figure 5.6: Upper graph: Calculated total energy per unit cell (full line; left axis) and band gap (dashed line; right axis) as functions of the lattice constant a. Lower graph: Calculated unit cell volume (full line, left axis) and band gap (dashed line; right axis) *versus* internal pressure.

Together with the mentioned energy *versus* lattice constant data, Fig. 5.6 (top) also shows the pattern of PBE calculated band gap *versus* lattice constant and Fig. 5.6 (bottom) shows the cell volume and gap *versus* pressure patterns. Internal pressure at each

volume (Since YAG is a cubic cell, $V_{cell} = a^3$) can be obtained as $P = -\frac{\partial E}{\partial V}$. The pressure dependence of the GAP shows a linear behavior with slope 0.0041 eV/GPa, six times smaller than the 0.025 eV/GPa reported on Ref. [171], obtained from LDA calculations and fixed internal positions of the cell.

5.2.2 Band structure

As commented in Section 2.5.1, the first Brillouin zone is a uniquely defined primitive cell in reciprocal space. The boundaries of this cell are given by planes related to points on the reciprocal lattice and it is found by the same method as the Wigner-Seitz cell in the Bravais lattice (real space). Because it depends on the $\{\vec{b}_i\}$ vectors and such $\{\vec{b}_i\}$ depend on the $\{\vec{a}_i\}$ of the real space cell (Eq. 2.42) , the symmetry of the real unit cell determines completely the symmetry of the reciprocal unit cell. Actually, each cell belonging to a given space group generates a Brillouin zone (BZ) belonging as well to any other of the 230 space groups.

YAG cell (body centered cubic, bcc) belongs to the most symmetric space group $Ia\bar{3}d$ (230) and its reciprocal lattice is a face centered cubic (fcc) cell of the $Fm\bar{3}m$ (225) space group (Fig. 5.7, left). Some special points of high symmetry of this cell are highlighted in Fig. 5.7. For YAG, we calculated the band structure from Γ(center of the BZ) to N (center of a face), from N to H (four axis vertex), from H to P (three axis vertex) and from P to Γ.

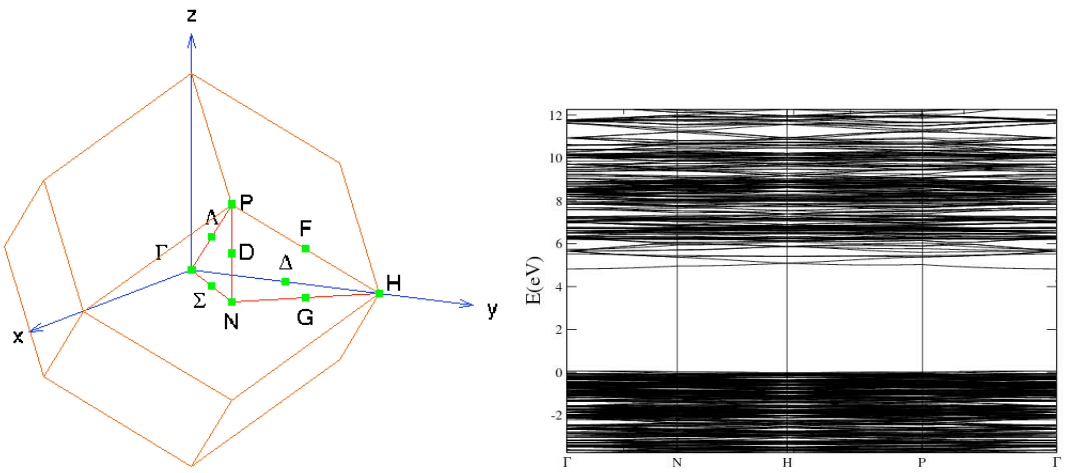

Figure 5.7: Left: $Fm\bar{3}m$ reciprocal cell of YAG. High symmetry points highlighted. Right: DFT (PBE) calculated energy bands of YAG.

Thus, the YAG band structure computed at the theoretically DFT (PBE) determined structure (Fig. 5.7, right) shows a direct band gap at Γ of 5.0 eV, corresponding to an insulator material, 22% smaller than the optical experimental value of 6.5 eV [183]. This result is within the expected deviation for a DFT GGA calculation and compares favorably with the 4.71 eV of the LDA calculation in Ref. [171] and the 1.4 eV of the TB-LMTO

calculation in Ref. [173]. As in previous calculations [171, 173], the highest valence bands have no dispersion. In contrast to the two separate bands of the conduction band (CB) edge at Γ found in Ref. [171], the CB edge seems to be made of a simple band in our calculations, with main Y($4d$+$5s$) character.

5.2.3 DOS and PDOS

Total and projected density of states (DOS/PDOS) plots obtained for YAG are shown in Fig. 5.8. Orbitals with a Y-$4p$ dominant character appear at -20 eV and those of O-$2s$ around -16 eV. The valence band (VB) extends over a 6 eV region and it is very much dominated by the O-$2p$ orbitals. The bottom of the CB is dominated by the Y-$5s$ and $4d$ orbitals, which extend over an energy region 5 eV wide. Above that, the CB has almost pure Al character, with even contributions from the octahedrally (Al_{oct}) and tetrahedrally (Al_{tet}) coordinated ones.

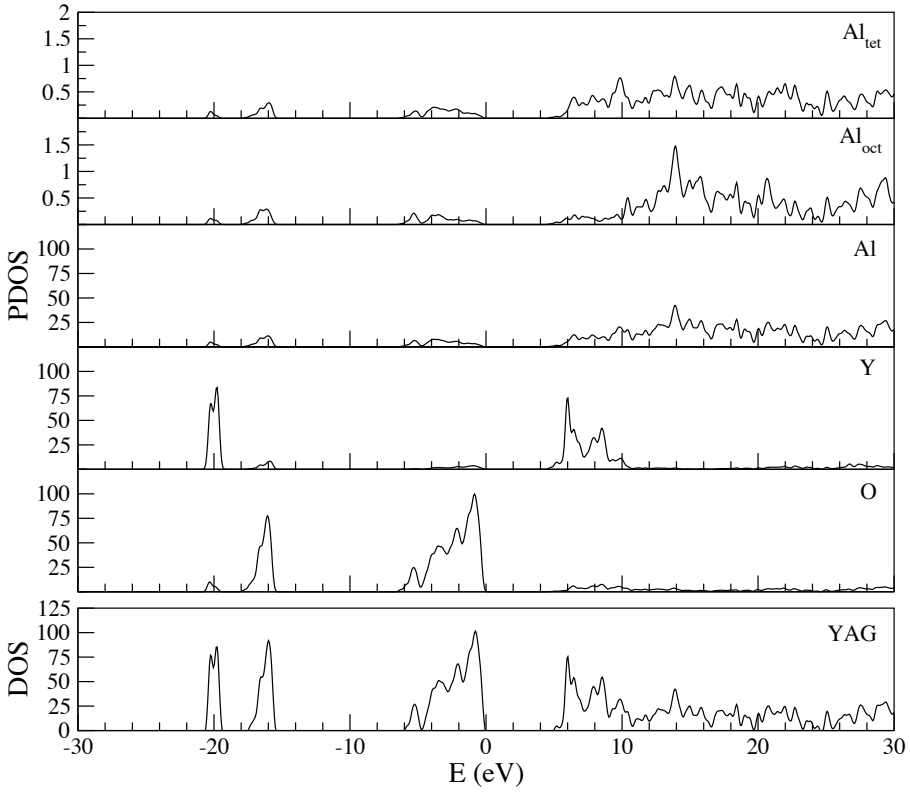

Figure 5.8: Calculated density of states (DOS) of YAG and projected density of states (PDOS) onto species Y, Al and O and onto individual octahedrally (Al_{oct}) and tetrahedrally (Al_{tet}) coordinated atoms.

Orbital projected DOS are known to be able to give a first line of interpretation of electron-loss near-edge spectroscopy (ELNES), which are available for YAG [184]. For instance, the experimental Al $L_{2,3}$ near-edge (shown in Fig. 7 of Ref [184]). is related

with the Al(s+d) PDOS (shown here in Fig. 5.9) because of the $\Delta l = \pm 1$ dipole selection rule governing the core electron excitations involved in ELNES.

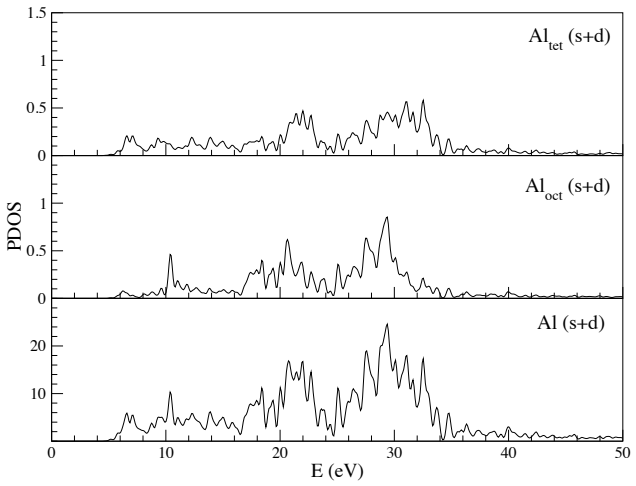

Figure 5.9: Calculated PDOS of the s and d unoccupied orbitals of all the Al in YAG unit cell, Al(s+d), and of individual Al atoms with 4 and 6 coordination index, Al$_{tet}(s+d)$ and Al$_{oct}(s+d)$.

A comparison of both shows an acceptable agreement in the significant features and a poorer agreement of the relative intensities, which depend on the relative values of the transition moments [174]. The Al $L_{2,3}$ ELNES feature A at around 8 eV can be identified here with a peak starting at 6 eV, which is almost entirely due to Al_{tet}, not shown in previous calculations [171, 184, 174]. The sharp ELNES feature B at 13 eV seems to correspond with the PDOS peak just under 11 eV, due to Al_{oct}. Features C and D between 14 and 18 eV correspond with similar features in the PDOS at almost the same energies, the second one with a marked Al_{oct} character. The E feature around 22 eV is shown here at the same energy with its initial and final parts having Al_{oct} and Al_{tet} characters respectively. The F feature cannot be clearly distinguished here. Finally, the marked G feature more than 10 eV wide peaking at 34 eV appears here shifted at lower energies (peaking at almost 30 eV) and not so wide (10 eV wide). It is preceded by a valley which shows up in the PDOS.

Similarly, the experimental Al K near-edge (shown in Fig. 9 of Ref. [184]) is related with the Al(p) PDOS (shown here in Fig. 5.10).

The ELNES features are also shown in the PDOS diagram, although with a rather systematic underestimation of the energies: The prominent C peak at 18 eV is shown in the PDOS at 14 eV, almost entirely due to Al_{oct}; the B shoulder between 12 and 14 eV corresponds with the PDOS peak at 10 eV, due to Al_{tet}; and the D shoulder between 20 and 22 eV with the 17-19 eV PDOS features and the E prominence between 26 and 28 eV with the 25-27 eV PDOS features, both of them due to both Al_{oct} and Al_{tet}.

Finally, the experimental Y $L_{2,3}$ near-edge (shown in Fig. 5 of Ref. [184]) shows a single wide peak centered at 9 eV, which corresponds with the Y(s+d) PDOS features

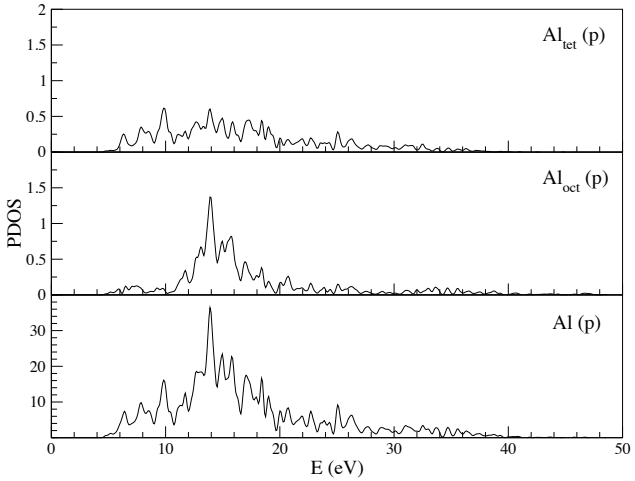

Figure 5.10: Calculated PDOS of the p unoccupied orbitals of all the Al in YAG unit cell, Al(p), and of individual Al atoms with 4 and 6 coordination index, Al$_{tet}$(p) and Al$_{oct}$(p).

(shown here in Fig. 5.11) which extend from 5 to 11 eV.

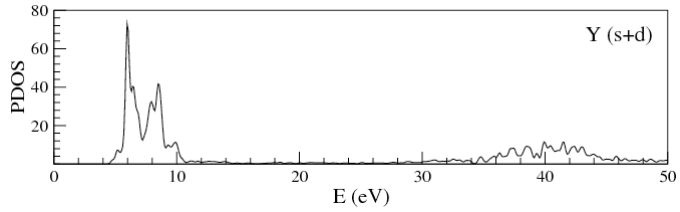

Figure 5.11: Calculated PDOS of the s and d unoccupied orbitals of all the Y in YAG unit cell.

5.3 Related crystals

The study of other species containing Y, Al and O is performed in this work using the same pseudopotentials and basis sets generated for YAG in order to test their transferability to further calculations where the chemical environment is not exactly the same, i.e. YAG not pure nor perfect anymore. Moreover, calculated energies of these species allow us to compute formation energies of YAG.

5.3.1 Structural parameters

Alumina (Al_2O_3) and yttria (Y_2O_3) are two of the most important ceramic materials. Between these two stable crystals, there are three congruently melted compounds with different Y, Al and O ratios: $Y_3Al_5O_{12}$ (YAG), $YAlO_3$ (YAP) and $Y_4Al_2O_9$ (YAM). All

they form the so-called "Y-Al-O" system. The phase diagram of this system is available [185] and discussed within the context of YAG as the most important of them, industrially speaking [186]. All three have complex structures with different local atomic coordinations. Whereas YAG presents the garnet structure shown before, YAP has an orthorhombic $GdFeO_3$-type perovskite structure [187] and the most peculiar and less studied YAM has a monoclinic structure, with nine O, four Y and two Al sites [188]. Whereas electronic structure and properties of Al_2O_3 have been quite widely studied, e.g. [189], work on Y_2O_3 is limited [190, 191, 192] and that of YAP and YAM are scarce [185, 193, 194, 195].

In order to perform a transferability test of our generated pseudopotentials and basis sets, structural data, bulk modulus and effective charges of YAP, yttria and alumina crystals (Fig. 5.12) have been calculated in parallel to those of YAG in an equivalent way, using PBE functional, relaxing all the atoms and lattice vectors of the different unit cells without symmetry restrictions and with convergence both in the fineness of real space and in k-points for Brillouin zone integration.

Results on these crystals are reflected in Table 5.3 in comparison with the available theoretical and experimental results we are aware of. An excellent agreement between experimental data and theoretical results for YAG and YAP is found. A good matching with experimental results is achieved with Y_2O_3 and Al_2O_3 lattices as well, taking into account that pseudopotentials and basis sets were obtained for a solid containing Y, Al and O and Y_2O_3 and Al_2O_3 lack of Al and Y respectively. Then, these data, together with the good agreement obtained for pure and perfect YAG, lead us to the conclusion that our pseudopotentials and basis sets are reliable enough for further calculations.

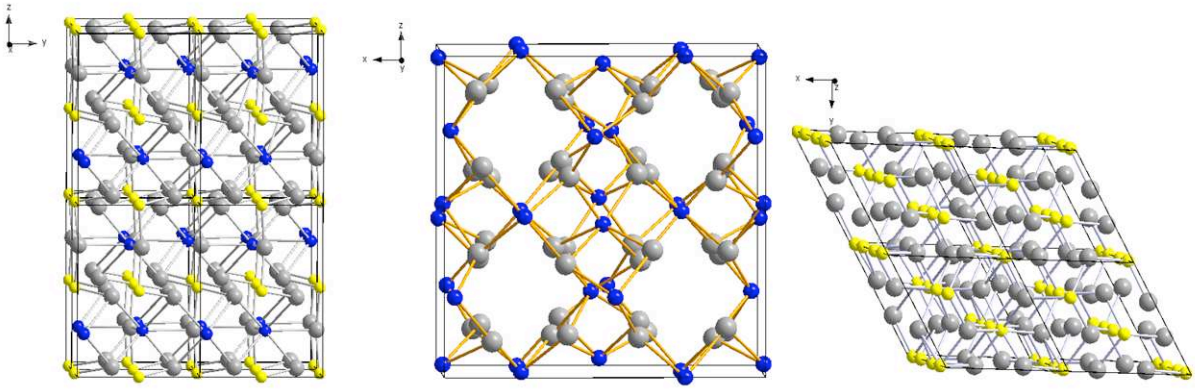

Figure 5.12: Left: $2 \times 2 \times 2$ supercell of $YAlO_3$ (YAP).Center: unit cell of Y_2O_3 (yttria). Right: $2 \times 2 \times 1$ supercell of Al_2O_3 (alumina).

5.3.2 Mulliken population analysis

Mulliken charges The calculated Mulliken effective ionic charges (Q(A) in Section 3.5.6) of each atom specie in YAG, YAP, yttria and alumina are shown in Table 5.4. The picture of the chemical bond in YAG is that of covalent interactions between Al and O, more covalent on Al_{tet} with its four surrounding oxygens (that can be considered as AlO_4 moieties) and less covalent interactions of the Al_{oct} with its six oxygens. The interactions between Y and the lattice can be considered pretty ionic. From these data, Y seems to be more ionic in YAG than in yttria, and the charges of Al and O seem to be far from the ionic limit in all crystals.

These mentioned AlO_4 moieties are distributed in the lattice connected by Y atoms along the three axis of YAG unit cell. We will see in Chapter 6 that the peculiar distortion pattern of the solid around impurities along these AlO_4-Y-AlO_4-Y directions suggests a picture of YAG as a solid containing infinite -AlO_4-Y-AlO_4-Y- *chains* interconnected by Al_{oct} cations, as shown on Fig. 5.13.

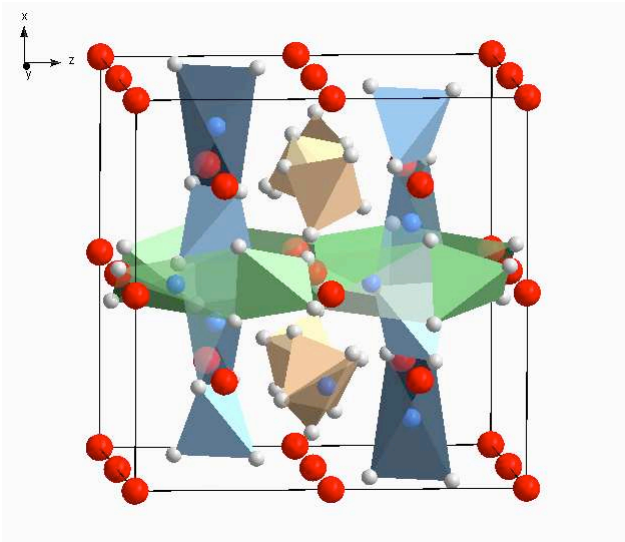

Figure 5.13: Unit cell of YAG. AlO_4 moieties (solid polyhedra) and Y atoms (translucent polyhedra) shown along x (blue), y (salmon pink) and z (green) axes. Red Al_{oct} between colored *chains* shown.

Mulliken overlap populations Calculated atomic overlap populations are 0.23 for Al_{oct}-O (at 1.948 Å) and 0.34 for Al_{tet}-O (at 1.788 Å), slightly larger than the values of α-Al_2O_3, 0.22 and 0.17, at 1.855 and 1.972 Å respectively. Overlap populations for Y-O are low, 0.02-0.03, slightly smaller than the values in Y_2O_3, of around 0.06. The O-O overlap populations are very low in all cases and sometimes negative, which means that they are not meaningful and O-O bonding interactions are not relevant in these materials according to the present calculations. Finally, the overlap populations between Y and Al are negligible, both Y-Al_{oct} and Y-Al_{tet}, so that our calculations do not support the

suggestions of Ref. [171], according to which Y and Al_{tet} may interact covalently in spite of the fact that they are both cations.

5.3.3 Reaction energies

The calculated energies per unit cell of YAG, YAP, ytrria and alumina are reflected in Table 5.5. Taking into account the number of formulae unit ($f.u.$) per cell, the energy per formula is calculated. Then, the stoichiometric coefficients (ν) of each specie involved (reactants i and products f) in reactions below are used together with such energy/formula values and the reaction energies (ΔE) are calculated from

$$\Delta E = \sum_f \nu_f (E/f.u.)_f - \sum_i \nu_i (E/f.u.)_i$$

From these data sets, the calculated formation energies corresponding to the following reactions has been calculated:

a. $3Y_2O_3 + 5Al_2O_3 \rightleftharpoons 2Y_3Al_5O_{12}$ $\Delta H = -7.39$ eV

b. $Al_2O_3 + 3YAlO_3 \rightleftharpoons Y_3Al_5O_{12}$ $\Delta H = 0.644$ eV

c. $Y_2O_3 + Al_2O_3 \rightleftharpoons 2YAlO_3$ $\Delta H = -2.89$ eV

These reaction energies coincide with reaction enthalpies at zero pressure. There are no experimental data available to check with, as far as we know. The only previous theoretical results we are aware of are the shell-model pair potential simulations of Ref. [196], which are reported to be –4.8 eV, –1.6 eV, and –0.1 eV, respectively, for reactions a, b, and c. These results have the problem that they are not consistent with the condition $\Delta H_a - 2\Delta H_b - 3\Delta H_c = 0$, which makes difficult to make direct comparisons. Our results picture YAP and YAG with a very similar energetic stability, so that their relative stability must be controlled by the entropy factor.

5.4 Conclusions

We have performed first-principles PBC-DFT (LDA and PBE) calculations on pure and perfect YAG, as well as on YAG-related crystals (YAP, yttria and corundum), using pseudopotentials and basis sets specifically generated in our own for this work. To the best of our knowledge, we perform for the first time calculations relaxing both lattice constant and internal parameters of YAG. The best agreement of lattice constant, internal positions and bulk modulus with experimental results is achieved with PBE functional, which predicts a lattice constant 1% larger than the experimental one. This supports the use of only PBE functional for further structural calculations on defects in YAG.

Calculated band structure shows an acceptable underestimation of the band gap, as expected for conventional density functionals as PBE. Calculated DOS and PDOS shows the O($2p$)-character of the top of the valence band, whereas the bottom of the conduction

band has a Y($4d + 5s$) character. The structure of the conduction band is coherent with the available ELNES experimental data.

The picture of the chemical bond in YAG given by Mulliken population analysis, is that of covalent interactions within the AlO_4 moieties, less covalent interactions between Al_{oct} and oxygens surrounding and pretty ionic interactions between Y and the lattice.

Calculations of reaction energies involving yttria, corundum, YAP and YAG, predict both YAG and YAP having similar energetic stability, so that their relative stability must be controlled by the entropy factor.

5.5 *Conclusiones*

Hemos realizado cálculos PBC-DFT (LDA y PBE) en el YAG puro y perfecto, así como en otros cristales relacionados con el YAG (YAP, yttria y corundum), usando pseudopotenciales y conjuntos de base específicamante generados por nosotros para este trabajo.

Hasta donde sabemos, realizamos por primera vez un cálculo en YAG relajando tanto las constantes de celda como las posiciones internas de los átomos. Los datos obtenidos con PBE se ajustan mejor a los datos experimentales en las constantes de celda, las posiciones internas y el módulo de volumen, dando una constante de celda 1% más alta del valor experimental. Esto apoya el uso de PBE para futuros cálculos de defectos en YAG.

La estructura de bandas calculada muestra una aceptable subestimación del gap, dentro de los valores esperables para funcionales DFT convencionales como el PBE. Las DOS y PDOS calculadas muestran que los estados más altos ocupados en YAG tienen carácter de oxígeno $2p$, mientras que los estados más bajos de la banda de conducción tienen un carácter mixto de yttrio $4d + 5s$. La estructura de la banda de conducción es coherente con los datos ELNES disponibles.

La imagen obtenida sobre el enlace en YAG mediante análisis de población de Mulliken es la de interacciones covalentes el las unidades AlO_4, interacciones menos covalentes entre Al_{oct} y sus oxígenos e interacciones bastante iónicas de Y^{3+} con la celda.

Los cálculos de energías de reacción involucrando las especies YAG, YAP, yttria y corundum predicen a YAG y YAP como compuestos de estabilidad energética similar, de modo que su estabilidad relativa debe de estar controlada por factores entrópicos.

5.6 Data tables

Table 5.1: Parameters used in pseudopotential generation (Section 3.5.1.2). (Radii in Å). *Relativistic calculation.

	Ref. configuration	XC	r_s	r_p	r_d	r_f	r_{NLCC}
Y	$5s^2 4p^6 4d^1 4f^0$	LDA	2.960	1.490	1.510	2.490	1.500
		GGA	3.000	1.500	1.500	1.500	2.500
Al	$3s^2 3p^1 3d^0 4f^0$	LDA	1.800	1.970	2.140	2.130	-
		GGA	1.800	1.974	2.139	2.129	-
O	$2s^2 2p^4 3d^0 4f^0$	LDA	1.500	1.500	2.000	2.500	-
		GGA	1.150	1.150	1.150	1.150	-
Ce*	$5s^2 5p^6 5d^0 4f^1$ (3^+)	GGA	1.650	2.200	2.600	1.200	-
La*	$5s^2 5p^6 5d^0 4f^0$ (3^+)	GGA	2.050	2.200	2.800	1.250	1.550
Ga	$4s^2 4p^1 4d^0 4f^0$	GGA	1.800	2.500	2.500	2.000	-

Table 5.2: Optimized basis set parameters (Section 3.5.2.2) for Y, Al, O, Ga, La and Ce. * The parameters of the La-6s orbital, due to an abrupt ending of the double-ζ obtained orbital, were adjusted by hand, leading to a softer tailoring of such orbital.

		r_c	r_s^l	V_0	r_i			r_c	r_s^l	V_0	r_i
Y	$5s$	3.47821	2.05846	79.07440	1.53609	La	$5s$	4.50485	-	20.58528	2.53244
	$4p$	4.95291	2.68924	39.78150	2.88605		$6s^*$	6.00000	4.30000	46.00000	4.50000
	$5p$	3.49053	-	53.65420	2.11913		$5p$	5.43122	3.21280	13.00342	2.74912
	$4d$	5.34904	2.96063	13.15813	2.36694		$6p$	3.06664	-	36.90871	2.07921
							$5d$	5.59569	2.86017	5.04181	0.74000
Al	$3s$	6.57596	4.80418	37.31483	4.78631		$4f$	4.33635	-	19.41054	2.43210
	$3p$	8.64030	6.20373	27.14427	5.95105						
	$3d$	6.11970	-	54.82308	0.02273	Ce	$5s$	4.53061	-	1.76771	2.54693
							$6s$	4.43383	3.44292	66.38287	1.93414
O	$2s$	4.76827	2.11912	64.28600	1.22481		$5p$	5.82482	3.41723	7.38791	3.46479
	$2p$	5.35605	2.03400	35.15066	2.24160		$6p$	2.91627	-	20.29418	1.16599
	$3d$	2.71415	-	21.82850	1.23314		$5d$	5.81158	3.90641	4.07520	2.86942
							$4f$	5.29589	-	8.04140	3.70444
Ga	$4s$	7.32490	5.13240	34.25696	5.21408						
	$4p$	7.99083	6.04751	4.22656	5.28631						
	$4d$	6.04861	-	49.29102	0.05232						

Table 5.3: Structural data and bulk moduli of YAG ($Y_3Al_5O_{12}$), YAP ($YAlO_3$), yttria (Y_2O_3), and alumina (α-Al_2O_3). Space groups and special positions are indicated. HF≡Hartree-Fock; TB≡TB-LTMO-LDA≡tight-binding linearized muffin-tin orbital LDA; SCAD≡self-consistent atomic deformation; PP-SM≡pair-potential shell-model.

YAG ($Y_3Al_5O_{12}$) [230 $Ia\overline{3}d$; O 96(h)]

		a(Å)	x(O)	y(O)	z(O)			B(GPa)	dB/dP
PBE	This work	12.114	-0.0306	0.0519	0.1491	PBE	This work	221.0	3.09
LDA	This work	11.691	-0.0290	0.0510	0.1499	LDA	Ref. [171]	220.7	4.12
LDA	Ref. [171]	11.904	–	–	–	PP-SM	Ref. [197]	198.0	–
Exp.	Ref. [179]	12.000	-0.0306	0.0512	0.1500	PP-SM	Ref. [198]	220.0	–
						Exp.	Ref. [199]	220.0	–
						Exp.	Ref. [200]	200.0	–
						Exp.	Ref. [201]	180.0	4.42

YAP ($YAlO_3$) [62 $Pbnm$; Y 4(c); O_I 4(c); Al 4(b); O_{II} 8(d)]

		a(Å)	b(Å)	c(Å)	b/a	c/a			B(GPa)	dB/dP
PBE	This work	5.210	5.359	7.427	1.029	1.425	PBE	This work	207.1	7.85
Exp.	Ref. [202]	5.178	5.328	7.367	1.029	1.422	GGA	Ref. [195]	188	3.82
							LDA	Ref. [185]	234	3.75
		x(Y)	y(Y)	x(O_I)	y(O_I)		TB	Ref. [194]	218.4	-
PBE	This work	-0.013	0.051	0.087	0.476		Exp.	Ref. [193]	192	7.3
Exp.	Ref. [202]	-0.010	0.053	0.086	0.475		Exp.	Ref. [203]	204.9	-
		x(O_{II})	y(O_{II})	z(O_{II})						
PBE	This work	-0.297	0.290	0.048						
Exp.	Ref. [202]	-0.297	0.293	0.044						

Yttria (Y_2O_3) [206 $Ia\overline{3}$; Y_{II} 24(d); O 18(e)]

		a(Å)	x(Y_{II})	x(O)	y(O)	z(O)			B(GPa)	dB/dP
PBE	This work	10.405	-0.034	0.393	0.152	0.379	PBE	This work	189.2	2.76
Exp.	Ref. [204]	10.607	-0.032	0.392	0.151	0.380	LDA	Ref. [205]	183	4.01
							Exp.	Ref. [206]	170	–

Alumina (α-Al_2O_3) [167 $R\overline{3}c$ (hexagonal axes); Al 12(c); O 48(e)]

		a(Å)	c(Å)	c/a	z(Al)	x(O)			B(GPa)	dB/dP
PBE	This work	4.812	13.092	2.721	0.353	0.311	PBE	This work	234.6	4.48
Exp.	Ref. [207]	4.760	12.993	2.729	0.352	0.308	LDA	Ref. [189]	242	3.24
							HF	Ref. [208]	243.8	4.305
							TB	Ref. [194]	265.8	-
							SCAD	Ref. [209]	265	-
							Exp.	Ref. [210]	254	–
							Exp.	Ref. [211]	254.4	4.275

Table 5.4: Mulliken effective ionic charge of YAG, YAP, yttria, and alumina.

	YAG	YAP	Yttria	α-Alumina
O	–0.96	–0.99 –1.00	–1.33	–0.91
Y	+2.33	+2.27	+2.01 (S_6) +1.99 (C_2)	
Al	+0.99 (oct) +0.83 (tet)	+0.72		+1.36

Table 5.5: Calculated YAG, YAP, Y_2O_3 and Al_2O_3 energies per unit cell.

	E/cell (eV)	formulae/cell	$E/f.u.$ (eV)
YAG	-71143.689862	8	-8892.961233
YAP	-9419.098289	4	-2354.774572
Y_2O_3	-46037.958429	16	-2877.372401
Al_2O_3	-10975.692671	6	-1829.282111

Chapter 6

Single substitutional defects in YAG

In this work, substitutional defects of three cations have been studied: Ce (giving rise to our parent luminescent material of study Ce:YAG), and La and Ga since they are known to red and blue shift the first $4f \rightarrow 5d$ absorption of Ce:YAG [28, 38, 39, 40]. This chapter is addressed to study the structure and the electronic structure of these single substitutional defects, as a previous step to the study of the double Ce-La and Ce-Ga defects in Chapters 9 and 10.

Ce and La in YAG do substitute an Y (c site), with local D_2 symmetry. Then, in this work, we often use the labels Ce_Y and La_Y for Ce and La defects. The nomenclature Ce:YAG and La:YAG is used for YAG doped with one atom of Ce and La per unit cell respectively. In YAG, Ga substitutes an Al atom. Since there are two different Al positions in YAG, the nomenclature Ga_{oct}:YAG and Ga_{tet}:YAG is used for YAG unit cells containing one Ga atom in octahedral (a site) or tetrahedral (d site) positions of YAG. Ce_Y substitutional defect is our reference regarding results present in Chapters 9, 10 and 11 but, since Ce_Y and La_Y are both defects occupying D_2 symmetry sites of YAG, we treat them together in Section 6.1, for a better understanding of the differences between them. On the other hand, defects involving Ga (Ga_{oct} and Ga_{tet}) are treated in Section 6.2 in a comparative way. A brief Mulliken population analysis of these materials in comparison with YAG is performed in Section 6.3. Section 6.4 states some conclusions about this chapter and Section 6.6 collects the data tables corresponding to this chapter.

In sections 6.1 and 6.2, calculated geometry around each substitutional defect introduced is analyzed, paying attention not only to the first coordination shell, which suffers the major distortion, but also to the second neighbors shell. Because of the complex crystal structure, these distortions around the defect are not easy to systematize. Thus, an attempt to show a global and intuitive picture of them is performed in this work: we split the whole distortion suffered by the atoms around the simple defect into *radial* and *perpendicular* displacements. In Fig. 6.1, it is schematically shown how *radial* displacement can tell us about the "breathing" of the surroundings where defect is introduced and how far its effect is significant. On the other hand, *perpendicular* displacement tell us about how strong is the deformation of this environment where the defect is introduced. The angle Θ gives us an idea of the latter as well.

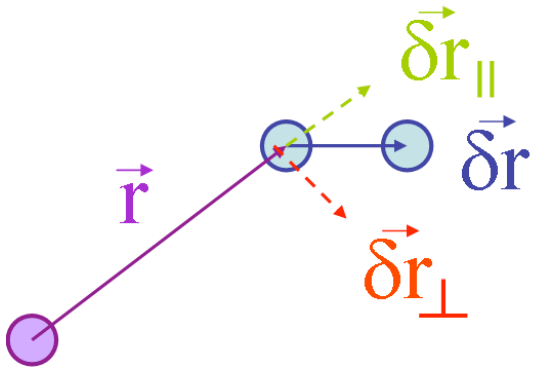

Figure 6.1: Some parameters involved in the displacement of a given atom (blue sphere) with respect to the substituted position (purple sphere).

A complete description of these distortions should include the value of another angle giving us the rotation of the displaced atoms around direction $\vec{r}$ and, then, an additional reference framework should be necessary. It is far from the aims of this chapter, focused on giving a visual picture of the distortions, and then, $\delta r_{\parallel}$, $\delta r_{\perp}$ and Θ are given as parameters measuring the strength and general features of the deformations.

It is important to mention that the validity of this simplified description is based in the fact that the doping atom (Ce, La, Ga) occupies the same place as the original Y or Al, staying on-center after relaxation. Then, this position (purple atom in Fig. 6.1) can be taken as a reference. Moreover, calculations show that all the equivalent atoms around the substituted atom behave in the same way, that is, according to its point symmetry with respect to the reference atom, and can be considered as a single class of atom. Otherwise, it would become necessary a set of geometrical parameters for each individual atom and the data given here would not make sense by themselves. These approaches are useful in these single substitutional defects, but we cannot use them when the defects are not punctual anymore and do not constitute themselves a symmetry center (antisite defects, codoped YAG and Ce:YAG considering antisite defects).

6.1 Ce^{3+} and La^{3+}

6.1.1 Structural information

Single substitutional defects studied in this section come from substitution of one Y cation per YAG unit cell by Ce or La, that is Ce:YAG, $Y_{2.875}Ce_{0.125}Al_5O_{12}$, and La:YAG, $Y_{2.875}La_{0.125}Al_5O_{12}$. Once substitution is done, all the 160 atoms of the unit cell are relaxed without symmetry restrictions under a conjugate gradients scheme. Preliminary calculations show the tendency of all the introduced cations to enlarge their distances with surrounding atoms. Then, a first series of calculations was performed in order to predict the validity of the calculated lattice constant for pure YAG or the necessity of a YAG

cell with a significantly bigger lattice constant. Plots of energy *versus* lattice constant a (each point including relaxed internal structure) are in Fig. 6.2.

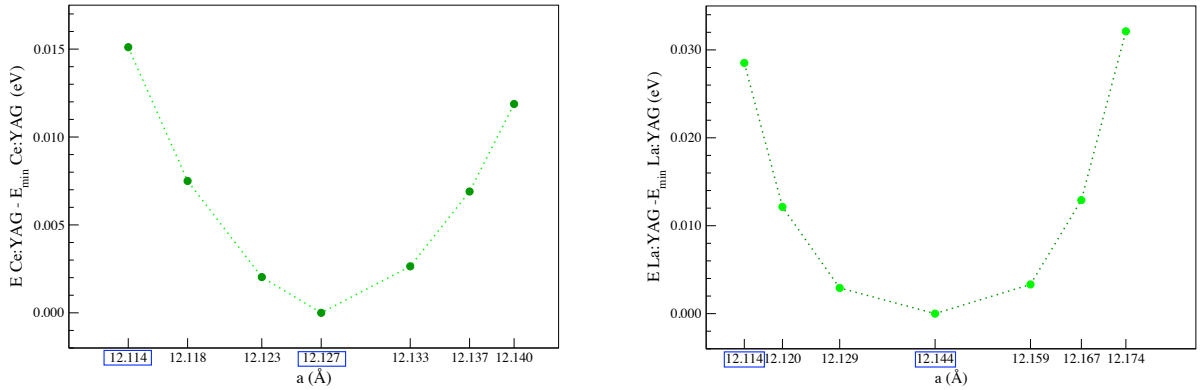

Figure 6.2: Left: PBE calculated total energy as a function of lattice constant of Ce:YAG. One Ce per cell. Right: PBE calculated total energy as a function of lattice constant of La:YAG. One La per cell.

These single defects correspond to a substitution of one atom of the 24 Y equivalent positions, that is, our concentration of defects is ∼4%. With this concentration, lattice constant of Ce:YAG increases from the pure YAG value of 12.114 Å to 12.127 Å (+0.11%) and lattice constant of La:YAG increases from 12.114 Å to 12.144 Å (+0.25%). Due to even the highest increment is small enough, we have considered them negligible and we use as starting point for our substitutions the calculated cell of pure YAG, i.e. $a = 12.114$ Å and corresponding oxygen parameters.

Local environment, including first and second coordination shells, around D_2 YAG sites is shown in Fig. 6.3. Such M position is occupied by Y, Ce or La atom in pure YAG, Ce:YAG and La:YAG respectively. First coordination shell includes eight oxygen atoms, four of them at shorter distances to M connecting M with two Al_{tet} along a given axis (labeled as O_s in Fig. 6.3) and four at longer distances (labelled as O_l in Fig. 6.3). Second coordination shell includes four Al_{oct}, four Y, the two mentioned Al_{tet} along the axis (Al^1_{tet}) and four different Al_{tet} (Al^2_{tet}) atoms. Only two of the four Al_{oct} and Y, and only one of the four Al^2_{tet} are shown in Fig. 6.3 for clarity.

Distortion parameters according to Fig. 6.1 when M=Ce and M=La are reflected in Table 6.1 according to labels on Fig. 6.3, where subindexes "a", "b", etc, are included only for convenience in order to define the α angles within the cluster.

Only first shell and second shell data have been included in Table 6.1 since, beyond that, no significant distortion is observed. Quantitatively speaking, a $\delta r \geq 0.005$ Å has been chosen as the threshold in order to considerate significant distortions.

As expected, a major distortion is produced on the first shell of oxygens around M. Distortions produced by La are larger than those produced by Ce, as expected for the the larger ionic radius of La. From data of the two different kinds of oxygens around M, it is observed that the bonds involving O_s and O_l become larger in the same proportion

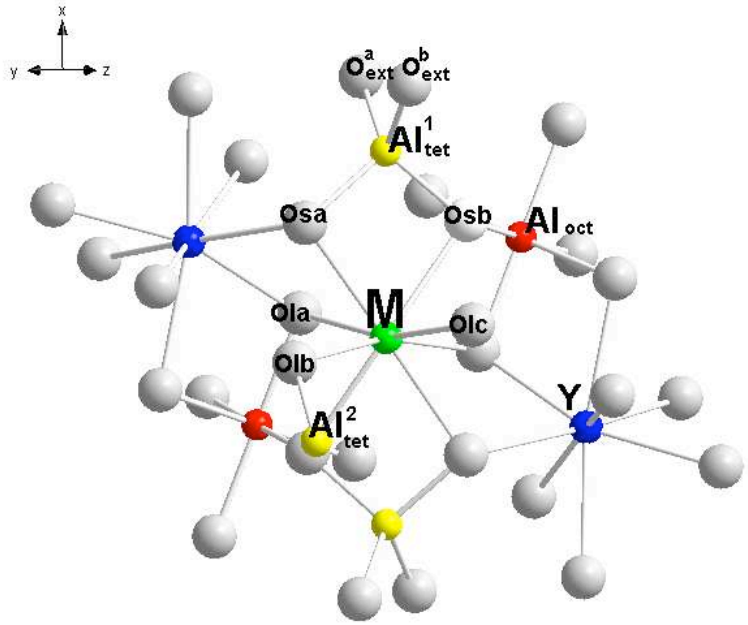

Figure 6.3: Local environment of a (c) site of YAG. M=Y, Ce or La in pure YAG, Ce:YAG and La:YAG respectively. Complete first coordination shell, partial second coordination shell and selected atoms of the third coordination shell shown.

in La:YAG, whereas the enlargement experimented by Ce-O_s/Ce-O_l bonds with respect to the original distances follows a 2/1 ratio. The radial displacement of oxygens is much higher than the perpendicular one for M=Ce and the magnitude of perpendicular displacement increases for M=La, since its effects are higher and oxygens cannot breath out freely. Even if we have not imposed symmetry, local D_2 symmetry is retained upon both substitutions and Ce-O_s and Ce-O_l computed distances are in a good agreement with those obtained in Ref. [41] by means of embedded cluster calculations, in spite of the big differences between the two methods.

The analysis of the cations of the second coordination shell is very interesting. The first observation is the decrease of displacement values. However, since the distortion induced by La is bigger, its effects are more present in the second neighbors shell than in Ce case. $\delta r_{\parallel}$ is greater than $\delta r_{\perp}$ as well, as seen from Al_{oct} and Y data. Moreover, the case of Al^1_{tet} show an interesting feature: as seen in Fig. 6.3, two Al^1_{tet} and M are placed on an axis direction (x axis in this picture) and displacements of those Al^1_{tet} are exclusively radial, i.e. they only have $\delta r_{\parallel}$. This $\delta r_{\parallel}$ is longer if M=La and, even in this case, they do not suffer from the $\delta r_{\perp}$ suffered by the O_s (between M and Al^1_{tet}). At this point, the question is whether the AlO_4 moiety (involving Al^1_{tet}, two O_{ext} and two short oxygens O_s, as shown in Fig. 6.3) moves as a unity when Ce or La enter the cavity or not. The first clue about that is, as said above, oxygens belonging to the third coordination shell (O_{ext}) only move $\sim$ mÅ. Then, a internal distortion within the AlO_4 moiety is a

reasonable guess. Data of Table 6.2 confirm such internal distortion: when M=Ce, the Al^1_{tet}-O_s bonds suffer a light enlargement, and, as a consequence, the other two Al^1_{tet}-O_{ext} bonds in the moiety contract, remaining the distance M-O_{ext} practically unchanged. Even when the distortions are bigger, as in M=La, such distance M-O_{ext} scarcely changes. In this case, both d(Al_{tet}-O_{ext}) and d(Al_{tet}-O_s) become smaller than in YAG, cushioning the presence of La far away from this cavity.

All these data reveal the particular behavior of the distortions patterns around M=Ce_Y, La_Y impurities along the ...-AlO_4-M-AlO_4-Y-... axis: distortion along this axis is preferred since it is cushioned by the flexible AlO_4 moieties. Such flexibility arises from the angular stress that the AlO_4 moieties do suffer in YAG sharing oxygen atoms with Y and presenting then angles smaller than the tetrahedral ones. Thus, a radial displacement of O_s upon substitution by bigger cations as Ce or La, releases part of this angular stress and allows involved Al_{tet} to have more sp^3 character. Actually, last entry of Table 6.2 shows how the O_{sa}-Al_{tet}-O_{sb} angle changes from $\sim$ 100° in YAG to higher values closer to the ideal tetrahedral angle upon Ce and La substitutions.

Then, on the one hand, it is reasonable to picture YAG as a solid containing *chains* along these axis as depicted in Fig. 5.13 and, on the other hand, when considering M=Ce, the structure formed by the CeO_8 moiety plus the two adjacent AlO_2 moieties along such axis is a reasonable cluster choice for our further embedded cluster calculations of Ce:YAG spectra.

Angles around oxygen In YAG, each oxygen is connected with two Y atoms, one Al_{tet} and one Al_{oct} (Fig. 6.4).

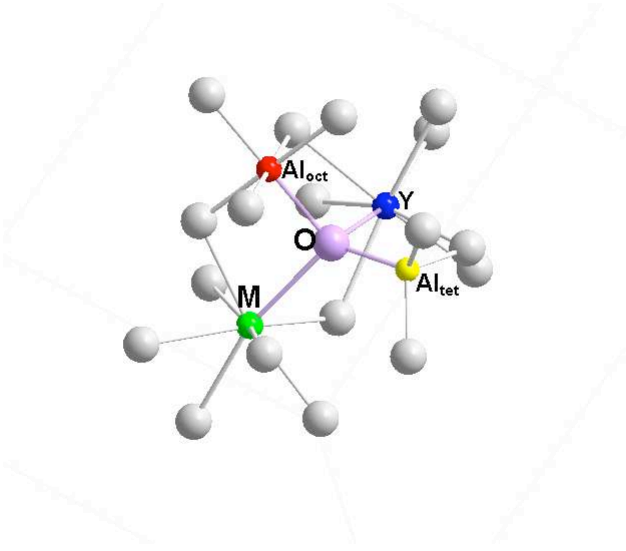

Figure 6.4: Tetrahedrally coordinated oxygen (lilac) and M=Y, Ce or La in pure YAG, Ce:YAG and La:YAG respectively.

In order to measure how far is it from a hypothetical tetrahedral *sp*3 hybridization, the angles of such pseudotetrahedron have been measured, not only when M=Y (YAG)

but also when M=Ce, La. Results are in Table 6.3. These angles in YAG show again the angular stress involving the Al_{tet} of the -AlO_4-Y-AlO_4-Y- *chain*: the M-O-Al_{tet} angle for M=Y is also significantly lower than the 109.5° of a tetrahedron and the other two angles involving Al_{tet} (Al_{tet}-O-Al_{oct} and Al_{tet}-O-Al) are larger than the ideal tetrahedron ones, whereas the other angles not involving Al_{tet} are very close to the ideal value. Substitution of Y for larger ions (La above all) releases as well part of the angular stress of the M-O-Al_{tet} angle. All other angles suffer much less pronounced changes.

La and Ce pseudopotential and basis sets transferability tests: $LaAlO_3$ and La_2O_3 As for Y, Al and O, transferability test have been performed for La and Ce pseudopotentials and basis sets generated (Section 5.1), using them in PBE calculations on other solids involving these atoms and oxygen, as their first coordination shell in YAG. Thus, lattice constants and internal parameters were obtained for low temperature $LaAlO_3$ and two polymorphic forms of La_2O_3 (Fig. 6.5), in good agreement with experimental and other theoretical results (Table 6.4).

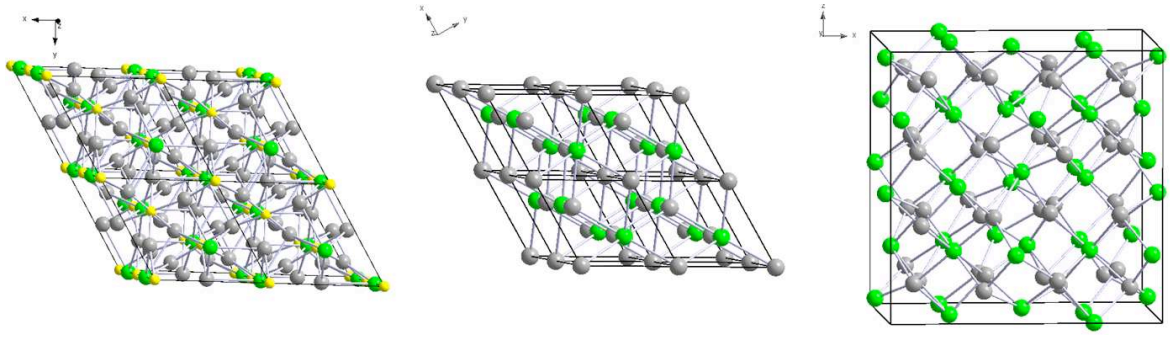

Figure 6.5: Left: $LaAlO_3$ ($2 \times 2 \times 1$ supercell). Center: hexagonal La_2O_3 ($2 \times 2 \times 1$ supercell). Right: cubic La_2O_3 unit cell.

Unfortunately, some fruitless calculations were performed in $CeAlO_3$ [212], due to the intrinsic difficulties arising both to general convergence of calculations where Ce is present and to the antiferromagnetic character of this structure, that lead us to an extra and deeper effort far away from the aims of this work. Then, reliability of La pseudopotentials and basis set are endorsed by results on these solids and that of Ce pseudopotentials comes from the good agreement between our calculations and calculation in Ref. [41] regarding the CeO_8 predicted structure.

6.1.2 Electronic structure

Fig. 6.6 shows the band structure of La:YAG and Ce:YAG. That of La:YAG does not present any visible significant change, neither on shape or dispersion, with respect to pure YAG band structure. On the contrary, a new occupied band appears in Ce:YAG clearly differentiated from the top of pure YAG valence band.

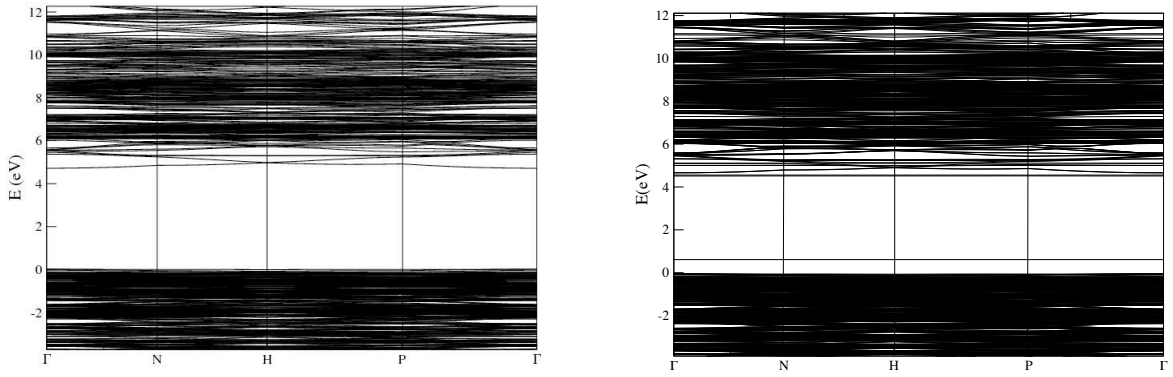

Figure 6.6: Left: La:YAG band structure. Right: Ce:YAG band structure.

Both the role, if any, of La in YAG electronic structure and this interesting new feature of Ce:YAG band structure can be discussed in terms of La:YAG and Ce:YAG DOS and PDOS, plotted in Figs. 6.7 and 6.8.

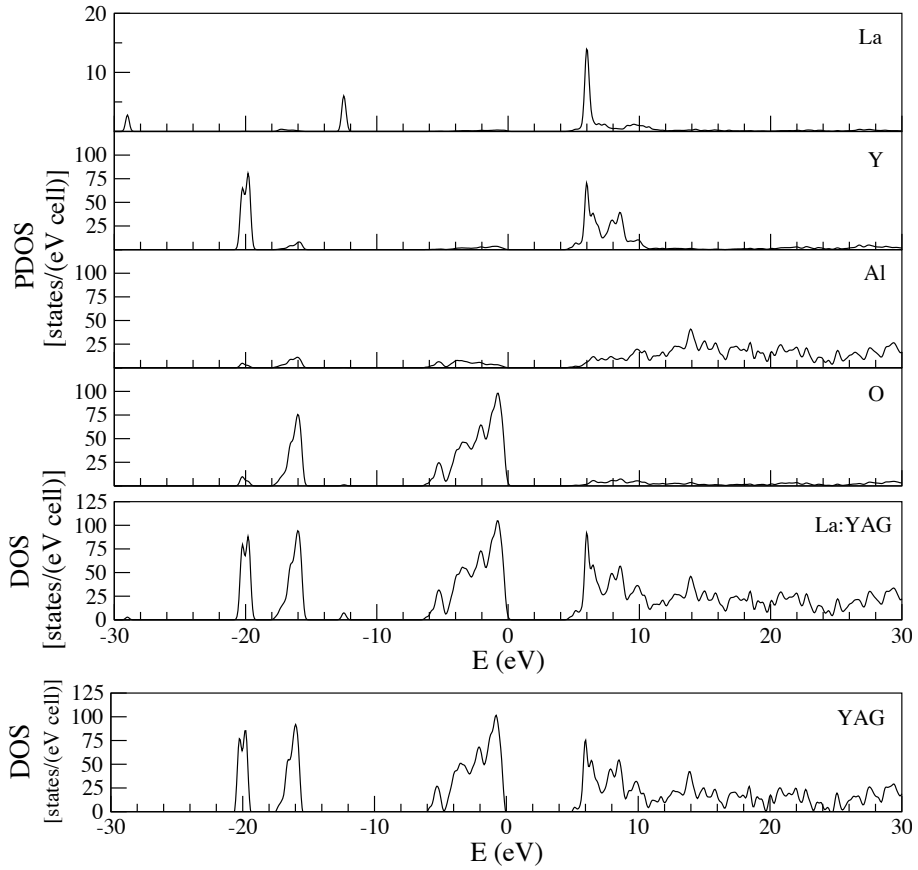

Figure 6.7: Top: DOS and PDOS of La:YAG (one La atom/cell). Bottom: YAG DOS.

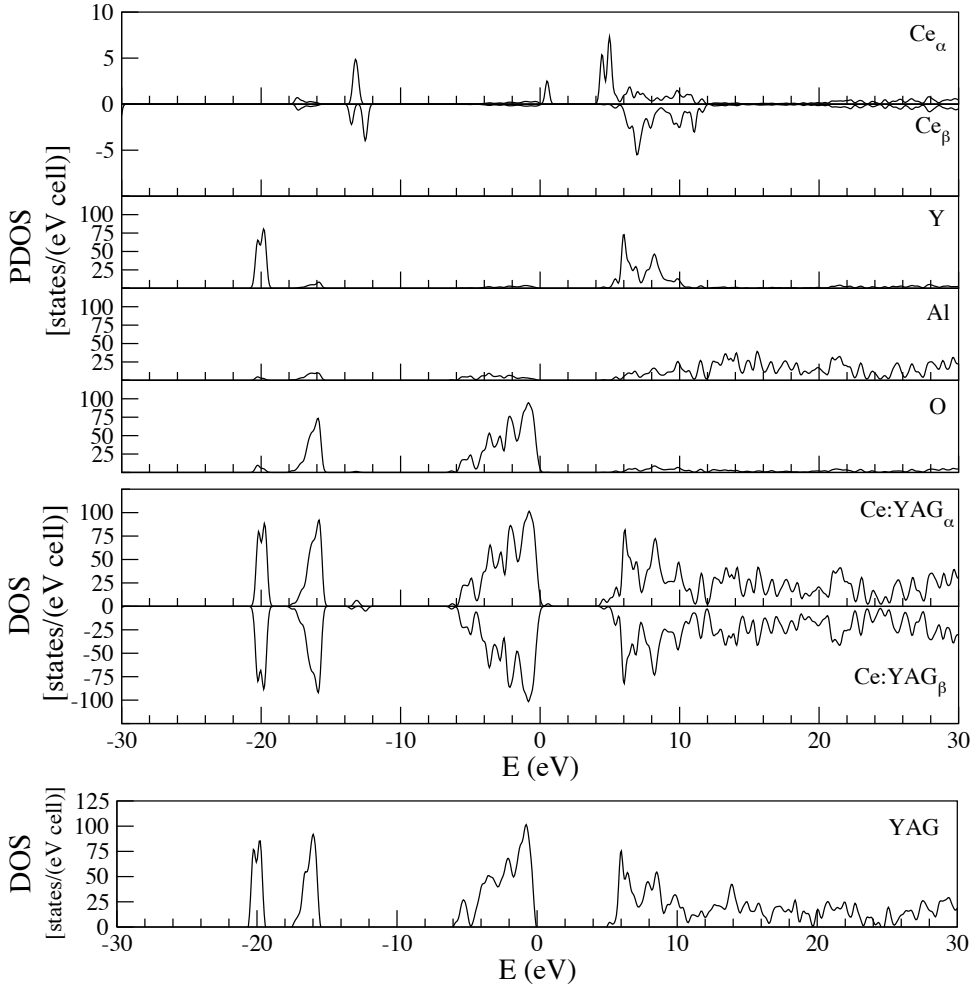

Figure 6.8: Top: DOS and PDOS of Ce:YAG (one Ce atom/cell), α and β spins. Bottom: YAG DOS.

From these pictures, it can be said that La atom does not substantially affect YAG electronic structure, although local geometries are altered. La introduces new occupied states around -13 eV (without affecting the gap) and some unoccupied states (around +6 eV) in the same region of unoccupied Y states.

More interesting results are found in Ce:YAG PDOS (Figs. 6.8 and 6.9).

Despite the geometrical distortion induced by Ce is smaller than the one produced by La, Ce influence on electronic structure is crucial because new α states appear above the oxygen ones in the top of YAG valence band (Fig. 6.8). Projection over Ce orbitals (Fig. 6.9, top) reveals the $4f$ character of these new α states. Moreover, Ce provides states in the lowest unoccupied zone (of main Y character in YAG), of mixed $4f$ and $5d$ character, presenting two prominent $4f$ peaks at 4.25 and 4.75 eV (Fig. 6.9, center). The difference between these occupied and empty states of the Ce impurity is 2.63 eV. Even if the presence of these states will be important in excitations and, thus, in luminescence of Ce:YAG, this value is not to be compared with the lowest $4f \rightarrow 5d$ transitions in

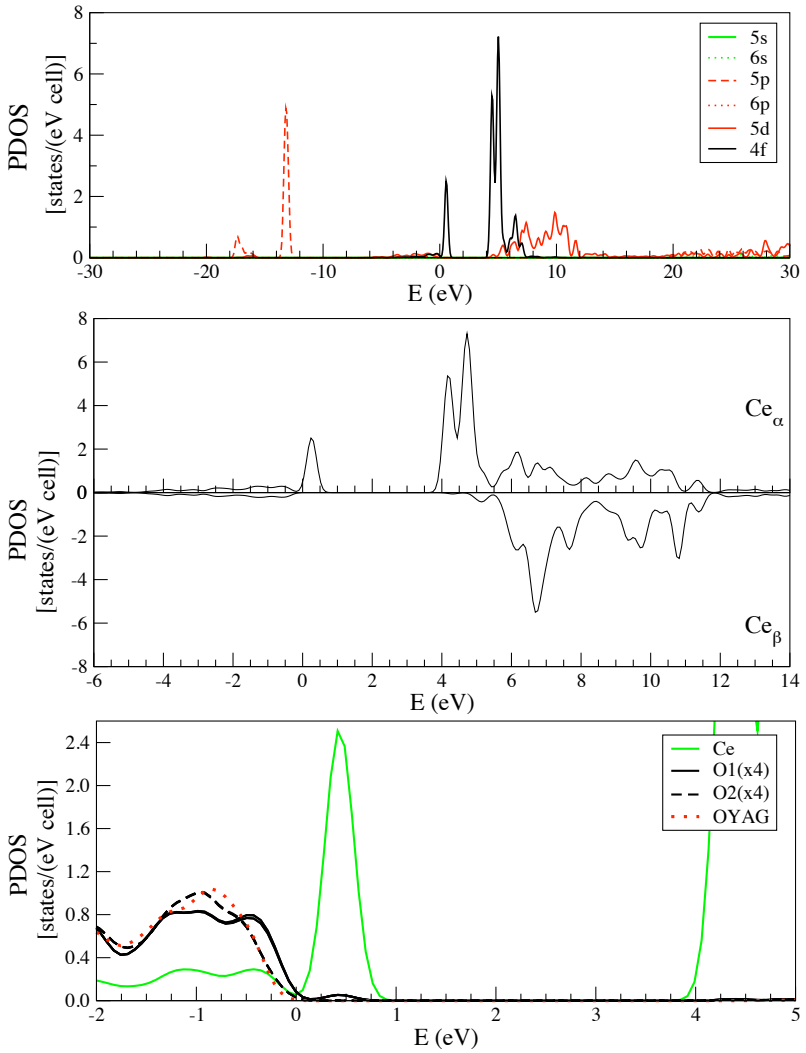

Figure 6.9: Top: α PDOS Ce:YAG on valence orbitals. Center: zoom over the gap zone of the Ce α and β spins. Bottom: PDOS on Ce, one type-s oxygen atom and one type-l oxygen atom.

Ce:YAG, which are in fact much less energetic [41], because changes in the occupancies of the empty shells would make the DOS and PDOS change very much. We can observe the different effect of the Ce impurity on the two kinds of oxygens of the first coordination shell in Fig. 6.9 (bottom). Oxygens of type l (O2 in Fig. 6.9) remain almost intact with respect to regular oxygen atoms in YAG. However, PDOS of short-type oxygens (O1 in Fig. 6.9, those forming the Y-AlO_4-Y-AlO_4 *chain*) rise in energy, indicating a significant interaction between Ce-4f atomic orbitals and 2p orbitals of these atoms.

6.1.3 Energetic balances

Formation energies The energies for replacing an Y^{3+} ion by a Ce^{3+} and a La^{3+} ion are 0.113 eV (11 kJ/mol) and 3.710 eV (358 kJ/mol) respectively, which refer to the processes

$$8\ Y_3Al_5O_{12} + M^{3+}_{\text{vacuum}} \rightarrow 8\ Y_{2.875}M_{0.125}Al_5O_{12} + Y^{3+}_{\text{vacuum}}$$

with M being Ce and La, respectively. These defect formation energies are small, the Ce one being smaller than that of La. Both of them are much smaller than the equivalent ones of Ca-substitutional and Mg-substitutional defects, which amount around 20 eV per defect as calculated in empirical shell-model simulations in Ref. [213].

Stress energies We have seen that the overall distortion created by La_Y in YAG is larger than the one created by Ce_Y. This is also shown by the stress energies of each material, E_{stress}, defined as the difference between the energies per unit cell of the doped material with the fixed original structure of the host (YAG) and with the fully relaxed structure. These E_{stress} are 323 meV/defect (31.2 kJ/mol) for La:YAG and 125 meV/defect (12.1 kJ/mol) for Ce:YAG, according to the bigger size of La.

6.2 Ga^{3+}_{oct} and Ga^{3+}_{tet}

6.2.1 Structural information

Single defects of Ga appear when it substitutes an Al atom. Since YAG has two lattice positions occupied by Al (Al_{oct} and Al_{tet}), Ga can generate Ga_{oct}:YAG and Ga_{tet}:YAG defects. In Ga_{oct}:YAG, Ga substitutes one of the 16 Al_{oct} atoms of the unit cell, leading to a concentration of defect ∼6%. In Ga_{tet}:YAG, one out of 24 Al_{tet} atoms is substituted, giving a defect concentration of ∼4%. Plots of energy *versus* lattice constant are in Fig. 6.10, from where it can be seen that equilibrium lattice constants for both Ga_{oct}:YAG and Ga_{tet}:YAG increase from 12.114 Å to 12.134 Å (+0.16%) with respect to pure YAG.

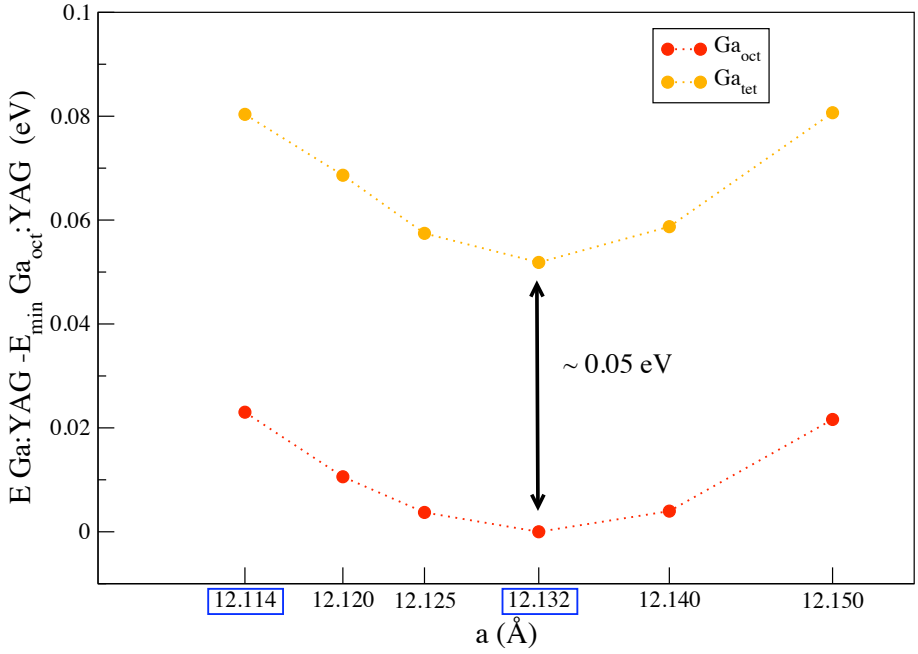

Figure 6.10: PBE calculated total energy as a function of lattice constant of Ga_{oct}:YAG (red line) and Ga_{tet}:YAG (orange line). One Ga atom per cell.

Fig. 6.10 also contains information about the relative stability of Ga_{oct} and Ga_{tet} defects. Since atoms involved in substitution are exactly the same, the energies of Ga_{oct}:YAG and Ga_{tet}:YAG can be directly compared. Not only in the minimum of energy, but also all along the curve, the Ga_{oct} defect is around 50 meV (4.8 kJ/mol) more stable than the Ga_{tet} one.

Local geometries around YAG (*a*) symmetry sites (octahedral B position) and (*d*) symmetry sites (tetrahedral T position) are shown in Fig. 6.11. All the six (or all the four) oxygen atoms around a B (or T) position in YAG are equivalent and we use the labels "a", "b", "c" and "d" in Fig. 6.11 only for convenience when describing angles involving these atoms.

Table 6.5 (upper chart) shows that displacements caused by Ga_{oct} are larger than those

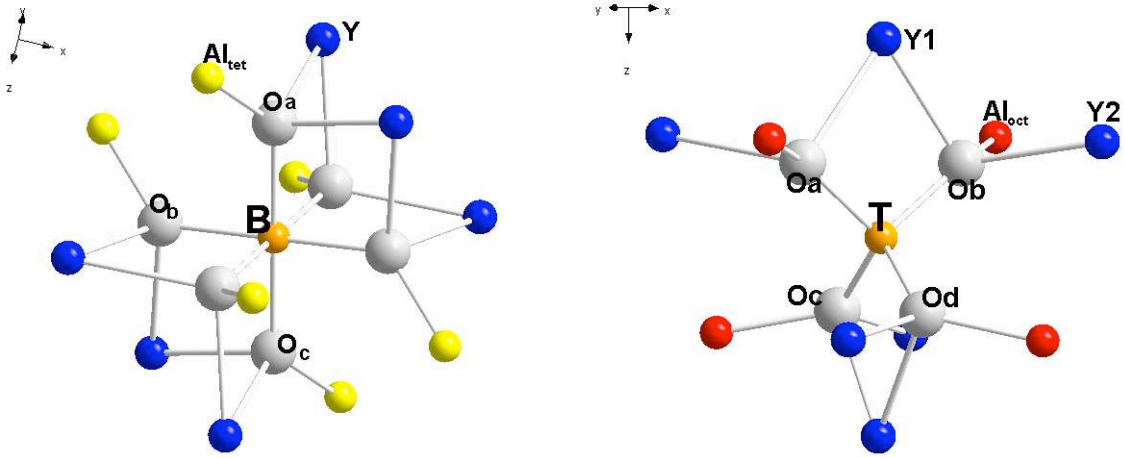

Figure 6.11: Left: local environment of an (a) site of YAG. B=Al or Ga in pure YAG and Ga_{oct}:YAG respectively. Right: local environment of a (d) site of YAG. T=Al or Ga in pure YAG and Ga_{tet}:YAG respectively.

produced by La or Ce, not only in absolute value but also with respect to the original distances, since the original Al_{oct}-O bonds were shorter than any of the Y-O ones. Local symmetry is maintained around Ga_{oct}, as it can be seen from the α values. As expected, distortions on the first coordination shell are larger than distortions on the second one and radial displacements are larger than lateral ones.

Regarding Ga_{tet}:YAG, from data in Table 6.5 (bottom chart), it can be said that, among the studied cases in this work, Ga_{tet} stamps the major local distortion in YAG. The original Al_{tet}-O bond increases $\sim$ 8% when substituted by Ga but angles do not change at all, so that the local symmetry is also retained. As in La and Ce-doped YAG, displacements in atoms along the -AlO_4-Y-GaO_4-Y-AlO_4- direction are mainly radial. This supports the idea that the AlO_4 moieties tightly bonded to Y atoms to form -Y-AlO_4-Y-AlO_4- *chains* are flexible enough so as to cushion out distortions in and beyond the third coordination shell of a given defect.

Angles around oxygen As said before, in YAG, each oxygen is connected with two Y atoms, one Al_{tet} and one Al_{oct}. The angles around it have been calculated when Al is substituted by Ga_{oct} position (B=Ga) or in Ga_{tet} position (T=Ga) (Fig. 6.12). Results are on Table 6.6.

The Y^1-O-Al_{tet} angle is not affected significantly for the presence of a Ga in Al_{oct} place (B=Ga) but, when such Al_{tet} is substituted by Ga (T=Ga), there is even a reduction of the angle with respect to YAG and with respect to the ideal tetrahedron angle. Then, the structure become even more constrained. The other two angle values involving T position remain unchanged with respect to those of YAG.

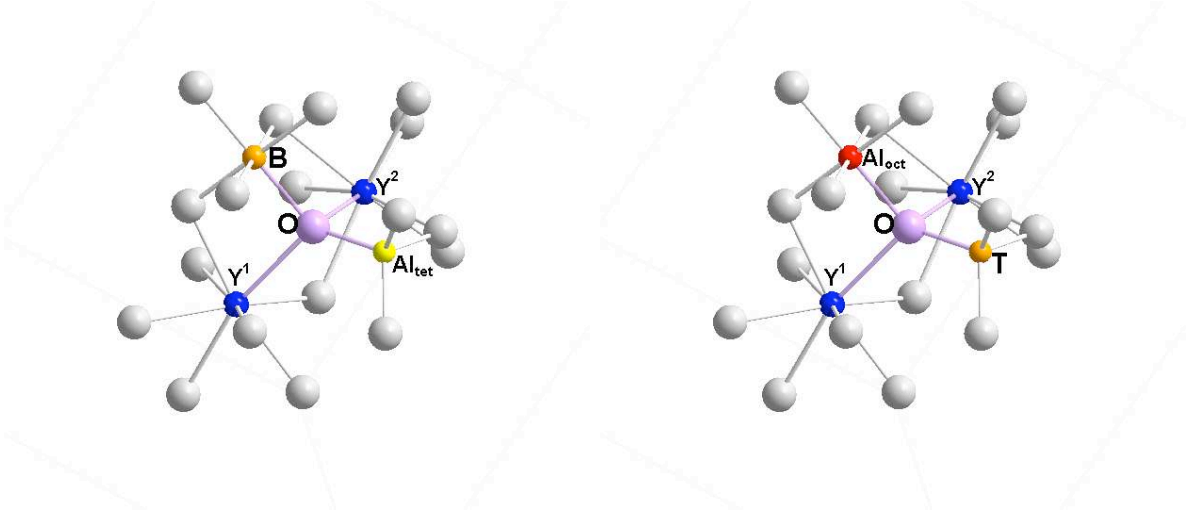

Figure 6.12: Four coordinated oxygen, (h) positions in YAG. Left: B=Al_{oct}(YAG) or Ga_{oct} (Ga_{oct}:YAG). Right: T=Al_{tet}(YAG) or Ga_{tet} (Ga_{tet}:YAG)

6.2.2 Electronic structure

Band structures of Ga_{oct}:YAG and Ga_{tet}:YAG are shown in Fig. 6.13.

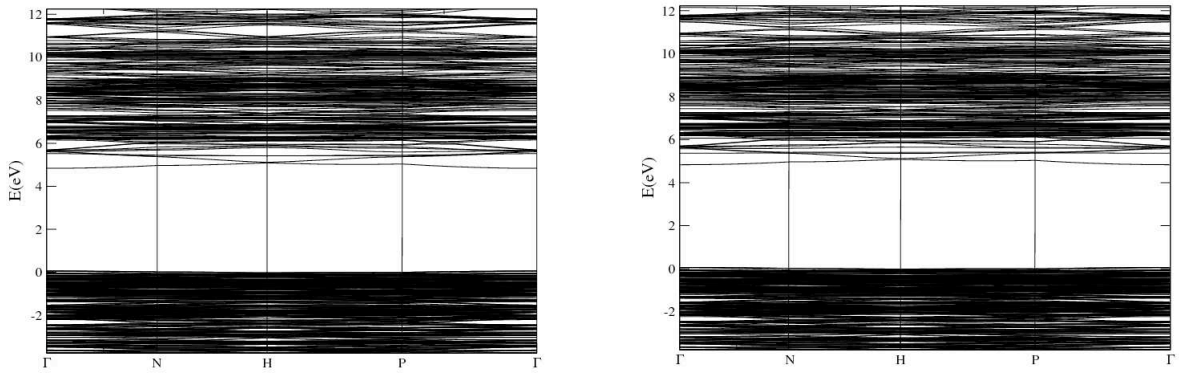

Figure 6.13: Left: Ga_{oct}:YAG band structure. Right: Ga_{tet}:YAG band structure.

At this scale, they do not present any particularity with respect to pure YAG band structure. A detailed analysis of DOS and PDOS of Ga_{oct}:YAG and Ga_{tet}:YAG (Figs. 6.14) shows that no states appear at new energies since Ga_{oct} and Ga_{tet} profiles are completely analogous to former Al_{oct} and Al_{tet} ones.

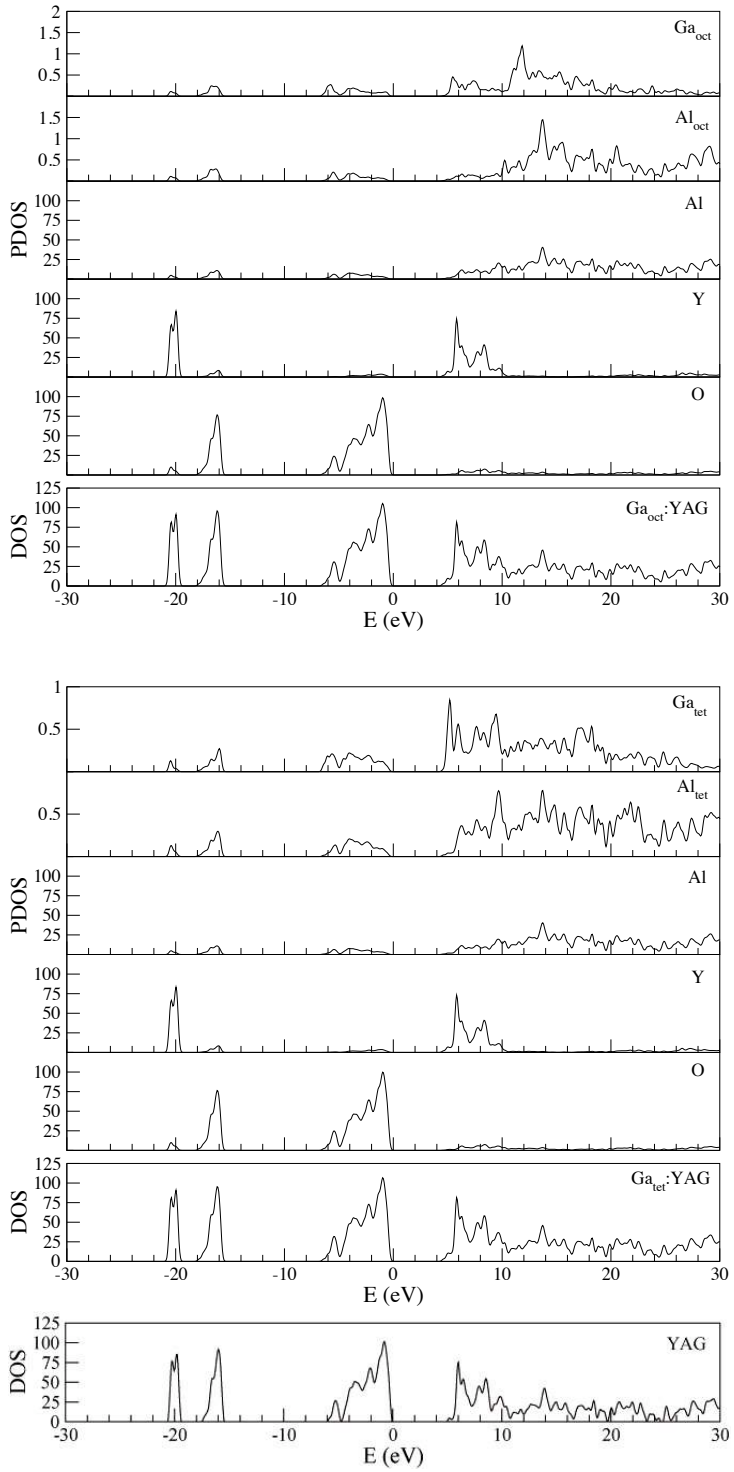

Figure 6.14: Top: TOTAL DOS and PDOS of Ga_{oct}:YAG and Ga_{tet}:YAG (one Ga atom/cell). Bottom: YAG DOS.

6.2.3 Energetic balances

Formation energies The formation energies of Ga_{oct} and Ga_{tet} single substitutional defects at low concentrations according to the processes

$$8\ Y_3Al_5O_{12} + Ga^{3+}_{vacuum} \rightarrow 8Y_3Al^{oct}_{1.875}Ga^{oct}_{0.125}Al^{tet}_{3}O_{12} + Al^{3+}_{vacuum}$$

and

$$8\ Y_3Al_5O_{12} + Ga^{3+}_{vacuum} \rightarrow 8\ Y_3Al^{oct}_{2}Al^{tet}_{2.875}Ga^{tet}_{0.125}O_{12} + Al^{3+}_{vacuum}$$

are 1.062 eV/defect (102.5 kJ/mol) and 1.105 eV/defect (106.6 kJ/mol) respectively, which means that substitution in an Al_{oct} site is more favorable than in an Al_{tet} site by 43 meV/defect (4.1 kJ/mol). As we have seen in Fig. 6.10, this quantity only slightly changes to 50 meV/defect when the lattice constant is optimized for each defect. This result means that, at low concentrations, the formation of Ga_{oct} defects is only slightly preferred over the formation of Ga_{tet} defects. However, this little difference does not support the common assumption that, at concentrations between 10 and 80 at.%, substitutions at octahedral sites are clearly made before substitutions at tetrahedral sites [39, 40]. This assumption is based in part in the fact that Ce luminescence shows a monotonously increasing blue shift between 10 and 40 at.% of Ga_{Al} (40 at.% is the concentration of Al_{oct} sites in YAG), whereas it shows a negligible shift above this concentration and up to 80 at.% [39].

Stress energies The pattern of formation energies mentioned above is closely related to the stress energies of Ga-doped YAG cells, due to the big size of the Ga^{3+} ion. In this respect, it is interesting to observe that, according to the present calculations, substitution of Al_{oct} in a *rigid*, unrelaxed YAG lattice is clearly preferred, since it is 633 meV/defect (61 kJ/mol) more favorable than substitution of Al_{tet}. However, as said before, if both defects can relax freely, Ga_{oct} is only 43 meV more favorable than Ga_{tet} after relaxation . That means that the stress energy (the stabilization energy gained by structure relaxation) is much larger in Ga_{tet} than in Ga_{oct} by 590 meV/defect ($E_{stress}(Ga_{oct})$=600 meV/defect, $E_{stress}(Ga_{tet})$=1190 meV/defect). So, the emerging picture is one in which Ga_{Al} substitutions at octahedral sites are only slightly preferred over substitutions at tetrahedral sites under no relaxation constraints, although any hindering of relaxation strongly favors the formation of the octahedral substitutional defects. Since increasing defect concentration tends to hinder relaxation, we should expect that Ga_{oct} substitutions are dominant over Ga_{tet} substitutions at defect concentrations of 10 at.% and above, which are significantly higher than the present one (6 %), the reason being that octahedral substitutions create much less stress than tetrahedral ones.

6.3 Mulliken population analysis

Calculated Mulliken ionic charge of Ce:YAG, La:YAG, Ga_{oct}:YAG and Ga_{tet}:YAG are compared with those of YAG in Table 6.7. Oxygen atoms, the nearest neighbors of

the impurities, slightly change their charge upon Ce_Y, La_Y and Ga_{oct} doping but their covalency increases when a Ga_{tet} approaches them in the small (d) cavity, since Ga_{tet} is a bigger and softer cation with respect to Al. In general, cations on second coordination shell maintain their charge character whatever the substituted atom is.

6.4 Conclusions

We have performed first-principles PBC-DFT (PBE) calculations on Ce:YAG and La:YAG, Ce and La substituting both an Y atom in the YAG cell, and on Ga_{oct}:YAG and Ga_{tet}:YAG, Ga substituting an Al_{oct} and an Al_{tet} atom respectively. Pseudopotentials and basis sets for these atoms have been also generated in this work with the PBE functional.

The Ce_Y and La_Y substitutional defects produce expansions around them, much more pronounced for the bigger La_Y, which is reflected also in the high formation energy of the La_Y defect. First coordination shell suffers the main distortion, whereas computed distortions are negligible beyond the second coordination shell.

The structure of the first coordination shell found in Ce:YAG is similar to that of the previous embedded cluster calculation of Ref. [41].

Distortions of the second coordination shell are small but not negligible, being the analysis of structures and deformations of the covalent AlO_4 moieties of great interest. This moieties appear to be tightly bonded to Y atoms in -Y-AlO_4-Y-AlO_4- infinite *chains* along a given axis, presenting a great internal flexibility on the Al_{tet}-O bond lengths and O-Al_{tet}-O angles when bigger impurities like Ce and La substitute Y, cushioning distortions.

Regarding Ga substitutions, Ga_{oct}:YAG cells are around 50 meV more stable than Ga_{tet}:YAG cells after relaxation, when one Ga per cell is introduced. This is in agreement with the big size of Ga^{3+} cations and the smaller size of the tetrahedral cavity in comparison to the octahedral one. Displacements caused by both Ga_{oct} and Ga_{tet} are larger than those produced by Ce and La both in first and second coordination shells, but, anyway, distortions can be considered negligible beyond that. Ga_{oct} produces an isotropic distortion and also Ga_{tet}, which enters the -Y-GaO_4-Y-AlO_4- *chain*, produces a purely radial distortion in those atoms placed along the *chain* direction, supporting again our picture of YAG as interleaving -Y-AlO_4-Y-AlO_4- *chains* linked by Al_{oct}.

Band structures of La:YAG, Ga_{oct}:YAG and Ga_{tet}:YAG materials do not present any significant change with respect to band structure of parent material YAG. PDOS on the substituting atoms shows that La introduces new occupied stated without affecting the gap nature, whereas Ga_{oct} and Ga_{tet} PDOS are completely analogous to original Al_{oct} and Al_{tet} ones.

More interesting is the obtained band structure and DOS/PDOS of Ce:YAG material. In spite of the distortion printed by Ce is smaller than that printed by La and Ga, Ce produces significant changes in the electronic structure. New states with $\alpha - 4f$ character do appear above the top of the valence band in YAG, changing the nature of the gap. Moreover, Ce provides states in the lowest unoccupied zone.

6.5 *Conclusiones*

Hemos realizado cálculos PBC-DFT(PBE) en Ce:YAG, La:YAG, Ce y La sustituyendo un átomo de Y en la celda de YAG, y en Ga_{oct}:YAG y Ga_{tet}:YAG, donde el Ga sustituye un Al_{oct} y un Al_{tet} respectivamente. Pseudopotenciales y sets de base han sido generados en este trabajo para estos átomos con el funcional PBE.

Los defectos Ce_Y y La_Y producen expansiones alrededor, mucho más pronunciadas en el caso del La_Y, de mayor tamaño, lo cual se refleja también en la alta energía de formación del defecto de La_Y. La primera esfera de coordinación sufre la mayor distorsión, mientras que más allá de la segunda esfera de coordinación, las distorsiones observadas son despreciables.

La estructura de la primera esfera de coordinación encontrada para Ce:YAG es similar a la obtenida en cálculos previos con la aproximación de *cluster* embebido y métodos basados en la función de onda en la Ref. [41].

Las distorsiones en la segunda esfera de coordinación son pequeñas pero no despreciables, siendo el análisis de las estructuras y deformaciones de la unidad covalente de AlO_4 de gran interés. Estas unidades resultan estar estrechamente unidas a los átomos de Y en cadenas infinitas -Y-AlO_4-Y-AlO_4- a lo largo de cada eje, presentando una gran flexibilidad interna en las distancias Al_{tet}-O y los ángulos O-Al_{tet}-O, lo cual amortigua las distorsiones generadas cuando Ce o La substituyen a Y.

Respecto a las substituciones de Ga, Ga_{oct}:YAG es alrededor de 50 meV más estable que Ga_{tet}:YAG despues de la relajación de los átomos cuando un átomo de Ga por celda es introducido. Esto está de acuerdo con el gran tamaño de los iones Ga^{3+} y el menor tamaño del hueco tetraédrico respecto al octaédrico. Los desplazamientos producidos por Ga_{oct} y Ga_{tet} son mayores que los producidos por Ce y La, tanto en la primera esfera de coordinación como en la segunda, pero, aun así, la distorsión más allá de la segunda esfera de coordinación puede considerarse despreciable. Ga_{oct} produce una distorsión isotrópica, y también Ga_{tet}, que entra en una cadena del tipo -Y-GaO_4-Y-AlO_4-, produce un distorsion radial pura en los atomos situados en la dirección de la cadena, apoyando el modelo propuesto para el YAG como cadenas de -Y-AlO_4-Y-AlO_4- unidas por Al_{oct}.

Las estructuras de bandas de La:YAG, Ga_{oct}:YAG y Ga_{tet}:YAG no presentan ningún cambio significativo respecto a la estructura de bandas del YAG. La PDOS sobre los átomos sustituyentes muestra que el La aporta nuevos estados ocupados que no afectan a la naturaleza del gap, mientras que las PDOS de Ga_{oct} y Ga_{tet} son completamente análogas a las de los Al_{oct} y Al_{tet} a los que sustituyen.

Más interesante es el análisis de la estrucutura de bandas y DOS/PDOS de Ce:YAG. Pese a que la distorsión que produce el Ce es menor que la producida por La y Ga, el Ce provoca cambios significativos en la estructura electrónica. Aparecen nuevos estados con carácter α-$4f$ por encima de la banda de valencia del YAG puro, cambiando la naturaleza del gap. Además, el Ce aporta estados desocupados en la parte más baja de la banda de conducción.

6.6 Data Tables

Table 6.1: Pure YAG structural parameters around Y (c, D_2) position and distortion parameters (first and second coordination shells) of Ce and La-doped YAG. Distances in Å. Angles in degree. Labels according to Fig. 6.3.

		M=**Y** (YAG)	M=**Ce**(Ce:YAG)	M=**La**(La:YAG)
		1^{st} coordination shell		
d(M-O_s)		2.333	2.373	2.410
d(M-O_l)		2.446	2.468	2.522
α(O_{sa}-M-O_{sb})		72.20	72.07	70.92
α(O_{la}-M-O_{lb})		108.16	107.92	107.47
α(O_{lb}-M-O_{lc})		73.55	73.74	74.08
	$\delta r_{\parallel}$	-	0.041	0.076
O_s	$\delta r_{\perp}$	-	0.004	0.027
	Θ	-	6.45	19.57
	$\delta r_{\parallel}$	-	0.023	0.076
O_l	$\delta r_{\perp}$	-	0.006	0.019
	Θ	-	12.03	14.20
		2^{nd} coordination shell		
d(M-Al^1_{tet})		3.028	3.046	3.063
d(M-Al_{oct})		3.386	3.401	3.410
d(M-Y)		3.707	3.718	3.726
d(M-Al^2_{tet})		3.707	3.718	3.727
	$\delta r_{\parallel}$	-	0.012	0.034
Al^1_{tet}	$\delta r_{\perp}$	-	$\sim$0	$\sim$0
	Θ	-	$\sim$0	$\sim$0
	$\delta r_{\parallel}$	-	0.013	0.023
Al_{oct}	$\delta r_{\perp}$	-	0.005	0.005
	Θ	-	20.43	12.70
	$\delta r_{\parallel}$	-	0.007	0.017
Y	$\delta r_{\perp}$	-	0.003	0.004
	Θ	-	25.20	13.90
	$\delta r_{\parallel}$	-	0.009	0.020
Al^2_{tet}	$\delta r_{\perp}$	-	0.003	0.003
	Θ	-	20.20	7.75

Table 6.2: Calculated Al_{tet}-O_s, Al_{tet}-O_{ext} and M-O_{ext} distances and O_{sa}-Al_{tet}-O_{sb} angles for M=Y (YAG), M=Ce (Ce:YAG) and M=La (La:YAG); distances in Å, angles in degrees. Labels according to Fig. 6.3.

	M=**Y** (YAG)	M=**Ce**(Ce:YAG)	M=**La**(La:YAG)
d(M-Al_{tet})	3.028	3.046	3.063
d(Al_{tet}-O_s)	1.788	1.792	1.779
d(Al_{tet}-O_{ext})	1.788	1.783	1.776
d(M-O_{ext})	4.393	4.399	4.400
α(O_{sa}-Al_{tet}-O_{sb})	100.5	102.3	103.6

Table 6.3: Angles, in degrees, of the pseudotetrahedral environment of oxygen. M=Y, Ce or La in pure YAG, Ce:YAG and La:YAG respectively. Labels according to Fig. 6.4.

	M=**Y** (YAG)	M=**Ce** (YAG:Ce)	M=**La** (YAG:La)
α(M-O-Y)	101.79	101.03	99.92
α(M-O-Al_{tet})	93.64	92.77	99.77
α(M-O-Al_{oct})	104.20	103.34	101.97
α(Y-O-Al_{tet})	121.56	122.09	122.76
α(Y-O-Al_{oct})	100.20	100.50	99.99
α(Al_{tet}-O-Al_{oct})	129.96	130.52	131.51

Table 6.4: Calculated GGA(PBE) lattice constants and internal parameters of $LaAlO_3$ ($R\overline{3}c$, 167), in comparison with experimental data [214] and LDA and GGA calculations [215]. Calculated GGA(PBE) lattice constants and internal parameters of *hexagonal*-La_2O_3 ($P\overline{3}m1$, 164) and *cubic*-La_2O_3 ($Ia3$, 206), in comparison with experimental data [216] and LDA calculations [217].

	$LaAlO_3$				La_2O_3(*hexagonal*)			La_2O_3(*cubic*)		
	Exp [214]	LDA [215]	GGA [215]	This work	Exp. [216]	LDA [217]	This work	Exp. [216]	LDA [217]	This work
a (Å)	5.36977	5.306	5.417	5.375	3.933	3.936	3.888	11.360	11.392	11.388
c (Å)	13.0860	12.931	13.189	12.942	6.129	6.166	6.128	-	-	-
x_O	0.5288	0.533	0.541	0.523	-	-	-	0.385	0.3892	0.3796
y_O	-	-	-	-	-	-	-	0.145	0.1482	0.1492
z_O	-	-	-	-	0.630	0.6454	0.655	0.380	0.3787	0.3782
x_{La}	-	-	-	-	-	-	-	0.965	0.9709	0.9712
z_{La}	-	-	-	-	0.235	0.2469	0.2307	-	-	-

Table 6.5: Original YAG parameters around Al_{oct} and distortion parameters (first and second coordination shells) of Ga_{oct}-doped YAG. Original YAG parameters around Al_{tet} and distortion parameters (first and second coordination shells) of Ga_{tet}-doped YAG. Distances in Å. Angles in degrees. Labels according to Fig. 6.11

		B=**Al**$_{oct}$ (YAG)	B=**Ga**$_{oct}$(Ga$_{oct}$:YAG)
		1^{st} coordination shell	
d(B-O)		1.948	2.039
α(O_a-B-O_b)		93.49	94.02
α(O_b-B-O_c)		86.47	85.07
α(O_a-B-O_c)		179.96	179.99
α dihedral		0.02	0.01
	$\delta r_{\parallel}$	-	0.091
O	$\delta r_{\perp}$	-	0.022
	Θ	-	13.69
		2^{nd} coordination shell	
d(B-Al_{tet})		3.386	3.424
d(B-Y)		3.386	3.407
	$\delta r_{\parallel}$	-	0.039
Al_{tet}	$\delta r_{\perp}$	-	0.011
	Θ	-	16.50
	$\delta r_{\parallel}$	-	0.021
Y	$\delta r_{\perp}$	-	0.008
	Θ	-	20.51
		T=**Al**$_{tet}$ (YAG)	T=**Ga**$_{tet}$ (Ga$_{tet}$:YAG)
		1^{st} coordination shell	
d(T-O)		1.788	1.924
α(O_a-T-O_b)		100.48	100.30
α(O_a-T-O_c)		114.14	114.25
α(O_a-T-O_d)		114.13	114.24
α(O_b-T-O_c)		114.16	114.24
α(O_b-T-O_d)		114.15	114.25
α(O_c-T-O_d)		100.48	100.30
	$\delta r_{\parallel}$	-	0.135
O	$\delta r_{\perp}$	-	0.036
	Θ	-	15.04
		2^{nd} coordination shell	
d(T-Al_{oct})		3.386	3.416
d(T-Y1)		3.028	3.047
d(T-Y2)		3.709	3.726
	$\delta r_{\parallel}$	-	0.030
Al_{oct}	$\delta r_{\perp}$	-	0.002
	Θ	-	3.53
	$\delta r_{\parallel}$	-	0.018
Y1	$\delta r_{\perp}$	-	$\sim$0
	Θ	-	$\sim$0
	$\delta r_{\parallel}$	-	0.017
Y2	$\delta r_{\perp}$	-	0.004
	Θ	-	13.30

Table 6.6: Tetrahedrally coordinated oxygen,(h) positions in YAG. B=Al or Ga in pure YAG and in Ga_{oct}:YAG respectively. T=Al or Ga in pure YAG and in Ga_{tet}:YAG respectively. Angles in degrees. Labels according to Fig. 6.12.

	B=$\mathbf{Al}_{oct}$ (YAG)	B=$\mathbf{Ga}_{oct}$ (YAG:Ga_{oct})
$\alpha(Y^1\text{-O-}Y^2)$	101.79	102.90
$\alpha(Y^1\text{-O-}Al_{tet})$	93.64	95.88
$\alpha(Y^1\text{-O-B})$	104.20	103.18
$\alpha(Y^2\text{-O-}Al_{tet})$	121.56	124.36
$\alpha(Y^2\text{-O-B})$	100.20	98.08
$\alpha(Al_{tet}\text{-O-B})$	129.96	127.81
	T=$\mathbf{Al}_{tet}$ (YAG)	T=$\mathbf{Ga}_{tet}$ (YAG:Ga_{tet})
$\alpha(Y^1\text{-O-}Y^2)$	101.79	104.80
$\alpha(Y^1\text{-O-T})$	93.64	90.69
$\alpha(Y^1\text{-O-}Al_{oct})$	104.20	106.10
$\alpha(Y^2\text{-O-T})$	121.56	120.40
$\alpha(Y^2\text{-O-}Al_{oct})$	100.20	104.94
$\alpha(T\text{-O-}Al_{oct})$	129.96	125.55

Table 6.7: Mulliken effective ionic charge of YAG, Ce:YAG, La:YAG, Ga_{oct}:YAG and Ga_{tet}:YAG. Data of the *adjacent* atoms to the substitutional defects (oxygens, 1^{st} coordination shell and cations, 2^{nd} shell). * No Al_{oct} in the second coordination shell of a B position.

	YAG	La:YAG	Ce:YAG	Ga_{oct}:YAG	Ga_{tet}:YAG
La		+1.85			
Ce			+1.89 (55%α, 45%β)		
Ga				+0.78	+0.56
O	-0.96	–0.92(O_s)	–0.92(O_s)	–0.91	–0.86
		–0.94(O_l)	–0.94(O_l)		
Y	+2.33	+2.33	+2.33	+2.32	+2.32 (Y1)
					+2.33 (Y2)
Al_{oct}	+0.99	+1.01	+1.02	*	+0.99
Al_{tet}	+0.84	+0.86	+0.87	+0.84	+0.82
		+0.85	+0.86		

Chapter 7

Antisite defects in YAG

Despite the garnet structure $A_3B'_2B''_3O_{12}$ is thought to be cubic of space group $Ia\bar{3}d$, some experimental results [218, 219] suggested that the garnet structure deviates from cubic symmetry. However, no significant deviation from cubicity was detected by early X-ray diffraction. The question became clarified twenty years later, due to the contribution of Chenavas *et al.* [220], since they found some weak X-ray diffraction peaks which showed a slight anisotropy along the [111] axis. The difficulties in studying the non-cubic symmetry of garnets arise because of the deviation is very small and conventional X-ray diffraction is not sensitive enough to determine it.

Extended X-ray absorption fine-structure (EXAFS) appeared as a stronger tool for structure determination and the contribution of Dong and Lu confirmed its utility in the question of non-cubicity of materials such $Y_3Fe_5O_{12}$, $Gd_3Ga_5O_{12}$, $Y_3Ga_5O_{12}$, $Er_3Al_5O_{12}$ and $Y_3Al_5O_{12}$ [43]. For YAG, they found a change from $Ia\bar{3}d$ symmetry, with four $\overline{3}$ axes in the cube diagonals, to the trigonal $R\bar{3}$ symmetry, with only one remaining $\overline{3}$ [111] axis. Together with this information, some peaks corresponding to the exchange of two Al_{oct} atoms with two Y atoms per unit cell are found. A pair of one Y in Al_{oct} position (Y_{Al}) plus one Al in a Y site (Al_Y) is called *antisite defect* (AD, Fig. 7.1). Then, two ADs are found per unit cell in the work of Dong and Lu.

However, no information about the relative position of these exchanged atoms is given in such work, neither within an AD nor the relative position of two of them. Experimentally, only partial information on the local order around Y atoms has been reported [178]. Theoretically, antisite defects in YAG have been the subject of very few theoretical studies. Pair potential atomistic simulations have been performed in the framework of an empirically parametrized shell-model in order to describe the energetics of formation of these and other defects like interstitials and vacancies [196, 221]. These calculations concluded that antisite defects have a lower energetic demand than other kinds of intrinsic defects and that the exchange between Y and Al_{oct} is energetically preferred over the exchange between Y and Al_{tet}, in agreement with the experimental observations. Regarding first-principles studies, we are not aware of first-principles studies on antisite defects in YAG.

Then, the study of YAG containing antisite defects performed in this work is interesting

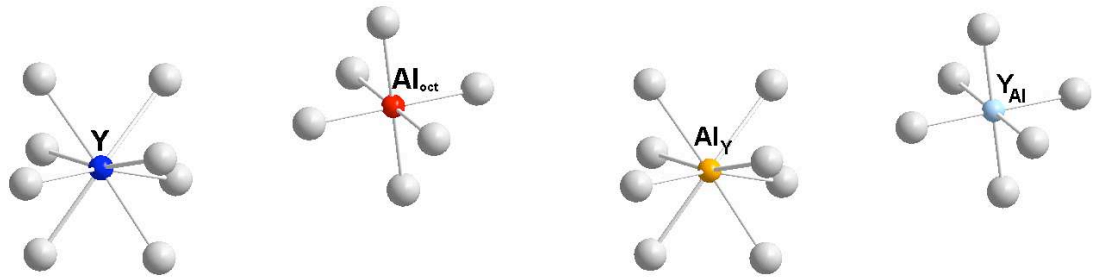

Figure 7.1: Representation of Y and Al_{oct} positions in perfect YAG (left) and antisite defect Al_Y and Y_{Al} (right).

by itself, since it provides an atomistic description of real YAG not performed so far to the best of our knowledge. Moreover, these ADs are known to act as electron trappers and they do affect the structure and the luminescence patterns not only of pure YAG [222], but also of Ce:YAG [44, 46], being the study of YAG antisite defects then definitely of interest in the context of Ce:YAG luminescence, specifically regarding their possible effect on Ce:YAG Stokes shift.

This chapter comprises the structural and electronic structure study on YAG containing one and two antisite defects; the study on the interplay between ADs and Ce when both in YAG will be presented in Chapter 11. In this chapter, we firstly present in Section 7.1 our results in both Y_{Al} and Y_{Al} treated as single substitutional defects, without their other antisite counterparts. Later, and following the Dong and Lu model, Sections 7.2 and 7.3 tackle the study of one and two antisite defects per cell, called 1AD:YAG and 2AD:YAG along this work, regarding structure and electronic structure respectively. Section 7.4 outlines the main conclusions of this chapter. Data tables of this chapter are collected in Section 7.6.

7.1 Al_Y and Y_{Al} single substitutional defects

For a reference, we have studied the individual Al_Y and Y_{Al} defects in YAG separately, that is, both the $Y_{23}Al_{41}O_{96}$ and $Y_{25}Al_{39}O_{96}$ cells arising for single Al_Y or Y_{Al} substitutions in YAG without the corresponding antisite counterpart. Fig. 7.2 shows the eightfold coordination of Al and the sixfold coordination of Y in their new environments. Structural data of relaxed defects (second column of Table 7.2) show a homogeneous distortion around single defects; Al_Y retains D_2 symmetry reducing the distance with respect to oxygens as corresponds to a Al^{3+} cation smaller than Y^{3+}, whereas Y_{Al} isotropically expands its octahedral first coordination shell. Energy involved in formation of both

defects separated at infinite distance can be calculated from the equation sum of the two individual formation processes:

$$\begin{gathered}\text{YAG } (Y_{24}Al_{40}O_{96}) + Al^{3+}_{\text{vacuum}} \rightarrow Al_Y\text{:YAG } (Y_{23}Al_{41}O_{96}) + Y^{3+}_{\text{vacuum}} \\ \text{YAG } (Y_{24}Al_{40}O_{96}) + Y^{3+}_{\text{vacuum}} \rightarrow Y_{Al}\text{:YAG } (Y_{25}Al_{39}O_{96}) + Al^{3+}_{\text{vacuum}} \\ 2 \text{ YAG} \rightarrow Al_Y\text{:YAG} + Y_{Al}\text{:YAG}\end{gathered}$$

Our calculated energy for this last process from the two first ones is 4.45 eV. This quantity represents the formation energy of the two parts of the antisite in a non-interaction situation, that is, separated by infinite distance.

Stress energies of these single substitutional defects in YAG, calculated as the energy of substituted YAG cell with pure YAG structure minus the energy of substituted relaxed cell, are +0.834 eV for Al_Y and +4.86 eV for Y_{Al}; the differences arising from the different cation/cavity size: since Al^{3+} is smaller than Y^{3+}, Y_{Al} suffers a bigger stress in former smaller Al_{oct} cavity and *vice versa*.

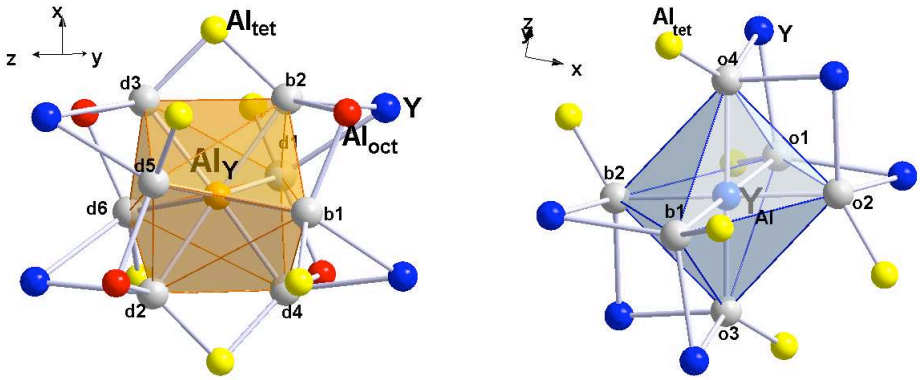

Figure 7.2: Single substitutional defects. Left: Al atom in Y site (Al_Y orange). Right: Y atom in Al_{oct} site (Y_{Al} light blue). First coordination shell (grey oxygen atoms) and second coordination shell (blue Y atoms, yellow Al_{tet} atoms and red Al_{oct} atoms) shown.

7.2 Energetic and structural information

7.2.1 Deviation from cubicity

As in doped-YAG cases discussed above, the first question is if the use of the pure YAG lattice constant is convenient or not. Thus, single point calculations varying lattice constant a were performed both in 1AD:YAG and in 2AD:YAG. Since there are more than one YAG structure containing one AD or two ADs per cell (see below), such E *vs* a curves were performed for all the possible structures of 1AD:YAG and 2AD:YAG structures relaxing ions in the cell and maintaining cubicity of the cell. We obtain the same lattice constant a for all 1AD:YAG cases studied, as well all the 2AD:YAG cases present

the same minimum a. The largest increase was found in 2AD:YAG cases, not exceeding more than 0.5 % from the initial a =12.114 Å value. Thus, this lattice constant has been maintained (12.114 Å) in all these calculations. Plots of the E *vs* a curves for the most stable 1AD:YAG and 2AD:YAG (Fig.7.3) show such increase from 12.114 Å to 12.156 Å (+0.35 %) in 1AD:YAG case, whereas the 2AD:YAG situation reaches a lattice constant of 12.172 Å (+0.48 %).

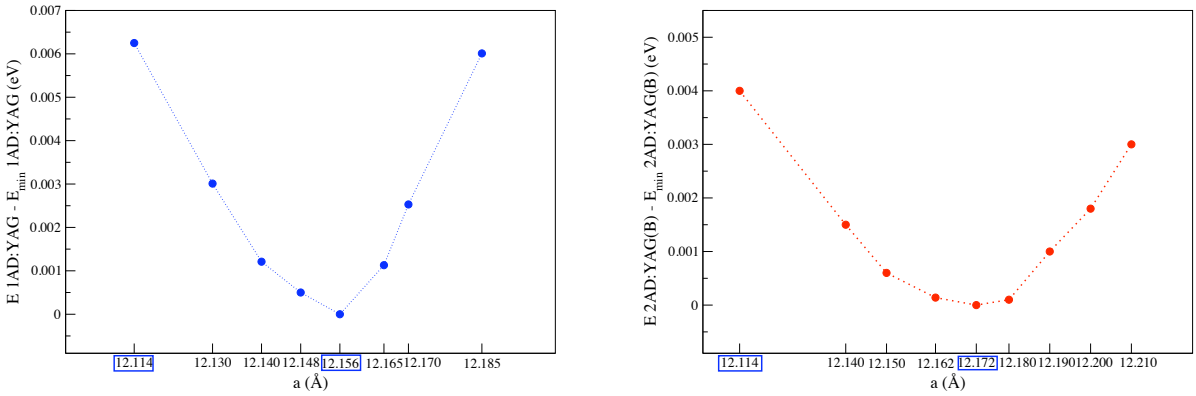

Figure 7.3: Calculated total energy per unit cell as a function of lattice constant for 1AD:YAG most stable case (left) and 2AD:YAG most stable case (right).

In order to study the experimental deviation from cubicity suffered by the experimental 2AD:YAG cells reported by Dong and Lu [43], we have relaxed both lattice vectors and internal positions in the most stable 2AD:YAG structure. Averaged lattice constant of the situations along the [111] axis is a=12.176 Å, +0.51 % with respect to the calculated perfect YAG structure but absolutely comparable to the calculated minimum on Fig. 7.3 (right). Average angle of the new cell is $\alpha = \beta = \gamma = 89.63°$. This information states that, according to cited experiments, deviation from cubicity is very small and the symmetry loss does not arise from a drastic change in the shape of the cell but from the new disposition and rearrangements of the atoms within the cell. We analyze these features in Section 7.2.3.

7.2.2 One antisite defect

Four different Y_{Al}-Al_Y single antisite defects can be created with a defect concentration of one AD per cell. They are shown in Fig. 7.4 and they can be classified according to the distance between Al_{oct} and Y in perfect YAG: 3.386, 5.459, 6.938, and 8.155 Å.

In all the four cases, the positions of all the 160 atoms were optimized after the exchange without symmetry restrictions under the conjugate gradients scheme and the total energy computed at the final geometry was obtained. For each single antisite defect in Fig. 7.4, energetic balance of reaction

$$\text{YAG} \rightarrow Y_{Al}\ Al_Y\ \text{:YAG}\ ,$$

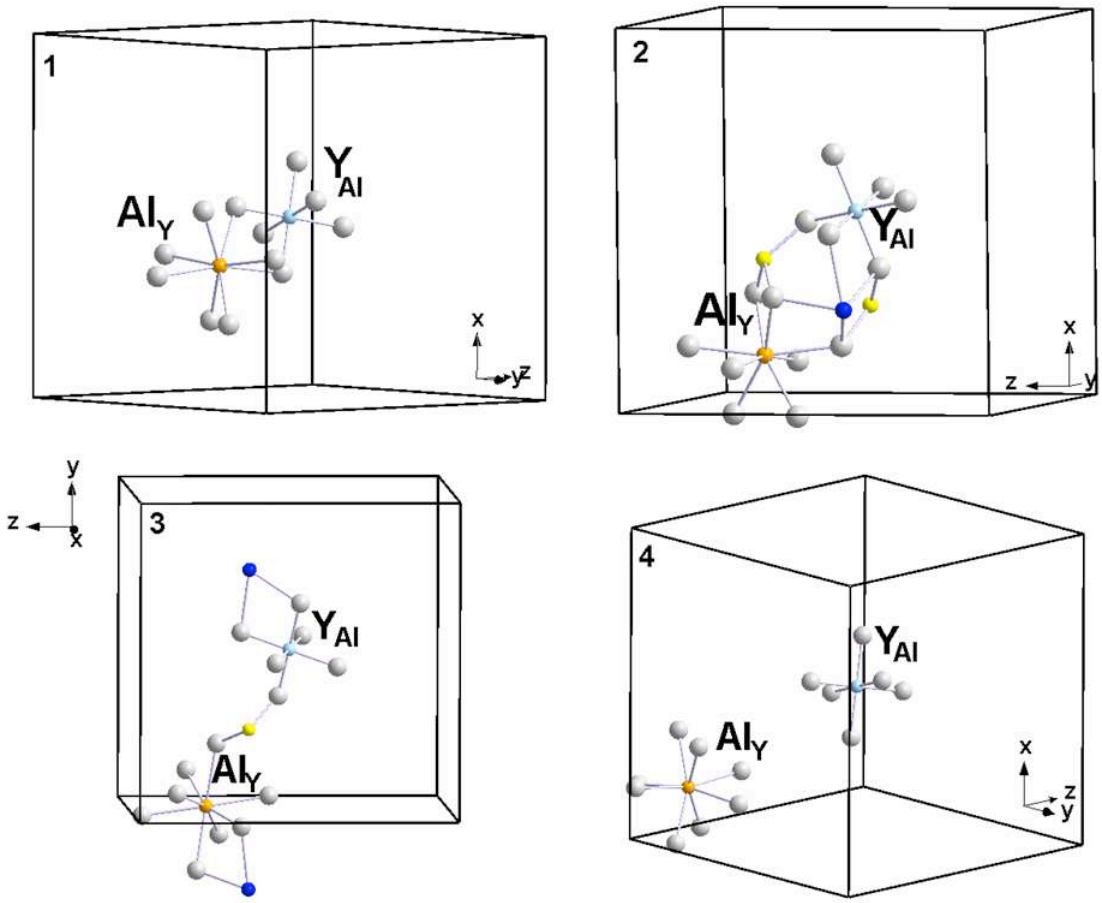

Figure 7.4: The four possible 1AD:YAG, ordered according to to the Y-Al distance before relaxation: (1) 3.39 Å (2) 5.46 Å (3) 6.94 Å and (4) 8.16 Å. First coordination shell (grey oxygen atoms) and, where appropriate, blue Y atoms and yellow Al_{tet} shared atoms of the second coordination shell shown.

can be expressed as E(1AD)-E(YAG) and quantifies the formation energy per antisite defect, E_f(1AD). These energies are tabulated in Table 7.1 (upper chart). The energy value for d(Y_{Al} -Al_Y) = ∞, in order to represent the situation of the two unconnected single defects, has been estimated from calculations on Al_Y:YAG and Y_{Al}:YAG, as explained in Section 7.1. We can observe that the most stable single AD corresponds to the shortest distance between Al and Y, which means an effective attraction between the single substitutional defects Y_{Al} and Al_Y. Binding energies within the substitutional defect with respect to the isolated defects situation, E_b(1AD)=$E_{f,\infty}$(1AD)-E_f(1AD), are reflected in Table 7.1, showing an attraction energy of 0.74 eV for the most stable single AD. This is what one expects of the electrostatic interaction between these defects, because a) they are both uncharged and b) the individual substitutions do not change basically the symmetry and the orientations of the multipoles of the two sites. So, the *static* electrostatic interactions between them (meaning the interactions between the Y_{Al} and Al_Y defects without any deformations induced by their mutual interaction) should basically be the same as

the interaction between Y and Al in perfect YAG. Then, the attractive interaction between the induced multipoles would be dominant. In other words, the elastic deformations around Y_{Al} and Al_Y due to their mutual interaction in Y_{Al} -Al_Y antisite defects are such that they attract each other. Although we are used to think in electrostatic terms because all observations fit the paradigm very naturally, strain-mediated interactions between the substitutional defects could also be responsible for their attraction.

According to our first-principles calculations, the formation of a single antisite defect is a very endothermic process (3.72-4.32 eV/defect, 360-415 kJ/mol). The available pair potential simulations led to a significantly less endothermic antisite defect formation energy (0.9 eV/defect, 87 kJ/mol) [196]. Although the first-principles value could be overestimated, it seems to indicate that the concentration of these entropic established defects is determined at high temperatures (close to the temperature of crystal growth), since they get kinetically trapped at lower temperatures by large energy barriers.

Relaxation energies, E_r(1AD), are also shown in Table 7.1. They are defined as the energies of each relaxed structure, E(1AD), minus the energy of the corresponding stressed structures after Y and Al exchange their positions, E_0(1AD). They are within the -6.18 to -5.56 eV/defect range, and follow the same pattern as formation energies do. Thus, the fact that the more favorable the relaxation energy is, the more stable the AD structure is, suggests an important role of the flexibility of the local environments around exchanged positions.

A detailed picture of the most stable single antisite defect (defect 1 in Fig. 7.4) is shown in Fig. 7.5. Structural data of defect 1 in comparison to analogous site environments of perfect YAG and individual Al_Y/Y_{Al} defects are in Table 7.2.

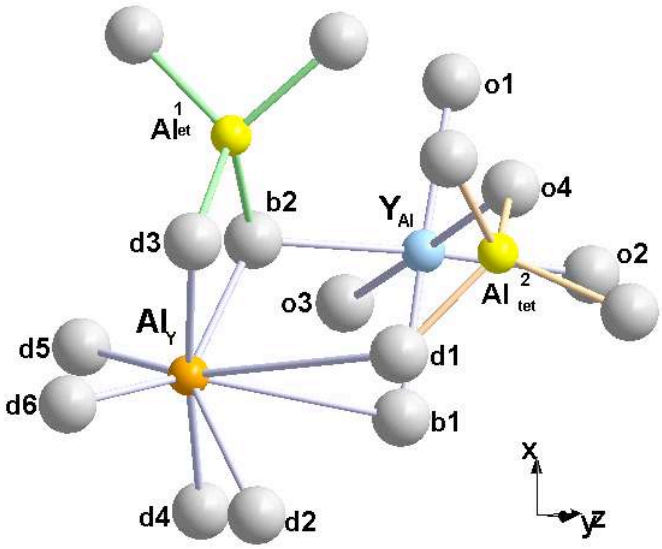

Figure 7.5: Relaxed structure of the most stable 1AD:YAG (1 in Fig. 7.4). Al_Y (orange), Y_{Al} (light blue) and adjacent Al_{tet} atoms (yellow) shown.

They show that Al is prone to shorten its distance with all the oxygen atoms to a closer value to the d(Al_{oct}-O) in pure YAG. However, this shortening is only present in six of the eight surrounding oxygens, whereas two of them remain significantly far from the Al_Y, showing the preference of Al for a six-folded coordination. The distances between Al_Y and these two oxygens are very long compared with usual Al-O distances and they might be considered basically unbound to Al_Y. Regarding Y_{Al}, Y tends to expand its bond distances with oxygens but, different from Al, does not recover its original eight-folded coordination. To illustrate that, we have measured not only the six Y_{Al}-O distances, but also the distances between Y_{Al} and the two closest oxygens not belonging to the original AlO_6 moiety: O_{d3} and O_{d1}. These two distances are almost equal to the corresponding Al-O_{d3} and Al-O_{d1} ones in pure YAG and do not correspond to bonding distances. Both Al_Y and Y_{Al} suffer from a remarkable off-center displacement with respect to original positions in YAG, because of their internal rearrangements into the new sites. As expected, it is more pronounced for Al_Y (0.598 Å) than for Y_{Al} (0.130 Å). That leads to a significant increase of the Y-Al distance from 3.38 Å to 3.66 Å.

As in (Ce, La, Ga):YAG, the major distortion is on the first coordination shell. Effects on second coordination are more difficult to systematize than in (Ce, La, Ga):YAG, due to the symmetry loss. However, the same flexibility of the AlO_4 moieties is observed upon stress produced by oxygen rearrangement. An example to illustrate that can be extracted from Fig. 7.5, where two Al_{tet} belonging to the second coordination shell are shown as a reference, together with their four oxygens. The contraction around Al_Y is followed by a shortening of the distance between this site and Al^1_{tet} from 3.028 to 3.000 Å. Then, the response of the four Al_{tet}-O distances (in light green in Fig. 7.5) is an enlargement from 1.788 Å (in YAG) to values within the 1.795 to 1.826 Å range, compensating the attractive effect of Al_Y. In parallel, the opposite situation is found around Y_{Al}. Due to the repulsion effect of Y_{Al} within the octahedral environment, the distance between this site and Al^2_{tet} increases from 3.385 Å (in YAG) to 3.443 Å in 1AD:YAG. In this case, the four Al^2_{tet}-O distances (in salmon pink in Fig. 7.5), contract from 1.788 Å (YAG) to values between 1.776 and 1.747 Å. All this minimizes displacements of the oxygens in the third coordination shell of the Y_{Al}-Al_Y antisite.

Since the structure far away from the third coordination shell tends to be preserved, the major stability of this AD can be seen as a mechanism of local geometric compensation, where the major contribution seems to be due to the enlargement/shortening of the Y_{Al}-O/Al_Y-O bonds along their bonds with shared oxygens, which affects in a major extent, all the Al_Y-O bonds. A stabilizing contribution arises from the "flexible" environment around substituted atoms.

7.2.3 Two antisite defects

The study of two antisite defects per unit cell, 2AD:YAG, is largely simplified by considering experimental findings exposed above and our computational results for a single AD (subsection 7.2.2). As said before, the [111] axis is retained in the $R\bar{3}$ symmetry.

Then, the two yttrium atoms must replace two aluminum atoms placed in such axis and the two Al must replace two of the eight Y positions non-equivalent with respect to the axis with equal probability. However, according to our calculations in 1AD:YAG, the minimum distance is preferred between Y_{Al} and Al_Y, and then only three of such eight Y non-equivalent positions (and their analogous with respect to the axis) are near enough to form the calculated stable antisite defects (Fig. 7.6).

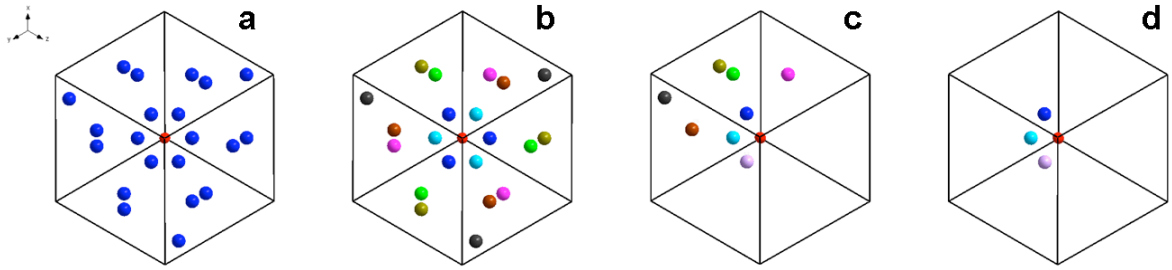

Figure 7.6: YAG unit cell: view along [111] axis. Only Y atoms (blue) and Al_{oct} in the axis (red) are shown. (a) All Y positions represented. (b) Equivalent Y atoms with respect to the [111] axis highlighted in the same color. (c) Non-equivalent Y positions. (d) The only three non-equivalent Y positions closest to Al_{oct} atoms of the [111] axis.

Assuming these premises, only ten different cases with a concentration of 2ADs per cell arise: four corresponding to the situation of *alternated* Y_{Al} in the axis (A series) and six corresponding to the situation of two Y_{Al} *contiguous* in the [111] axis (C series) both of them taking into account the possible distributions of the two Al_Y at the nearest positions. All these ten different 2AD:YAG cases are outlined in Fig. 7.7.

After conjugate gradients relaxations without constraints of each cell, all structures belonging to A series, with alternated Y_{Al}, are more stable than those with contiguous Y_{Al}, C series. Generation of two antisite defects from YAG according to the process

$$\text{YAG} \rightarrow 2\times Y_{Al}\ ,2\times Al_Y\ :\text{YAG}\ ,$$

require more energy in absolute value (E(2AD)-E(YAG)) than analogous reaction for 1AD:YAG (E(1AD)-E(YAG)) . However, interesting information can be extracted from the calculated formation energies per antisite defect. Such formation energies per AD of all the 10 cases, E_f(2AD), have been calculated from the total energies per unit cell of the relaxed structures as ((E(2AD)-E(YAG))/2) and tabulated in Table 7.1 (bottom chart). Also relaxation energies and binding energies expressed per antisite defect are useful to visualize the role of each antisite in the 2AD structure with respect to a single antisite 1AD. Thus, corresponding relaxation energies per AD, E_r(2AD)=(E(2AD)-E_0(2AD))/2, and binding energies between the two single ADs, E_b(2AD)=2E_f(1AD(structure 1))-2E_f(2AD), in each studied 2AD:YAG case are also shown in Table 7.1 (bottom chart). According to these calculations, two independent single AD attract each other so that the most stable 2AD:YAG is energetically more favorable than two separated single ADs,

with a binding energy of 0.22 eV (0.11 eV/AD, 10.7 kJ/mol). This situation presents as well the most favorable relaxation energy per AD. From binding energies in Table 7.1, it can be observed that not all the 2AD configurations are binding.

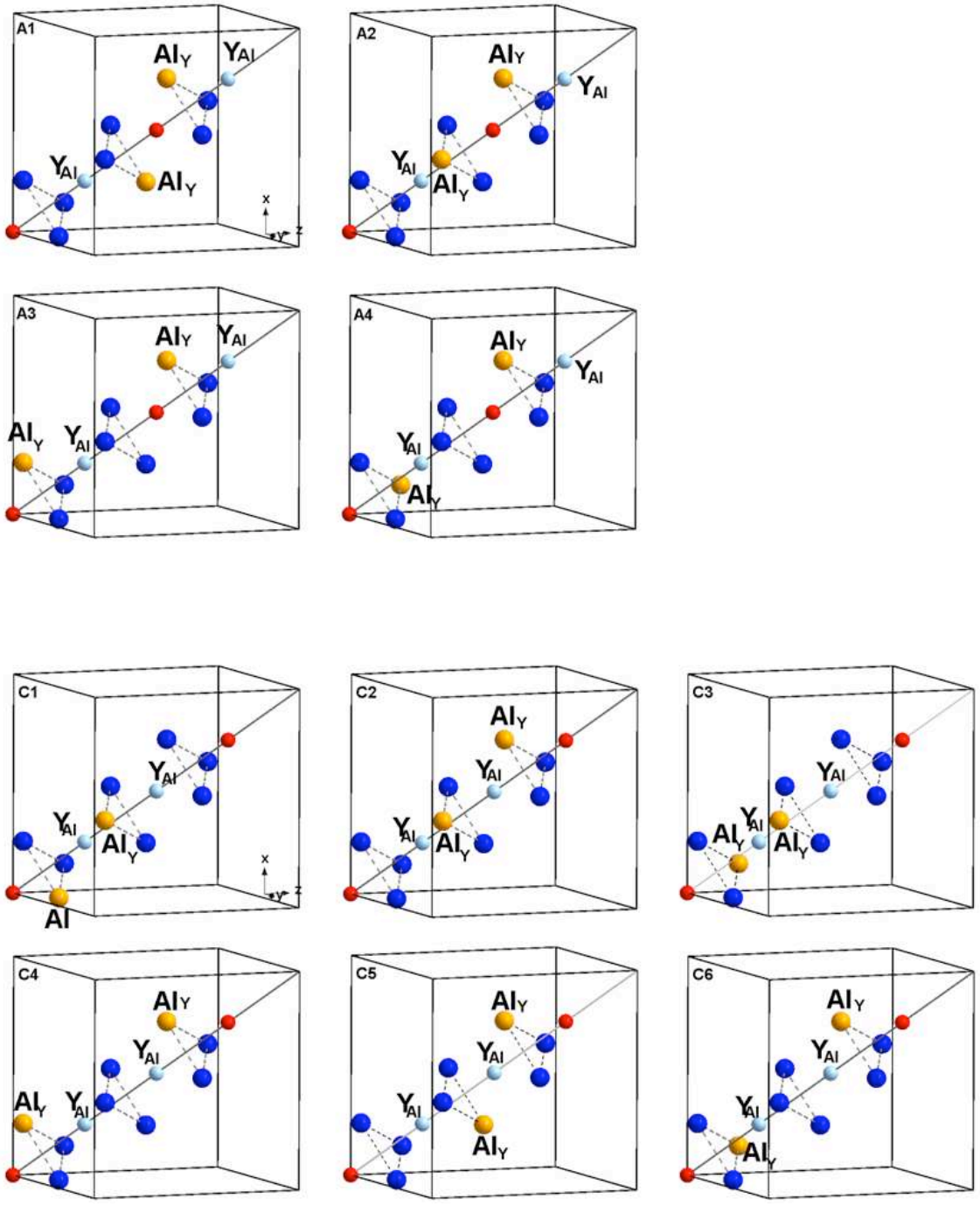

Figure 7.7: Studied 2AD:YAG cells with alternated Y_{Al} positions (A series: from A1 to A4). Studied 2AD:YAG cells with contiguous Y_{Al} positions (C series: from C1 to C6). [111] axis shown. Positions before structural relaxation. Colors: Al_Y atoms, orange; Y_{Al} atoms, light blue; Y atoms, blue and Al_{oct} atoms, red.

The alternated distribution of the ADs, with the atomic sequence -Al_{oct}-Y_{Al}-Al_{oct}-Y_{Al}- all along the [111] axis, is more stable than the contiguous distribution, with the atomic sequence -Al_{oct}-Al_{oct}-Y_{Al}-Y_{Al}-. Forming pairs of adjacent ADs has an energy cost of 0.2-0.3 eV/defect (20-30 kJ/mol) over distributing them evenly along the [111] axis. On the other hand, the energies of all the alternated structures are not very different. The two alternated structures whose Y_{Al}-Al_Y vectors have an antiparallel projection on the [111] axis (A1 and A2), and somehow tend to oppose each other and diminish the local dipole moment, are more stable than the other two alternated structures (A3 and A4), whose Y_{Al}-Al_Y vectors have a parallel projection on the [111] axis and tend to push back each other and increase the local dipole moment. Among all, the most stable structure is A1, which is shown in Fig. 7.8 and is the only one with inversion symmetry respect to the unit cell center. Because of this, it is the only structure of 2AD:YAG with zero local dipole moment with respect to (1/2,1/2,1/2). A detailed picture of the A1 structure is shown in Fig. 7.8 and some of its structural details are presented in Table 7.2.

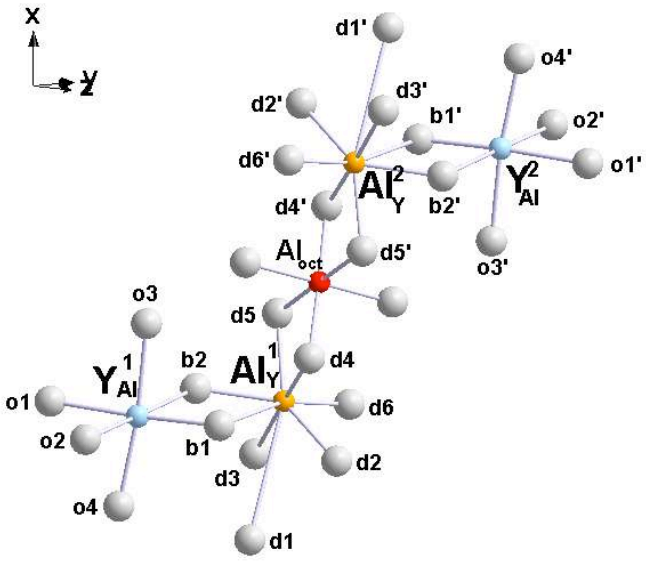

Figure 7.8: Relaxed structure of the most stable 2AD:YAG (Fig. 7.7, A1). Al_Y (orange), Y_{Al} (light blue) and inversion center Al_{oct} (red) shown.

Because of the presence of one Al_{oct} as inversion center in (1/2,1/2,1/2), the structure of both antisite defects are identical and, moreover, very similar to the structure of a single AD. In particular, they also show the interesting features of one bridge oxygen between Al and Y becoming only bound to Y_{Al} (O_{b1} and $O_{b1'}$) and one oxygen initially bound to Y becoming unbound to Al_Y (O_{d1} and $O_{d1'}$). In this structure, the Al_{oct} atom linking the two ADs seems to play an important role in its stability, because the Al_{oct}-O distances shorten from the initial value in YAG, 1.95 Å, to 1.89, 1.91 and 1.94 Å, closer to Al-O distances in other compounds, like 1.86 Å in Al_2O_3 [210] and 1.89 Å in $LaAlO_3$ [214].

7.3 Electronic structure

Band structures of 1AD:YAG and 2AD:YAG are shown in Fig. 7.9.

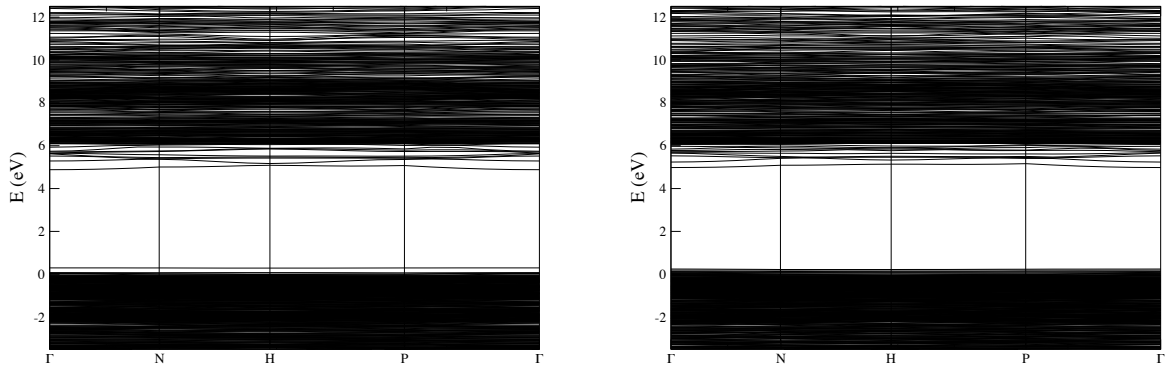

Figure 7.9: Band structures of the most stable 1AD:YAG (left) and 2AD:YAG (right).

If we compare the 1AD:YAG band structure with perfect YAG band structure (Fig. 5.7), we see in the figures that a new occupied band appears slightly above the top of the perfect YAG valence band (taken as our zero for reference). For 2AD:YAG, we can observe some bands above the top of perfect YAG valence band. We do resort to DOS and PDOS of these materials to clarify the nature of these states.

Total density of states (DOS) of the most stable 1AD:YAG, 2AD:YAG and YAG are shown together in Fig. 7.10(a), where the zero reference corresponds to the top of the valence band of pure and perfect YAG. Although no significant differences between 1AD:YAG and YAG are observed in the big picture, a closer look to the highest valence and lowest conduction states (Fig. 7.10, b) reveals interesting features: some of the valence states split up by the AD formation, introducing defect levels in the gap shifted upwards 0.25 eV with respect to the perfect YAG highest valence levels.

An analysis of the oxygen projected DOS (PDOS) of 1AD:YAG shows that it is almost identical to the total DOS in the highest energy region of the valence, as it was the case in YAG (Section 5.2.3), which indicates that the gap reduction is due to changes in the electronic structure of the oxygen atoms. A Mulliken population analysis of the twelve oxygens directly involved in the AD formation does not show any significant differences in the change of their total and overlap populations; however, the PDOS of the individual oxygens are revealing. They are shown in Fig. 7.10(c) together with the PDOS of oxygen in perfect YAG. It can be observed that the states on the two oxygens which remain at a long distance from Al_Y (O_{b1} at 2.9 Å and O_{d1} at 3.2 Å) increase their energy, the longer the distance the larger the energy increase. O_{b1} and O_{d1} present a very similar PDOS profile, though shifted respect to each other. Among these two oxygens, O_{b1} was initially a bridge atom sharing the coordinations of the reference Y and Al atoms in YAG and it becomes unbound to Al_Y and remains bound only to Y_{Al} in 1AD:YAG (besides to the other two on-site atoms Y and Al_{tet}; note that each O atom in YAG is bound to one Al_{oct}, one Al_{tet}, and two Y atoms). O_{d1}, however, which was not bound to the reference Al_{oct}

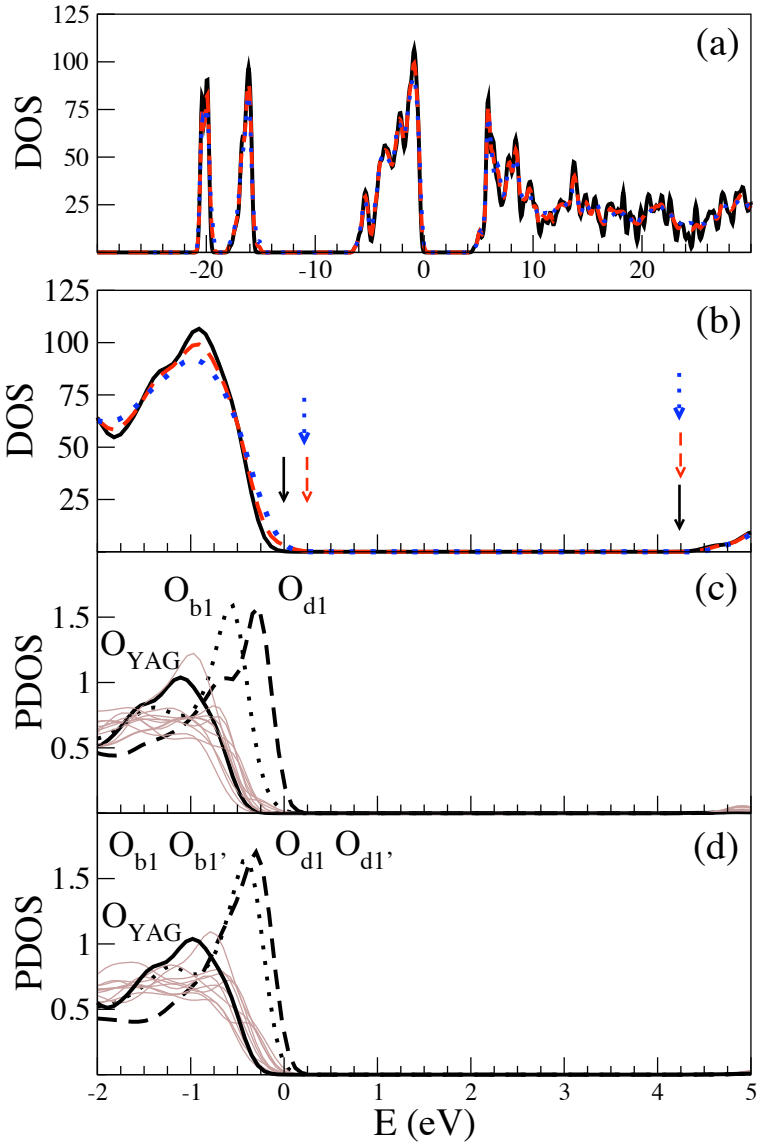

Figure 7.10: (a) Total DOS of YAG (black solid line), 1AD:YAG (red dashed line) and 2AD:YAG (blue dotted line). (b) Zoom over the gap zone. Vertical arrows indicate the end of the valence bands and the beginning of the conduction bands (same lines as in (a)). (c) PDOS on oxygen atoms of 1AD:YAG. Labels according to Fig. 7.5. (d) PDOS on oxygen atoms of 2AD:YAG. Labels according to Fig. 7.8.

atom in YAG and was only bound to the reference Y, is now basically unbound to Al_Y in 1AD:YAG. It is around this oxygen where the highest valence states 0.25 eV above those of YAG are localized. Thus, the new bands appearing in the band structure of 1AD:YAG and 2AD:YAG (Fig. 7.9) can be associated to states of these *unbound* oxygens to Al_Y in 1AD:YAG. Such structure becomes more complicated in the 2AD:YAG case (Fig. 7.10, d), since more oxygen atoms are involved, rising their energy to a greater or lesser extent (brown lines in Fig. 7.10) and generating this set of bands above the top of the perfect YAG valence band.

7.4 Conclusions

We have performed first-principles PBC-DFT (PBE) calculations on the distribution, atomistic structure and electronic structure of antisite defects (ADs) in YAG, taking into account concentrations of one and two ADs per unit cell. Each AD considered comprises a pair of exchanged ions: one Al atom in an Y site (Al_Y) and the corresponding Y atom in an Al_{oct} site (Y_{Al}).

The most stable single AD is made of the Al_Y and Y_{Al} as close as possible, i.e. being second neighbors and sharing two oxygens of their first coordination shells. Such an arrangement presents a binding energy of 0.74 eV with respect to the individual substitutional defects. In this structure, while Y_{Al} maintains the original sixfold coordination from the AlO_6 moiety of YAG and increases all Y_{Al}-O distances, Al_Y cannot retain two of the eight oxygen atoms of the original YO_8 dodecahedral moiety, which move away and can be considered *unbound* to Al_Y. The remaining six Al_Y-O distances get shorter to typical Al-O bond length values, becoming Al_Y sixfold coordinated. One of the two unbound oxygen atoms is one of the two bridge oxygens shared by Y and Al in perfect YAG; the other belongs only to YO_8 in YAG.

This has a consequence on the electronic structure with respect to YAG. The upper electronic levels localized in these unbound oxygens shift upward, especially those on the oxygen only belonging to the YO_8 moiety, introducing levels in the gap of perfect YAG 0.25 eV above the top of the valence band.

The most stable structure containing two antisite defects, considering that each single antisite preserves the structure above described, is the only one which preserves the inversion center with respect to the (1/2,1/2,1/2) position occupied by an Al_{oct} atom. In consequence, has zero dipole moment with respect to the unit-cell center. This structure is made of two single ADs linked by such mentioned AlO_6 moiety, which seems to play an important role in the stability of the structure. It has basically the same electronic structure as the most stable single AD, since it presents four unbound oxygens, two from each single AD.

The formations of one and two antisite defects per unit cell are quite endothermic and the formation energy per defect is lower in 2AD than in 1AD, which is in agreement with the fact that two antisite defects per cell are found experimentally in synthetic YAG. Actually, we find a binding energy between the two ADs of 0.22 eV.

7.5 *Conclusiones*

Hemos realizado cálculos PBC-DFT de la distribución, estructura a nivel atómico y estructura electrónica de los defectos *antisite* (ADs) en YAG, considerando concentraciones de uno y dos ADs por celda unidad. Cada AD considerado contiene un par de iones intercambiados: un átomo de Al en una posicion de Y (Al_Y) y el correspondiente Y en posición de Al_{oct} (Y_{Al}).

En el antisite sencillo más estable, Y_{Al} y Al_Y adoptan las posiciones más cercanas,

esto es, son segundos vecinos que comparten dos oxígenos de sus primeras esferas de coordinación. Esta disposición presenta una energía de interacción favorable de 0.74 eV respecto a los dos defectos substitucionales individuales. En esta estructura, mientras que el Y_{Al} mantiene la coordinación original de AlO_6 por elongación de los seis enlaces Y_{Al}-O, Al_Y no puede retener la coordinación dodecaédrica de la unidad YO_8, viéndose dos oxígenos desplazados, a los cuales podemos considerar no enlazados a Al_Y. Las otras seis distancias Al_Y-O se acortan hasta valores típicos del enlace Al-O. Uno de los oxígenos no enlazados a Al_Y es uno de los dos oxígenos puente compartidos entre los cationes, el otro sólo pertenece a la unidad YO_8 en YAG.

Este hecho tiene consecuencias en la estructura electrónica del material respecto al YAG perfecto. Los niveles electrónicos más altos localizados en estos dos oxígenos suben en energía, especialmente aquellos niveles del oxígeno que sólo pertenece a la unidad YO_8, inroduciendo niveles en el gap 0.25 eV más por encima de la banda de valencia del YAG perfecto.

La estructura más estable de dos defectos *antisite*, considerando que cada antisite sencillo conserva la estructura descrita anteriormente, es la única que conserva el centro de inversión respecto a la posición (1/2,1/2,1/2), ocupada por un Al_{oct}. Por tanto, tiene un momento dipolar nulo con respecto al centro de la celda unidad. Esta estructura está formada por dos antisites sencillos unidos por la mencionada unidad AlO_6, que parece jugar un papel importante en la estabilidad de la estructura. Su estructura electrónica es bastante similar a la del YAG con un defecto *antisite* sencillo puesto que contiene cuatro oxígenos no enlazados, dos de cada defecto.

La formación de uno y dos defectos *antisite* es bastante endotérmica, siendo la energía de formación por defecto menor en el caso de dos defectos, lo cual está de acuerdo con la concentración encontrada experimentalmente de dos defectos *antisite* por celda de YAG. De hecho, encontramos una energía de interacción favorable entre los dos defectos de 0.22 eV.

7.6 Data Tables

Table 7.1: Calculated antisite defect formation energies, E_f, and relaxation energies, E_r, per antisite defect in different 1AD:YAG and 2AD:YAG cells. In parentheses, differences with respect to the lowest. Calculated binding energies, E_b, between Y_{Al} and Al_Y in 1AD:YAG and between single ADs in 2AD:YAG, in eV. 1 eV/defect = 96.4853 kJ/mol.

1AD:YAG

Structure (Fig. 7.4)	d(Y_{Al}-Al_Y) (Å) YAG	1AD	E_f(1AD)[a]	E_r(1AD)[b]	E_b(1AD)[c]
1	3.39	3.65	3.72 (0.11)	-6.18 (0.14)	0.74
2	5.46	5.33	4.02 (0.41)	-5.86 (0.46)	0.44
3	6.94	6.50	4.08 (0.49)	-5.81 (0.51)	0.36
4	8.16	8.16	4.32 (0.71)	-5.56 (0.76)	0.14
-	∞	∞	4.46 (0.85)	-5.44 (0.88)	

2AD:YAG

Structure	E_f(2AD)[d]	E_r(2AD)[e]	E_b(2AD)[f]
Alternated series (Fig. 7.7)			
A1	3.61 (0.00)	-6.32 (0.00)	0.22
A2	3.68 (0.07)	-6.22 (0.10)	0.08
A3	3.70 (0.09)	-6.19 (0.13)	0.04
A4	3.74 (0.13)	-6.15 (0.17)	-0.04
Contiguous series (Fig.7.7)			
C1	3.83 (0.22)	-6.10 (0.22)	-0.22
C2	3.84 (0.23)	-6.08 (0.24)	-0.24
C3	3.89 (0.28)	-6.05 (0.27)	-0.34
C4	3.91 (0.30)	-6.03 (0.29)	-0.38
C5	3.93 (0.32)	-6.01 (0.31)	-0.42
C6	3.94 (0.33)	-6.00 (0.32)	-0.44

[a] E_f(1AD)=E(1AD)-E(YAG)
[b] E_r(1AD)=E(1AD)-E_0(1AD)
[c] E_b(1AD)=$E_{f,\infty}$(1AD)-E_f(1AD)
[d] E_f(2AD)=(E(2AD)-E(YAG)/2
[e] E_r(2AD)=(E(2AD)-E_0(2AD))/2
[f] E_b(2AD)=2E_f(1AD(structure 1))-2E_f(2AD)

Table 7.2: Al-O, Y-O and Al-Y distances, in Å, in perfect YAG, single substitutional defects Al_Y and Y_{Al}, and most stable single antisite defect 1AD:YAG (1 in Fig. 7.4) and double antisite defect 2AD:YAG (A1 in Fig. 7.7). Atomic labels used in Figs. 7.5 and Fig. 7.8.

		dodecahedral site		
Oxygen	YAG d(Y-O)	Al_Y:YAG d(Al_Y-O)	1AD:YAG d(Al_Y-O)	2AD:YAG d(Al_Y-O)
d1	2.446	2.384	3.216	3.34
b1	2.446	2.383	2.889	2.86
d2	2.333	2.150	2.314	2.10
d3	2.333	2.150	2.189	2.17
b2	2.333	2.150	2.064	2.06
d4	2.333	2.147	2.058	2.06
d5	2.446	2.374	1.964	2.08
d6	2.446	2.375	1.954	1.97
	d(Y-Al_{tet1})	d(Al_Y-Al_{tet1})	d(Al_Y-Al_{tet1})	
	3.028	2.963	3.000	
	d(Al_{tet1}-O)	d(Al_{tet1}-O)	d(Al_{tet1}-O)	
	1.79×4	1.80-1.81	1.80-1.83	
		octahedral site		
	YAG d(Al_{oct}-O)	Y_{Al}:YAG d(Y-O)	1AD:YAG d(Y_{Al}-O)	2AD:YAG d(Y_{Al}-O)
o1	1.947	2.176	2.233	2.22
o2	1.947	2.176	2.226	2.22
o3	1.947	2.176	2.223	2.22
b2	1.947	2.176	2.211	2.21
o4	1.947	2.176	2.186	2.19
b1	1.947	2.176	2.128	2.12
d3[1]	4.313	4.328	4.204	4.19
d1[1]	3.784	3.778	3.783	3.86
	d(Al_{oct}-Al_{tet2})	d(Y_{Al}-Al_{tet2})	d(Y_{Al}-Al_{tet2})	
	3.385	3.458	3.442	
	d(Al_{tet2}-O)	d(Al_{tet2}-O)	d(Al_{tet2}-O)	
	1.79×4	1.78-1.80	1.75-1.78	
	d(Y-Al_{oct})		d(Y_{Al}-Al_Y)	d(Y_{Al}-Al_Y)
	3.384		3.655	2× 3.66

[1] This oxygen does not belong to the first, sixfold coordination shell of Al_{oct} in YAG

Chapter 8

Effect of codoping and antisite defects on Ce:YAG luminescence: an introduction

Experimental findings on the two central problems studied in this work (shifts induced via codoping and Ce:YAG Stokes shift) show that the complex spectroscopy of Ce:YAG is linked, in one way or another, to the (at least local) structure around Ce_Y.

In the search of new phosphors via codoping [32, 33, 34], different shifts are found for different codopant atoms. For instance, Tb^{3+} in Ce:YAG acts as a co-activator, enhancing the red spectral emission intensity and improving the color rendering index [34]. Gd^{3+} and La^{3+} in Ce:YAG shift the yellow luminescence of Ce^{3+} to longer wavelengths (red shift) [39, 40], and, on the contrary, Ga^{3+} shifts it to shorter wavelengths (blue shift) [28, 39, 40]. These differential shifts formed the basis of an empirical rule in use [32], according to which substitutions of Y^{3+} by larger ions red shift the Ce^{3+} emission and substitutions of octahedral Al^{3+} by larger ions blue shift it [39, 40]. However, the lattice constants increase with both types of codopants, Gd^{3+} or La^{3+} on one side and Ga^{3+} on the other [39], which complicates the interpretations on the basis of increasing and decreasing crystal field splittings of the Ce^{3+} $5d$ shell [32], and makes it difficult to advance predictions. Actually, codoping with Mg^{2+} and Si^{4+} red shifts the Ce emission [40] and a similar red shift was predicted for codoping with Mg^{2+} and Ti^{4+}, but a blue shift was found instead and the luminescence was severely quenched [32]. Then, it is reasonable to think that the global influence of codopants cannot be studied within such a general framework and a detailed knowledge of the local structures of the substitutional defects in each particular case, as well as of their electronic structures, is convenient in order to understand the luminescence dependence on codoping and, ultimately, to be able to control the color of the Ce:YAG phosphor via codoping.

Regarding the problem of Ce:YAG Stokes shift, not solved with calculations on perfect Ce:YAG [41], it is known that intrinsic antisite defects (ADs) are present in garnets, giving as a result a change on the internal structure and, then, a decrease of symmetry of the perfect crystal from cubic to trigonal [43]. As we have seen in Chapter 7, ADs have a

large structural impact on YAG cell, more local considering one AD and more pronounced and extended in the cell in the experimental case of two ADs per unit cell. Moreover, the interest of such antisite defects in the context of luminescence arises from the intrinsic luminescence patterns of YAG associated to ADs, specifically to the Y_{Al} centers [44, 45, 223]. Such luminescence arises as wide complex bands in UV range of spectrum and their position, shape and intensity depend on the abundance and distribution of ADs via the features of sample preparation and temperature of measurements [44]. That is not the only reason: it is also known that such emission associated to Y_{Al} centers induces excitation of the Ce_Y impurity centers on Ce:YAG. This interplay is not observed in single-crystalline films of Ce:YAG, since they are synthesized at much lower temperature than the bulk material and, thus, are practically antisite defect-free [45, 46]. In this context, it is reasonable to think that ADs can modify the luminescence patterns of Ce:YAG and, then, a detailed description of the interplay between Ce_Y and the ADs present in the YAG host is definitely of interest, giving a more realistic picture of the real behavior of Ce_Y as impurity in YAG.

Taking into account all the above, we can say that the two main problems tackled in this work have a common feature: in the understanding of the complex Ce:YAG luminescence, a detailed knowledge of the local structures at the atomistic level of the materials is convenient and perhaps necessary.

Then, in Section 8.1, we describe our approach in the understanding of the structure-luminescence relationship in these materials.

Later, in Section 8.2, we present our results on the absorption spectrum of Ce:YAG, which is taken as a reference when analyzing spectra of materials with double defects. Moreover, we do compare our results with those in Ref. [41], the only available *ab initio* calculation on Ce:YAG so far to the best of our knowledge, which comprises analogous Ce:YAG embedded-cluster CASSCF/CASPT2 calculations plus spin-orbit coupling effects. Since both calculations are totally comparable at the CASPT2 level and the effect of spin-orbit coupling on the $4f \rightarrow 5d$ transitions is, roughly speaking, an even 1000 cm^{-1} increment in all of them, spin orbit effects obtained in Ref. [41] allow to predict such effects in our calculations.

8.1 A common methodological approach

So far, we have studied in detail structural features of the host material YAG (pure and perfect), as well as those of the individual defects Ce:YAG, La:YAG, Ga_{oct}:YAG, Ga_{tet}:YAG, 1AD:YAG and 2AD:YAG. From now on, we focus on the study of double defects, i.e. cells containing both Ce_Y and other cation or antisite defect/defects.

Our study follows three main subsequent steps: first, we perform a PBC-DFT structural analysis of the cells containing double defects; second, we do calculate the absorption spectra of these materials under the embedded cluster approach using as cluster coordinates those arising from such PBC-DFT calculations and, finally, we do analyze these absorption spectra in comparison with our Ce:YAG reference one in terms of the components of a given transition. Details of these three steps are outlined in the following.

8.1.1 Structure and electronic structure

Obtaining structural information about the double defects by means of experimental techniques (like extended X-ray absorption fine structure, EXAFS) is very difficult and, actually, not even the local structure of the single substitutional defect Ce_Y is known.

We are aware of a few first-principles studies on perfect YAG and other garnets [171, 173, 224, 172, 176] as well as on Ce^{3+} single substitutional defects [41], together with our results presented in Chapters 5, 6 and 7 on perfect YAG, single substitutional defects and antisite defects. Moreover, some pair-potential empirically parametrized atomistic simulations aiming at describe the energetics of formation of a number of defects such as impurities, interstitials and vacancies are also available [213, 196, 221].

However, to the best of our knowledge, atomistic structures of double defects Ce,La:YAG, Ce,Ga:YAG and Ce,ADs:YAG (and their associated electronic structures) have not been reported previously. Thus, the relationship between such structural changes and the change in the absorption spectrum with respect to single-doped Ce:YAG is not known either.

Regarding the structural analysis of the double defects in this study, we have analyzed the problem using the same PBC-DFT methodology described before for single defects, using the SIESTA program [97]. We have browsed all the possible non-equivalent cells that can be formed with each double defects and, after a total relaxation of the internal positions, we have focused on the most stable structures to study in detail the changes in the local structure around Ce_Y (which are used as cluster coordinates in the embedded cluster spectra calculations) and the changes in the electronic structure with respect to Ce:YAG.

In the case of Ce,1AD:YAG and Ce,2AD:YAG, we have taken into account the information obtained previously for 1AD:YAG and 2AD:YAG cells (Chapter 7) to construct the cells, preserving the initial disposition of the antisite defects (i.e. Y_{Al} and Al_Y sharing two oxygen atoms in each single antisite defect plus the presence of the inversion center on the 2AD:YAG cell) and placing the Ce_Y wherever appropriate.

8.1.2 Spectra calculations

The optical absorption energies corresponding to the Ce^{3+} $4f \rightarrow 4f$, $4f \rightarrow 5d$, and $4f \rightarrow 6s$ transitions in Ce:YAG, Ce,La:YAG, Ce,Ga_{tet}:YAG, Ce,Ga_{oct}:YAG , Ce,1AD:YAG and Ce,2AD:YAG have been calculated with embedded cluster wave function based methods according to the guidelines described in the following.

We study two different clusters in this work: one smaller $(CeO_8)^{13-}$ containing the Ce^{3+} ion and its first coordination shell, and a bigger $(CeO_8Al_2O_4)^{15-}$ that additionally contains two AlO_2 moieties along a given axis, taking into account the tight relationship between the CeO_8 moiety and the adjacent AlO_4 moieties shown before, each one sharing two oxygen atoms with Ce. The coordinates of these clusters come entirely from ground-state PBC-DFT calculations.

The AIMP embedding for these clusters, accounting for the classical electrostatic plus quantum-mechanical contributions, consists in one unit cell of YAG (cube of length a_0, containing Y^{3+}, Al^{3+}_{oct}, Al^{3+}_{tet} and O^{2-}). Beyond this, point charges are used within a cube of length $2.5a_0$ using the nominal charges of Y^{3+}, Al^{3+}_{oct}, Al^{3+}_{tet} and O^{2-}except for the frontier ions, bearing fractional charges, according to Evjen's method [153]. This cluster/AIMP shell/point charges distribution for our system is represented in Fig. 8.1 for the $(CeO_8Al_2O_4)^{15-}$ considered cluster.

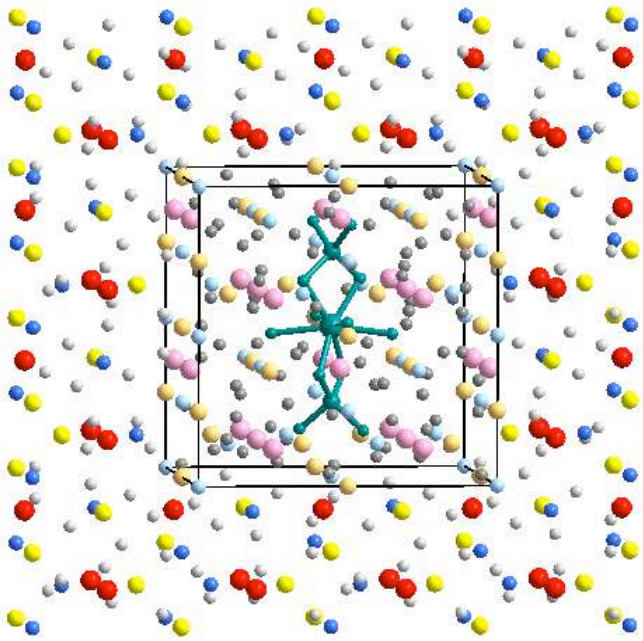

Figure 8.1: $(CeO_8Al_2O_4)^{15-}$ cluster (greeny blue) embedded in one YAG cell of AIMPs (pink Al_{oct}, orange Al_{tet}, light blue Y and dark grey O) and a symbolic representation of multiple YAG cells as point charges (red Al_{oct}, yellow Al_{tet}, blue Y and light grey O).

We take the original position of the Y ion to be substituted by Ce in pure YAG as coordinates origin, in order to have a common framework for the cluster, the AIMP shell and the point charges arrangement, even if the impurity Ce_Y becomes off-center from this original position because of distortions produced by codoping or antisites, as we will see in chapters 9, 10 and 11.

In every case, calculated pure and perfect YAG unit cell ($a_0 = 12.114$ Å, x(O)= -0.0306, y(O)= 0.0519, y(O)= 0.1491, Section 5.2) is used to set the point charges arrangements.

The cluster coordinates and the AIMP shell coordinates for each system are taken as they come out from the PBC-DFT calculations of the previous step. If we compare these spectra of double defects (Ce,La:YAG, Ce,Ga:YAG, Ce,ADs:YAG), calculated using both the cluster and the AIMP shell coordinates of the corresponding PBC-DFT calculation, with Ce:YAG one, we can quantify the total effect that the presence of a second defect exerts on Ce:YAG spectrum. This total difference between the spectra comes from three different sources: distortion on the cluster geometry (different cluster geometries considered in the calculation), the different distortion printed by the defects in the whole cell (different AIMP embedding coordinates) and the electronic effects due to the presence of a different atom in the substituted position (use of AIMP of La, Ga, Al_Y and Y_{Al} wherever appropriate).

In order to quantify the changes in the spectra arising individually from each one of these sources, we have performed two additional calculations in Ce,La:YAG, Ce,Ga:YAG and Ce,ADs:YAG. From now on, A refers to the reference Ce:YAG calculation and D the double defect calculation considering distortion both on the cluster and on the AIMP cell and considering AIMPs of the substituted atoms. The first additional calculation, let us say B, is performed taking into account the cluster coordinates distorted according to the double defect, but the AIMP embedding used is the one of the Ce:YAG calculation and no AIMPs of defects are considered but AIMPs of the original atoms in YAG. Then, the change in the calculated spectra from A to B is only due to distortions on the cluster structure. The second additional calculation, let us call it C, is performed using both cluster and AIMP coordinates distorted according to the double defect and still considering YAG AIMPs in the positions of the defects. Then, the changes from B to C arise from distortions on the cell only and, thus, the changes from A to C are due to the full distortion printed by the new defect both in the cluster and in the cell. The changes on the spectra from C to D, where the AIMPs of the substituted atoms are considered, are due only to the electronic effects of these atoms as represented by their AIMPs. Thus, the global effect from A to D is decomposed in subsequent steps, each one accounting for a different source of change. The total scheme is outlined in Table 8.1. The analysis of the $4f \rightarrow 5d$ transition outlined in Section 8.1.3 will be performed for spectra arising from calculation A in Ce:YAG and for calculations B, C and D in Ce,La:YAG, Ce,Ga:YAG and Ce,ADs:YAG.

Table 8.1: Features of the three spectroscopic calculations B, C and D performed in Ce,X:YAG (X≡La,Ga,ADs) in comparison with Ce:YAG (A) calculation.

	Calculation			
	A	B	C	D
Cluster coordinates	Ce:YAG	Ce,X:YAG	Ce,X:YAG	Ce,X:YAG
AIMP coordinates	Ce:YAG	Ce:YAG	Ce,X:YAG	Ce,X:YAG
AIMPs	YAG	YAG	YAG	X
	Effect accounted for			
	$A \rightarrow B$	$B \rightarrow C$	$A \rightarrow C$	$C \rightarrow D$
	Cluster distortion	Cell distortion	Full distortion	Electronic
		$A \rightarrow D$		
		Total		

The same formal AIMPs used to incorporate the embedding effects are used to represent the effects of the cores of Y, Al, O and Ce, with the particularity of including scalar relativistic effects for Ce (Refs. [225, 96, 226]). Then,

- For Ce, a [Kr] spin-free relativistic Cowan-Griffin core plus a $(14s10p10d8f3g)/[6s5p6d4f1g]$ Gaussian valence basis set is used [227].

- For O, a [He] effective core potential and a $(5s6p1d)/[3s4p1d]$ valence basis set is used [225], extended with one p-type diffuse function for anion [228] and one d-type polarization function [229].

- For Al (only in the $(CeO_8Al_2O_4)^{15-}$ cluster), we use a [Ne] core potential and a $(7s6p1d)/[2s3p1d]$ valence basis set [225] including one d-type polarization function [229].

Extra basis sets are included in those cations adjacent to the clusters, to improve the degrees of orthogonality between the cluster molecular orbitals and the environmental orbitals. For Y^{3+}, we represent $3d, 4s, 4p$ orbitals with a $(13s10p7d)/[1s1p1d]$ basis and for Al^{3+}, we represent the $2s, 2p$ orbitals with $(11s8p)/[1s1p]$ basis. Around $(CeO_8)^{13-}$ cluster, there are four Y^{3+} and ten Al^{3+}(four Al_{oct} and six Al_{tet}) as *second neighbors*. Around $(CeO_8Al_2O_4)^{15-}$ cluster, there are ten $Y^{3+}$and twelve Al^{3+}(eight Al_{oct} and four Al_{tet}). We will show in Chapter 9 that La^{3+} is one of these *second neighbors* in Ce,La:YAG. Then, we use the La^{3+} $4d, 5s, 5p$ ($(15s10p8d)/[1s1p1d]$) atomic orbitals as obtained in self-consistent embedded-ion calculations on $LaMnO_3$ [230].

Once defined the cluster, the AIMP embedding and the point charges array, spin-orbit free relativistic calculations have been performed in such embedded $(CeO_8)^{13-}$ and $(CeO_8Al_2O_4)^{15-}$ clusters. Bonding, static and dynamic correlation, and scalar relativistic effects are taken into account in state-average complete active space self consistent field (SA-CASSCF) [160, 161, 162] plus multistate second-order perturbation theory (MS-CASPT2) [70, 231, 232, 233] calculations performed with a scalar relativistic many-electron Hamiltonian. These calculations are performed with the program MOLCAS [101].

In the SA-CASSCF calculations, a $[4f, 5d, 6s]^1$ CAS was used, meaning that the wave functions are configuration interaction (CI) wave functions of all configurations with the unpaired electron occupying one of the thirteen molecular orbitals of main character Ce-$4f$, Ce-$5d$, and Ce-$6s$. The molecular orbitals are chosen so as to minimize the average energy of the thirteen states. No symmetry was used in these calculations. However, in Ce:YAG, our material of reference, DFT structure is found to retain the local D_2 symmetry (Section 6.1), and the states can be classified as follows: the first seven states result from the splitting of the $4f^1\ {}^2F$ atomic term (1^2A, 1^2B_1, 2^2B_1, 1^2B_2, 2^2B_2, 1^2B_3, and 2^2B_3), five states well above result from the splitting of the $5d^1\ {}^2D$ atomic term (2^2A, 3^2A, 3^2B_1, 3^2B_2, and 3^2B_3), and a final state is linked to the $6s^1\ {}^2S$ atomic term (4^2A). We will see in chapters 9, 10 and 11 how this symmetry is lost because of the presence of codopant atoms or antisite defects and, then, the thirteen states belong to the only irreducible representation of the point group C_1. They are classified as $1-13^2A$, although the relative energies of the $4f^1$, $5d^1$, and $6s^1$ configurations are maintained, as we will see later, and $1-7^2A$ are basically of Ce-$4f^1$ character, $8-12^2A$ are basically of Ce-$5d^1$ character, and 13^2A of Ce-$6s^1$ character.

Using the CASSCF (configuration interaction) wave functions and the (occupied and virtual) molecular orbitals, MS-CASPT2 calculations are done where the dynamic correlation effects (which are missing at the CASSCF level) of the $5s, 5p, 4f$ and $5d$ electrons of Cerium and the $2s$ and $2p$ electrons of the eight oxygen atoms are added.

8.1.2.1 Emission spectra

Since PBC-DFT is a ground state theory, geometries obtained for Ce:YAG, Ce,La:YAG, Ce,Ga:YAG and Ce,ADs:YAG can be used only to calculate absorption spectra. However, the problem of the Stokes shift, studied within the Ce,ADs:YAG framework in this work, requires the calculation of emission spectra as well. Then, we have followed an inverse procedure: using the embedding coordinates of Ce,ADs:YAG, we relax the cluster coordinates for the first $5d$ state and, using them, we calculate the vertical emission spectra.

Because of the lack of symmetry in our systems, optimizations of geometry are only affordable at the CASSCF level. For the same reason, we perform the geometry relaxations in different stages. In a first stage, we fix the coordinates of the two AlO_2 moieties, allowing the CeO_8 moiety of the $(CeO_8Al_2O_4)^{15-}$ cluster to move. We use a $(14s10p10d8f)/[5s4p5d3f]$ basis for Ce, a $(5s6p)/[2s3p]$ basis for O and a $(7s6p)/[2s3p]$

basis for Al, smaller than the basis used for absorption spectra calculations. In a second stage and, using the coordinates arising from the previous calculation, we allow also the two AlO_2 moieties to relax, keeping the same *small* basis. Using this structure, we fix again the AlO_2 moieties and use a larger basis, the same basis as for absorption spectra calculations: Ce $(14s10p10d8f3g)/[6s5p6d4f1g]$, O $(5s6p1d)/[3s4p1d]$ and Al $(7s6p1d)/[2s3p1d]$. The resulting structure is used in the final stage, where the two AlO_2 moieties are also allowed to relax and we use the bigger basis. Each final structure of stages above can be used to calculate a vertical spectrum at the CASPT2 level using the $(CeO_8Al_2O_4)^{15-}$ cluster.

This procedure is also followed for the first f state, in order to find the final ground state geometry and calculate the absorption and emission spectra within an unified framework. These ground state geometries calculated at the CASSCF level, are expected to be different to a greater or lesser extent to those obtained from PBC-DFT calculations, because of the intrinsic differences between both approaches.

All the vertical spectra of both ground and first excited states and, then, the Stokes shift, have been calculated using the $(CeO_8Al_2O_4)^{15-}$ cluster, even if the geometry relaxed in a given stage is only that of the CeO_8 moiety.

8.1.3 Analysis of the spectra

Each set of (seven f, five d and one s) levels obtained in the calculations detailed in the previous section allow us to calculate vertical transitions between any of these levels. Focusing on the transition from the lowest states of the Ce-$4f^1$ and Ce-$5d^1$ electronic configurations, which we will call here $1-4f^1$ and $1-5d^1$ for simplicity, we can decompose it in terms involving both the $4f^1$ and $5d^1$ centroids and the $4f^1$ and $5d^1$ ligand fields contributions, as seen on diagram of Fig. 8.2.

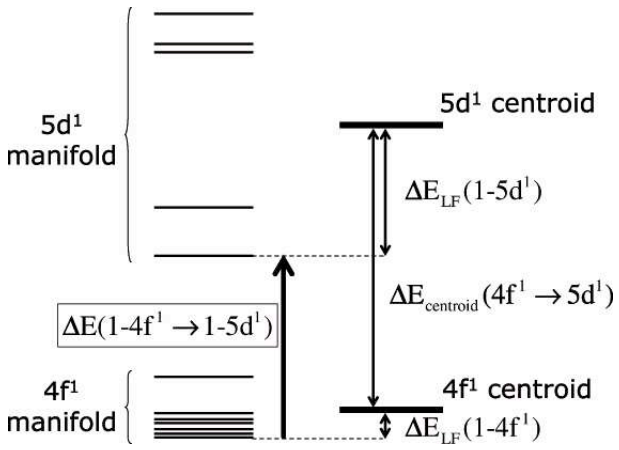

Figure 8.2: Schematic representation of the $4f^1$ and $5d^1$ manifolds of the Ce_Y defect.

According to the diagram, the transition energy between these state can be expressed as the following sum,

$$\Delta E(1-4f^1 \rightarrow 1-5d^1) = \Delta E_{\text{centroid}}(4f^1 \rightarrow 5d^1) + \Delta E_{\text{ligand-field}}(1-4f^1 \rightarrow 1-5d^1)\,.$$

The centroid contribution is the energy difference between the averages of the two configurations,

$$\Delta E_{\text{centroid}}(4f^1 \rightarrow 5d^1) = \frac{1}{5}\sum_{i=1,5} E(i-5d^1) - \frac{1}{7}\sum_{i=1,7} E(i-4f^1)\,,$$

and the ligand-field contribution is the difference between the stabilization energies of the initial and the final states with respect to their configurational averages,

$$\Delta E_{\text{ligand-field}}(1-4f^1 \rightarrow 1-5d^1) = \Delta E_{\text{LF}}(1-4f^1) - \Delta E_{\text{LF}}(1-5d^1)\,,$$

$$\Delta E_{\text{LF}}(1-4f^1) = \frac{1}{7}\sum_{i=1,7} E(i-4f^1) - E(1-4f^1)\,,$$

$$\Delta E_{\text{LF}}(1-5d^1) = \frac{1}{5}\sum_{i=1,5} E(i-5d^1) - E(1-5d^1)\,.$$

$\Delta E_{\text{LF}}(1-4f^1)$ and $\Delta E_{\text{LF}}(1-5d^1)$ are a measure of the effective ligand field strengths on the $4f$ and $5d$ shells, respectively. The same analysis can be applied to any of the individual $4f \rightarrow 5d$ transitions.

We perform this analysis to transitions of interest in all the A, B, C and D spectra (outlined in Table 8.1) and, then, we can not only quantify the total change in the transition when going along the $A \rightarrow B \rightarrow C \rightarrow D$ series but also extract information on the specific effect exerted by the codopant/ADs on each component of the transition. Thus, this is an added tool for a deeper understanding on the structure-luminescence relationship.

8.2 A reference: Ce:YAG absorption spectrum

Pure YAG starts absorbing light above 50000 cm^{-1} [222] but the presence of Ce^{3+} makes the material to absorb a much lower energies; four absorptions are detected at 22000, 29400, 37000 and 44000 cm^{-1} [28]. In principle, the three first transitions could be assigned to the absorption from the lowest lying f state (1^2B_2) to the first three d states (2^2A, 3^2B_3 and 3^2A) of Ce^{3+} [234]. However, this assignment has been carefully revised and refused later on, and works of Tanner *et al.* [235] and Zhao *et al.* [236] conclude that the 37000 cm^{-1} band is not due to the impurity, confirming the initial assignment of Blasse and Bril [28]. Actually, Zorenko *et al.* attribute this 37000 cm^{-1} band to self-trapped excitons intrinsic to the host [237]. As we will see in this section, our calculations and previous high level *ab initio* calculations [41] support this picture, since the third calculated absorption lies around 47000-48000 cm^{-1}, much closer to the fourth peak detected (44000 cm^{-1}). Only an early *ab initio* calculation does associate the 37000 cm^{-1} with the impurity [238], but it lacks of dynamic correlation within the $(CeO_8)^{13-}$ cluster and uses a crude embedding potential just made of point charges, which is known to be insufficient for these materials [18].

The relative energies of the Ce $4f$, Ce $5d$ and Ce $6s$ levels of Ce:YAG according to our calculations are shown in Table 8.2, in comparison to those of Ref. [41]. Ce-O distances of ground state $4f^1$ $(CeO_8)^{13-}$ clusters of both calculations are in a good agreement, in spite of they are calculated in two completely different ways: we do obtain the cluster coordinates from PBC-DFT calculations relaxing all the atoms in the cell and, in Ref. [41], they are obtained by relaxation of only the cluster at CASPT2 level, imposing D_2 symmetry in the Ce_Y site. According to labels of Fig. 6.3, d(Ce-O_s)/d(Ce-O_l) are 2.373/2.468 in this work and 2.370/2.441 in Ref. [41].

Two different calculations using two different sets of embedding coordinates have been performed for each $(CeO_8)^{13-}$and $(CeO_8Al_2O_4)^{15-}$: One the one hand, the AIMP embedding shell from the perfect YAG unit cell calculated in this work and (Table 8.2, data columns 2 and 4), on the other, the YAG unit cell as coming from DFT calculations after relaxation without imposing restrictions (Table 8.2, data columns 3 and 5). In both $(CeO_8)^{13-}$ and $(CeO_8Al_2O_4)^{15-}$, we observe that spectra obtained by using YAG or Ce:YAG AIMP coordinates are almost identical, which supports the picture of a major distortion only in the substituted site and surroundings (cluster), whereas the small differences are due to the lesser distortion in second coordination shell and, residually, beyond. From now on, we will take as a reference spectra of columns 3 and 5 of Table 8.2, that is, the more realistic Ce:YAG spectra, in the sense that distortion printed by Ce_Y is also taken into account in the AIMP shell, no matter how small it is.

If we compare these absorption spectra with the experimental 22000, 29400 and 44000 cm^{-1} values attributed to Ce^{3+} mentioned above, we see that, for $(CeO_8)^{13-}$ our calculations overestimate the three first $4f \rightarrow 5d$ transitions in $\sim$ 5000, 800 and 4000 cm^{-1}. This is partially corrected in $\sim$ 1000 cm^{-1} for the first transition when we go to the $(CeO_8Al_2O_4)^{15-}$ cluster, but both second and third transitions remain unchanged.

Spin-orbit coupling effects are missing in these calculations, but, since our calculations and those on Ref. [41] are comparable up to the CASPT2 level and structural changes due to spin-orbit effects are expected to be irrelevant, we assume that the differences between the spectra when including spin-orbit effects should be very similar in both calculations. Then, as found in Ref. [41], we can predict a (3+4) splitting in the $4f$ manifold which increases the $4f$ centroid in $\sim$1000 cm^{-1}, whereas the five $5d$ levels would rise in energy uniformly $\sim$1000 cm^{-1} (and, thus, also the $5d$ centroid). Then, all the $4f \rightarrow 5d$ transitions of Ce:YAG are predicted to experiment a uniform increment of around 1000 cm^{-1}. Moreover, we expect such uniform increment in the vertical spectra calculated both in the ground state geometry $4f$ and in the first excited state $5d$ one. Thus, if the increment of the transition is the same for both geometries, the Stokes shift, which is the target of this work and involves the same transition in both geometries, would not change upon spin-orbit effects.

Table 8.2: Relative energies of the levels of the Ce-$4f^1$, Ce-$5d^1$, and Ce-$6s^1$ configurations of Ce:YAG. The atomistic structures of the $(CeO_8)^{13-}$ and $(CeO_8Al_2O_4)^{15-}$ embedded clusters have been calculated in ground state periodic DFT calculations. Results in comparison with calculations on $(CeO_8)^{13-}$ of Ref. [41]. All numbers in cm^{-1}.

Material:				Ce:YAG		
Embedded cluster:		$(CeO_8)^{13-}$	$(CeO_8)^{13-}$	$(CeO_8)^{13-}$	$(CeO_8Al_2O_4)^{15-}$	$(CeO_8Al_2O_4)^{15-}$
Embedding AIMP		YAG[1]	YAG[2]	Ce:YAG[3]	YAG[2]	Ce:YAG[3]
	D_2	Ref. [41]	This work	This work	This work	This work
$4f^1$ levels						
	$1\ ^2B_2$	0	0	0	0	0
	$1\ ^2B_3$	280	284	274	24	38
	$1\ ^2B_1$	440	291	290	172	202
	$1\ ^2A$	620	526	518	405	416
	$2\ ^2B_1$	700	588	577	440	443
	$2\ ^2B_2$	710	649	638	514	516
	$2\ ^2B_3$	2710	2551	2530	2409	2419
$5d^1$ levels						
	$2\ ^2A$	23010	24791	24887	23740	23853
	$3\ ^2B_3$	30670	30076	30187	30086	30169
	$3\ ^2A$	47040	48050	48080	48113	48112
	$3\ ^2B_2$	51600	49704	49705	48621	48700
	$3\ ^2B_1$	52840	52665	52568	52307	52221
$6s^1$ level						
	$4\ ^2A$		67375	67133	61427	61214

[1] YAG experimental coordinates, Ref.[179]

[2] perfect YAG calculated coordinates, Section 5.2

[3] relaxed Ce:YAG calculated coordinates, Section 6.1

Chapter 9

La codoped Ce:YAG

This chapter is aimed to report the calculated shift induced by La-codoping on Ce:YAG absorption spectrum and analyze the reasons behind it. This is performed following the steps described in Section 8.1. Then, we present in Section 9.1 the results of ground state PBC-DFT calculations on the local structure around the active impurity Ce_Y in YAG cells containing one Ce_Y plus one La_Y atoms per unit cell, that is, $Y_{2.75}Ce_{0.125}La_{0.125}Al_5O_{12}$ (Ce,La:YAG). The effects of La-codoping on electronic structure of Ce:YAG are presented in Section 9.2. In Section 9.3, PBC-DFT calculated structures are used in wavefunction-based CASSCF/CASPT2 calculations and Ce-4f, 5d and 6s levels are compared to those of Ce:YAG (Section 8.2). $(CeO_8)^{13-}$ and $(CeO_8Al_2O_4)^{15-}$ clusters are embedded in different cells with increasingly level of realism and the shift of the Ce-4f, 5d and 6s levels with respect to those of the reference Ce:YAG are analyzed for each embedding, in terms of the variation of the different component of the spectra. Conclusions of this chapter are outlined in Section 9.4 and data tables collected in Section 9.6.

9.1 Effects of La on the local structure of the active defect Ce_Y

In the $Y_{2.75}Ce_{0.125}La_{0.125}Al_5O_{12}$ material under study in this work, both Ce^{3+} and La^{3+} ions substitute one out of the 24 Y positions of the YAG unit cell, leading to a $\sim 4\%$ of each lanthanide. With this concentration, seven Ce_Y-La_Y different double substitutional defects can be formed, corresponding to all double substitutions of this kind in which the distance between the Ce_Y and La_Y sites placed in the same YAG unit cell are, before relaxation, smaller than or equal to the distance between this Ce_Y site and another translation equivalent La_Y site lying in a different unit cell. These seven defects are shown in Fig. 9.1, where the La_Y are labeled from 1 to 7 (from the nearest to the furthest to Ce_Y). In Table 9.1 we show the corresponding Ce_Y-La_Y distances and the relative energies of the seven double defects (ΔE_{rel}) with respect to the most stable, together with the Y-Y reference distances in YAG and the nearest distances between impurities in adjacent unit cells.

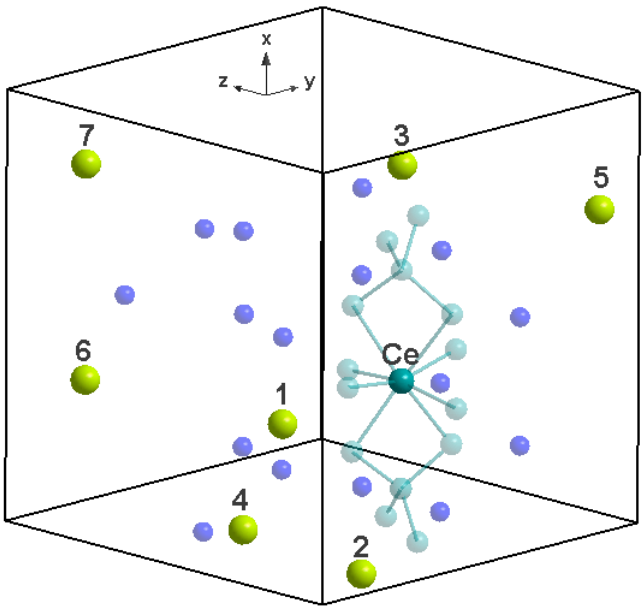

Figure 9.1: Scheme of the seven different La_Y (green) - Ce_Y (greenish blue) ordered according to the La_Y-Ce_Y distance before relaxation: (1) 3.709 Å, (2) 5.666 Å, (3) 6.057 Å, (4) 6.772 Å, (5) 7.103 Å, (6) 8.566 Å and (7) 10.491 Å. Other equivalent Y positions in semitransparent blue. $CeO_8Al_2O_4$ moiety in semitransparent greenish blue.

The energy differences between the defects are not large, but two of them are clearly more stable than the others: they correspond to the shortest Ce-La distances.

In Table 9.1 the interaction energies between the single defects, (ΔE_{sd}), are also shown. They correspond to the following process

$$8\ Y_{2.875}Ce_{0.125}Al_5O_{12} + 8\ Y_{2.875}La_{0.125}Al_5O_{12} \rightarrow 8\ Y_3Al_5O_{12} + 8\ Y_{2.75}Ce_{0.125}La_{0.125}Al_5O_{12}$$

and measure the change in energy from the two non-interacting defects placed in different cells to the situation of both in the same YAG cell. The binding energy between two relaxed single defects to form one relaxed double defect results to be favorable in all cases, being 59 meV for defect 1 and 62 meV for defect 2, both much smaller than the binding energies found between defects in ADs:YAG (Chapter 7).

At this point, we should point out that the E *versus* lattice constant analysis for double defects 1 and 2 (with internal relaxation in each point) shows an increment of +0.32% for defect 1 (a=12.153 Å) and +0.30% for defect 2 (a=12.150 Å). From these values, we decide to use the perfect YAG lattice constant (a=12.114 Å) as in previous defects. Moreover, it can be seen than the closer the La_Y, the bigger the lattice constant. This leads us to state that defects 1 and 2 are a little bit more separated in energy than it is shown in Table 9.1 because for the current lattice constant a, defect 1 is a little bit more strained than defect 2 and a rigorous use of different equilibrium lattice constants would lead to a more stabilization of defect 1 with respect to defect 2. Anyway, and because the

energy differences are indeed small, we carry out our study of double defects 1 and 2 in parallel.

The respective formation energies of defects 1 and 2 at low concentration according to the process

$$8\ Y_3Al_5O_{12} + Ce^{3+}_{vacuum} + La^{3+}_{vacuum} \rightarrow 8\ Y_{2.75}Ce_{0.125}La_{0.125}Al_5O_{12} + 2 \times Y^{3+}_{vacuum}$$

are 3.764 eV and 3.767 eV for defect 1 and defect 2 respectively, mainly coming from the high formation energy of the La_Y defect (Section 6.1.3).

The stress energies of the cells containing double defects 1 and 2, that is, the energy descents when all atoms relax their positions after Ce and La substitute two Y in the YAG lattice, are 465 meV and 460 meV/defect respectively. These values are only slightly larger than the sum of the stress energies of the individual defects (Ce_Y, 125 meV/defect; La_Y, 323 meV/defect; total 448 meV).

The structures of the two most stable double defects (defect 1 and defect 2 in Table 9.1) are shown in Fig. 9.2 and detailed in Table 9.1 (bottom chart).

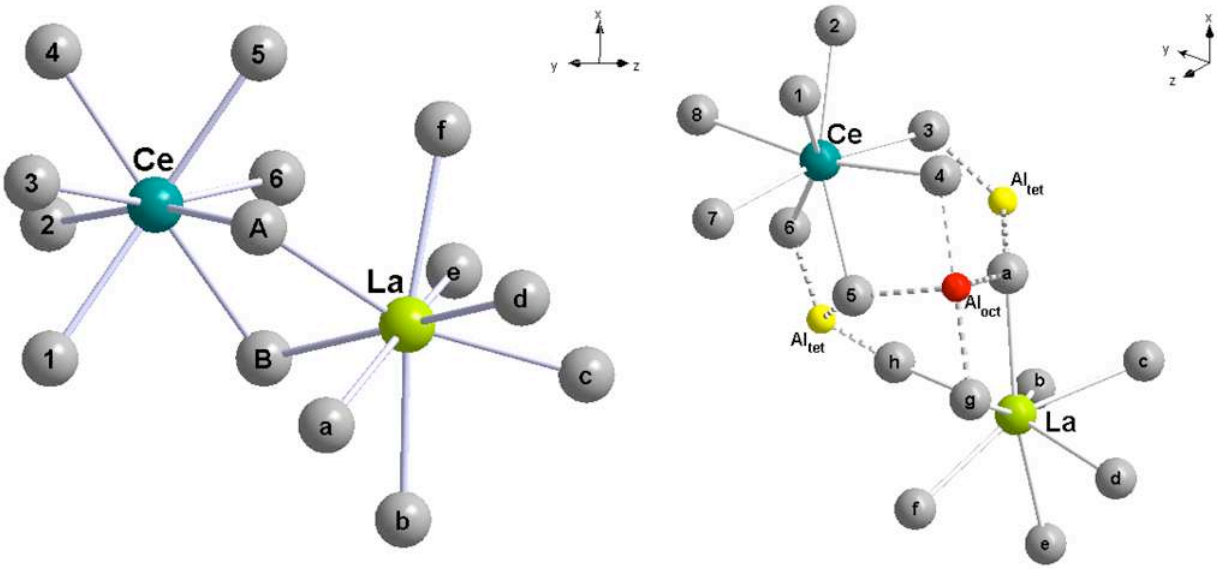

Figure 9.2: Representation of the two most stable Ce_Y-La_Y disubstitutional defects. Left: defect 1. Right: defect 2.

In defect 1, which is the most stable of all, there are significant distortions around the Ce_Y and La_Y sites with respect to the single defects. The overall effect of La on the coordination shell of Ce is an expansion (of 0.010 Å on average). On average, the four oxygens of type O_s (1, 4, 5, B), which are the nearest to Ce, experience an expansion of 0.019 Å, whereas the remaining four oxygens, of type O_l (2, 3, 6, A), which are the most distant to Ce, maintain their distance (average expansion of 0.001 Å). On the other hand, the overall effect of Ce on the coordination shell of La is a contraction (of 0.006 Å on average). In this case, the four nearest oxygens of type O_s maintain their average distance

to La whereas the more distant O_l oxygens experience an average contraction of 0.013 Å. Individually, the eight oxygens around Ce and the eight around La suffer very different displacements from their reference positions, resulting in eight different Ce-O distances and eight different La-O distances, with the D_2 local site symmetries around Ce_Y in Ce:YAG and around La_Y in La:YAG being completely lost in Ce,La:YAG. The largest displacement is experienced by O_B, which is one of the two bridging oxygens between the CeO_8 and LaO_8 moieties; it increases its distance to Ce by 0.054 Å and gets closer to La by 0.040 Å. However, the other bridging oxygen, O_A, does not experience an important displacement. The displacement of O_B may be observed together with the change in the Ce-La distance and the displacements of other oxygens: Ce-La suffers an elongation of 0.01 Å with respect to Ce-Y in Ce:YAG, which indicates that Ce and La push each other and they shift away in order to relax the stress energy; Ce gets closer to O_2 and La to O_c and to O_d, all of them around 0.01 Å, as a result of Ce and La pushing each other away (these are all oxygens opposite to the respective codopant), and the remaining oxygens either stay or shift away a little bit from the impurities in order to accommodate the previous atomic rearrangements.

It is interesting to see that the Ce-La distance is very similar to the Y-La distance in La:YAG whereas it is significantly longer than the Ce-Y distance in Ce:YAG. This means that the relative positions of the cations is dominated by La, which pushes away Ce and Y in an equal amount. Then, the effect of La-codoping on Ce in defect 1 can be described as an anisotropic pushing that forces Ce to weaken its bonding with the bridging oxygen O_B; this oxygen gets away from Ce and closer to La and the remaining oxygens slightly relocate their positions, both around Ce and around La.

In defect 2, where Ce and La locate at around 5.7 Å from each other, the distortions around La with respect to La:YAG are negligible and the Ce-La distance is virtually equal to the Y-La distance in La:YAG, although 0.01 Å shorter than Ce-Y in Ce:YAG. This supports the idea developed after the analysis of defect 1 that La controls the relative cation location (Ce-La in Ce,La:YAG and Y-La in La:YAG). As in defect 1, the anisotropic effect of La on the Ce site alters the bonding between Ce and the oxygens, which in this case makes significantly longer Ce-O_3 and Ce-O_5 and shorter O_4 bonds, with an overall expansion of the first coordination shell of oxygens of 0.009 Å (on average, the closest oxygens of type O_s expand 0.005 Å and the most distant O_l oxygens expand 0.012 Å). However, the feedback effect of these rearrangements on the LaO_8 moiety are negligible in this case because no bridging oxygens are present and the surroundings of La are basically untouched with respect to La:YAG.

9.2 Effects of La on Ce:YAG electronic structure

Band structures of defects 1 and 2 are shown in Fig. 9.3. They present the same pattern as Ce:YAG band structure (Fig. 6.6), with Ce states placed within the pure YAG gap, not only at the top of the valence band but also at the bottom of the conduction band. More information can be extracted for PDOS of Ce,La:YAG material. Fig. 9.4 shows the total

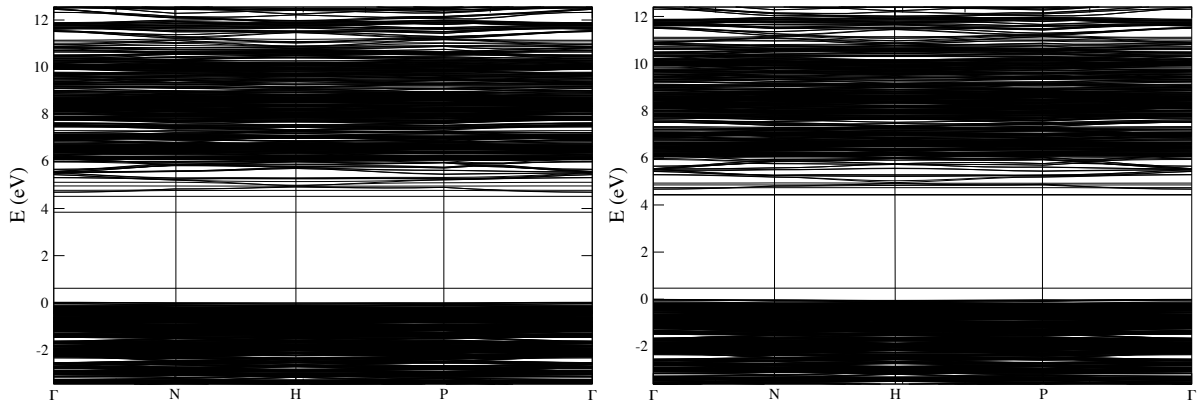

Figure 9.3: Band structure of the two most stable Ce_Y-La_Y disubstitutional defects. Left: defect 1. Right: defect 2.

DOS of Ce,La:YAG corresponding to the structure of defect 1, together with its PDOS of Ce, La, Y, Al, and O atoms and the orbital decomposition of the Ce PDOS.

Equivalent results in the case of defect 2 are very similar to these. The total DOS of Ce,La:YAG resembles very much those of the parent materials Ce:YAG and La:YAG, because the contribution of Y, Al, and O are very similar in the three materials. Some features to remark are, first, that Ce,La:YAG shows the peaks between -14 and -12 eV that correspond to the superposition of basically independent La-5p and Ce-5p states, and, second, that the structure of the O-2p valence band is remarkably closer to the same band in Ce:YAG than in La:YAG; this is a consequence of the contribution of $4f$ states with energies in the O-2p window, which is significant in Ce but negligible in La.

It is interesting to observe in the bottom of Fig. 9.4 the shift of 0.25 eV experimented to lower energies by the Ce-$4f$ peak upon La codoping. We observe that this shift is also experienced by Ce innermost $5s$ and $5p$ orbitals, which indicates that this is not a bonding effect, but the consequence of the change of the electrostatic field on Ce due to its off-center displacement forced by the presence of La. Also we observe changes in the PDOS of O_B in Ce,La:YAG, which is the oxygen in the CeO_8 moiety that suffers the biggest effect upon La-codoping. When we compare it with its PDOS in Ce:YAG we can see how the higher energy contribution is slightly shifted to lower energies. This is a consequence of the bonding between Ce and O_B diminishing, since this is the contribution of the states with highest mixing between Ce-$4f$ and O-2p.

As we mentioned before in the case of Ce:YAG, we cannot identify peaks in the DOS lying above the Fermi level of Ce,La:YAG with the observed $4f \rightarrow 5d$ blue absorptions of the Ce defects and, as a consequence, we cannot use these results to calculate the red-shift experienced by these transitions upon La-codoping. In this respect, wave function based embedded-cluster calculations on this materials take advantage of the present structural studies and be used to make reliable predictions on the effects of La-codoping on the shift of the $4f \rightarrow 5d$ electronic transitions. Such kind of results for Ce,La:YAG are present in Section 9.3.

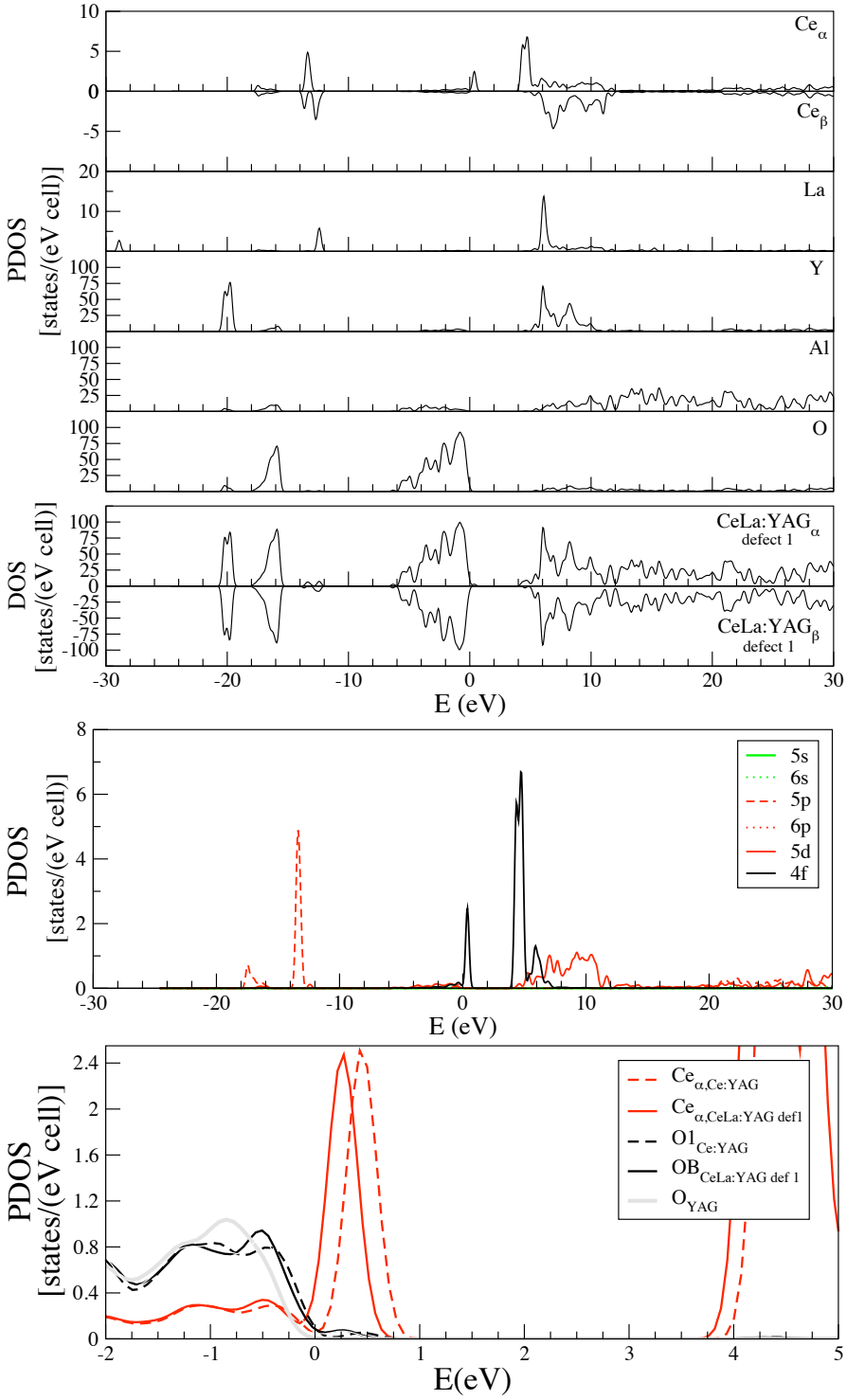

Figure 9.4: PDOS of Ce, La, Y, Al, and O atoms, total DOS, and orbital decomposition of the Ce α PDOS for the most stable double substitutional defect (defect 1) in Ce,La:YAG.

9.3 Effects of La on Ce:YAG absorption spectrum

In Table 9.2, we show the energies of the levels of the Ce-$4f^1$, Ce-$5d^1$, and Ce-$6s^1$ configurations relative to the ground state, as calculated in this work for $(CeO_8)^{13-}$and $(CeO_8Al_2O_4)^{15-}$for the most stable Ce,La:YAG cell (defect 1) and compared to those of Ce:YAG (Section 8.2).

The differences between these two calculations, tabulated as *shifts* for each level upon La-codoping in Table 9.2, arise from the different final geometries of the clusters involved, the different embedding potentials (unit cell of YAG distorted according to the presence of only Ce or both Ce and La) and the presence of one La atom in Ce,La:YAG represented by the corresponding AIMP. The position of La_Y with respect to the $(CeO_8)^{13-}$ and $(CeO_8Al_2O_4)^{15-}$ clusters of Ce,La:YAG (defect 1) used in these calculations is shown in Fig. 9.5.

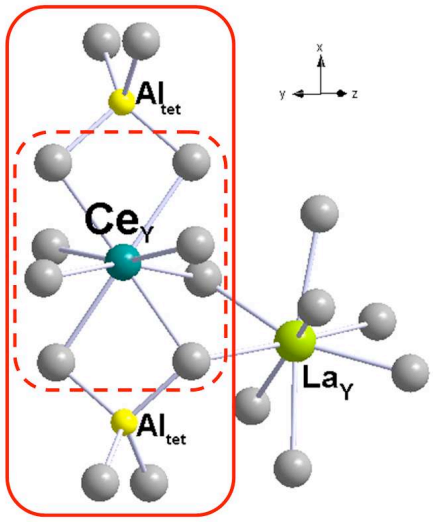

Figure 9.5: $(CeO_8)^{13-}$ (dashed red line) and $(CeO_8Al_2O_4)^{15-}$ (solid red line) clusters with La_Y as second neighbor in Ce,La:YAG (defect 1) .

Data on Table 9.2 show that we find very similar shifting results for $(CeO_8)^{13-}$ and $(CeO_8Al_2O_4)^{15-}$. The overall result for both is absolutely comparable: the first $4f \rightarrow 5d$ transition is predicted to have red shift (243 cm^{-1} in $(CeO_8)^{13-}$and 220 cm^{-1} in $(CeO_8Al_2O_4)^{15-}$) and the second $4f \rightarrow 5d$ transition is predicted to have a blue shift (543 cm^{-1} in $(CeO_8)^{13-}$and 586 cm^{-1} in $(CeO_8Al_2O_4)^{15-}$). Moreover, the analysis of the factors leading to these shifts is totally analogous for both clusters. Accordingly, the qualitative analysis is presented and discussed in terms on the $(CeO_8Al_2O_4)^{15-}$ cluster results.

These results are in agreement with experimental findings. Red shift of the $4f \rightarrow 5d$ Ce:YAG luminescence is found to appear as a consequence of La codoping of Ce:YAG [38], and of Gd codoping [28, 32, 38, 39, 40]. Particular red shift of the first $4f \rightarrow 5d$ transition has been observed upon Gd codoping [28]. The reasons behind the shifts are thought to

be mostly structural and the same for Gd and La codopings [38, 35]. Detailed quantitative comparisons between experimental and theoretical values of the red shifts cannot be made because absorption experiments in the specific material studied in this work, $Y_{2.75}Ce_{0.125}La_{0.125}Al_5O_{12}$, are missing and the shifts are known to be quantitatively different for La and Gd codoping [38], for absorption and emission [28], and for different codopant concentrations [39, 35]. In any case, we think our computed red shift might be overestimated, because Tien *et al.* [39] obtained an approximate rate of 80 cm^{-1} red shift per 10 atom % of Gd codoping for the excitation peak of Ce,Gd:YAG, whereas the theoretical 220 cm^{-1} red shift corresponds to 4.1 atom% of La codoping and La produces smaller red shifts than Gd [38].

We can also compare our calculated blue shift experimented by the second $4f \rightarrow 5d$ transition with the blue shift measured by Blasse and Bril in such transition of Gd,Ce:YAG [28], in opposite to the red shift of the first absorption. They found a 200 cm^{-1} blue shift upon 50 atom % of Gd codoping (from 29400 cm^{-1} to 29600 cm^{-1}). As before, we think that our calculated value of 586 cm^{-1} is overestimated. The fact that the shifts of the two first $5d^1$ levels have opposite signs is an indication of the strong anisotropy of the effects of the present codopings, because both states would be expected to shift more or less uniformly under isotropic perturbations, such as uniform increments or decrements of the ligand field. Shifts of higher $5d^1$ states, as well as of $4f^1$ and $6s^1$ states, upon codoping have not been reported, to the best of our knowledge. The calculations predict much smaller shifts of the $4f^1$ states than the lowest $5d^1$ states, and a much larger shift of the $6s^1$ state. It is interesting to analyze the reasons behind these shifts because the interpretation by means of an increase of the ligand field as a consequence of a local compression around Ce (Ref. [35]) is not supported by the global expansion found in our calculations. Moreover, the effective ligand field on the $5d$ shell, as measured by the $5d$ shell splitting, does not only result from the distances between ligands and Ce, but also from bonding and electronic effects in general. Besides, not only the effective ligand field on Ce can change upon La-codoping, but also the energy difference between the averages of the $5d^1$ and $4f^1$ manifolds ($5d^1$ and $4f^1$ centroids), and both of them can contribute to the red/blue shift experimented by first and second $4f \rightarrow 5d$ transitions. Then, we resort to the analysis outlined in Section 8.1.3.

We use the diagram on Fig. 8.2 in order to analyze the different contributions of the spectra on the individual $4f \rightarrow 5d$ transitions. These transitions are decomposed according to

$$\begin{aligned}\Delta E(4f \rightarrow 5d) &= \Delta E_{\text{centroid}}(4f \rightarrow 5d) + \Delta E_{\text{ligand-field}} \\ &= \Delta E_{\text{centroid}}(4f \rightarrow 5d) + \Delta E_{\text{LF}}(4f) - \Delta E_{\text{LF}}(5d).\end{aligned}$$

Moreover, using this diagram in the A, B, C and D calculations described in Section 8.1.2, we can track how each contribution of the total shift of a given transition do change when going from Ce:YAG to Ce,La:YAG. Particularly in this chapter, A is our reference calculation, in which both cluster coordinates and AIMP embedding come from DFT relaxed structure of Ce:YAG. D is the final Ce,La:YAG calculation, in which both

cluster coordinates and AIMP embedding come from the relaxed structure of Ce,La:YAG. The first intermediate calculation, B, is performed using the Ce,La:YAG coordinates of the $(CeO_8Al_2O_4)^{15-}$ cluster but keeping the AIMP embedding of Ce:YAG from calculation A. In this way, $A \rightarrow B$ accounts for changes due to only structural distortions on the cluster, that is, direct effects of La in the immediate neighborhood of Ce_Y. The second intermediate calculation, C, is performed using both Ce,La:YAG coordinates and AIMP embedding but without taking into account the presence of La, that is, with a Y AIMP in the Y site occupied by La. Thus, $B \rightarrow C$ accounts for the long-range distortions that the presence of La stamps in the whole YAG unit cell. The final calculation D goes a step beyond C by including the AIMP for La wherever appropriate. Thus, $C \rightarrow D$ accounts only for the electronic effects of the La_Y defect leading to the global change $A \rightarrow D$.

Ce-$4f^1$, Ce-$5d^1$, and Ce-$6s^1$ levels of A, B, C and D calculations, as well as the components of the first and second $4f \rightarrow 5d$ transitions according to Fig. 8.2, are shown in Table 9.3.

The variation on the components in each step along the $A \rightarrow B \rightarrow C \rightarrow D$ series is tabulated in Table 9.4.

In the last column of Table 9.4, we can see that the red shift of the first $4f \rightarrow 5d$ transition (-220 cm^{-1}) has significant ligand field contributions (-97 cm^{-1}) and centroid contributions (-123 cm^{-1}), in similar amounts. The centroid contribution is dominated by the structural distortions (-101 cm^{-1}) and, among them, by the first-shell distortion (-77 cm^{-1}). On the other hand, the ligand field contribution to the red shift is not due to the structural distortions induced by codoping, but to the electronic effects of La itself (-149 cm^{-1}); in fact, the contribution from the structural distortions is a blue shift (+52 cm^{-1}) that results from a reduction of the effective ligand field on the $5d$ shell, which is consistent with the average expansion experienced by the eight oxygens of the first coordination shell of Ce and the rest of the lattice upon La-codoping. This expansion is, in turn, consistent with the fact that the lattice constant of Ce:YAG has been found to increase with Gd and La codoping [39, 35].

The blue shift of the second $4f \rightarrow 5d$ transition (586 cm^{-1}) is mostly due to ligand field effects (709 cm^{-1}), which result mainly from an important rising of the $2-5d^1$ level among the $5d^1$ manifold (of 659 cm^{-1} with respect to the $5d^1$ centroid), most of it due to the first-shell distortion. This result, put together with the small effect that the lattice distortions have on the effective $5d$ ligand field, as we have seen above, indicate large ligand field anisotropies induced by the La-codoping.

It is also remarkable that the $4f-5d$ centroid, $\Delta E_{\text{centroid}}(4f^1 \rightarrow 5d^1)$, is lower upon La-codoping in spite of the fact that the ligands expand around Ce, because the only model which is under use for this quantity, to the best of our knowledge, is that of Judd and Morrison [6, 7, 8] and, according to it, the $4f-5d$ centroid should increase when the distances Ce-O increase. In this model, the centroid is exclusively due to the different ligand (oxygen) polarization by a Ce-$4f$ and a Ce-$5d$ electron and the distance between the electron and the Ce nucleus is assumed to be negligible with respect to the Ce-O distance. This model is useful for a rationalization of $4f-5d$ centroids of lanthanide ions in many

hosts [9] but, according to these first-principles calculations, it can be misleading if used for predicting small centroid shifts associated to small ligand distortions around lanthanides. Similar limitations of the model have been found in previous *ab initio* calculations [239].

Regarding defect 2, where La_Y is not a second neighbor of Ce_Y anymore, we have performed analogous calculations of the $4f$, $5d$ and $6s$ levels and their shift from Ce:YAG. These data are in Table 9.5. We find again that similar quantitative results are found for $(CeO_8)^{13-}$ and $(CeO_8Al_2O_4)^{15-}$ predicting both of them a blue shift for the first and the second $4f \rightarrow 5d$ transitions. We have performed analogous intermediate $A \rightarrow B \rightarrow C \rightarrow D$ calculations using embedding potentials of defect 2 (Table 9.6) to track the variation of the different elements of the transitions (Fig. 8.2). In these calculations, as in defect 1 ones, calculation A is our reference, with the $(CeO_8Al_2O_4)^{15-}$ cluster embedded in Ce:YAG AIMP. Calculation B changes $(CeO_8Al_2O_4)^{15-}$ coordinates to those of Ce,La:YAG defect 2 but keeps the Ce:YAG embedding coordinates. Calculation C contains both Ce,La:YAG $(CeO_8Al_2O_4)^{15-}$ and AIMP shell coordinates with an Y AIMP in the La_Y site and, finally, calculation D is the more realistic picture, with both Ce,La:YAG $(CeO_8Al_2O_4)^{15-}$ and AIMP shell coordinates and a La AIMP wherever appropriate. Here again, $A \rightarrow B$ accounts for the distortions on the cluster due to the presence of La in Ce,La:YAG (defect 2); $B \rightarrow C$ accounts for the long range distortions induced in the whole YAG cell and $C \rightarrow D$ accounts for the electronic effects of La_Y on the cluster.

Results on the analysis of the A, B, C and D calculations in terms of the components of the transitions is reflected in Table 9.7. Since both first and second $4f \rightarrow 5d$ transitions in Ce,La:YAG defect 2 are predicted to suffer from a blue shift, we analyze in the following only the components of the first one. We can immediately see from the third data column of Table 9.7 that the $4f$, $5d$ and $6s$ levels scarcely feel the presence of an AIMP of La in this particular position in defect 2. As said before, La_Y of defect 2 is not a second neighbor of Ce_Y. It belongs, actually, to the fourth coordination shell.

We can see that the blue shift of the first $4f \rightarrow 5d$ in Ce,La:YAG defect 2 (111 cm^{-1}) has a very strong component of the ligand field (131 cm^{-1}) not compensated enough by the slight red shift of the centroids (-20 cm^{-1}). The centroid contribution is dominated by structural factors being the first shell distortion (-55 cm^{-1}) partially compensated by the cell distortion contribution with opposite sign (34 cm^{-1}). In defect 1, both first shell and long-range distortions led to a red shift and, thus, the total red shift associated to the centroid was larger. On the other hand, the ligand field contribution is a large blue shift (131 cm^{-1}), arising solely from first (39 cm^{-1}) and much larger long-range (96 cm^{-1}) structural distortions. It actually makes sense because La_Y is not strictly in the vicinity of the cluster in defect 2 and, since La is a big cation an prints a big distortion around (Section 6.1.1), the distortions associated to La_Y and surroundings distortions are only taken into account with long-range distortions, whereas the cluster is less distorted by its presence. The main difference with respect to defect 1 (Table 9.4) is the absence of electronic effects of La (only -4cm^{-1}), that makes the ligand field contribution a large red shift component to the total red shift of the first $4f \rightarrow 5d$ transition in defect 1, resulting in a blue shift in defect 2.

9.4 Conclusions

Following the steps described in Section 8.1, we have firstly performed first-principles PBC-DFT (PBE) calculations on the distribution, atomistic structure and electronic structure of YAG cells containing one Ce_Y and one La_Y atoms. Among the seven non-equivalent Ce_Y-La_Y pairs that can be formed, the most stable is that one with Ce and La in the closest positions, sharing two oxygens of their first coordination shells, one of the short and one of the long kind around Ce. In this structure, there are significant distortions around the Ce_Y and La_Y sites with respect to the previously studied single defects. Actually, La, a bigger cation, prints a strong anisotropic distortion in Ce surroundings. As a consequence, the cations push away each other and the local D_2 symmetry of Ce_Y and La_Y sites are lost. Specifically, the bridging short oxygen gets away from Ce.

DOS and PDOS of this Ce,La:YAG material resemble very much those of parent materials Ce:YAG and La:YAG. However, we have found two main differences: on the one hand, the aforementioned oxygen away from Ce suffer a slight shift to lower energies because of the bond diminishing and the strong mixing between Ce $4f$ and O $2p$ orbitals. On the other hand, there is a uniform shifting of all the Ce states due to the change in the electrostatic field suffered by Ce in it new off-center position because of the presence of La.

According to our calculations, these two defects are favored to be together by $\sim$60 meV with respect to the individual defects.

CASSCF/CASPT2 embedded cluster calculations are performed on the Ce $4f$ and Ce $5d$ manifolds of Ce,La:YAG using the cluster structures arising from such PBC-DFT calculations and are compared with those performed on Ce:YAG. Calculations show that La-codoping of Ce:YAG causes a red shift of the lowest $4f \rightarrow 5d$ transition, together with a blue shift of the second $4f \rightarrow 5d$ transition, both in agreement with experimental observations.

The redshift of the first $4f \rightarrow 5d$ transition appears as the result of a decrease in the difference between the energy centroids of the $5d^1$ and $4f^1$ configurations and an increase in the effective ligand field on the Ce $5d$ shell associated with electronic effects of La. These effects are slightly mitigated by the ligand field decrease associated with the local expansion around Ce, which gives a blue shift contribution of a smaller value. The change in the energy difference between the centroids of the configurations could not be anticipated by the usual model for this quantity where local expansions are associated with blue shifts and *vice versa*, showing up the importance of the detailed study of local structures of these materials in a deeper understanding of these experimented shifts.

9.5 *Conclusiones*

Siguiendo los pasos descritos en la sección 8.1, hemos realizado en primer lugar cálculos PBC-DFT (PBE) en la distribución, estructura a nivel atómico y estructura electrónica de celdas de YAG que contienen un Ce_Y y un La_Y. Entre los siete pares Ce_Y-La_Y que se pueden formar, el más estable es aquel con Ce y La en las posiciones más cercanas, compartiendo dos oxígenos de sus primeras esferas de coordinación, uno de tipo largo y otro del tipo corto en el caso del Ce. En esta estructura, hay distorsiones significativas alrededor de ambas posiciones respecto a las encontradas para los defectos sencillos. De hecho, el La, un catión más grande, ejerce una fuerte distorsión anisotrópica en los alrededores del Ce. Como consecuencia, los cationes se empujan mutuamente y la simetría D_2 de ambos sitios desaparece. Específicamente, el oxígeno puente de tipo corto se aleja notablmente del Ce.

Las DOS y PDOS de Ce,La:YAG se parecen mucho a las de los materiales con los defectos sencillos Ce:YAG y La:YAG. Sin embargo, encontramos dos diferencias principales: por un lado, el oxígeno mencionado que se aleja del Ce baja a menores energías por la disminución del enlace y la fuerte mezcla entre los orbitales $4f$ del Ce y $2s$ del oxígeno. Por otro lado, hay un desplazamiento uniforme de todos los estados del Ce debido al cambio en el campo electróstatico experimentado por el Ce en su nueva posición *off-center*.

Según nuestros cálculos, los dos defectos interaccionan favorablemente con una energía de ∼60 meV con respecto a los defectos individuales.

Hemos realizado cálculos CASSCF/CASPT2 mediante el método de *cluster* embebido en el conjunto de estados Ce-$4f$ y Ce-$5d$ de Ce,La:YAG, usando las estructuras calculadas anteriomente con métodos PBC-DFT. Estos resultados han sido comparados con los obtenidos para Ce:YAG. Los cálculos muestran que el codopaje de Ce:YAG con La provoca un despalzamiento al rojo de la primera transición $4f \rightarrow 5d$, junto con un desplazamiento al azul de la segunda transición $4f \rightarrow 5d$, ambos en acuerdo con las observaciones experimentales.

El desplazamiento al rojo de la primera transición $4f \rightarrow 5d$ aparece como resultado de una disminución de la diferencia entre los centroides de las configuraciones $5d^1$ y $4f^1$ y un incremento en el campo ligando sufrido por la capa $5d$ asociado con efectos electrónicos debidos a La. Estos efectos se ven ligeramente mitigados por un desplazamiento al azul debido al decrecimiento del campo ligando asociado a la expansión local alrededor del Ce. El cambio en la diferencia de energía ente los centroides no podía ser anticipado por el modelo usual aplicado a estas transiciones, donde expansiones locales se asocian a desplazamientos al azul y *vice versa*, revelando la importancia de un detallado estudio de las estructuras locales de estos materiales para una comprensión más profunda de estos desplazamientos observados.

9.6 Data tables

Table 9.1: Upper chart: Ce_Y-La_Y different double defects. Intra-cell and shortest inter-cell Ce-La distances given. Relative defect energies with respect to the most stable, ($\Delta E_{\rm rel}$), and interaction energies between single defects ($\Delta E_{\rm sd}$) in meV (kJ/mol in parenthesis). Bottom chart : Ce_Y-La_Y, Ce_Y-O and La_Y-O distances in the two most stable Ce_Y-La_Y double defects. In parentheses, differences with respect to such values in single Ce_Y or La_Y defects. Labels according to Figure 9.2. All distances in Å.

	YAG	Ce,La:YAG			
	d(Y-Y) intra-cell	d(Ce_Y-La_Y) inter-cell	d(Ce_Y-La_Y) ΔE_{rel}	$\Delta E_{\rm sd}$	
defect 1	3.709	3.728(+0.019)	9.314 x 1	0 (0)	59(5.7)
defect 2	5.666	5.654(-0.012)	8.290 x 1	3 (0.3)	62(6.0)
defect 3	6.057	6.058(+0.001)	6.058 x 1	48 (4.6)	107(10.3)
defect 4	6.772	6.781(+0.009)	6.783 x 1	35 (3.4)	94(9.1)
defect 5	7.103	7.117(+0.014)	9.329 x 1, 9.334 x 1	12 (1.2)	71(6.8)
defect 6	8.566	8.573(+0.007)	8.559 x 1, 8.563 x 1, 8.569 x 1	20 (1.9)	79(7.6)
defect 7	10.491	10.494(+0.003)	10.484-10.499 x 7	21 (2.1)	80(7.7)

	YAG	Ce:YAG	La:YAG	Ce,La:YAG
	d(Y-Y)	d(Ce-Y)	d(Y-La)	d(Ce-La)
defect 1	3.709	3.718	3.726	3.728
defect 2	5.666	5.668	5.651	5.654
		d(Ce-O)		d(La-O)
			Oxygens of type s	
defect 1	O_B	2.427 (+0.054)	O_A	2.417 (+0.007)
	O_1	2.385 (+0.012)	O_a	2.412 (+0.002)
	O_4	2.374 (+0.001)	O_c	2.399 (-0.011)
	O_5	2.383 (+0.010)	O_e	2.416 (+0.006)
			Oxygens of type l	
	O_A	2.470 (+0.002)	O_B	2.482 (-0.040)
	O_2	2.460 (-0.008)	O_b	2.522 (0.000)
	O_3	2.513 (0.000)	O_d	2.510 (-0.012)
	O_6	2.477 (+0.009)	O_f	2.524 (+0.002)
			Oxygens of type s	
defect 2	O_1	2.373 (0.000)	O_b	2.409 (-0.001)
	O_2	2.366 (-0.007)	O_c	2.411 (+0.001)
	O_5	2.407 (+0.034)	O_f	2.409 (-0.001)
	O_6	2.367 (-0.006)	O_g	2.411 (+0.001)
			Oxygens of type l	
	O_3	2.512 (+0.044)	O_a	2.524 (+0.002)
	O_4	2.453 (-0.015)	O_d	2.524 (+0.002)
	O_7	2.475 (+0.007)	O_e	2.522 (0.000)
	O_8	2.476 (+0.008)	O_h	2.518 (-0.004)

Table 9.2: Relative energies of the levels of the Ce-$4f^1$, Ce-$5d^1$, and Ce-$6s^1$ configurations of the materials Ce:YAG and Ce,La:YAG (defect 1) and the shift induced by La-codoping of Ce:YAG. All numbers in cm^{-1} .

Material:		Ce:YAG			Ce,La:YAG (defect 1)			
Cluster:		$(CeO_8)^{13-}$	$(CeO_8Al_2O_4)^{15-}$		$(CeO_8)^{13-}$		$(CeO_8Al_2O_4)^{15-}$	
	D_2	Energies (Sec. 8.2)	Energies (Sec. 8.2)	C_1	Energies	Shift	Energies	Shift
$4f^1$ levels								
	$1\ ^2B_2$	0	0	$1\ ^2A$	0		0	
	$1\ ^2B_3$	274	38	$2\ ^2A$	224	-50	62	25
	$1\ ^2B_1$	290	202	$3\ ^2A$	361	71	248	46
	$1\ ^2A$	518	416	$4\ ^2A$	544	26	490	74
	$2\ ^2B_1$	577	443	$5\ ^2A$	596	19	541	98
	$2\ ^2B_2$	638	516	$6\ ^2A$	692	54	620	104
	$2\ ^2B_3$	2530	2419	$7\ ^2A$	2500	-30	2422	4
$5d^1$ levels								
	$2\ ^2A$	24887	23853	$8\ ^2A$	24644	-243	23633	-220
	$3\ ^2B_3$	30187	30169	$9\ ^2A$	30729	543	30756	586
	$3\ ^2A$	48080	48112	$10\ ^2A$	47893	-187	47659	-454
	$3\ ^2B_2$	49705	48700	$11\ ^2A$	49886	181	49267	567
	$3\ ^2B_1$	52568	52221	$12\ ^2A$	51647	-1011	51376	-845
$6s^1$ level								
	$4\ ^2A$	67133	61214	$13\ ^2A$	68684	1551	63110	1896

Table 9.3: $4f^1$, $5d^1$, and $6s^1$ levels of the $(CeO_8Al_2O_4)^{15-}$ cluster in several embedding potentials. Ce,La:YAG ≡ Ce,La:YAG defect 1.

	Calculation			
	A	B	C	D
Cluster coordinates	Ce:YAG	Ce,La:YAG	Ce,La:YAG	Ce,La:YAG
Embedding coordinates	Ce:YAG	Ce:YAG	Ce,La:YAG	Ce,La:YAG
Embedding potential on La_Y	Y	Y	Y	La
		$4f^1$ levels		
$1\ ^2A$	0	0	0	0
$2\ ^2A$	38	43	52	62
$3\ ^2A$	202	218	228	248
$4\ ^2A$	416	455	458	490
$5\ ^2A$	443	498	503	541
$6\ ^2A$	516	562	585	620
$7\ ^2A$	2419	2382	2390	2422
		$5d^1$ levels		
$8\ ^2A$	23853	23861	23803	23633
$9\ ^2A$	30169	30678	30690	30756
$10\ ^2A$	48112	47660	47659	47659
$11\ ^2A$	48700	49157	49123	49267
$12\ ^2A$	52221	51402	51404	51376
		$6s^1$ level		
$13\ ^2A$	61214	62566	62186	63110
$\Delta E_{\text{centroid}}(4f^1 \rightarrow 5d^1)$	40035	39958	39933	39912
$\Delta E_{\text{LF}}(1-4f^1)$	576	594	603	626
$\Delta E_{\text{LF}}(1-5d^1)$	16758	16691	16733	16905
$\Delta E_{\text{ligand-field}}(1-4f^1 \rightarrow 1-5d^1)$	-16182	-16097	-16130	-16279
$\Delta E_{\text{LF}}(2-5d^1)$	10442	9874	9846	9782
$\Delta E_{\text{ligand-field}}(1-4f^1 \rightarrow 2-5d^1)$	-9866	-9280	-9243	-9156

Table 9.4: Analysis of the first and second $4f \rightarrow 5d$ transitions shift from Ce:YAG to Ce,La:YAG (defect 1). All numbers in cm^{-1}.

	Contributions				
	$A \rightarrow B$	$B \rightarrow C$	$A \rightarrow C$	$C \rightarrow D$	$A \rightarrow D$
	First-shell distortion	Cell distortion	Full distortion	La_Y	All
$\Delta E_{\text{centroid}}(4f^1 \rightarrow 5d^1)$	-77	-24	-101	-22	-123
$\Delta E_{\text{LF}}(1-4f^1)$	18	8	26	24	50
		$1-4f^1 \rightarrow 1-5d^1$ transition			
$\Delta E_{\text{LF}}(1-5d^1)$	-68	43	-25	173	147
$\Delta E_{\text{ligand-field}}$ [a]	85	-33	52	-149	-97
ΔE [b]	8	-58	-50	-170	-220
		$1-4f^1 \rightarrow 2-5d^1$ transition			
$\Delta E_{\text{LF}}(2-5d^1)$	-568	-28	-596	-63	-659
$\Delta E_{\text{ligand-field}}$ [a]	586	37	623	87	709
ΔE [b]	509	12	521	65	586

[a] $\Delta E_{\text{ligand-field}} = \Delta E_{\text{LF}}(1-4f^1) - \Delta E_{\text{LF}}(1-5d^1)$, see Fig. 8.2

[b] $\Delta E = \Delta E_{\text{centroid}} + \Delta E_{\text{ligand-field}}$, see Fig. 8.2

Table 9.5: Relative energies of the levels of the Ce-$4f^1$, Ce-$5d^1$, and Ce-$6s^1$ configurations of the materials Ce:YAG and Ce,La:YAG (defect 2) and the shift induced by La-codoping of Ce:YAG. All numbers in cm^{-1} .

Material:		Ce:YAG			Ce,La:YAG (defect 2)			
Cluster:		$(CeO_8)^{13-}$	$(CeO_8Al_2O_4)^{15-}$		$(CeO_8)^{13-}$		$(CeO_8Al_2O_4)^{15-}$	
	D_2	Energies (sec. 8.2)	Energies (sec. 8.2)	C_1	Energies	Shift	Energies	Shift
$4f^1$ levels								
	$1\ ^2B_2$	0	0	$1\ ^2A$	0		0	0
	$1\ ^2B_3$	274	38	$2\ ^2A$	265	-9	29	-9
	$1\ ^2B_1$	290	202	$3\ ^2A$	293	3	190	-12
	$1\ ^2A$	518	416	$4\ ^2A$	505	-13	409	-7
	$2\ ^2B_1$	577	443	$5\ ^2A$	557	0	434	-9
	$2\ ^2B_2$	638	516	$6\ ^2A$	632	-6	513	-3
	$2\ ^2B_3$	2530	2419	$7\ ^2A$	2488	-42	2378	-41
$5d^1$ levels								
	$2\ ^2A$	24887	23853	$8\ ^2A$	25008	121	23964	111
	$3\ ^2B_3$	30187	30169	$9\ ^2A$	30376	189	30368	199
	$3\ ^2A$	48080	48112	$10\ ^2A$	47827	-253	47642	-470
	$3\ ^2B_2$	49705	48700	$11\ ^2A$	49590	-115	48829	129
	$3\ ^2B_1$	52568	52221	$12\ ^2A$	52448	-120	52095	-126
$6s^1$ level								
	$4\ ^2A$	67133	61214	$13\ ^2A$	67765	632	61977	763

Table 9.6: $4f^1$, $5d^1$, and $6s^1$ levels of the $(CeO_8Al_2O_4)^{15-}$ cluster in several embedding potentials. Ce,La:YAG ≡ Ce,La:YAG defect 2.

	Calculation			
	A	B	C	D
Cluster coordinates	Ce:YAG	Ce,La:YAG	Ce,La:YAG	Ce,La:YAG
Embedding coordinates	Ce:YAG	Ce:YAG	Ce,La:YAG	Ce,La:YAG
Embedding potential on La_Y	Y	Y	Y	La
			$4f^1$ levels	
$1\ ^2A$	0	0	0	0
$2\ ^2A$	38	8	30	29
$3\ ^2A$	202	158	195	190
$4\ ^2A$	416	380	412	409
$5\ ^2A$	443	414	439	434
$6\ ^2A$	516	492	516	513
$7\ ^2A$	2419	2373	2381	2378
			$5d^1$ levels	
$8\ ^2A$	23853	23837	23967	23964
$9\ ^2A$	30169	30216	30372	30368
$10\ ^2A$	48112	47639	47655	47642
$11\ ^2A$	48700	48707	48841	48829
$12\ ^2A$	52221	52229	52077	52095
			$6s^1$ level	
$13\ ^2A$	61214	62081	61878	61977
$\Delta E_{\text{centroid}}(4f^1 \rightarrow 5d^1)$	40035	39980	40014	40015
$\Delta E_{\text{LF}}(1-4f^1)$	576	546	568	565
$\Delta E_{\text{LF}}(1-5d^1)$	16758	16689	16615	16616
$\Delta E_{\text{ligand-field}}(1-4f^1 \rightarrow 1-5d^1)$	-16182	-16143	-16047	-16051

Table 9.7: Analysis of the first $4f \rightarrow 5d$ transition shift from Ce:YAG to Ce,La:YAG (defect 2). All numbers in cm^{-1}.

	Contributions				
	A → B	B → C	A → C	C → D	A → D
	First-shell distortion	Cell distortion	Full distortion	La_Y	All
$\Delta E_{\text{centroid}}(4f^1 \rightarrow 5d^1)$	-55	34	-21	1	-20
$\Delta E_{\text{LF}}(1-4f^1)$	-30	22	-8	-3	-11
			$1-4f^1 \rightarrow 1-5d^1$ transition		
$\Delta E_{\text{LF}}(1-5d^1)$	-69	-74	-143	1	-142
$\Delta E_{\text{ligand-field}}$ [a]	39	96	135	-4	131
ΔE [b]	-16	130	114	-3	111

[a] $\Delta E_{\text{ligand-field}} = \Delta E_{\text{LF}}(1-4f^1) - \Delta E_{\text{LF}}(1-5d^1)$, see Fig. 8.2

[b] $\Delta E = \Delta E_{\text{centroid}} + \Delta E_{\text{ligand-field}}$, see Fig. 8.2

Chapter 10

Ga codoped Ce:YAG

In this chapter, we report the calculated shift induced by Ga-codoping on Ce:YAG absorption spectrum and we do analyze the reasons behind it, as done for La-codoping in Chapter 9, following the recipe in Section 8.1. Since there are two different Al atoms suitable for substitution, Al_{oct} and Al_{tet}, we have studied the codoped Ce:YAG cells with both Ga_{oct} and Ga_{tet}. Then, we present in Section 10.1 the results of ground state PBC-DFT calculations on the local structure around the active impurity Ce_Y in YAG cells containing one Ce_Y plus one Ga_{Al} per unit cell in octahedral or tetrahedral environment, that is, Ce,Ga_{oct}:YAG and Ce,Ga_{tet}:YAG. The effects of Ga-codoping on electronic structure of Ce:YAG are presented in Section 10.2. In Section 10.3, we present our first-principles study and analysis on the effects that Ga-codoping has on the on the shift of the lowest $4f \rightarrow 5d$ absorption, completely analogous to that performed for Ce,La:YAG in the previous chapter. Conclusions and data tables of this chapter are included in Sections 10.4 and 10.6 respectively.

10.1 Effects of Ga on the local structure of the active defect Ce_Y

In order to study Ce_Y-Ga_{oct} and Ce_Y-Ga_{tet} double substitutional defects in YAG, we have performed calculations on the doubly doped materials $Y_{2.875}Ce_{0.125}Al^{oct}_{1.875}Ga^{oct}_{0.125}Al^{tet}_{3}O_{12}$ and $Y_{2.875}Ce_{0.125}Al^{oct}_{2}Al^{tet}_{2.875}Ga^{tet}_{0.125}O_{12}$. We call them Ce,$Ga_{oct}$:YAG and Ce,$Ga_{tet}$:YAG respectively, for simplicity. Since there are 16 Al_{oct} and 24 Al_{tet} in the YAG unit cell, as well as 24 Y positions, these materials have an atomic percentage of dopant atoms of $\sim 4\%$ in Ce_Y plus $\sim 6\%$ in Ga_{oct} and $\sim 4\%$ in Ga_{tet} respectively. We have considered all non-equivalent double defects of each kind. These are four in Ce,Ga_{oct}:YAG and seven in Ce,Ga_{tet}:YAG, which are schematically shown in Fig. 10.1 and listed in Table 10.1 according to their respective Y-Al_{oct} and Y-Al_{tet} distances in perfect YAG.

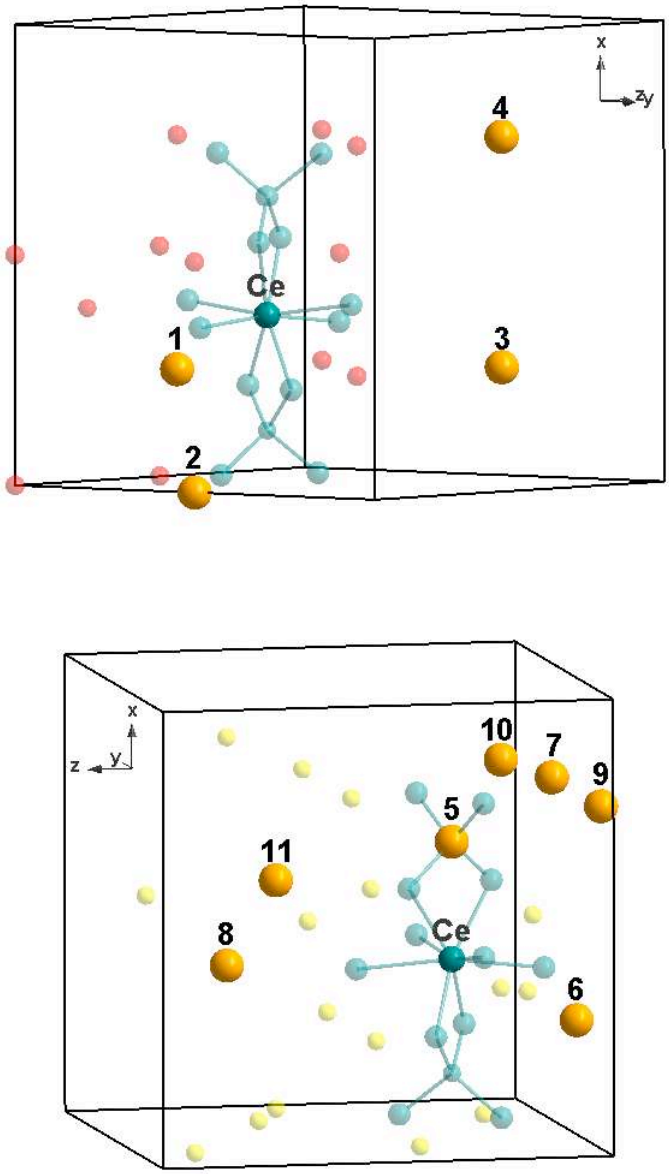

Figure 10.1: Top: scheme of the four different Ga_{oct}(orange)-Ce_Y(greenish blue) double defects ordered according to the Ga_{oct}-Ce_Y distance before relaxation. Other equivalent Al_{oct} positions in semitransparent red. Bottom: scheme of the seven different Ga_{tet}(orange)-Ce_Y(greenish blue) double defects ordered according to the Ga_{tet}-Ce_Y distance before relaxation. Details in Table 10.1. Other equivalent Al_{tet} positions in semitransparent yellow. $(CeO_8Al_2O_4)^{15-}$cluster in semitransparent greenish blue.

In Table 10.1, the Ce_Y-Ga_{oct} and Ce_Y-Ga_{tet} distances between impurities in the optimized structures are also collected, together with the next distances between impurities and their multiplicity, the relative energies of the double defects with respect to the lowest,

and the interaction energies between single defects, ΔE_{sd}, defined as the energy difference of the processes

$$8\ Y_{2.875}Ce_{0.125}Al_5O_{12} + 8\ Y_3Al^{oct}_{1.875}Ga^{oct}_{0.125}Al^{tet}_3O_{12} \rightarrow$$
$$8\ Y_3Al_5O_{12} + 8\ Y_{2.875}Ce_{0.125}Al^{oct}_{1.875}Ga^{oct}_{0.125}Al^{tet}_3O_{12}$$
and
$$8\ Y_{2.875}Ce_{0.125}Al_5O_{12} + 8\ Y_3Al^{oct}_2Al^{tet}_{2.875}Ga^{tet}_{0.125}O_{12} \rightarrow$$
$$8\ Y_3Al_5O_{12} + 8\ Y_{2.875}Ce_{0.125}Al^{oct}_2Al^{tet}_{2.875}Ga^{tet}_{0.125}O_{12}$$

in the Ce,Ga_{oct}:YAG and Ce,Ga_{tet}:YAG cases respectively, that is, the change in energy from having the two single defects isolated in different YAG cells to have both in the same YAG cell. As shown by the ΔE_{sd} values, the single defects attract themselves and tend to get close to each other when both Ce_Y and Ga_{Al} are at intermediate distances; however, the local expansions brought about by Ga_{Al} and, in a lesser extent, Ce_Y, cannot be accommodated at the same time below a critical distance of around 5.5 Å, under which they repel each other.

As we can see in Table 10.1, the most stable double substitutional defects are formed with Ga substituting for Al in the second cation layer around Ce (that is, in its fourth coordination shell), both in octahedral (defect 2, at 5.46 Å) and tetrahedral (defect 7, at 5.66 Å) sites. Among them, the octahedral position for Ga is preferred. The analysis of E *versus* lattice constant for both defects 2 and 7 (with internal relaxation in each point) shows the same increment of the lattice constant from pure and perfect YAG lattice constant (a_0 = 12.114 Å) of +0.22% (a_0 = 12.141 Å), slightly higher that those of the individual defects (+0.11% for Ce:YAG and +0.15% for Ga_{Al}:YAG) but small enough to use a_0 = 12.114 Å in our calculations.

Their respective formation energies at low concentration according to the processes

$$8\ Y_3Al_5O_{12} + Ce^{3+}_{vacuum} + Ga^{3+}_{vacuum} \rightarrow$$
$$8\ Y_{2.875}Ce_{0.125}Al^{oct}_{1.875}Ga^{oct}_{0.125}Al^{tet}_3O_{12} + Y^{3+}_{vacuum} + Al^{3+}_{vacuum}$$
and
$$8\ Y_3Al_5O_{12} + Ce^{3+}_{vacuum} + Ga^{3+}_{vacuum} \rightarrow$$
$$8\ Y_{2.875}Ce_{0.125}Al^{oct}_2Al^{tet}_{2.875}Ga^{tet}_{0.125}O_{12} + Y^{3+}_{vacuum} + Al^{3+}_{vacuum}$$

are 1.137 eV/defect (109.7 kJ/mol) for defect 2 and 1.195 eV/defect (115.3 kJ/mol) for defect 7. All other defects with impurities at longer distances are slightly more unstable and the instability is larger for the defects with shorter Ce-Ga distances. As it happens with Ga_{oct} and Ga_{tet} single defects, in the case of double defects the formation of Ce_Y-Ga_{oct} is only slightly preferred over the formation of Ce_Y-Ga_{oct}, by 58 meV/defect. Calculation of their stress energies (E_{stress}(Ce_Y-Ga_{oct})=760 meV/defect (73.3 kJ/mol), E_{stress}(Ce_Y-Ga_{tet})=1334 meV/defect (128.7 kJ/mol)) reveals that the relaxation of the double defects 2 and 7 is only slightly larger than that stress energy per independent single defect (E_{stress}(Ce_Y)=125 meV, E_{stress}(Ga_{oct})=600 meV, E_{stress}(Ga_{tet})=1190 meV) by 35 meV and 19 meV respectively, so that the influences of Ce on the different stress energies of the two double defects are minimal. As in the case of single defects, we should

expect that stress effects (dominated by Ga_{Al} over Ce_Y) make the formation of Ce_Y-Ga_{oct} double substitutions preferred over the formation of Ce_Y-Ga_{tet} double substitutions at high concentrations.

Local environments around the two most stable double defects Ce_Y-Ga_{oct} (defect 2) and Ce_Y-Ga_{tet} (defect 7) are shown in Fig. 10.2. Detailed geometrical parameters are presented in Table 10.1.

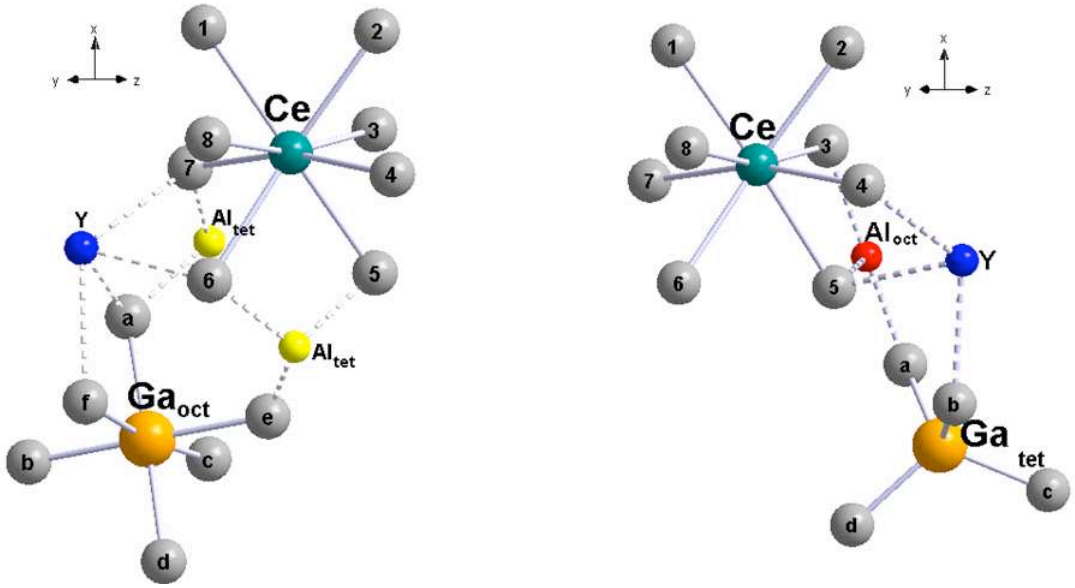

Figure 10.2: Representation of the most stable Ce_Y-Ga_{oct} (above) and Ce_Y-Ga_{tet} (below) double substitutional defects. Atom labels correspond to Table 10.1.

The main effect of Ga-codoping on the local structure around the optically active Ce_Y defect is an overall anisotropic expansion of its first coordination shell, both when Ga substitutes for Al_{oct} and for Al_{tet}; however, the detailed distortions are very different in both cases: in the former, two of the four closest oxygens move away 0.03 Å and two of the four most distant oxygens approach 0.01 Å, whereas in the latter, one close oxygen moves away 0.07 Å and one distant oxygen approaches 0.01 Å, all other oxygens experiencing shorter displacements. The expansions around Ce_Y supports one of the points of the current interpretation for the Ga-codoping induced blue shift (lowering the crystal-field around Ce), but their high anisotropies do not support at all the other point (forcing a more cubic environment around Ce) [240, 28, 38, 32]. We discuss in Section 10.3 the relationship between this structure and the blue shift induced by Ga-codoping.

10.2 Effects of Ga on Ce:YAG electronic structure

Band structures of defects 1 and 2 are shown in Fig. 10.3. They present the same pattern as Ce:YAG band structure (Fig.6.6), with Ce states placed in pure YAG gap, not only at the top of the valence band but also at the bottom of the conduction band.

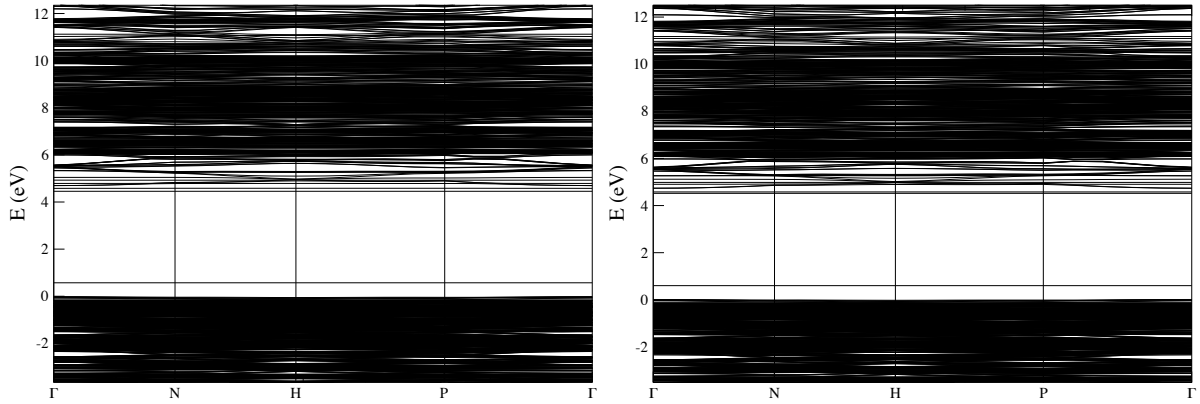

Figure 10.3: Band structure of the two most stable Ce_Y-Ga_{oct} and Ce_Y-Ga_{tet} double substitutional defects in Ce,Ga:YAG. . Left: defect 2. Right: defect 2.

DOS and PDOS of Ce,Ga_{oct}:YAG and Ce,Ga_{tet}:YAG, as seen on Fig. 10.4, do not show significant differences from that of Ce:YAG (Fig. 6.8). Moreover, the PDOS of Ga_{oct} and Ga_{tet} in these disubstituted cells are remarkably similar to their respective PDOS in Ga_{oct}:YAG and Ga_{tet}:YAG shown in Fig. 6.14. Moreover, the orbital decomposition of Ce PDOS for both Ce,Ga_{oct}:YAG and Ce,Ga_{tet}:YAG (as shown in Fig. 10.5, top and center) presents the same pattern as Ce:YAG PDOS (Fig. 6.8). So, from the point of view of the electronic structure, the single defects involved in Ce_Y-Ga_{oct} and Ce_Y-Ga_{tet} can be considered independent. If we compare in detail Ce α PDOS of Ce,Ga_{oct}:YAG and Ce,Ga_{tet}:YAG with that of Ce:YAG (Fig. 10.5, bottom), we can see that the highest $4f$-character contribution is slightly shifted to lower energies upon Ga_{Al} codoping (curves for Ce,Ga_{oct}:YAG and Ce,Ga_{tet}:YAG practically overlap in Fig. 10.5, bottom). As it happens in Ce,La:YAG (defect 1), the innermost $5s$ and $5p$ also suffer from this shift, which indicates again a change in the electrostatic field suffered by Ce_Y when codoping and when it goes off-center because of the presence of the codopant. However, this shift is much less pronounced than in Ce,La:YAG (Fig. 9.4, bottom), which responds to the fact that La_Y (second neighbor) is closer to Ce_Y than Ga_{Al} (fourth coordination shell) and prints a stronger off-center displacement on Ce_Y.

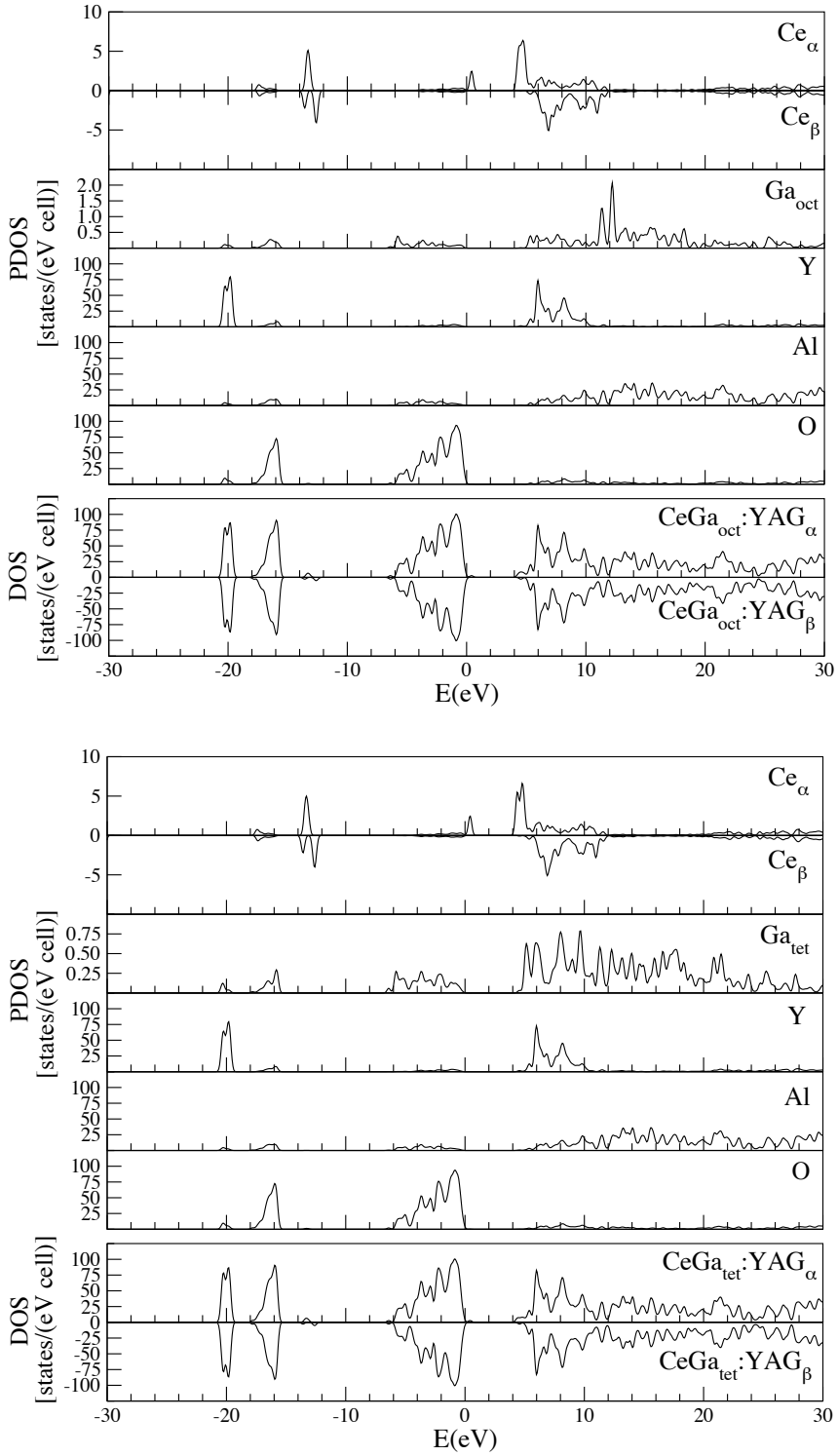

Figure 10.4: Total DOS and PDOS of Ce, Ga, Y, Al, and O atoms of the two most stable Ce_Y-Ga_{oct} and Ce_Y-Ga_{tet} double substitutional defects in Ce,Ga:YAG. . Top: defect 2. Bottom: defect 7.

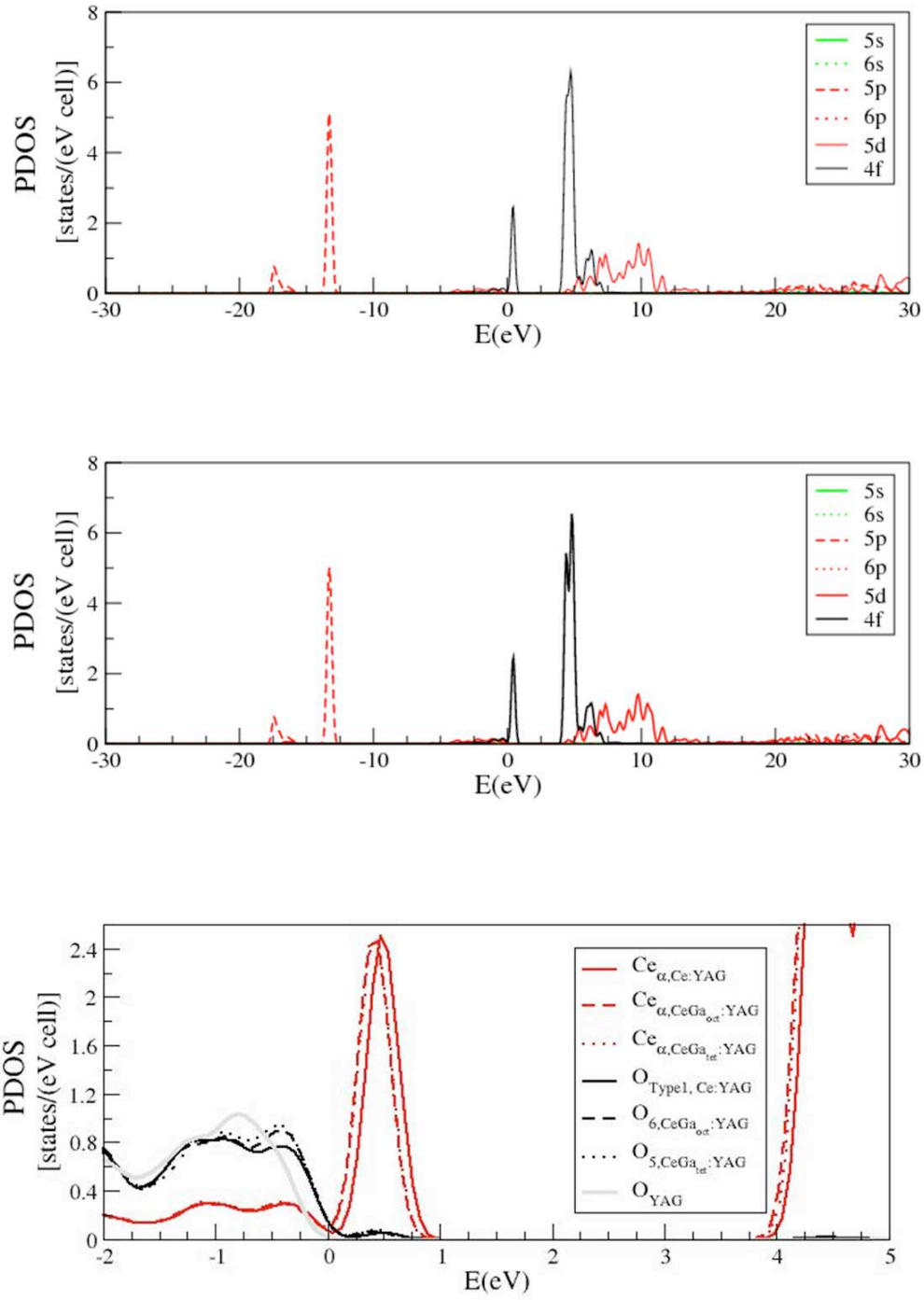

Figure 10.5: Orbital decomposition of the Ce α PDOS for defect 2 (top) and defect 7 (center). Bottom: comparison of Ce α PDOS of Ce_Y-Ga_{oct}:YAG and Ce_Y-Ga_{tet}:YAG with Ce:YAG. Zoom over the gap area.

10.3 Effects of Ga on Ce:YAG absorption spectrum

In Table 10.2 we show the transition energies from the ground state to the many-electron states of the configurations Ce-$4f^1$, Ce-$5d^1$, and Ce-$6s^1$ of $(CeO_8)^{13-}$ and $(CeO_8Al_2O_4)^{15-}$ clusters of materials Ce,Ga_{oct}:YAG (defect 2) and Ce,Ga_{tet}:YAG (defect 7) materials in comparison to those of Ce:YAG (Section 8.2).

The differences between these calculations arise from the different cluster coordinates, the different AIMP embedding shell according to the defects present in each material and the presence of Ga as represented by the corresponding AIMP.

Data on Table 10.2 show that we find very similar shifting results for $(CeO_8)^{13-}$ and $(CeO_8Al_2O_4)^{15-}$ in the two materials under study. The overall result for both clusters is absolutely comparable: For Ce,Ga_{oct}:YAG , the first $4f \rightarrow 5d$ transition is predicted to have blue shift (44 cm^{-1} in $(CeO_8)^{13-}$ and 74 cm^{-1} in $(CeO_8Al_2O_4)^{15-}$) and the second $4f \rightarrow 5d$ transition is predicted to have a blue shift as well (55 cm^{-1} in $(CeO_8)^{13-}$ and 76 cm^{-1} in $(CeO_8Al_2O_4)^{15-}$). Ce,Ga_{tet}:YAG is predicted to suffer larger blue shifts than Ce,Ga_{oct}:YAG in the first and the second $4f \rightarrow 5d$ transitions: 176 cm^{-1} (in $(CeO_8)^{13-}$) and 211 cm^{-1} (in $(CeO_8Al_2O_4)^{15-}$) for the first $4f \rightarrow 5d$ transition and 96 cm^{-1} (in $(CeO_8)^{13-}$) and 109 cm^{-1} (in $(CeO_8Al_2O_4)^{15-}$) for the second $4f \rightarrow 5d$ transition. Moreover, the analysis of the factors leading to these shifts is totally analogous for both clusters. Accordingly, the qualitative analysis is presented and discussed in terms on the larger cluster ($(CeO_8Al_2O_4)^{15-}$) results for each material.

This calculated blue shift is in qualitative agreement with experiments because blue shifts induced by Ga-codoping have been observed at all doping concentration levels [28, 38, 39, 32]. Since the formation of Ga_{Al}^{oct} is preferred over Ga_{Al}^{tet}, as discussed above, it is the 74 cm^{-1} blue shift at 6 at.% the number to be compared to experiments. Although all of them have been done at higher doping levels, a 50 cm^{-1} blue shift is deduced from extrapolation of the measurements of Tien *et al.* [39] at 10 and 20 at.%. The agreement is quite good with some overestimation, as it was the case with the red shift induced by La-codoping.

In order to analyze the reasons behind the blue shift found, we use the same diagram (Fig.8.2) as for Ce,La:YAG (Section 9.3) for the first $4f \rightarrow 5d$ transition, and we track the components involved in such transition according to

$$\begin{aligned}\Delta E(4f \rightarrow 5d) &= \Delta E_{\text{centroid}}(4f \rightarrow 5d) + \Delta E_{\text{ligand-field}} \\ &= \Delta E_{\text{centroid}}(4f \rightarrow 5d) + \Delta E_{\text{LF}}(4f) - \Delta E_{\text{LF}}(5d).\end{aligned}$$

As for Ce,La:YAG, we have performed additional intermediate calculations from Ce:YAG to Ce,Ga:YAG, in order to visualize the effect of the short and long range distortions and electronic effects of Ga_{Al} on each component of the transition (Section 8.1.2). Calculation *A* is our Ce:YAG reference, calculation *B* is performed using the $(CeO_8Al_2O_4)^{15-}$ coordinates according to relaxed Ce,Ga_{oct}:YAG and Ce,Ga_{tet}:YAG maintaining the Ce:YAG AIMP embedding; calculation *C* contains both $(CeO_8Al_2O_4)^{15-}$ and AIMP coordinates from relaxed Ce,Ga_{oct}:YAG and Ce,Ga_{tet}:YAG cells but there is an Al AIMP in the corresponding Ga_{Al} site, that finally is substituted by a Ga AIMP in calculation *D* to represent

as realistically as possible the effects of Ga-codoping on Ce_Y center luminescence. Thus, for Ce,Ga_{oct}:YAG and Ce,Ga_{tet}:YAG materials, $A \rightarrow B$ accounts for the distortions on the cluster due to the presence of Ga_{Al} in Ce,Ga:YAG; $B \rightarrow C$ accounts for the long range distortions induced in the whole YAG cell and $C \rightarrow D$ accounts for the electronic effects of Ga_{Al} on the cluster. The Ce $4f$, $5d$ and $6s$ levels of these A, B, C and D calculations are tabulated in Tables 10.3 and 10.4 for Ce,Ga_{oct}:YAG and Ce,Ga_{tet}:YAG respectively as well as the calculated values of the components of the first $4f \rightarrow 5d$ transition. The variation of such components along the $A \rightarrow B \rightarrow C \rightarrow D$ series is tabulated in Table 10.5 for both materials.

Let's analyze these data for Ce,Ga_{oct}:YAG and Ce,Ga_{tet}:YAG separately. In the last column of Table 10.5 for Ce,Ga_{oct}:YAG, we can see that the blue shift of the first $4f \rightarrow 5d$ transition (74 cm^{-1}) is entirely due to a variation of the ligand field (72 cm^{-1}), mostly coming from a decrease of the 1-$5d^1$ ligand field (-57 cm^{-1}), whereas the centroid contribution can be considered negligible (2 cm^{-1}), not only in the global process $A \rightarrow D$ but also along all the intermediate changes considered. We can see that the main contributor on the 1-$5d^1$ ligand field decrease is the first-shell distortion (-42 cm^{-1}), whereas the distortion of the whole cell (-15 cm^{-1}) is considerably smaller. No significant electronic effects because of the presence of Ga_{oct} are found in these calculations. Regarding Ce,Ga_{tet}:YAG, the first observation is a larger blue shift (211 cm^{-1}), as expected from the stronger local distortion generated by Ga_{tet} due to the small size of the tetrahedral cavity (Section 6.2). This blue shift comes mainly from a large ligand field component (240 cm^{-1}), slightly mitigated by a red shift of the centroid contribution(-29 cm^{-1}). This small red shift comes entirely from first-shell distortions (-27 cm^{-1}). The ligand field contributor is clearly dominated by a large decrease on the 1-$5d^1$ ligand field (-235 cm^{-1}), whereas negligible changes on the 1-$4f^1$ ligand field arise from our calculations (5 cm^{-1}), in which the short-range (21 cm^{-1}) and long-range (-16 cm^{-1}) effects are compensated. The 1-$5d^1$ ligand field contribution arises in the same extent from short-range (-131 cm^{-1}) and long-range (-105 cm^{-1}) distortions, results in agreement with the fact commented above that Ga_{tet} prints a huge distortion around and in defect 7 is not placed in the vicinity of the cluster so that their effects are taken into account from calculations $B \rightarrow C$. Electronic effects do not affect any component of the transition (1 cm^{-1} for the centroid, zero contribution for the 1-fd^1 ligand field, -1cm^{-1} for the 1-$5d^1$ ligand field; zero cm^{-1} total).

As a conclusion of this analysis we can say that the effects of Ga-codoping on the blue shift of the lowest Ce^{3+} $4f \rightarrow 5d$ transition of Ce:YAG can be described with a simple model in which Ga acts only by provoking an expansion around Ce_Y, whose main effect is lowering the $5d$ shell splitting [39, 40, 32]. However, this model cannot be applied to the red shift induced by La-codoping, where the direct electronic effects of La and the centroid energy shift are instrumental. The reason for such a different behavior could lie in the distance between the dopant and the Ce impurity, which is shorter in Ce_Y-La_Y (3.73 Å) than in Ce_Y-Ga_{Al}^{oct} (5.46 Å) and Ce_Y-Ga_{Al}^{tet} (5.66 Å).

10.4 Conclusions

A combined PBC-DFT (PBE) embedded cluster CASSCF/CASPT2 first principles calculation (according to Section 8.1) has been performed in materials containing one Ce_Y plus one Ga_{oct} or Ga_{tet} atom per YAG unit cell, analogously to the study performed on Ce,La:YAG materials.

The first-principles PBC-DFT (PBE) calculations on the distribution, atomistic structure and electronic structure of Ce,Ga:YAG cells show that both Ga_{oct} and Ga_{tet} prefer Al sites located in the fourth coordination shell (second cation coordination shell) with respect to Ce_Y. Among them, the Ga_{oct} substitution is preferred over the Ga_{tet} one by ~ 60 meV, similar to the difference between single Ga_{oct} and Ga_{tet} defects in YAG. Relaxation energies of the double Ce-Ga defects are only slightly larger than the sum of individual relaxation energies so that we can say that the interaction between Ce and Ga defects is minimal in terms of formation and stress.

The main effect of Ga-codoping on the local structure around the optically active Ce_Y defect is an overall anisotropic expansion, which supports the model of a blue shift associated to such expansion via lowering the crystal field around Ce but, due to the highly anisotropic character of the distortion, does not support the model of such blue shift associated also to a more cubic environment around it.

The DOS/PDOS of Ce,Ga:YAG materials are quite similar to Ce:YAG ones. However, as in Ce,La:YAG, a shift of all the Ce states to lower energies is found, being the magnitude of the shift much smaller, in agreement with the fact that Ce and Ga are placed farther than Ce and La, and, then, the off-center displacement of Ce is much less pronounced.

CASSCF/CASPT2 embedded cluster calculations are performed on the Ce $4f$ and Ce $5d$ manifolds of Ce,Ga_{oct}:YAG and Ce,Ga_{tet}:YAG materials using the cluster structures arising from the above PBC-DFT calculations and are compared with those on Ce:YAG. These calculations show that Ga-codoping of Ce:YAG causes a blue shift of the first $4f \rightarrow 5d$ transition, in agreement with experimental observations. In Ce,Ga_{oct}:YAG, this blue shift is entirely due to a variation on the ligand field, mostly coming from a decrease of the 1-$5d^1$ ligand field mainly due to distortions in the first coordination shell, whereas the centroid contribution is negligible. The presence of Ga does not provide any significant electronic effect on the transition. Regarding Ce,Ga_{tet}:YAG, a slightly larger blue shift is predicted, also coming mainly from the ligand field component with a small red shift coming from the centroid term due to first-shell distortions. The ligand field contribution is dominated by a large decrease of the 1-$5d^1$ ligand field, arising from first-shell and long-range distortions equally. This is in agreement with the fact that Ga_{tet}, which is not in the vicinity of Ce_Y, produces larges distortions not only in Ce_Y coordination shell, but also in its surroundings. As in Ce,Ga_{oct}:YAG, there are no electronic effects associated to the presence of Ga_{tet}. This behavior is opposite to the Ce,La:YAG case, where the electronic effect of the La atom directly linked to Ce_Y is a key factor in the calculated and observed red shift of the first $4f \rightarrow 5d$ transition. The reason of this difference could lie in the the larger Ga-Ce distance with respect to the La-Ce one. That points out again

that the detailed study of the structures involving both defects is perhaps necessary in the understanding of these luminescences.

10.5 *Conclusiones*

Hemos combinado cálculos PBC-DFT (PBE) y CASSCF/CASPT2 en *cluster* embebido (según la sección 8.1) en materiales que contienen un átomo de Ce_Y más un átomo de Ga_{oct} o Ga_{tet} por celda unidad de YAG, analogamente al estudio realizado en Ce,La:YAG.

Los cálculos PBC-DFT sobre la distribución, estructura a nivel atómico y estructura electrónica de estas celdas Ce,Ga:YAG muestran que tanto el Ga_{oct} como Ga_{tet} prefieren posiciones en la cuarta esfera de coordinación del Ce, esto es, en la segunda capa de cationes. Entre ambas, la sustitución con Ga_{oct} se ve favorecida frente a la de Ga_{tet} por $\sim$ 60 meV, diferencia similar a la encontrada en los defectos sencillos. Las energías de relajación de los defectos dobles Ce-Ga son solamente ligeramente superiores a la suma de las energías de relajación de los defectos individuales, de modo que podemos decir que la interacción entre Ce y Ga es mínima en términos de formación y estrés.

El principal efecto del codopaje con Ga sobre la estructura local del defecto ópticamente activo de Ce es una expansión anisotrópica, lo cual apoya el modelo de desplazamiento al azul asociado a expansión por medio de un decrecimiento del campo cristalino alrededor del Ce pero, debido a la alta anisotropía de la distorsión, no apoya el modelo de un desplazamiento al azul asociado a un entorno más cúbico.

Las DOS/PDOS de Ce,Ga:YAG son bastante similares a las de Ce:YAG. Sin embargo, también encontramos el fenómeno del desplazamiento de los estados de Ce a menores energías, como en Ce,La:YAG, aunque la magnitud del desplazamiento es menor. Esto está de acuerdo con el hecho de que Ce y Ga están situados más lejos que Ce y La y, por tanto, el Ce en Ce,Ga:YAG no sufre tanto desplazamiento *off-center*.

Hemos realizado cálculos CASSCF/CASPT2 mediante el método de *cluster* embebido en el conjunto de estados Ce-4f y Ce-5d de Ce,Ga_{oct}:YAG y Ce,Ga_{tet}:YAG, usando las estructuras calculadas anteriomente con métodos PBC-DFT y hemos comparado los resultados con los realizados en Ce:YAG. Estos cálculos muestran que el codopaje de Ce:YAG con Ga provoca un desplazamiento al azul de la primera transición $4f \rightarrow 5d$, reproduciendo la observación experimental. En Ce,Ga_{oct}:YAG, este desplazamiento al azul se debe completamente a la variación del campo de ligando, mayormente por una disminución del campo ligando de 1-5d^1 debido a distorsiones en la primera esfera de coordinación, mientras que la contribución del centroide es despreciable. La presencia de Ga no ejerce ningún efecto electrónico en la transición. Con respecto a Ce,Ga_{tet}:YAG, los cálculos predicen un desplazamiento al azul ligeramente mayor, también proveniente del componente del campo de ligando, junto a un pequeño desplazamiento al rojo proveniente del término del centroide y debido a distorsiones en la primera esfera de coordinación. La contribución del campo de ligando está dominada por una gran disminución del campo de ligando en el estado 1-5d^1, debido, en igual magnitud, a distorsiones tanto locales como en toda la celda. Esto está de acuerdo con el hecho de que el Ga_{tet}, que no está cerca

de Ce_Y, provoca una gran distorsión también a su alrededor, no solo alrededor del Ce_Y. Como en el caso de Ce,Ga_{oct}:YAG, no hay efectos electrónicos asociados a la presencia de Ga_{tet}. Este comportamiento es opuesto al caso de Ce,La:YAG, donde el efecto electrónico del La unido a Ce_Y es un factor clave en el calculado y observado desplazamiento al rojo de la primera transición $4f \rightarrow 5d$. La razón de esta diferencia podría estar en la distancia entre el Ce y el codopante, más corta en Ce-La que en Ce-Ga. Esto pone de manifiesto de nuevo que el estudio detallado de las estructuras que involucran ambos defectos es quizá necesario para la comprensión de estas luminiscencias.

10.6 Data tables

Table 10.1: Upper chart: Ce_Y -Ga_{Al} different double defects. Intra-cell and shortest inter-cell Ce-Ga distances given. Relative defect energies with respect to the most stable, (ΔE_{rel}), and interaction energies between single defects (ΔE_{sd}) in meV (kJ/mol in parenthesis). Bottom chart : Ce_Y -Ga_{Al}, Ce_Y-O and Ga_{Al}-O distances in the most stable Ce-Ga_{oct} and Ce-Ga_{tet} double defects. In parentheses, differences with respect to such values in single Ce_Y or Ga_{Al} defects. Labels according to Figure 10.2. All distances in Å.

	YAG	Ce_Y-Ga_{oct} double substitutional defects			
	d(Y-Al_{oct})	d(Ce_Y-Ga_{oct}) intra-cell	d(Ce_Y-Ga_{oct}) inter-cell	ΔE_{rel}	ΔE_{sd}
defect 1	3.386	3.436 (+0.050)	9.165 x 1	154 (14.8)	116 (11.1)
defect 2	5.459	5.456 (–0.003)	8.156 x 1	0 (0)	–38 (–3.7)
defect 3	6.938	6.938 (0.000)	6.955 x 1	17 (1.6)	–21 (–2.1)
defect 4	8.155	8.155 (0.000)	8.155 x 1	39 (3.8)	1 (0.1)
	YAG	Ce_Y-Ga_{tet} double substitutional defects			
	d(Y-Al_{tet})	d(Ce_Y-Ga_{tet}) intra-cell	d(Ce_Y-Ga_{tet}) inter-cell		
defect 5	3.028	3.056 (+0.028)	9.059 x 1	255 (24.6)	174 (16.8)
defect 6	3.709	3.755 (+0.046)	9.312 x 1	281 (27.1)	200 (19.3)
defect 7	5.666	5.655 (–0.011)	8.294 x 1	58 (5.6)	–23 (–2.2)
defect 8	6.057	6.056 (–0.001)	6.058 x 1	86 (8.3)	5 (0.5)
defect 9	7.103	7.104 (+0.001)	9.331 x 1, 9.337 x 1	83 (8.0)	2 (0.2)
defect 10	8.566	8.562 (-0.004)	8.565 x 1, 8.567 x 1, 8.569 x 1	86 (8.3)	5 (0.5)
defect 11	9.085	9.087 (+0.002)	9.085 x 1, 9.087 x 1, 9.089 x 1	84 (8.1)	3 (0.3)

YAG	d(Y-Al_{oct})	5.459	d(Y-Al_{tet})	5.666
Ce:YAG	d(Ce_Y-Al_{oct})	5.461	d(Ce_Y-Al_{tet})	5.667
Ga:YAG	d(Y-Ga_{oct})	5.461	d(Y-Ga_{tet})	5.668
Ce,Ga:YAG	Ce,Ga_{oct}:YAG (defect 2)		Ce,Ga_{tet}:YAG (defect 7)	
	d(Ce_Y-Ga_{oct})	5.456	d(Ce_Y-Ga_{tet})	5.655
	CeO_8 moiety			
	Oxygens of type s			
	d(Ce_Y -O_1)	2.406 (+0.033)	d(Ce_Y -O_1)	2.367 (–0.006)
	d(Ce_Y -O_2)	2.371 (–0.002)	d(Ce_Y -O_2)	2.368 (–0.005)
	d(Ce_Y -O_5)	2.373 (0.000)	d(Ce_Y -O_5)	2.440 (+0.067)
	d(Ce_Y -O_6)	2.407 (+0.034)	d(Ce_Y -O_6)	2.370 (–0.003)
	Oxygens of type l			
	d(Ce_Y -O_3)	2.473 (+0.005)	d(Ce_Y -O_3)	2.454 (–0.014)
	d(Ce_Y -O_4)	2.471 (+0.003)	d(Ce_Y -O_4)	2.470 (+0.002)
	d(Ce_Y -O_7)	2.454 (–0.014)	d(Ce_Y -O_7)	2.461 (–0.007)
	d(Ce_Y -O_8)	2.456 (–0.012)	d(Ce_Y -O_8)	2.472 (+0.004)
	GaO_6 moiety		GaO_4 moiety	
	d(Ga_{oct} -O_a)	2.053 (+0.014)	d(Ga_{tet} -O_a)	1.924 (0.000)
	d(Ga_{oct} -O_b)	2.040 (+0.001)	d(Ga_{tet} -O_b)	1.921 (–0.003)
	d(Ga_{oct} -O_c)	1.962 (–0.077)	d(Ga_{tet} -O_c)	1.928 (+0.004)
	d(Ga_{oct} -O_d)	2.043 (+0.004)	d(Ga_{tet} -O_d)	1.926 (+0.002)
	d(Ga_{oct} -O_e)	2.054 (+0.015)		
	d(Ga_{oct} -O_f)	2.040 (+0.001)		

Table 10.2: Relative energies of the levels of the Ce-$4f^1$, Ce-$5d^1$, and Ce-$6s^1$ configurations of the materials Ce,Ga_{oct}:YAG (defect 2, upper chart) and Ce,Ga_{tet}:YAG (defect 7, lower chart) and the shift induced by Ga-codoping Ce:YAG. All numbers in cm^{-1} .

Material:		Ce:YAG			Ce,Ga_{oct}:YAG			
Cluster:		$(CeO_8)^{13-}$	$(CeO_8Al_2O_4)^{15-}$		$(CeO_8)^{13-}$		$(CeO_8Al_2O_4)^{15-}$	
	D_2	Energies (sec. 8.2)	Energies (sec. 8.2)	C_1	Energies	Shift	Energies	Shift
$4f^1$ levels								
	$1\ ^2B_2$	0	0	$1\ ^2A$	0		0	
	$1\ ^2B_3$	274	38	$2\ ^2A$	267	-7	51	13
	$1\ ^2B_1$	290	202	$3\ ^2A$	322	32	244	42
	$1\ ^2A$	518	416	$4\ ^2A$	504	-14	421	5
	$2\ ^2B_1$	577	443	$5\ ^2A$	590	13	473	30
	$2\ ^2B_2$	638	516	$6\ ^2A$	634	-4	524	8
	$2\ ^2B_3$	2530	2419	$7\ ^2A$	2522	-8	2420	1
$5d^1$ levels								
	$2\ ^2A$	24887	23853	$8\ ^2A$	24931	44	23927	74
	$3\ ^2B_3$	30187	30169	$9\ ^2A$	30242	55	30247	76
	$3\ ^2A$	48080	48112	$10\ ^2A$	48251	171	48328	216
	$3\ ^2B_2$	49705	48700	$11\ ^2A$	50046	341	49080	380
	$3\ ^2B_1$	52568	52221	$12\ ^2A$	51858	-710	51555	-666
$6s^1$ level								
	$4\ ^2A$	67133	61214	$13\ ^2A$	67536	403	61957	743

Material:		Ce:YAG			Ce,Ga_{tet}:YAG			
Cluster:		$(CeO_8)^{13-}$	$(CeO_8Al_2O_4)^{15-}$		$(CeO_8)^{13-}$		$(CeO_8Al_2O_4)^{15-}$	
	D_2	Energies (sec. 8.2)	Energies (sec. 8.2)	C_1	Energies	Shift	Energies	Shift
$4f^1$ levels								
	$1\ ^2B_2$	0	0	$1\ ^2A$		0		
	$1\ ^2B_3$	274	38	$2\ ^2A$	291	17	64	26
	$1\ ^2B_1$	290	202	$3\ ^2A$	304	14	231	29
	$1\ ^2A$	518	416	$4\ ^2A$	513	-5	409	-7
	$2\ ^2B_1$	577	443	$5\ ^2A$	591	14	445	2
	$2\ ^2B_2$	638	516	$6\ ^2A$	651	13	529	13
	$2\ ^2B_3$	2530	2419	$7\ ^2A$	2507	-23	2390	-29
$5d^1$ levels								
	$2\ ^2A$	24887	23853	$8\ ^2A$	25063	176	24064	211
	$3\ ^2B_3$	30187	30169	$9\ ^2A$	30283	96	30278	109
	$3\ ^2A$	48080	48112	$10\ ^2A$	47819	-261	47884	-228
	$3\ ^2B_2$	49705	48700	$11\ ^2A$	49986	281	48990	290
	$3\ ^2B_1$	52568	52221	$12\ ^2A$	52059	-509	51719	-502
$6s^1$ level								
	$4\ ^2A$	67133	61214	$13\ ^2A$	67339	206	61627	413

Table 10.3: $4f^1$, $5d^1$, and $6s^1$ levels of the $(CeO_8Al_2O_4)^{15-}$ cluster in several embedding potentials. Ce,Ga_{oct}:YAG ≡ Ce,Ga_{oct}:YAG defect 2.

Material	Ce:YAG		Ce,Ga_{oct}:YAG	
Calculation	A	B	C	D
Cluster	Ce:YAG	Ce,Ga_{oct}:YAG	Ce,Ga_{oct}:YAG	Ce,Ga_{oct}:YAG
AIMP shell	Ce:YAG	Ce:YAG	Ce,Ga_{oct}:YAG	Ce,Ga_{oct}:YAG
AIMP Ga_{Al}	Al	Al	Al	Ga
$4f^1$ levels				
1 ^2A	0	0	0	0
2 ^2A	38	25	56	51
3 ^2A	202	217	249	244
4 ^2A	416	404	425	421
5 ^2A	443	458	478	473
6 ^2A	516	506	527	524
7 ^2A	2419	2411	2424	2420
$5d^1$ levels				
8 ^2A	23853	23794	23931	23927
9 ^2A	30169	30200	30251	30247
10 ^2A	48112	48336	48335	48328
11 ^2A	48700	48950	49105	49080
12 ^2A	52221	51648	51536	51555
$6s^1$ level				
13 ^2A	61214	62308	61866	61957
$\Delta E_{centroid}$ $(4f^1 \rightarrow 5d^1)$	40035	40032	40037	40037
$\Delta E_{LF}(1-4f^1)$	576	589	594	591
$\Delta E_{LF}(1-5d^1)$	16758	16716	16701	16701
$\Delta E_{ligand-field}$ $(1-4f^1 \rightarrow 1-5d^1)$	-16182	-16127	-16107	-16110

Table 10.4: $4f^1$, $5d^1$, and $6s^1$ levels of the $(CeO_8Al_2O_4)^{15-}$ cluster in several embedding potentials. Ce,Ga_{tet}:YAG ≡ Ce,Ga_{tet}:YAG defect 7.

Material	Ce:YAG		Ce,Ga_{tet}:YAG	
Calculation	A	B	C	D
Cluster	Ce:YAG	Ce,Ga_{tet}:YAG	Ce,Ga_{tet}:YAG	Ce,Ga_{tet}:YAG
AIMP shell	Ce:YAG	Ce:YAG	Ce,Ga_{tet}:YAG	Ce,Ga_{tet}:YAG
AIMP Ga_{Al}	Al	Al	Al	Ga
$4f^1$ levels				
$1\ ^2A$	0	0	0	0
$2\ ^2A$	38	51	64	64
$3\ ^2A$	202	227	231	231
$4\ ^2A$	416	413	410	409
$5\ ^2A$	443	439	445	445
$6\ ^2A$	516	540	529	529
$7\ ^2A$	2419	2403	2390	2390
$5d^1$ levels				
$8\ ^2A$	23853	23868	24064	24064
$9\ ^2A$	30169	30243	30278	30278
$10\ ^2A$	48112	47957	47881	47884
$11\ ^2A$	48700	48990	48991	48990
$12\ ^2A$	52221	51793	51713	51719
$6s^1$ level				
$13\ ^2A$	61957	61978	61621	61627
$\Delta E_{\text{centroid}}$ $(4f^1 \rightarrow 5d^1)$	40035	40008	40004	40006
$\Delta E_{\text{LF}}(1-4f^1)$	576	597	581	581
$\Delta E_{\text{LF}}(1-5d^1)$	16758	16627	16522	16523
$\Delta E_{\text{ligand-field}}$ $(1-4f^1 \rightarrow 1-5d^1)$	-16182	-16030	-15940	-15942

Table 10.5: Analysis of the first $4f \rightarrow 5d$ transition's shift from Ce:YAG to Ce,Ga_{oct}:YAG (defect 2) and to Ce,Ga_{tet}:YAG (defect 7). All numbers in cm^{-1}.

	Contributions				
	$A \rightarrow B$ First-shell distortion	$B \rightarrow C$ Cell distortion	$A \rightarrow C$ Full distortion	$C \rightarrow D$ Ga_{oct}	$A \rightarrow D$ All
			Ce,Ga_{oct}:YAG		
$\Delta E_{centroid}(4f^1 \rightarrow 5d^1)$	-3	5	2	0	2
$\Delta E_{LF}(1-4f^1)$	13	5	18	-3	15
		$1-4f^1 \rightarrow 1-5d^1$ transition			
$\Delta E_{LF}(1-5d^1)$	-42	-15	-57	0	-57
$\Delta E_{ligand-field}$ [a]	55	21	76	-4	72
ΔE [b]	52	26	78	-4	74
			Ce,Ga_{tet}:YAG		
$\Delta E_{centroid}(4f^1 \rightarrow 5d^1)$	-27	-3	-30	1	-29
$\Delta E_{LF}(1-4f^1)$	21	-16	5	0	5
		$1-4f^1 \rightarrow 1-5d^1$ transition			
$\Delta E_{LF}(1-5d^1)$	-131	-105	-236	1	-235
$\Delta E_{ligand-field}$ [a]	152	89	241	-1	240
ΔE [b]	125	86	211	0	211

[a] $\Delta E_{ligand-field} = \Delta E_{LF}(1-4f^1) - \Delta E_{LF}(1-5d^1)$, see Fig. 8.2

[b] $\Delta E = \Delta E_{centroid} + \Delta E_{ligand-field}$, see Fig. 8.2

Chapter 11

Ce:YAG with antisite defects

Intrinsic antisite defects (ADs) are known to be present in garnets, giving as a result a decrease of symmetry of the perfect crystal from cubic to trigonal [43]. Intrinsic luminescence patterns of YAG are associated to these antisite defects, specifically to the Y_{Al} centers. Such luminescence arises as wide complex bands in UV range of spectrum and their position, shape and intensity depend on the abundance and distribution of ADs via the features of sample preparation and temperature of measurements [44]. Moreover, it is known that such emission associated to Y_{Al} centers induces excitation of the Ce_Y impurity centers on bulk Ce:YAG. This interplay is not observed in single-crystalline films of Ce:YAG, since they are synthesized at much lower temperature than the bulk material and, thus, are practically antisite defect-free [45].

In this context, a detailed description of the interplay between Ce_Y luminescence and the ADs present in the YAG host is definitely of interest, giving a more realistic picture of the real behavior of Ce^{3+} as impurity in YAG. More specifically, the joint study of Ce and ADs in YAG aims to evaluate the influence of antisite defects in Ce:YAG Stokes shift, since previous embedded cluster calculations considering perfect YAG underestimate the experimental value for this quantity [41]. Besides, to the best of our knowledge, these two defects have not been studied together and the detailed added distortions in the surroundings of Ce_Y because of the presence of ADs are unknown experimentally.

As for Ce,La:YAG (Chapter 9) and for Ce,Ga:YAG (Chapter 10), we have studied the effect of one and two antisite defects on Ce:YAG absorption spectrum following the steps described in Section 8.1. Then, a PBC-DFT study on YAG cells containing both Ce and antisite defects is performed and results on structure and electronic structure are presented in Sections 11.1 and 11.2 respectively. Results of the embedded cluster CASSCF/CASPT2 calculations on the Ce $4f$ and $5d$ manifolds of Ce,ADs:YAG materials using the ground state PBC-DFT obtained structures are presented in Section 11.3 in comparison with those of Ce:YAG. The study of cluster geometries in excited states according to the recipe depicted in Section 8.1.2.1 and the results obtained on the study of the Stokes shift in Ce:YAG cells containing antisite defects are presented in Section 11.4. Finally, conclusions of this chapter and table data are presented in Sections 11.5 and 11.7 respectively.

11.1 Effects of antisite defects on the local structure of the active defect Ce_Y

We have studied YAG unit cells containing one Ce_Y defect per unit cell plus one antisite defect or two antisite defects per unit cell. In order to browse all the possible different cases, we resort to the information previously obtained about the structure of the antisite defects in pure YAG (Chapter 7).

All the possible cells containing one Ce_Y defect plus one antisite defect (Ce,1AD:YAG) maintaining the structural properties of a single antisite (Section 7.2.2) are shown in Fig. 11.1 (top).

Because of the symmetry loss within the cell because of the single antisite defect, all the remaining 23 Y positions after creating the antisite defect lead to different Ce_Y substitutions. Energies of such cells, after relaxation of the whole structure, are reflected in Table 11.1. Table 11.1 also shows the off-center displacements suffered by all the three defects Ce_Y, Y_{Al} and Al_Y, with respect to original Y, Al_{oct} and Y positions in YAG. Since in Ce:YAG Ce_Y remains on-center in the original Y position (Section 6.1.1) this off-center displacement measures as well the effect of the antisite defect on Ce_Y. We find a wide variety of Ce_Y off-center displacements from 0.004 (practically on-center) to 0.114 Å. On the other hand, we can see that the major off-center displacement is suffered by the antisite atoms, as we have seen before. The effect of Ce_Y is measured with respect to those off-center displacements of Al_Y and Y_{Al} in 1AD:YAG (Section 7.2.2) and tabulated in parentheses together with displacements with respect to YAG. We observe only a light effect of Ce on Al_Y and Y_{Al}, being the measured maximum extra displacement ~ 0.030 Å. We do not find any correspondence between these off-center displacements and the energy patterns. The distances between the Ce_Y impurity and the components of the antisite, Al_Y and Y_{Al} in Ce,1AD:YAG are shown in Table 11.2. The difference with respect to Ce-Y and Ce-Al_{oct} distances in Ce:YAG are tabulated in parentheses. This difference measures the effect of the antisite defect in such distance, and we can observe a wide variety of differences, which arise from the specific distortion within each case because of the antisite itself together with the presence of Ce. Original Y-Y and Y-Al_{oct} in YAG are also tabulated in Table 11.2 as a reference. It is interesting to observe for some Ce,1AD defects that such huge distortion of the overall structure places Ce_Y closer to antisite atoms of adjacent cells than those belonging the same unit cell. We do analyze below in detail this feature for the Ce,1AD:YAG most stable structure (defect 1a).

Regarding the cells containing one Ce_Y defect plus two antisite defect (Ce,2AD:YAG), we have taken into account the structure of two antisite defects connected by an Al_{oct} as inversion center (Section 7.2.3). Thus, all the non equivalent possible Ce_Y defects are shown in Fig. 11.1 (bottom).

Energies of such cells, after relaxation of the whole structure, are reflected in Table 11.3, ordered by relative energy with respect to the lowest. From these data, it can be seen that all the Ce,2AD:YAG structures are much closer in energy than the Ce,1AD:YAG, where the 1a structure is clearly preferred above all others. It does make sense because the

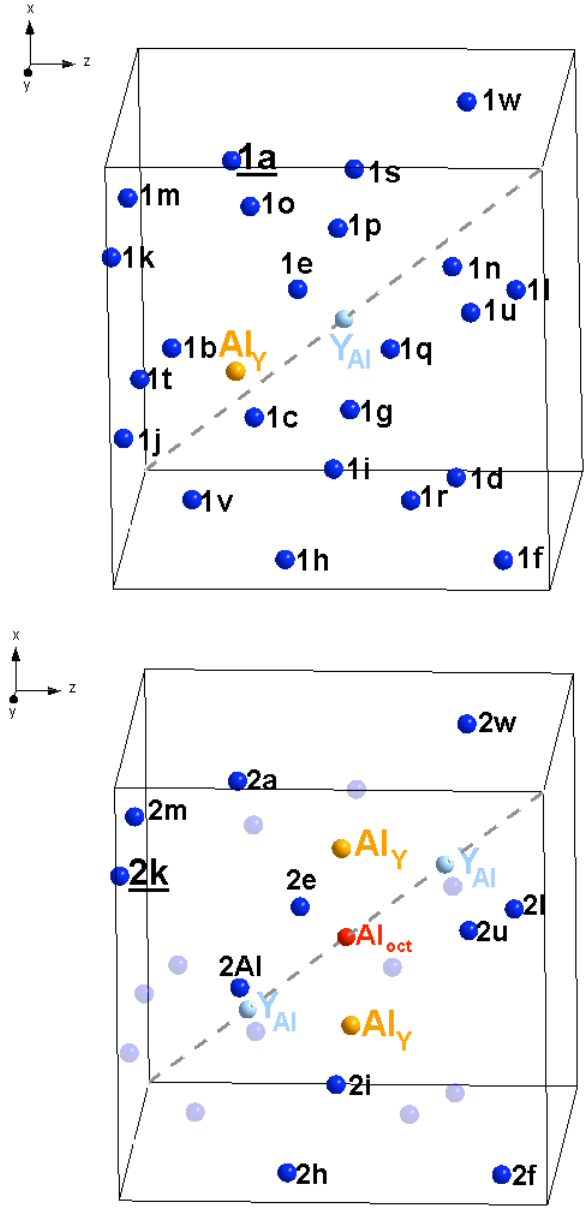

Figure 11.1: Top: representation of a single antisite defect (Al_Y and Y_{Al}) in a YAG cell together with all the non-equivalent Ce_Y positions giving rise to all Ce,1AD:YAG cells studied. Bottom: representation of a the double antisite defect (2 x Al_Y and 2 x Y_{Al}) with connecting inversion center Al_{oct} in a YAG cell together with all the non-equivalent Ce_Y positions giving rise to all Ce,2AD:YAG cells studied. Most stable situations for Ce_Y underlined. [111] axis shown as a visual reference.

two ADs structure occupy a considerable extension of the cell, making all the remaining Y positions (suitable for Ce_Y substitution) much more equivalent in terms of interactions and stress. Table 11.3 also reflects their corresponding off-center displacement of Ce_Y with respect to YAG. We do not observe higher displacements than for Ce,1AD:YAG,

but, different from Ce,1AD:YAG cases, none of the Ce_Y retains the on-center position. Due to the complexity of the Ce_Y-2AD defect (involves 5 centers), relative distortions of Ce_Y are measured with respect to the inversion center (Al_{oct} position) that connects the two antisite defects in the original structure (Fig. 7.8) and tabulated in Table 11.3. The variation with respect to Ce:YAG Ce_Y-Al_{oct} distance is given in parentheses.

The energy *versus* lattice constant a analysis for the most stable defects 1a and 2k shows that the equilibrium a_0 values are 12.134 Å and 12.168 Å, +0.17% and +0.44% respectively with respect to calculated pure and perfect YAG lattice constant. Thus, as in previous calculations, we use such a = 12.114 Å in all the calculations. Just to mention here that both a_0 of Ce,1AD:YAG and Ce,2AD:YAG are larger than the Ce:YAG a_0 (12.127 Å, +0.11%) but smaller than 1AD:YAG and 2AD:YAG equilibrium lattice constants (12.156 Å, +0.34% and 12.172 Å, +0.48% respectively). This indicates that, for these sets of defects at this concentration, the addition of a new Ce_Y in cells containing antisite defects does not increase the a_0, which actually slightly decreases.

The local structure of the most stable Ce,1AD:YAG (defect 1a) is shown in Fig. 11.2.

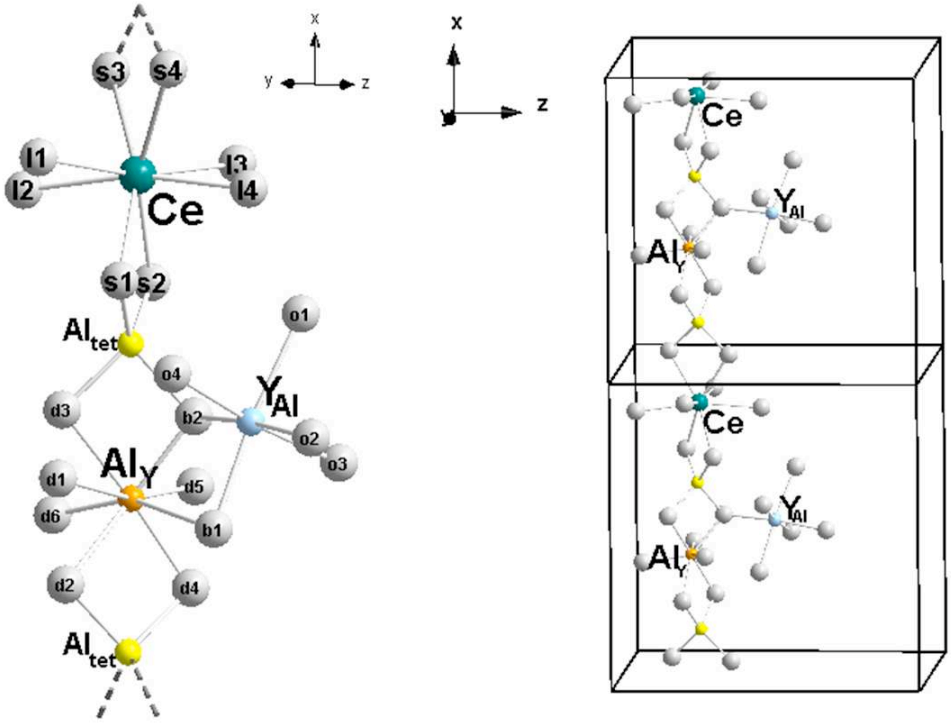

Figure 11.2: Representations of the most stable Ce_Y -1AD defect (defect 1a in Fig. 11.1). Left: isolated. Right: showing periodicity along the x-axis.

As said before, Ce_Y is in an Y D_2 site of YAG before relaxation, with four shorter and four larger Ce-O distances, labeled s1-s4 and l1-l4 in Fig. 11.2. It shows that Ce_Y

interacts with the antisite defect through its two *short* oxygens via AlO_4 moieties, along a ...-Ce_Y -AlO_4 -Al_Y -AlO_4 -Ce_Y -... axis (x axis in Fig. 11.2). That means that the original ...-Y-AlO_4 -Y- AlO_4 -... *chain* does not retain any Y atom and both Ce_Y and Al_Y are alternated between AlO_4 moieties. Moreover, Ce_Y moves and slightly increases its distance with respect to the Al_Y belonging to the same unit cell, becoming closer to the Al_Y of the adjacent unit cell ($d(Ce_Y\text{- }Al_Y)_{intracell} = 6.089$ Å, $d(Ce_Y\text{- }Al_Y)_{intercell} = 6.083$ Å; first entry in Table 11.2). This displacement is not purely vertical along the x axis: the structure $Al_{Y\ cell1}$-... -$Ce_{Y\ cell1}$ -... -$Al_{Y\ cell2}$ presents an angle of $\sim 169°$, 11° deviated from the 180° of the Y_{cell1}-... -Y'_{cell1}-... -Y_{cell2} structure in pure and perfect YAG, this coming from the off-center displacements of both Ce_Y and Al_Y.

Table 11.4 shows the distortions induced by the antisite defect on the Ce-O bonds and those induced by Ce in the Y_{Al}-O and Al_Y-O bonds. D_2 symmetry disappears and an overall expansion (+0.038 Å in average) is found in Ce_Y surroundings, short and long Ce_Y-O bonds being affected in a similar way. Distortions suffered by the antisite structure are also shown in Table 11.4. Distortions on the Al_Y first coordination shell tend to be compressive in the Al_Y -O short bonds (d3, b2, d2, d4), those in the ...-Ce_Y -AlO_4 -Al_Y -AlO_4 -Ce_Y -... direction, whereas the Al_Y -O long bonds (d1, d5, d6, b1) suffer mainly an expansion of a much lesser magnitude. The Y_{Al} moiety, out of the ...-Ce_Y -AlO_4 -Al_Y -AlO_4 -Ce_Y -... *chain*, is scarcely distorted.

Regarding Ce,2AD:YAG, the most stable structure (defect 2k) is shown in Fig. 11.3.

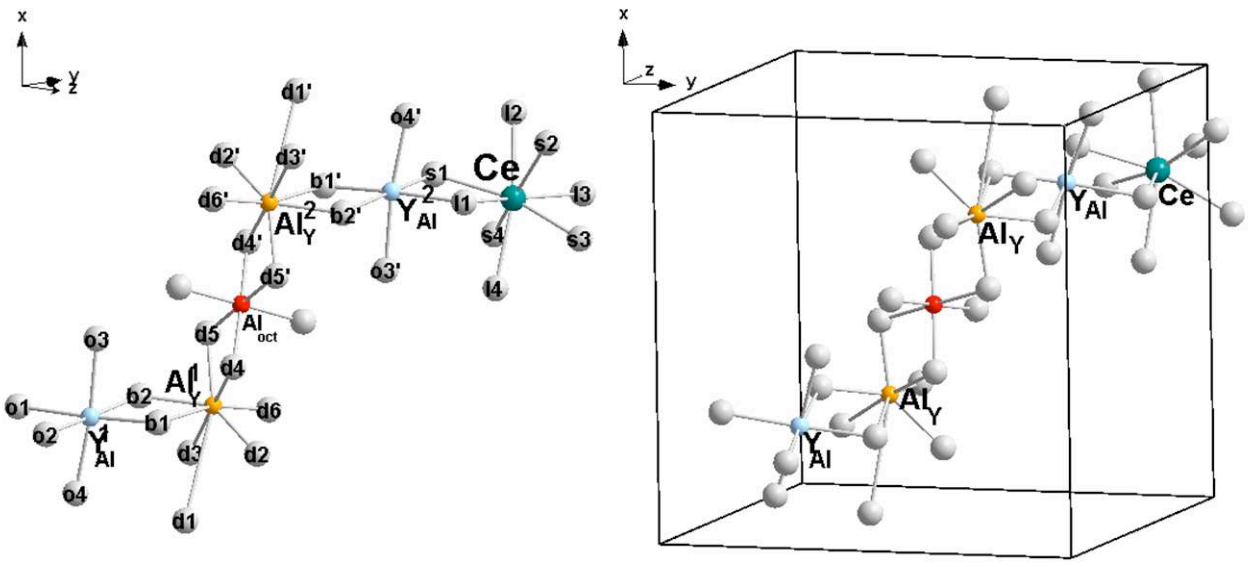

Figure 11.3: Representations of the most stable Ce_Y -2AD defect (defect 2k in Fig. 11.1). Left: isolated. Right: within the unit cell.

In this defect, Ce_Y is directly linked to one Y_{Al} of the ADs structure through one oxygen of each kind (short and long), different from the Ce,1AD:YAG case, where Ce_Y is linked to the AD via one AlO_4 moiety and two short-type oxygens are involved. Table 11.5 shows that distortions on the first coordination shell of Ce_Y are expansive (with average values of +0.038 Å in short Ce_Y-O bonds s1-s4 and +0.044 Å in long Ce_Y-O bonds) but more anisotropic than those distortions produced by one antisite defect. In fact, the two Ce_Y -O bonds with oxygens directly linked to the Y_{Al} of the antisite defect (s1 and l1) suffer a much smaller elongation than other bonds with oxygens not linked to the antisite, e.g. s4 and l4. However, the s1-Ce_Y -l1 angle does change, opening from 73.5° to 76.2° with respect to the single substitutional Ce_Y defect.

The formation energies of the most stable defects made of one Ce_Y and one or two Al_Y-Y_{Al} antisite defects, taking as a reference the Ce^{3+} and Y^{3+} free ions, are the following:

$$(Y_3Al_5O_{12})_8 + Ce^{3+} \rightarrow 1AD:(Y_{2.875}Ce_{0.125}Al_5O_{12})_8 + Y^{3+}\,,\ \Delta E = +3.308\ \text{eV}\,,$$
$$(Y_3Al_5O_{12})_8 + Ce^{3+} \rightarrow 2AD:(Y_{2.875}Ce_{0.125}Al_5O_{12})_8 + Y^{3+}\,,\ \Delta E = +7.022\ \text{eV}\,.$$

These, together with the corresponding formation energies of one Ce_Y defect (Section 6.1.3)

$$(Y_3Al_5O_{12})_8 + Ce^{3+} \rightarrow (Y_{2.875}Ce_{0.125}Al_5O_{12})_8 + Y^{3+}\,,\ \Delta E = +0.113\ \text{eV}\,,$$

and one and two Al_Y-Y_{Al} antisite defects (Section 7.2)

$$(Y_3Al_5O_{12})_8 \rightarrow 1AD:(Y_3Al_5O_{12})_8\,,\ \Delta E = +3.725\ \text{eV}\,,$$
$$1AD:(Y_3Al_5O_{12})_8 \rightarrow 2AD:(Y_3Al_5O_{12})_8\,,\ \Delta E = +3.492\ \text{eV}\,, \qquad (11.1)$$

allows us to complete Fig. 11.4, where the formation energies of single and multiple defects are summarized.

We can observe that the formation of one Ce_Y defect is 0.530 eV (51.1 kJ/mol) more favorable in YAG with one antisite defect per unit cell (–0.417 eV) than in perfect YAG (+0.113 eV). Equivalently, the formation of one Al_Y-Y_{Al} antisite defect is also 0.530 eV more favorable in Ce-doped YAG with one Ce_Y defect per unit cell (+3.195 eV) than in perfect YAG (+3.725 eV). –0.530 eV is just the interaction energy between the Ce_Y and Al_Y-Y_{Al} individual defects,

$$(Y_{2.875}Ce_{0.125}Al_5O_{12})_8 + 1AD:(Y_3Al_5O_{12})_8 \rightarrow 1AD:(Y_{2.875}Ce_{0.125}Al_5O_{12})_8 + (Y_3Al_5O_{12})_8\,,$$
$$\Delta E = -0.530\ \text{eV}.$$

Also from Fig. 11.4, it can be seen that the formation energy of a Ce_Y defect is more favorable in YAG containing two antisite defects (–0.195 eV) than in perfect YAG (+0.113 eV). Analogously, this favorable difference in energy (0.308 eV) is also found in the process of formation of two antisite defects from Ce:YAG (+6.909 eV) with respect to the formation of two antisite defects from pure YAG (+7.217 eV). Thus, –0.308 eV is the energy accounting for the interaction between the Ce_Y impurity and the defect formed by the two pairs of Y_{Al} and Al_Y :

$$(Y_{2.875}Ce_{0.125}Al_5O_{12})_8 + 2AD:(Y_3Al_5O_{12})_8 \rightarrow 2AD:(Y_{2.875}Ce_{0.125}Al_5O_{12})_8 + (Y_3Al_5O_{12})_8\,,$$
$$\Delta E = -0.308\ \text{eV}.$$

Figure 11.4: Schematic representation of defect formation energies. All energies in eV.

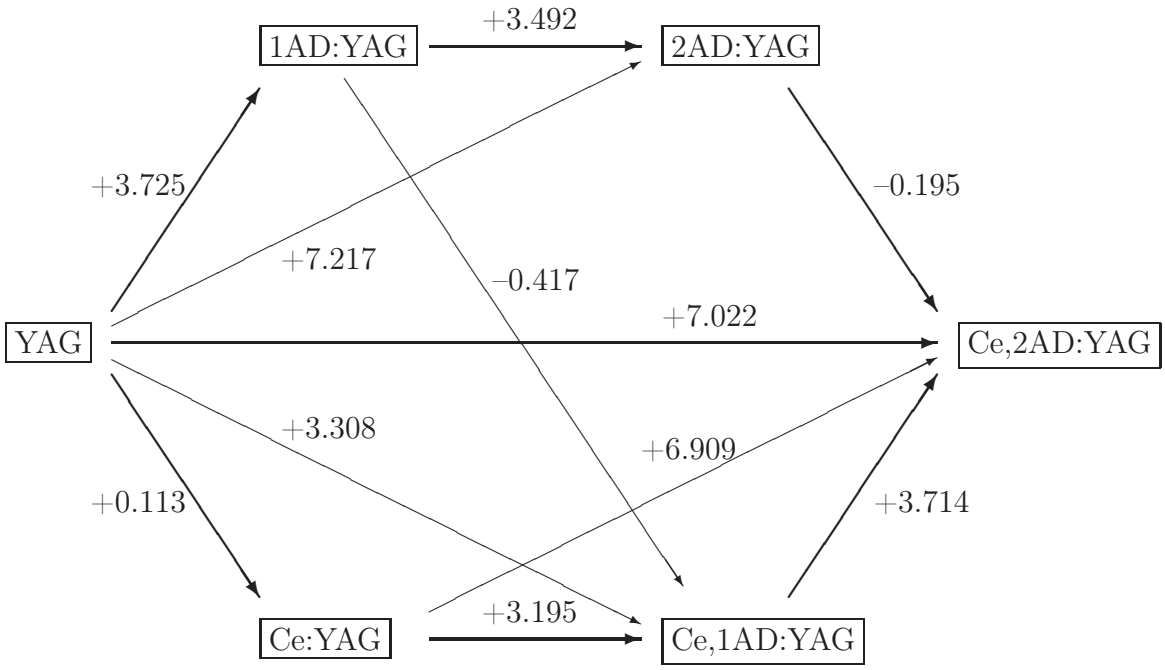

In this favorable interaction between the Ce_Y impurity and the antisite defects, relaxation cooperative factors do play a important role. In Ce,1AD:YAG, stress energy of the whole set of defects from perfect YAG structure is 6.612 eV, larger than the sum of separated relaxation energies of Ce_Y (in Ce:YAG) and 1AD (in 1AD:YAG), which is 6.305 eV. Regarding Ce,2AD:YAG, relaxation of the whole structure leads to a stabilization energy of 12.965 eV, larger than the sum of separated Ce_Y (in Ce:YAG) and 2AD (in 2AD:YAG), that is 12.765 eV.

Let us now discuss the successive formation of the first and the second antisite defect from Ce:YAG in comparison to the successive formation of the first and the second antisite defect in YAG. If we split the formation of two ADs from Ce:YAG ($Y_{2.875}Ce_{0.125}Al_5O_{12}$) as

$$\text{Ce:YAG} \rightarrow \text{Ce,1AD:YAG} \rightarrow \text{Ce,2AD:YAG}$$

we find an energy requirement of +3.195 eV in the addition of the first AD and +3.714 eV for the second one. The same process for YAG, that is,

$$\text{YAG} \rightarrow \text{1AD:YAG} \rightarrow \text{2AD:YAG}$$

needs +3.72 eV for the first AD and + 3.496 for the second AD. That means that the addition of the first AD is more favorable for Ce:YAG, whereas the addition of the second

is more favorable for YAG, because the less distorted 1AD:YAG (with respect to the Ce,1AD:YAG) is more likely to accommodate the second AD. Actually, the 2AD structure itself prints a huge distortion in YAG unit cell, and cannot be considered a point defect since involves many atoms and a large part of the YAG unit cell (Section 7.2.3). Anyway, and despite these hindrances, the global process is favorable to Ce:YAG by the 0.308 eV mentioned above.

From these energetic balances, it can be concluded that the presence of Ce_Y impurities at the concentrations studied in this work would diminish the concentration of antisite defects present in YAG, by favoring the formation of one antisite defect per unit cell, whereas for pure YAG, two antisite defects per cell are predicted, as stated in Section 7.2.3 and in agreement with experimental results [43].

11.2 Effects of antisite defects on Ce:YAG electronic structure

Band structures of defects 1a and 2k are shown in Fig. 11.5.

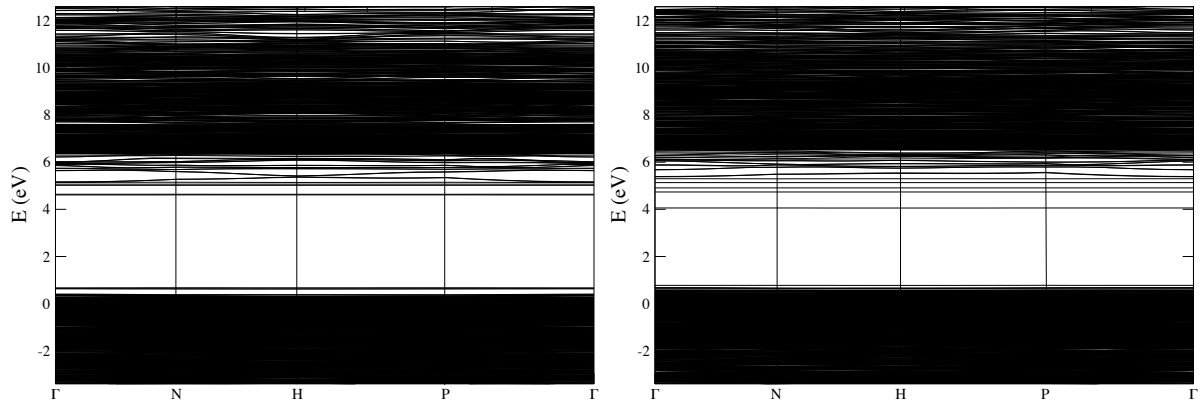

Figure 11.5: Left: Band structure of the most stable Ce_Y plus one antisite defect (defect 1a in Fig. 11.1). Right: Band structure of the most stable Ce_Y plus two antisite defects (defect 2k in Fig. 11.1).

They comprise features present in both Ce:YAG band structure (Fig. 6.6) and 1AD:YAG or 2AD:YAG band structures (Fig. 7.9). In Ce,1AD:YAG band structure, we can see, clearly above the top of YAG valence band, the occupied band from Ce. Differentiated from it, and also above the top of the perfect YAG valence band, we see some states that can be associated to the *unbound* oxygen atoms to Al_Y. More dispersion is observed in Ce,2AD:YAG band structure (as in 2AD:YAG band structure, Fig. 7.9, right) because, due to distortions involve many atoms in the cell, many oxygen states rise their energy. Then, we can observe a set of bands above the top of the YAG valence band and Ce states are not clearly differentiated from oxygen ones. PDOS, shown below, clarifies that the

highest occupied band is still belonging to Ce states and there are no oxygen states above it.

Calculated total densities of states (DOS) and projected densities (PDOS) of Ce,1AD:YAG (defect 1a) and Ce,2AD:YAG (defect 2k) are shown in Figs. 11.6 and 11.7 respectively, where zero of energies is taken as calculated top of the valence band of pure and perfect YAG.

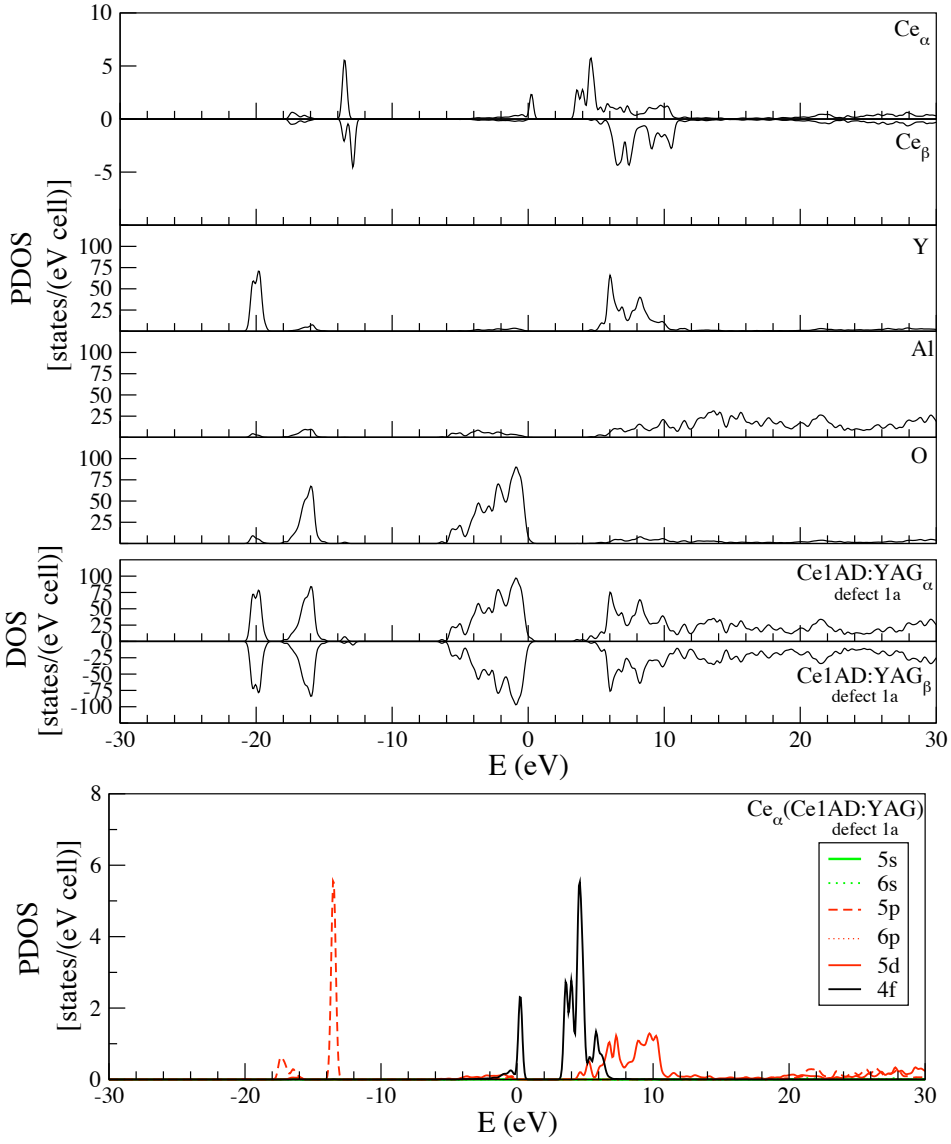

Figure 11.6: Top: PDOS of Ce, Y, Al and O species and total DOS of Ce,1AD:YAG (defect 1a). Bottom: Ce_α PDOS of this material projected on Ce valence orbitals.

Their pattern does not differ so much from those of Ce:YAG (Fig. 6.8); the Ce_Y impurity introduces $5p$ unoccupied states between -18 and -16 eV and between -14 and -12 eV with respect to pure YAG and changes the nature of the host gap by introducing occupied $4f$ states which spread over the top of the valence band and empty states of $4f$, $5d$ and $6s$ character in the bottom of the conduction band. Moreover, the upper levels of

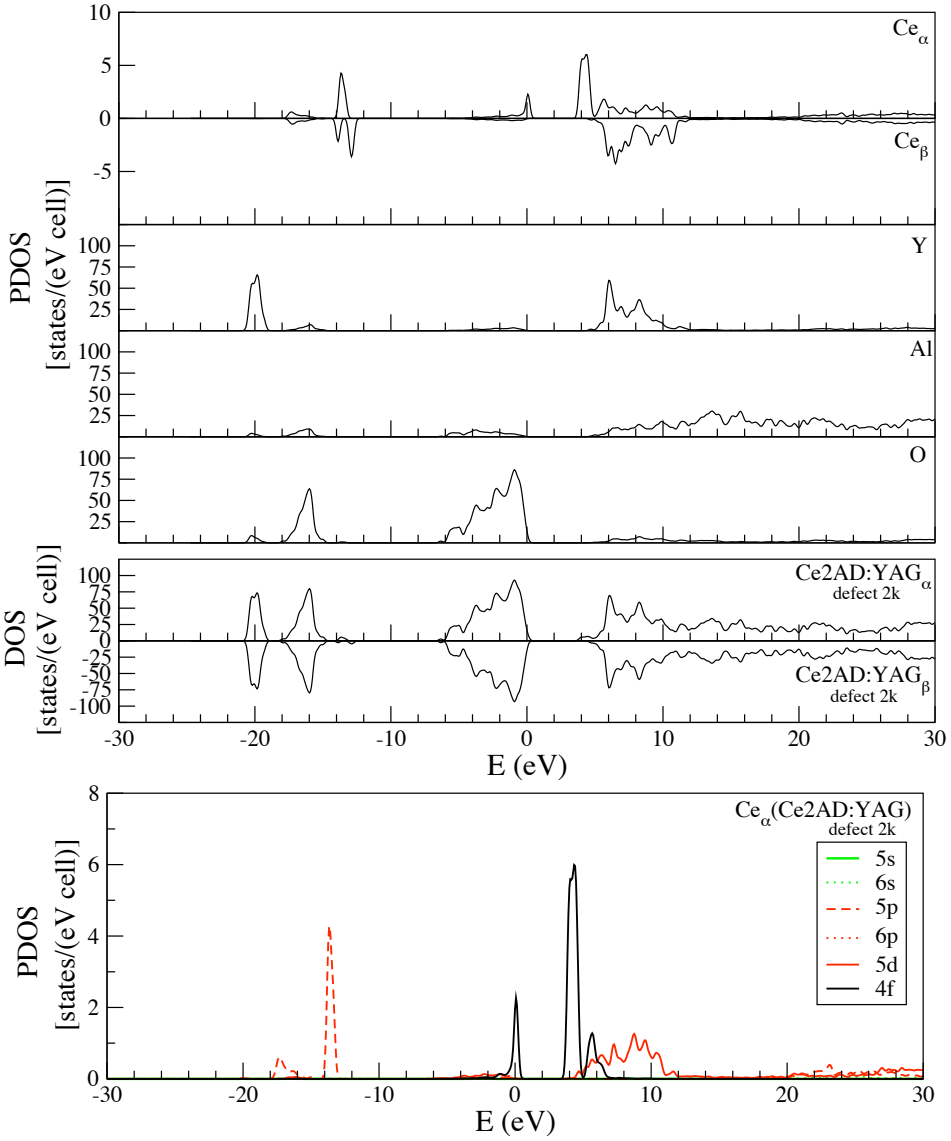

Figure 11.7: Top: PDOS of Ce, Y, Al and O species and total DOS of Ce,2AD:YAG (defect 2k). Bottom: Ce$_\alpha$ PDOS of this material projected on Ce valence orbitals.

the oxygen atoms belonging to the antisite defect(s) that are basically unbound to Al$_Y$ (oxygens d1 and b1 in tables 11.4 and 11.5) rise in energy, but, whereas in pure YAG these O $2p$ levels define the top of the valence band, they lie below Ce $4f$ levels in these doped materials so their role concerning the gap properties is less relevant than in pure YAG containing only ADs.

PDOS on Ce valence orbitals is shown in bottommost boxes of Figs. 11.6 and 11.7 for Ce,1AD:YAG and Ce,2AD:YAG respectively. In order to compare the different behavior of the Ce$_Y$ states involved in the gap, both are plotted together with Ce:YAG PDOS in Fig. 11.8.

Ce highest occupied states of Ce,1AD:YAG and Ce:2AD:YAG suffer a shift to lower energies (0.30 and 0.45 eV respectively) with respect to those of Ce:YAG. An equal shift

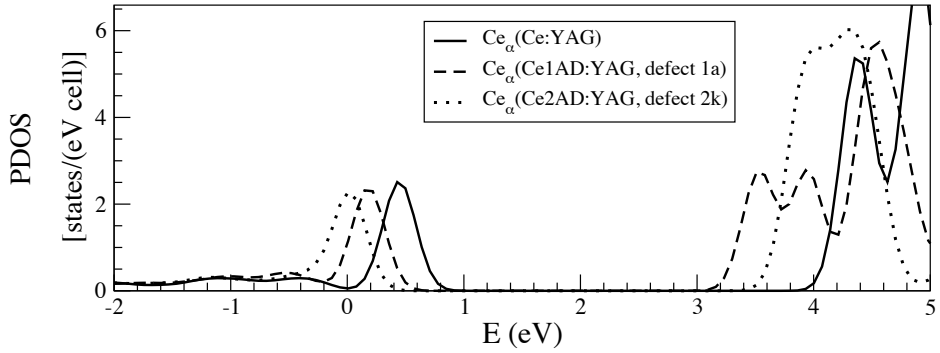

Figure 11.8: Ce_α PDOS of Ce,1AD:YAG and Ce,2AD:YAG in comparison of Ce_α PDOS of Ce:YAG.

is experienced by innermost Ce $5s$ and $5p$ orbitals, which indicates that these shifts are not due to bonding effects between Ce-$4f$ and O-$2p$ states involved in the top of the valence band, but because of the change of the electrostatic field on Ce due to the high and anisotropic distortion of its environment produced by the ADs, that forces it to a off-center displacement. This is in agreement with the fact that the higher the distortion is (Ce,2AD:YAG case), the higher the shift is. Regarding the lowest lying unoccupied states, we observe that they suffer a higher shift to lower energies than the Ce occupied states (0.80 and 0.50 eV for Ce,1AD:YAG and Ce,2AD:YAG respectively). The two prominent $4f$ peaks at 4.25 eV and 4.75 eV in Ce:YAG (Fig. 6.9) appear not so clearly defined in Ce,2AD:YAG but they still form a narrow band. However, this narrowness is lost in the Ce,1AD:YAG case, where a wide band with multiple peaks appears.

11.3 Effects of antisite defects on Ce:YAG absorption spectrum

In Table 11.6, we show the energies of the levels of the Ce-$4f^1$, Ce-$5d^1$, and Ce-$6s^1$ configurations relative to the ground state on $(CeO_8)^{13-}$and $(CeO_8Al_2O_4)^{15-}$ clusters of Ce,1AD:YAG and Ce:2AD:YAG as calculated with PBC-DFT in this work. The shift experienced by these levels upon the presence of antisite defects with respect to those of Ce:YAG with no antisite defects (Section 8.2) is also shown. This shift arises from the different coordinates of $(CeO_8)^{13-}$and $(CeO_8Al_2O_4)^{15-}$ clusters, the different atomic coordinates of the YAG unit cell used as AIMP embedding and the exchange of Y and Al in the antisite defects sites. The overall result for $(CeO_8)^{13-}$ and $(CeO_8Al_2O_4)^{15-}$ in both materials Ce,1AD:YAG and Ce,2AD:YAG is absolutely comparable: both the first and the second $4f \rightarrow 5d$ transitions are predicted to experience a blue shift with respect of those of perfect Ce:YAG.

From these data, we analyze the $4f \rightarrow 5d$ transitions following the approach outlined in Section 8.1.3. Then, according to Fig. 8.2, these transitions can be decomposed as

$$\begin{aligned}\Delta E(4f \rightarrow 5d) &= \Delta E_{\text{centroid}}(4f \rightarrow 5d) + \Delta E_{\text{ligand-field}} \\ &= \Delta E_{\text{centroid}}(4f \rightarrow 5d) + \Delta E_{\text{LF}}(4f) - \Delta E_{\text{LF}}(5d).\end{aligned}$$

The analysis of the obtained blue shift in terms of the components of the transitions is comparable as well for $(CeO_8)^{13-}$ and $(CeO_8Al_2O_4)^{15-}$ so that it is discussed below only for the larger $(CeO_8Al_2O_4)^{15-}$ cluster in both Ce,1AD:YAG and Ce,2AD:YAG materials.

In order to track the changes induced in all the components of the spectra from Ce:YAG calculation to final Ce,1AD:YAG and Ce,2AD:YAG calculations, we have performed some intermediate calculations (Section 8.1.2) that take into account the successive changes in cluster coordinates and embedding features, i.e the sources of the shift. These intermediate spectra are shown in Tables 11.7 and 11.8 for defects 1a and 2k respectively.

In Tables 11.7 and 11.8, calculation A is our Ce_Y:YAG reference; calculation B is performed using the $(CeO_8Al_2O_4)^{15-}$ coordinates according to relaxed Ce,1AD:YAG or Ce,2AD:YAG cells keeping the Ce:YAG AIMP embedding; calculation C contains both $(CeO_8Al_2O_4)^{15-}$ and AIMP embedding coordinates from relaxed Ce,1AD:YAG and Ce,2AD:YAG cells but we have used Al_{Al} and Y_Y AIMPs in antisite sites, which are finally exchanged in calculation D to represent as realistic as possible the effects of the embedding on Ce_Y. $A \rightarrow B$ accounts for the distortions on the $(CeO_8Al_2O_4)^{15-}$ cluster due to the presence of one or two antisite defects; $B \rightarrow C$ accounts for the long range distortions printed in the whole YAG cell and $C \rightarrow D$ accounts for the electronic effects caused by the exchange of Al and Y in the antisite positions as represented by the AIMP embedding potentials.

Calculated spectra components (Fig. 8.2) of each A, B, C and D calculations are also tabulated below their corresponding spectra in Tables 11.7 and 11.8. Using these data, successive changes in the first $4f \rightarrow 5d$ transition components are tabulated in Table 11.9 for both materials.

For Ce,1AD:YAG, last column of Table 11.9 shows that the blue shift of the first $4f \rightarrow 5d$ transition (461 cm^{-1}) has a strong ligand field contribution (502 cm^{-1}) coming entirely from the $5d$ manifold, not compensated by a much smaller centroid contribution (-41 cm^{-1}). The ligand field contribution is dominated by structural distortions (487 cm^{-1}) and, among them, the first-shell distortion appears to be more significant (357 cm^{-1}). This blue shift, resulting from a reduction of the effective ligand field on the $5d$ shell, is consistent with the average strong expansion experienced by the oxygens of the first coordination shell of Ce_Y and the rest of the lattice upon the presence of the antisite defect. On the other hand, the centroid provides a red shift contribution, mainly from first-shell distortions (-116 cm^{-1}) that is partially quenched when the total distortion of the cell is taken into account (+64 cm^{-1}, -52 cm^{-1} total). Neither the ligand field nor the centroid suffer in excess the electronic effects of the exchanged Y_{Al} and Al_Y (only 15 cm^{-1} and 11 cm^{-1} respectively), even if extra basis functions have been included in these atoms to improve degree of orthogonality between the cluster molecular orbitals

and the environmental orbitals because they are *second neighbors* of the $(CeO_8Al_2O_4)^{15-}$ cluster.

An analogous analysis of last column of Table 11.9 for Ce,2AD:YAG shows that, in comparison to the effect of one antisite defect, the higher blue shift of the first $4f \rightarrow 5d$ transition (792 cm^{-1}) has, on one hand, a stronger ligand field effect (1084 cm^{-1}) counteracted in part by a higher red shift on the centroid (-292 cm^{-1}). The total ligand field contribution comes from decrease of the ligand field of the $5d$ manifold (-1059 cm^{-1}) and it is largely dominated by the distortions on the cell, not only those on the first coordination shell (706 cm^{-1}) but also those on the whole YAG unit cell (539 extra cm^{-1}, total 1245 cm^{-1}). Red shift induced by the centroid in the Ce,2AD:YAG case is more important than in Ce,1AD:YAG case: $\sim 8\%$ of the ligand field component in Ce,1AD:YAG *versus* $\sim 27\%$ in Ce,2AD:YAG of opposite sign contribution of centroid with respect to the total ligand field contribution. It comes mainly from first-shell distortions (-223 cm^{-1}) only slightly corrected by whole cell distortions. Electronic effects coming from the Y_{Al} and Al_Y exchange have a higher effect in Ce,2AD:YAG (-242 cm^{-1}) case than in Ce,1AD:YAG case (26 cm^{-1}) and, actually, they provide contributions of opposite signs in each material. In Ce,2AD:YAG, the Y_{Al} and Al_Y exchange as represented by corresponding AIMPs induces a red shift not only in the ligand field component (-161 cm^{-1}), but also in the centroid (-81 cm^{-1}). Here, only one of the cations of the 2ADs structure is connected to the cluster (Y^2_{Al} in Fig. 11.3) but it is a *second neighbor*. Moreover, Ce_Y tends to approach the antisite structure and more electronic effects coming from the antisite atoms can be expected. We have found also this red shift associated to electronic effects of a *second neighbor* in Ce,La:YAG (Section 9.3) but, different from Ce,2AD:YAG, the blue shift due to distortions was not enough to quench this red shift and, finally, a total red shift was predicted. In Ce,1AD:YAG, Ce_Y is not linked directly to the antisite and, moreover, tends to go away from the 1AD structure. Accordingly, we have seen a lesser effect of the position exchange of the antisite cations in this case.

It is also remarkable that the $4f - 5d$ centroid, $\Delta E_{\text{centroid}}(4f^1 \rightarrow 5d^1)$, is lower upon the presence of antisite defects in spite of the fact that the ligands expand around Ce. The only model which is under use for this quantity, to the best of our knowledge, is that of Judd and Morrison [6, 7, 8] and, according to it, the $4f-5d$ centroid should increase when the distances Ce-O increase. This model is useful for a rationalization of $4f-5d$ centroids of lanthanide ions in many hosts [9] but, according to these first-principles calculations, it can be misleading if used for predicting small centroid shifts associated to small and/or anisotropic ligand distortions around lanthanides. Limitations of this model have been found not only in this work (Section 9.3) but also in previous *ab initio* calculations [239].

11.4 Effects of antisite defects on Ce:YAG Stokes shift

According to the strategy outlined in Section 8.1.2.1, we study the influence of antisite defects in Ce:YAG Stokes shift starting from optimizations of geometry of the local structures around Ce_Y in the first $4f$ and $5d$ states of Ce:YAG containing one and two antisite defects. Our approach consists in performing embedded cluster calculations where the starting coordinates of the target cluster ($(CeO_8Al_2O_4)^{15-}$) and the AIMP shell coordinates come from the above described ground state geometries obtained from PBC-DFT calculations in Ce,1AD:YAG and Ce,2AD:YAG species. Then, the embedded cluster $(CeO_8Al_2O_4)^{15-}$ is (totally or partially) allowed to relax in CASSCF calculations both for the $4f$ ground state and the first $5d$ excited state. Finally, we perform embedded-cluster CASPT2 calculations using these geometries to obtain the Ce $4f$, $5d$ and $6s$ levels. The Stokes shift is calculated by subtracting the difference of energy between the 1-$4f$ and the 1-$5d$ levels in the spectrum calculated with the $5d$ geometry (associated to the maximum of emission) to the difference of energy between the 1-$4f$ and the 1-$5d$ levels in the spectrum calculated with the $4f$ geometry (associated to the maximum of absorption).

As we have already seen, there is a lack of symmetry in the $CeO_8Al_2O_4$ moiety when ADs are present and this makes the optimization of geometry at a CASPT2 level of theory unaffordable. As a matter of fact, the optimization at the CASSCF level with the full basis used in all spectra calculations presented before is also very expensive in terms of computational required time. Then, our approach is the obtaining of the desired geometries in subsequent steps, first relaxing the CeO_8 moiety using a smaller basis and then, using this relaxed structure, allowing all the atoms in $CeO_8Al_2O_4$ to relax, also using the smaller basis. The next step would be the use of this structure as starting point of relaxations using the larger basis and, finally, full relaxation of the $CeO_8Al_2O_4$ moiety with the larger basis. We are performing all these steps in order to obtain a complete picture of the problem but the results presented in this work, which cover the optimization process using the smaller basis set, are already meaningful regarding the effect of the antisite defects in Ce:YAG Stokes shift since we don't expect a drastic effect of the basis set increase in cluster geometries and, then, in the Stokes shift either.

Ce_Y and one antisite defect Structure of the $(CeO_8Al_2O_4)^{15-}$ cluster after the optimization of geometry of the CeO_8 and $CeO_8Al_2O_4$ moieties of both $1-4f$ and $1-5d$ states using Ce $(14s10p10d8f)/[5s4p5d3f]$, O $(5s6p)/[2s3p]$ and Al $(7s6p)/[2s3p]$ basis sets and considering the AIMP embedding from the Ce,1AD:YAG case are tabulated in Table 11.10. Fig. 11.9 represents the cluster used and the smaller moiety relaxed in a first step.

Within the ground state, we observe the different geometries obtained for the $1-4f$ state in the CASSCF and in the PBC-DFT calculations. Some factors are responsible of these differences. Apart from being methods that use different physical approaches to the electronic problem (CASSCF is a wavefunction-based method and DFT is based on the electronic density), one of them is the different boundary conditions of the PBC-DFT

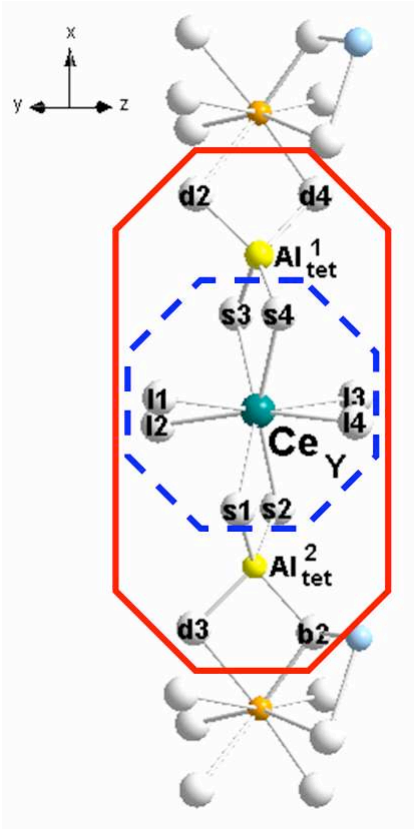

Figure 11.9: $(CeO_8Al_2O_4)^{15-}$ embedded cluster (solid red line). All its atoms relaxed in CASSCF calculations in the first $4f$ and $5d$ states. The CeO_8 moiety relaxed in a first step shown (dashed blue line). Antisite defect (Al_Y, orange and Y_{Al}, light blue) shown. Same atomic labels as in Fig. 11.2.

and the embedded cluster CASSCF calculations. The long-range distortions are more accurately treated in the PBC-DFT method and it provides dynamic correlation whereas CASSCF calculations lacks it. However, the CASSCF framework accounts for the exact exchange term, different from DFT. Moreover, there are some effects related to the basis sets used in both methods, different not only in size but also in features.

Regarding Ce_Y and the first coordination shell in the $1-4f$ ground state, we find in the CASSCF optimization of geometry a not uniform enlargement of the *short* Ce-O bonds and a simultaneous not uniform shortening of the *long* Ce-O bonds with respect to the values obtained in our PBC-DFT calculations. That leads to an average $d(Ce\text{-}O_s)/d(Ce\text{-}O_l)$ ratio more similar to that obtained in the embedded cluster calculations at the CASPT2 level of Ref. [41]. Very similar results are obtained when only the CeO_8 or the $CeO_8Al_2O_4$ moieties are allowed to relax. Regarding oxygens linked to the two Al_{tet} and not linked to Ce_Y, three of them significantly change their Ce-O distance with respect to DFT ones

when we relax all the $CeO_8Al_2O_4$ structure. However, the fourth oxygen, linked to Al_{tet}, Y_{Al} and Al_Y (b2 in Fig. 11.9), scarcely moves with respect to Ce_Y.

If we now compare the structure on the first $1-5d$ state with that of the $1-4f$ one, we can evaluate the occurred relaxation after a $4f \rightarrow 5d$ absorption prior to the $5d \rightarrow 4f$ emission. We see that the Ce-O_s bonds of the excited state are 0.018 Å shorter in average than those of the $1-4f$ both when the CeO_8 and the $CeO_8Al_2O_4$ moieties are relaxed. Decrease in the Ce-O_l distances is slightly smaller (average of 0.011 Å moving CeO_8 and of 0.008 Å moving $CeO_8Al_2O_4$). The reduction on such distances is of the same magnitude as the 0.014 Å decrease calculated at the CASPT2 level and using symmetry for both Ce-O_s and Ce-O_l bonds in Ref. [41]. Then, since the relaxation after the considered $4f \rightarrow 5d$ absorption is similar to that obtained in Ref. [41], we can anticipate similar calculated Stokes shifts as well.

As additional information about the structure of the cluster, we have measured the angles involving the atoms of the -Al_Y-AlO_4-Ce_Y-AlO_4-Al_Y- *chain*. We see that, regardless the moiety considered in the optimization procedure, the ground state structure is more constrained than in antisite-free cells because of the presence of the antisite defects along the *chain*, i.e. the O-Al_{tet}-O and the O_s-Ce-O_s angles are even smaller than the ∼100 and ∼72° of YAG or Ce:YAG (Tables 6.1 and 6.5). We already observed this in the PBC-DFT calculations. This situation get worse in the $1-5d$ state, since the structure contracts around Ce_Y, bringing about more stress.

These geometries optimized at the CASSCF level have been used to calculate the Stokes shift of the Ce,1AD:YAG material as treated in this approach. Then, we calculate Ce $4f$, $5d$ and $6s$ levels for each CeO_8 and $CeO_8Al_2O_4$ relaxed structures of both ground and excited states in embedded cluster calculations at the CASPT2 level considering always the $(CeO_8Al_2O_4)^{15-}$ cluster and the same AIMP embedding. In order to evaluate the effect of the basis size in the Stokes shift, we perform all these calculations not only using the basis set previously used for spectra calculations (Ce $(14s10p10d8f3g)/[6s5p6d4f1g]$, O $(5s6p1d)/[3s4p1d]$ and Al$(7s6p1d)/[2s3p1d]$) but also the smaller basis used in geometry optimization. These calculated levels are tabulated in Table 11.12.

In Ce:YAG, the maximum of the absorption profile is very close to the vertical energy differences between the 1-$4f$ and the 1-$5d$ states. However, the emission from the 1-$5d$ state involves the seven $4f$ states, giving rise a emission profile with two maxima. Among them, the one involving the ground state 1-$4f$ also involves the 2-$4f$ and 3-$4f$ ones. However, we calculate the Stokes shift as the difference of the vertical absorption and emission from/to the 1-$4f$ and the 1-$5d$ states. That leads to a underestimation of the Stokes shift in our calculations that depends on the concrete position of the 2-$4f$ and 3-$4f$ states. These calculated Stokes shift are tabulated together with the energy levels in Table 11.12.

We obtain a much smaller value than the experimental one (2400 cm^{-1}, Ref. [42]) regardless the moiety allowed to move and the size of the basis set used, all of them being in the 530-566 cm^{-1} range. We roughly estimate an maximum extra quantity of ∼120 cm^{-1} if we consider the energy of the 2-$4f$ and 3-$4f$ states.

Thus, our calculations considering one antisite defect underestimate the value in the same magnitude as Ref. [41] considering perfect YAG. Then, we can consider that the antisite defect has a negligible effect on Ce:YAG Stokes shift within the approach adopted in this work.

In order to evaluate the stability of this result, we analyze a little bit more in detail the different vertical spectra of the $(CeO_8Al_2O_4)^{15-}$ cluster obtained after relaxation of the $CeO_8/CeO_8Al_2O_4$ moieties and, both, calculated with the small basis used for geometry optimizations and with the larger one used so far for absorption spectra in this work. Regarding the effect of the relaxation of different clusters in Stokes shift, we observe that calculated spectra for relaxed CeO_8 and $CeO_8Al_2O_4$ for a common basis size used in the CASPT2 calculation, are quite similar, above all if we compare the first $4f \rightarrow 5d$ transitions. Then, the observed pronounced movement of the oxygens belonging to the AlO_4 moieties not linked to Ce (d2, d4, d3, b2) has no effect in the spectra and, thus, in the Stokes shift either. Considering relaxation of the same moiety, the effect of using the larger basis sets in spectra CASPT2 calculations is an uniform $\sim$1100 cm^{-1} increment of the first $4f \rightarrow 5d$ transition in all calculations performed, keeping the calculated Stokes shift untouched. For the second $4f \rightarrow 5d$ transition, we find again a uniform increment of 1300 cm^{-1}. Third, fourth and fifth transitions suffer uneven increments, smaller than those obtained for the two first transitions.

Ce_Y and two antisite defects In order to calculate the Ce:YAG Stokes shift upon the presence of two antisite defects, we follow the same approach adopted for Ce,1AD:YAG. Our final target calculations are CASPT2 vertical spectra calculations involving the $(CeO_8Al_2O_4)^{15-}$ geometries of the 1-4f and 1-5d states, them optimized at the CASSCF level in embedded cluster calculations with the larger basis.

However, we can already extract information of the Stokes shift from intermediate calculations previous to the target one, based on the particular features of the Ce,2AD:YAG structure and in the previous results obtained for Ce,1AD:YAG.

As depicted in Fig. 11.10, Ce_Y is linked to the antisite structure via two oxygen atoms of the first coordination shell in Ce,2AD:YAG, whereas the extra AlO_2 moieties are not linked to any antisite. Moreover, we have seen that in Ce,1AD:YAG case that, even though the AlO_4 moieties link Ce_Y and the antisite defect, the relaxation of the whole $CeO_8Al_2O_4$ structure does not affect the Stokes shift. Then, we expect that the most important effect of the antisite is printed in the first coordination shell of Ce_Y and relaxing the extra AlO_2 moieties in the $CeO_8Al_2O_4$ structure would not affect the value of the Stokes shift. Then, we have performed relaxations of the CeO_8 moiety at the CASSCF level in both ground and excited states of $(CeO_8Al_2O_4)^{15-}$ using AIMP embedding coordinates and starting cluster coordinates from ground state PBC-DFT calculations of Ce,2AD:YAG.

Obtained geometrical parameters around Ce_Y are shown in Table 11.11. The ground state structure predicted by our CASSCF calculations has shorter Ce-O_s bonds than the PBC-DFT calculated one (0.025 Å on average), suffering the smaller shortening the Ce-O bond of the oxygen atom linking Ce with the antisite defect (s1). Two of the four Ce-O_l

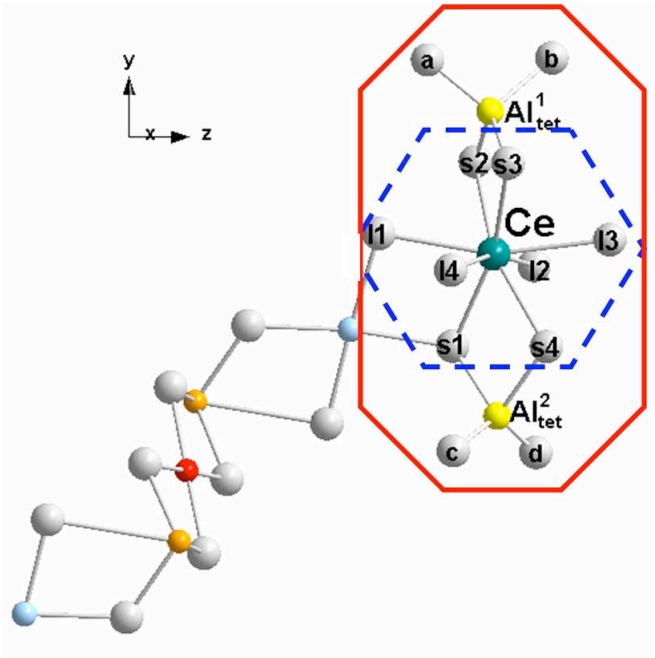

Figure 11.10: $(CeO_8Al_2O_4)^{15-}$ embedded cluster (solid red line). Atoms of the CeO_8 moiety (dashed blue line) relaxed in CASSCF calculations in the first $4f$ and $5d$ states. The two ADs linked to Ce_Y (Al_Y, orange and Y_{Al}, light blue) schematically shown. Same atomic labels as in Fig. 11.3.

bonds are considerably larger than in the DFT structure, the one involving the other linking atom to the antisite (l1) among them. If we now compare both ground state and excited state geometries calculated at the CASSCF level to evaluate the relaxation pattern after a $4f \rightarrow 5d$ absorption prior to the $5d \rightarrow 4f$ emission, we find shorter Ce-O distances in the $5d$ state, as in Ce,1AD:YAG and in Ref. [41]. Ce-O_s distances suffer a uniform decrease of 0.011 Å on average, less uniform that in Ce,1AD:YAG but of the same magnitude. The Ce-O_{l1} bond, involving one of the oxygen atoms that link Ce and Y_{Al}, suffers from the largest shortening among the Ce-O_l ones. Even though we find a less homogeneous decrease of the Ce-O bond lenghts in the excited state, we don't observe any remarkable feature in the structure that could make us expect a drastic increase in the calculated Stokes shift in comparison with those calculated so far.

Just to complete the structural analysis, we have measured the angles between the atoms along the -Y-AlO_4-Ce-AlO_4-Y *chain*. Since the antisite defects are not linked to Ce_Y via the AlO_4 moieties, such angles are more similar among them and to those of YAG, both in ground and excited states.

We have used these structures in embedded cluster calculations on the $(CeO_8Al_2O_4)^{15-}$ cluster at the CASPT2 level in order to get the corresponding Ce $4f$, $5d$ and $6s$ levels. Since we have seen that the effect of using a larger basis does not affect substantially the magnitude of the calculated Stokes shift, we perform these calculations with the small basis and we think that we should not expect drastic changes if the larger basis is used.

These spectra are tabulated in Table 11.13.

As in Ce,1AD:YAG, we calculate the Stokes shift as the difference between the vertical 1-4f-1-5d transitions obtained from ground and excited geometries. Such value is 438 cm^{-1}, plus an extra estimated shift of $\sim$80 cm^{-1} if we take into account the emission pattern to the three first $4f$ states commented above. These value is even smaller than the analogous Stokes shift calculated with the same basis and moving the CeO_8 moiety in Ce,1AD:YAG and, then, is even further to the experimental value. That confirms our statement that antisite defects have a negligible role in calculated Ce:YAG Stokes shift, because, even in the Ce,2AD:YAG case, where ADs are directly linked to Ce_Y via two oxygen atoms of the first coordination shell and relaxation patterns in the excited state are not uniform for all the Ce-O bonds, we do not find any change in the calculated value.

For completeness, we are currently performing optimizations of geometry that finally will lead to the full relaxation of the $CeO_8Al_2O_4$ moiety in both Ce,1AD:YAG and Ce,2AD:YAG materials with the larger basis set and we will obtain the corresponding vertical CASPT2 spectra also using the larger basis set but, according to the results already reported, we don't expect any relevant change in the final calculated Stokes shift, and, then, our conclusion regarding the negligible role of the antisite defects would hold.

11.5 Conclusions

We have performed a PBC-DFT (PBE) study on the distribution, atomistic structure and electronic structure of materials containing one Ce_Y plus one or two Y_{Al}-Al_Y antisite defects per YAG unit cell. We have kept the atomistic arrangement of the antisite defects structures previously obtained in this work and studied all the non-equivalent relative positions of Ce_Y.

The most stable Ce,1AD:YAG structure presents Ce_Y and Al_Y alternated along a ...-Ce_Y -AlO_4 -Al_Y -AlO_4 -Ce_Y -... *chain*, where the antisite defect forces Ce_Y to move toward the adjacent Al_Y. This, together with a overall expansion of all the Ce_Y-O bonds in a similar way, makes D_2 symmetry on Ce_Y site to disappear. Ce_Y prints a much less important distortion around the antisite atoms; this is specially true for the Y_{Al} out of the ...-Ce_Y -AlO_4 -Al_Y -AlO_4 -Ce_Y -... *chain*.

Regarding the most stable Ce,2AD:YAG structure, Ce_Y is linked only to the Y_{Al} of one of the two ADs via two oxygen atoms of the first coordination shell. This produces an expansion of the Ce_Y-O bonds, more anisotropic than in the Ce,1AD:YAG case. The AD structures are only slightly affected by the presence of Ce; actually we can consider Ce_Y non-interacting with the furthest AD. This set of defects cannot be considered a point defect, since distortion is extended all over the YAG cell to a greater or lesser extent.

As in other cases when Ce_Y becomes off-site due to the presence of other defects in the cell, DOS/PDOS of these materials show Ce states to be shifted to lower energies due to the change in the electrostatic field. Highest occupied states of many oxygens suffering displacements rise in energy but they lie always below Ce f states.

Our calculations show an attractive interaction between Ce_Y and one AD (0.530 eV), favorable to a lesser degree between Ce_Y and two ADs (0.308 eV). In these favorable interactions, cooperative relaxation factors play an important role. Formation of one AD in cells containing Ce_Y appears to be less energetically demanding than the same process from pure and perfect YAG. However, the successive formation of the second antisite defect is less energetic in the absence of Ce_Y. Then, from our calculations, it seems that Ce_Y impurities in YAG, at the concentrations studied in this work, would diminish the concentration of two antisite per unit cell found in pure YAG.

The effects of the antisite defects in Ce:YAG absorption spectrum have been studied by means of embedded cluster CASSCF/CASPT2 calculations on the Ce-$4f^1$ and Ce-$5d^1$ manifolds of Ce,1AD:YAG and Ce,2AD:YAG using cluster structures arising from PBC-DFT calculations. Antisite defects induce a large blue shift of the lowest Ce^{3+} $4f \rightarrow 5d$ transition, experimented in both Ce,1AD:YAG (461 cm^{-1}) and Ce,2AD:YAG (792 cm^{-1}) materials with similar patterns, enhanced in Ce,2AD:YAG because of the more pronounced distortions. These blue shifts of the first $4f \rightarrow 5d$ transition have been shown to be the result of a decrease of the effective ligand field on the Ce-$5d$ shell (associated with distortions not only in Ce_Y surroundings but in the whole YAG cell) only partially compensated by a slight decrease of the difference between the energy centroids of the $5d^1$ and $4f^1$ configurations, also incurred to structural distortions.

The effect of antisite defects on the Stokes shift of the first $4f \rightarrow 5d$ transitions of Ce:YAG have been studied by means of CASSCF/CASPT2 embedded cluster calculations on the Ce-$4f^1$ and Ce-$5d^1$ manifolds of Ce,1AD:YAG and Ce,2AD:YAG. The cluster structures of both $4f$ ground state and first $5d$ excited state have been optimized at the CASSCF level in embedded cluster calculations using AIMP embedding potentials located at the coordinates resulting from PBC-DFT calculations on these materials. A smaller basis set than that used for vertical spectra calculations is used in geometry optimizations. Using these structures optimized at the CASSCF level, the vertical $4f \rightarrow 5d$ absorption and $5d \rightarrow 4f$ emission have been calculated at the CASPT2 level. Our obtained Stokes shift from these vertical transitions still underestimates the experimental values and does not improve results of previous embedded cluster calculations considering perfect YAG host.

The reason behind this result is that we find similar structural differences between the ground state and the first excited state as in mentioned previous calculations.

We don't expect significant changes in the $CeO_8Al_2O_4$ structure of both ground and excited states if CASSCF optimizations of geometry are performed using a larger basis. This, together with the fact that we use the same AIMP embedding in all the calculations on each specie, leads us to conclude that we don't expect significant differences in the Stokes shift either.

Then, according to our calculations, the effect of antisite defects on the Stokes shift of the first $4f \rightarrow 5d$ transition of Ce:YAG is negligible. The relatively large difference between the experimental and the computed values of the Stokes shift remains unsolved.

11.6 *Conclusiones*

Hemos realizado cálculos PBC-DFT (PBE) de la distribución, estructura a nivel atómico y estructura electrónica de materiales que contienen un Ce_Y más uno o dos defectos *antisite* del tipo Y_{Al}-Al_Y. Hemos conservado las disposiciones atómicas previamente calculadas de las estructuras de estos defectos y hemos estudiado todos las posiciones relativas no equivalentes de Ce_Y.

La estructura más estable de Ce,1AD:YAG presenta Ce_Y y Al_Y alternados a lo largo de cadenas ...-Ce_Y -AlO_4 -Al_Y -AlO_4 -Ce_Y -..., donde el defecto *antisite* fuerza al Ce_Y a moverse hacia el Al_Y adyacente. Esto, junto a la homogenea expansión de los enlaces Ce_Y-O, hacen que la simetría D_2 del sitio Ce_Y desaparezca. El Ce_Y ejerce un efecto mucho menor sobre la estructura del defecto *antisite*; esto es verdad sobre todo en el caso del Y_{Al} fuera de la cadena ...-Ce_Y -AlO_4 -Al_Y -AlO_4 -Ce_Y -....

En cuanto a la estructura más estable de Ce,2AD:YAG, el Ce_Y está unido sólo al Y_{Al} de uno de los dos defectos *antisite* a través de dos átomos de oxígeno. Esto provoca una expansión de los enlaces Ce_Y-O, más anisotrópica que en el caso de Ce,1AD:YAG. Las estrucuras de los defectos *antisite* se ven sólo ligeramente afectadas por la presencia de Ce y, de hecho, se puede considerar que el Ce_Y y el defecto *antisite* más lejano no interactúan. Este conjunto de defectos no puede considerarse un defecto puntual, puesto que la distorsión se extiende por toda la celda de YAG en mayor o menor medida.

Como en otros casos donde el Ce_Y se desplaza *off-center* debido a la presencia de otros defectos en la celda, las DOS/PDOS de estos materiales muestran que los estados del Ce se desplazan a menores energías, debido al cambio en el campo cristalino. Los estados más altos ocupados de muchos oxígenos que sufren desplazamientos aumentan su energía, pero siempre están por debajo de los estados f del Ce.

Nuestros cálculos muestran una interacción atractiva entre Ce_Y y un defecto *antisite* (0.530 eV), tambien favorable pero en menor medida entre Ce_Y y dos defectos *antisite* (0.308 eV). En estas interacciones favorables, los factores de relajación cooperativos tienen un papel importante. La formación de un defecto *antisite* en celdas de YAG que contienen un átomo de Ce_Y requiere menos energía que la formacion de un defecto *antisite* en YAG puro. Sin embargo, la formación de un segundo defecto *antisite* requiere menos energía en ausencia de Ce_Y. Asi pues, podemos decir que según nuestros cálculos y a las concentraciones de defectos consideradas en este trabajo, las impurezas de Ce_Y cambiarían el patrón de dos defectos *antisite* por celda encontrados experimentalmente en YAG puro.

El efecto de los defectos *antisite* sobre el espectro de absorción del Ce:YAG han sido estudiados mediante cálculos CASSCF/CASPT2 de *cluster* embebido en los niveles Ce-$4f^1$ y Ce-$5d^1$ de Ce,1AD:YAG y Ce,2AD:YAG usando como estructuras de *cluster* las estructuras obtenidas con métodos PBC-DFT (Sección 8.1). Los defectos *antisite* inducen un desplazamiento al azul de la transición $4f \rightarrow 5d$ más baja en Ce^{3+}, experimentado en ambos materiales (461 cm^{-1} en Ce,1AD:YAG y 792 cm^{-1} en Ce,2AD:YAG) más pronunciado en Ce,2AD:YAG, donde las distorsiones son mayores. Hemos visto que estos desplazamientos al azul de la primera transición $4f \rightarrow 5d$ se deben a una disminución del

campo de ligando efectivo en la capa $5d$ (asociado a distorsiones locales alrededor del Ce y a distorsiones en toda la celda) sólo parcialmente compensada con una ligera disminución de la diferencia de energía entre los centroides de las configuraciones $4f$ y $5d$, también debida a distorsiones estructurales.

El efecto de los defectos *antisite* en el desplazamiento de Stokes de la primera transicion $4f \rightarrow 5d$ de Ce:YAG ha sido estudiado mediante cálculos de *cluster* embebido a nivel CASSCF/CASPT2 de los estados Ce-$4f^1$ y Ce-$5d^1$ de Ce,1AD:YAG y Ce,2AD:YAG. Las estructuras de los *cluster* en el estado fundamental $4f$ y en el primer estado excitado $5d$ han sido optimizadas a nivel CASSCF en cálculos de *cluster* embebido usando potenciales de *embedding* AIMP situados en las coordenadas obtenidas mediante cálculos PBC-DFT en estas especies. En la optimización de geometrías, hemos usado una base más pequeña que la utilizada para calcular los espectros verticales. Utilizando estas estructuras optimizadas a nivel CASSCF, hemos calculado la absorción vertical $4f \rightarrow 5d$ y la emisión vertical $5d \rightarrow 4f$ a nivel CASPT2. El Stokes shift obtenido a partir de estas transiciones verticales aún subestima los valores experimentales y no mejora los resultados obtenidos previamente con cálculos de *cluster* embebido considerando el YAG perfecto.

La razón de este resultado está en que encontramos diferencias estructurales similares entre el estado fundamental y el primer estado excitado a las encontradas en el mencionado cálculo.

No esperamos cambios significativos en la estructura de la unidad $CeO_8Al_2O_4$ ni en el estado fundamental ni en el excitado en una optimización a nivel CASSCF si utilizamos una base más grande. Esto, junto con el hecho de que usamos siempre el mismo *embedding* de AIMPs en todos los cálculos de cada especie, nos lleva a concluir que no podemos esperar diferencias significativas tampoco en el desplazamiento de Stokes.

Asi pues, según nuestros cálculos, el efecto de los defectos *antisite* en el desplazamiento de Stokes de la primera transición $4f \rightarrow 5d$ de Ce:YAG es despreciable. La razón de la relativamente grande diferencia entre los valores calculados y el experimental está todavía sin resolver.

11.7 Data tables

Table 11.1: Selected data of Ce,1AD:YAG cells studied (I). Off-center displacement (d_{off}) of Ce_Y in Ce,1AD:YAG[1] with respect to pure and perfect YAG[2] (Chapter 5) in Å. Off-center displacement of Y_{Al} and Al_Y with respect to YAG positions (Å) and difference with respect to off-center displacement in 1AD:YAG[3] (Section 7.2.2) in parentheses (Å). Relative defect energies with respect to the most stable, in meV (kJ/mol in parentheses). Labels according to Fig. 11.1 (top).

		d_{off}		ΔE
	Ce^1-Y^2	$Y_{Al}{}^1$-Al^2	$Al_Y{}^1$-Y^2	
defect 1a	0.013	0.134 (+0.004)[3]	0.596 (–0.002)[3]	0 (0)
defect 1b	0.070	0.135 (+0.005)	0.607 (+0.009)	154 (14.9)
defect 1c	0.004	0.129 (–0.001)	0.592 (–0.006)	163 (15.7)
defect 1d	0.010	0.125 (–0.005)	0.581 (–0.017)	180 (17.4)
defect 1e	0.010	0.124 (–0.006)	0.583 (–0.015)	185 (17.8)
defect 1f	0.009	0.122 (–0.008)	0.601 (+0.003)	196 (18.9)
defect 1g	0.119	0.140 (+0.010)	0.565 (–0.033)	200 (19.3)
defect 1h	0.042	0.134 (+0.004)	0.599 (+0.001)	202 (19.5)
defect 1i	0.003	0.126 (–0.004)	0.586 (–0.012)	208 (20.1)
defect 1j	0.052	0.122 (–0.008)	0.569 (–0.029)	210 (20.3)
defect 1k	0.013	0.134 (+0.004)	0.590 (–0.008)	215 (20.7)
defect 1l	0.014	0.114 (–0.016)	0.582 (–0.016)	285 (27.5)
defect 1m	0.023	0.131 (+0.001)	0.584 (–0.014)	295 (28.5)
defect 1n	0.076	0.132 (+0.002)	0.583 (–0.015)	303 (29.2)
defect 1o	0.023	0.130 (0.000)	0.579 (–0.019)	311 (30.0)
defect 1p	0.083	0.119 (–0.011)	0.590 (–0.008)	351 (33.9)
defect 1q	0.087	0.120 (–0.010)	0.591 (–0.007)	359 (34.6)
defect 1r	0.041	0.132 (+0.002)	0.592 (–0.006)	403 (38.9)
defect 1s	0.018	0.119 (–0.011)	0.591 (–0.007)	405 (39.1)
defect 1t	0.021	0.130 (0.000)	0.590 (–0.008)	432 (41.7)
defect 1u	0.021	0.132 (+0.002)	0.589 (–0.009)	436 (42.1)
defect 1v	0.022	0.131 (+0.001)	0.584 (–0.014)	438 (42.3)
defect 1w	0.029	0.128 (–0.002)	0.569 (–0.029)	478 (46.1)

Table 11.2: Selected data of Ce,1AD:YAG cells studied (II). Nearest distances between Ce and Y_{Al} and between Ce and Al_Y in Ce,1AD:YAG in comparison with distances between Ce and Al_{oct} and between Ce and Y in Ce:YAG (Section 6.1.1) and distances between Y and Al_{oct} and between Y and Y in pure and perfect YAG (Section 5.2). In parentheses, difference of Ce,1AD:YAG distances with respect to Ce:YAG ones. Labels according to Fig. 11.1 (top).

Material	YAG		Ce:YAG		Ce,1AD:YAG	
	d(Y-Al_{oct})	d(Y-Y)	d(Ce_Y-Al_{oct})	d(Ce_Y-Y)	d(Ce_Y-Y_{Al})	d(Ce_Y- Al_Y)
defect 1a	5.459	6.057	5.458	6.060	5.473 (+0.015)	6.083[1] (+0.023)
defect 1b	5.459	3.709	5.458	3.718	5.285 (–0.173)	3.898 (+0.180)
defect 1c	8.155	6.772	8.153	6.773	8.037[1] (–0.116)	6.401 (–0.372)
defect 1d	5.459	6.772	5.458	6.773	5.463 (+0.005)	6.450[1] (–0.323)
defect 1e	3.386	3.709	3.395	3.718	3.429 (+0.034)	3.818 (+0.100)
defect 1f	8.155	7.103	8.153	7.106	8.151 (–0.002)	7.075[1] (–0.031)
defect 1g	3.386	3.709	3.395	3.718	3.428 (+0.033)	3.833 (+0.115)
defect 1h	6.938	5.666	6.944	5.668	6.855 (–0.089)	6.064 (+0.396)
defect 1i	5.459	5.666	5.458	5.668	5.381 (–0.077)	6.232 (+0.564)
defect 1j	6.938	3.709	6.944	3.718	6.771 (–0.223)	3.628 (–0.090)
defect 1k	8.155	7.103	8.153	7.106	8.052 (–0.101)	7.219 (+0.113)
defect 1l	5.459	8.566	5.458	8.564	5.138[1] (–0.320)	8.482 (–0.082)
defect 1m	6.938	5.666	6.944	5.668	6.905 (–0.039)	5.381 (–0.287)
defect 1n	3.386	6.772	3.395	6.773	3.651 (+0.256)	7.189 (+0.416)
defect 1o	6.938	6.772	6.944	6.773	6.861[1] (–0.083)	6.395 (–0.378)
defect 1p	3.386	5.666	3.395	5.668	3.485 (+0.090)	5.591 (–0.077)
defect 1q	3.386	5.666	3.395	5.668	3.485 (+0.090)	6.285 (+0.617)
defect 1r	6.938	7.103	6.944	7.106	6.935 (–0.009)	7.171 (+0.065)
defect 1s	5.459	7.103	5.458	7.106	5.538 (+0.080)	6.989 (–0.117)
defect 1t	8.155	5.666	8.153	5.668	8.077 (–0.076)	5.378 (–0.290)
defect 1u	6.938	8.566	6.944	8.564	6.928[1] (–0.600)	7.964[1] (–0.016)
defect 1v	8.155	5.666	8.153	5.668	8.089 (–0.064)	5.378 (–0.290)
defect 1w	8.155	10.491	8.153	10.493	8.156[1] (+0.003)	10.440 (–0.053)

[1] nearest antisite-belonging atoms not located within the same unit cell as Ce_Y but in an adjacent one

Table 11.3: Selected data of Ce,2AD:YAG cells studied. Off-center displacement of Ce_Y with respect to YAG (and Ce:YAG) in Ce,2AD:YAG (d_{off}(Ce), in Å). Nearest distances between Ce and Al_{oct} in Ce,2AD:YAG in comparison with distances between Y and Al_{oct} in YAG (Section 5.2) and distances between Ce and Al_{oct} in Ce:YAG (Section 6.1.1). In parentheses, difference of Ce,2AD:YAG distances with respect to Ce:YAG ones. Relative defect energies with respect to the most stable, in meV (kJ/mol in parenthesis). Labels according to Fig. 11.1 (bottom).

	d_{off}(Ce)	YAG	Ce:YAG	Ce,2AD:YAG	
		d(Y-Al_{oct})	d(Ce_Y -Al_{oct})	d(Ce_Y -Al_{oct})	ΔE
defect 2k	0.039	8.155	8.153	8.133 (–0.020)	0 (0)
defect 2f	0.077	8.155	8.153	8.107 (–0.046)	38 (3.7)
defect 2w	0.086	8.155	8.153	8.134 (–0.019)	41 (4.0)
defect 2h	0.075	6.938	6.944	6.870[1](–0.074)	55 (5.3)
defect 2Al	0.083	3.386	3.395	3.378 (–0.017)	57 (5.5)
defect 2a	0.050	5.459	5.458	5.414 (–0.044)	71 (6.9)
defect 2u	0.031	6.938	6.944	6.910[1](–0.034)	89 (8.6)
defect 2i	0.026	5.459	5.458	5.469 (+0.011)	115 (11.1)
defect 2l	0.025	5.459	5.458	5.477 (+0.019)	118 (11.4)
defect 2m	0.019	6.938	6.944	6.938[1](–0.006)	135 (13.0)
defect 2a	0.115	3.386	3.395	3.332 (–0.063)	256 (24.7)

[1] nearest Al_{oct} atoms not located within the same unit cell as Ce_Y but in an adjacent one

Table 11.4: Ce_Y-O distances in the CeO_8 moiety in Ce,1AD:YAG defect 1a and differences with those in the single defect Ce:YAG (Section 6.1.1) in parentheses. Y_{Al}-O and Al_Y-O distances in the antisite defect of Ce,1AD:YAG defect 1a and differences with respect to analogous in 1AD:YAG (Section 7.2.2) in parentheses. All quantities in Å. Labels according to Fig. 11.2.

			Ce,1AD:YAG		
	d(Ce_Y-O)		d(Al_Y-O)		d(Y_{Al}-O)
s1	2.427 (+0.054)	d1	3.206 (-0.010)	b1	2.126 (-0.002)
s2	2.420 (+0.047)	d2	2.309 (-0.005)	b2	2.209 (-0.002)
s3	2.405 (+0.032)	d3	2.129 (-0.060)	o1	2.238 (+0.005)
s4	2.414 (+0.041)	d4	2.011 (-0.047)	o2	2.221 (-0.005)
l1	2.516 (+0.048)	d5	1.983 (+0.019)	o3	2.224 (+0.001)
l2	2.518 (+0.050)	d6	1.955 (+0.001)	o4	2.187 (+0.001)
l3	2.516 (+0.048)	b1	2.904 (+0.015)		
l4	2.450 (-0.018)	b2	2.019 (-0.045)		

Table 11.5: Ce_Y-O distances in the CeO_8 moiety in Ce,2AD:YAG defect 2k and differences with those in the single defect (Ce:YAG, Section 6.1.1) in parentheses. Y_{Al}-O and Al_Y-O distances in the two ADs of Ce,2AD:YAG defect 2k and differences with respect to analogous in 2AD:YAG (Section 7.2.3) in parentheses. All quantities in Å. Labels according to Fig. 11.3.

				Ce,2AD:YAG			
	d(Ce_Y-O)		d(Al_Y-O)	d(Al_Y-O)'		d(Y_{Al}-O)	d(Y_{Al}-O)'
s1	2.376 (+0.003)	d1	3.338 (0.000)	3.263 (-0.075)	b1	2.123 (0.000)	2.116 (-0.007)
s2	2.419 (+0.046)	d2	2.100 (0.000)	2.096 (-0.004)	b2	2.212 (0.000)	2.203 (-0.009)
s3	2.402 (+0.029)	d3	2.169 (0.000)	2.154 (-0.015)	o1	2.216 (0.000)	2.236 (+0.020)
s4	2.447 (+0.074)	d4	2.056 (0.000)	2.033 (-0.023)	o2	2.226 (0.000)	2.225 (-0.001)
l1	2.492 (+0.024)	d5	2.080 (0.000)	2.098 (+0.018)	o3	2.224 (0.000)	2.228 (+0.004)
l2	2.498 (+0.030)	d6	1.966 (0.000)	1.959 (-0.007)	o4	2.190 (0.000)	2.187 (-0.003)
l3	2.504 (+0.036)	b1	2.854 (0.000)	2.854 (0.000)			
l4	2.553 (+0.085)	b2	2.057 (0.000)	2.063 (+0.006)			

Table 11.6: Relative energies of the levels of the Ce-$4f^1$, Ce-$5d^1$, and Ce-$6s^1$ configurations of the materials Ce:YAG, Ce,1AD:YAG and Ce,2AD:YAG and the shift induced by the presence of one or two antisite defect per Ce:YAG unit cell. All numbers in cm^{-1}.

Material:		Ce_Y :YAG			Ce,1AD:YAG			
Cluster:		$(CeO_8)^{13-}$	$(CeO_8Al_2O_4)^{15-}$		$(CeO_8)^{13-}$		$(CeO_8Al_2O_4)^{15-}$	
	D_2	Energy	Energy	C_1	Energy	Shift	Energy	Shift
$4f^1$								
levels	$1\ ^2B_2$	0	0	$1\ ^2A$	0	0	0	0
	$1\ ^2B_3$	274	38	$2\ ^2A$	76	-198	63	26
	$1\ ^2B_1$	290	202	$3\ ^2A$	213	-77	159	-43
	$1\ ^2A$	518	416	$4\ ^2A$	339	-179	433	17
	$2\ ^2B_1$	577	443	$5\ ^2A$	364	-212	488	45
	$2\ ^2B_2$	638	516	$6\ ^2A$	477	-161	571	55
	$2\ ^2B_3$	2530	2419	$7\ ^2A$	2265	-266	2316	-102
$5d^1$								
levels	$2\ ^2A$	24887	23853	$8\ ^2A$	25300	413	24314	461
	$3\ ^2B_3$	30187	30169	$9\ ^2A$	30884	698	31093	923
	$3\ ^2A$	48080	48112	$10\ ^2A$	48290	210	47904	-208
	$3\ ^2B_2$	49705	48700	$11\ ^2A$	49434	-270	49318	618
	$3\ ^2B_1$	52568	52221	$12\ ^2A$	50556	-2012	50218	-2003
$6s^1$								
level	$4\ ^2A$	67133	61214	$13\ ^2A$	66548	-585	58984	-2230

Material:		Ce_Y :YAG			Ce,2ADs:YAG			
Cluster:		$(CeO_8)^{13-}$	$(CeO_8Al_2O_4)^{15-}$		$(CeO_8)^{13-}$		$(CeO_8Al_2O_4)^{15-}$	
	D_2	Energy	Energy	C_1	Energy	Shift	Energy	Shift
$4f^1$								
levels	$1\ ^2B_2$	0	0	$1\ ^2A$	0	0	0	0
	$1\ ^2B_3$	274	38	$2\ ^2A$	112	-162	36	-1
	$1\ ^2B_1$	290	202	$3\ ^2A$	291	1	271	69
	$1\ ^2A$	518	416	$4\ ^2A$	419	-100	461	45
	$2\ ^2B_1$	577	443	$5\ ^2A$	531	-46	492	49
	$2\ ^2B_2$	638	516	$6\ ^2A$	669	31	624	108
	$2\ ^2B_3$	2530	2419	$7\ ^2A$	2330	-200	2320	-98
$5d^1$								
levels	$2\ ^2A$	24887	23853	$8\ ^2A$	25568	681	24645	792
	$3\ ^2B_3$	30187	30169	$9\ ^2A$	30461	274	30505	336
	$3\ ^2A$	48080	48112	$10\ ^2A$	47146	-935	46695	-1418
	$3\ ^2B_2$	49705	48700	$11\ ^2A$	47706	-1999	47379	-1321
	$3\ ^2B_1$	52568	52221	$12\ ^2A$	52856	289	52497	276
$6s^1$								
level	$4\ ^2A$	67133	61214	$13\ ^2A$	69655	2522	64190	2976

Table 11.7: $4f^1$, $5d^1$, and $6s^1$ levels of the $(CeO_8Al_2O_4)^{15-}$ cluster of Ce,1AD:YAG in several embedding potentials.

Material	Ce:YAG		Ce,1AD:YAG	
Calculation	A	B	C	D
Cluster coordinates	Ce:YAG	Ce,1AD:YAG	Ce,1AD:YAG	Ce,1AD:YAG
Embedding coordinates	Ce:YAG	Ce:YAG	Ce,1AD:YAG	Ce,1AD:YAG
Embedding potential on	Y_Y Al_{Al}	Y_Y Al_{Al}	Y_Y Al_{Al}	Al_Y Y_{Al}
Al_Y Y_{Al}				
$4f^1$ levels				
$1\ ^2A$	0	0	0	0
$2\ ^2A$	38	112	85	63
$3\ ^2A$	202	142	152	159
$4\ ^2A$	416	460	441	433
$5\ ^2A$	443	510	498	488
$6\ ^2A$	516	601	587	571
$7\ ^2A$	2419	2354	2324	2316
$5d^1$ levels				
$8\ ^2A$	23853	24094	24288	24314
$9\ ^2A$	30169	31007	31135	31093
$10\ ^2A$	48112	47760	47820	47904
$11\ ^2A$	48700	49240	49294	49318
$12\ ^2A$	52221	51476	50296	50218
$6s^1$ levels				
$13\ ^2A$	61214	61311	60472	58984
$\Delta E_{\text{centroid}}$				
$(4f^1 \rightarrow 5d^1)$	40035	39919	39983	39994
ΔE_{LF}				
$(1-4f^1)$	576	597	584	576
ΔE_{LF}				
$(1-5d^1)$	16758	16421	16279	16256
$\Delta E_{\text{ligand-field}}$				
$(1-4f^1 \rightarrow 1-5d^1)$	-16182	-15824	-15695	-15680
ΔE_{LF}				
$(2-5d^1)$	10442	9508	9432	9477
$\Delta E_{\text{ligand-field}}$				
$(1-4f^1 \rightarrow 2-5d^1)$	-9866	-8911	-8848	-8901

Table 11.8: $4f^1$, $5d^1$, and $6s^1$ levels of the $(CeO_8Al_2O_4)^{15-}$ cluster of Ce,2AD:YAG in several embedding potentials.

Material	Ce:YAG		Ce,2AD:YAG	
Calculation	A	B	C	D
Cluster coordinates	Ce:YAG	Ce,2AD:YAG	Ce,2AD:YAG	Ce,2AD:YAG
Embedding coordinates	Ce:YAG	Ce:YAG	Ce,2AD:YAG	Ce,2AD:YAG
Embedding potential on Al_Y Y_{Al}	Y_Y Al_{Al}	2x(Y_Y Al_{Al})	2x(Y_Y Al_{Al})	2x(Al_Y Y_{Al})
$4f^1$ levels				
$1\ ^2A$	0	0	0	0
$2\ ^2A$	38	55	38	36
$3\ ^2A$	202	265	223	271
$4\ ^2A$	416	489	401	461
$5\ ^2A$	443	516	443	492
$6\ ^2A$	516	639	559	624
$7\ ^2A$	2419	2355	2271	2320
$5d^1$ levels				
$8\ ^2A$	23853	24336	24887	24645
$9\ ^2A$	30169	30703	30614	30505
$10\ ^2A$	48112	47077	46703	46695
$11\ ^2A$	48700	47510	47473	47379
$12\ ^2A$	52221	52517	52254	52497
$6s^1$ levels				
$13\ ^2A$	61214	63873	60256	64190
$\Delta E_{\text{centroid}}$ $(4f^1 \rightarrow 5d^1)$	40035	39812	39824	39743
ΔE_{LF} $(1-4f^1)$	576	617	562	601
ΔE_{LF} $(1-5d^1)$	16758	16093	15499	15699
$\Delta E_{\text{ligand-field}}$ $(1-4f^1 \rightarrow 1-5d^1)$	-16182	-15476	-14937	-15098
ΔE_{LF} $(2-5d^1)$	10442	9725	9773	9839
$\Delta E_{\text{ligand-field}}$ $(1-4f^1 \rightarrow 2-5d^1)$	-9866	-9109	-9210	-9238

Table 11.9: Analysis of the first $4f \rightarrow 5d$ transitions shift from Ce:YAG to Ce,1AD:YAG and to Ce,2AD:YAG according to data on Tables 11.7 and 11.8. All numbers in cm^{-1}.

	Contributions				
	$A \rightarrow B$ First-shell distortion	$B \rightarrow C$ Cell distortion	$A \rightarrow C$ Full distortion	$C \rightarrow D$ Al_Y Y_{Al}	$A \rightarrow D$ All
			Ce,1AD:YAG		
$\Delta E_{\text{centroid}}(4f^1 \rightarrow 5d^1)$	-116	64	-52	11	-41
$\Delta E_{\text{LF}}(1 - 4f^1)$	21	-13	8	-8	0
$\Delta E_{\text{LF}}(1 - 5d^1)$	-337	-142	-479	-23	-502
$\Delta E_{\text{ligand-field}}$ [a]	357	130	487	15	502
ΔE [b]	241	194	435	26	461
			Ce,2AD:YAG		
$\Delta E_{\text{centroid}}(4f^1 \rightarrow 5d^1)$	-223	12	-211	-81	-292
$\Delta E_{\text{LF}}(1 - 4f^1)$	41	-55	-14	39	25
$\Delta E_{\text{LF}}(1 - 5d^1)$	-665	-594	-1259	200	-1059
$\Delta E_{\text{ligand-field}}$ [a]	706	539	1245	-161	1084
ΔE [b]	483	551	1034	-242	792

[a] $\Delta E_{\text{ligand-field}} = \Delta E_{\text{LF}}(1 - 4f^1) - \Delta E_{\text{LF}}(1 - 5d^1)$, see Fig. 8.2
[b] $\Delta E = \Delta E_{\text{centroid}} + \Delta E_{\text{ligand-field}}$, see Fig. 8.2

Table 11.10: Ce_Y-O and Ce_Y-Al_{tet} distances (d(Ce_Y-X), in Å) in the $CeO_8Al_2O_4$ moiety in the ground state and first $4f \rightarrow 5d$ excited state optimized at the CASSCF level in Ce,1AD:YAG defect 1a after relaxation of the CeO_8 or $CeO_8Al_2O_4$ structures. Ground state PBC-DFT results (Table 11.4) included for comparison. Off-center displacement of Ce with respect to original Y position in YAG (d_{off}(Ce), in Å). Angles involving Ce_Y, Al_{tet} and O_s-type oxygen atom (α, in degrees). Labels according to Fig. 11.9.

	Ce,1AD:YAG				
		1-$4f^1$		1-$5d^1$	
Relaxed	All	CeO_8	$CeO_8Al_2O_4$	CeO_8	$CeO_8Al_2O_4$
Calculation:	PBC-DFT	CASSCF	CASSCF	CASSCF	CASSCF
			d(Ce_Y-X)		
X:					
s1	2.427	2.428(+0.001)[a]	2.439(+0.012)[a]	2.405(-0.023)[b]	2.417(-0.022)[c]
s2	2.420	2.429(+0.009)	2.424(+0.004)	2.412(-0.017)	2.405(-0.019)
s3	2.405	2.423(+0.018)	2.419(+0.014)	2.410(-0.013)	2.399(-0.020)
s4	2.415	2.429(+0.015)	2.442(+0.027)	2.411(-0.018)	2.424(-0.018)
l1	2.516	2.477(-0.039)	2.474(-0.042)	2.463(-0.014)	2.464(-0.010)
l2	2.518	2.491(-0.027)	2.485(-0.033)	2.479(-0.012)	2.479(-0.006)
l3	2.516	2.491(-0.025)	2.484(-0.032)	2.481(-0.010)	2.479(-0.005)
l4	2.450	2.442(-0.008)	2.442(-0.008)	2.434(-0.008)	2.433(-0.009)
Al^1_{tet}	3.165	3.163(-0.002)	3.169(+0.004)	3.164(+0.001)	3.174(+0.005)
Al^2_{tet}	3.168	3.170(+0.002)	3.174(+0.006)	3.169(-0.001)	3.174(0.000)
d2	4.596	4.594(-0.002)	4.564(-0.032)	4.595(+0.001)	4.560(-0.004)
d4	4.587	4.585(-0.002)	4.633(+0.046)	4.586(+0.001)	4.638(+0.005)
d3	4.630	4.632(+0.002)	4.698(+0.068)	4.631(-0.001)	4.703(+0.005)
b2	4.649	4.651(+0.002)	4.647(+0.002)	4.650(-0.001)	4.646(-0.001)
d_{off}(Ce)	0.013	0.016	0.019	0.014	0.018
			α (AlO_4-Ce-AlO_4 direction)		
α(s3-Al^1_{tet}-s4)	98.5	99.6	99.5	98.5	98.0
α(s3-Ce-s4)	69.8	69.9	69.8	69.5	69.3
α(s1-Al^2_{tet}-s2)	99.0	99.2	99.2	97.0	97.9
α(s1-Ce-s2)	69.1	69.0	68.8	68.7	68.5
α(d2-Al^1_{tet}-d4)	92.7	92.7	91.9	92.7	91.9
α(d1-Al^2_{tet}-d3)	87.5	87.8	84.0	87.5	83.8

[a] difference with respect to DFT-PBC calculations (data column 1)

[b] difference with respect to CASSCF calculation optimizing CeO_8 in the $1-4f$ state (data column 2)

[c] difference with respect to CASSCF calculation optimizing $CeO_8Al_2O_4$ in the $1-4f$ state (column 3)

Table 11.11: Ce_Y-O and Ce_Y-Al_{tet} distances (dCe_Y-X), in Å) in the $CeO_8Al_2O_4$ moiety in the ground state and first $4f \rightarrow 5d$ excited state optimized at the CASSCF level in Ce,2AD:YAG defect 2k after relaxation of the CeO_8 structure. Ground state PBC-DFT results (Table 11.5) included for comparison. Off-center displacement of Ce with respect to original Y position in YAG (d_{off}(Ce), in Å). Angles involving Ce_Y, Al_{tet} and O_s-type oxygen atom (α, in degrees). Labels according to Fig. 11.10.

		Ce,2AD:YAG	
	1-$4f^1$		1-$5d^1$
Relaxed	All	CeO_8	CeO_8
Calculation:	PBC-DFT	CASSCF	CASSCF
		dCe_Y-X)	
X:			
s1	2.376	2.361(-0.015)[a]	2.349(-0.012)[b]
s2	2.419	2.391(-0.028)	2.383(-0.008)
s3	2.402	2.383(-0.019)	2.370(-0.013)
s4	2.447	2.408(-0.039)	2.398(-0.010)
l1	2.492	2.530(+0.038)	2.506(-0.024)
l2	2.498	2.483(-0.015)	2.477(-0.006)
l3	2.504	2.514(+0.010)	2.500(-0.014)
l4	2.553	2.527(-0.026)	2.523(-0.004)
Al^1_{tet}	3.045	3.047(+0.002)	3.044(-0.003)
Al^2_{tet}	3.094	3.092(-0.002)	3.094(+0.002)
a	4.392	4.392(0.000)	4.389(-0.003)
b	4.376	4.380(+0.004)	4.379(-0.001)
c	4.409	4.405(-0.004)	4.406(+0.001)
d	4.466	4.466(0.000)	4.468(+0.002)
d_{off}(Ce)	0.038	0.032	0.031
		α (AlO_4-Ce-AlO_4 direction)	
α(s2-Al^1_{tet}-s3)	104.6	103.0	102.4
α(s2-Ce-s3)	71.6	71.9	71.6
α(s1-Al^2_{tet}-s4)	101.9	100.4	99.5
α(s1-Ce-s4)	69.84	70.3	69.8
α(a-Al^1_{tet}-b)	101.9	101.9	101.9
α(c-Al^2_{tet}-d)	101.4	101.4	101.4

[a] difference with respect to DFT-PBC calculations (data column 1)

[b] difference with respect to CASSCF calculation optimizing CeO_8 in the $1-4f$ state (data column 2)

Table 11.12: Relative energies of the levels of main character Ce-$4f^1$, Ce-$5d^1$, and Ce-$6s^1$ of Ce,1AD:YAG as calculated with the $(CeO_8Al_2O_4)^{15-}$ cluster at the CASPT2 level using CASSCF geometries of Table 11.10 and different basis sets. Calculated Stokes shifts. All numbers in cm^{-1}.

Material:	Ce,1AD:YAG							
State:	1-$4f^1$				1-$5d^1$			
Relaxed:	CeO_8	CeO_8	$CeO_8Al_2O_4$	$CeO_8Al_2O_4$	CeO_8	CeO_8	$CeO_8Al_2O_4$	$CeO_8Al_2O_4$
Basis:	small[a]	large[b]	small	large	small	large	small	large
				$4f^1$ levels				
1 ^2A	0	0	0	0	0	0	0	0
2 ^2A	30	5	50	15	32	7	35	12
3 ^2A	257	200	300	217	268	192	270	196
4 ^2A	435	453	466	466	507	495	514	497
5 ^2A	476	495	522	508	540	549	542	535
6 ^2A	563	584	584	603	639	659	659	680
7 ^2A	2380	2327	2402	2337	2472	2410	2471	2410
				$5d^1$ levels				
8 ^2A	23006	24163	23022	24156	22476	23613	22456	23594
9 ^2A	29758	31102	29793	31135	29910	31221	29984	31302
10 ^2A	48229	48914	48385	48963	48719	48999	48600	48954
11 ^2A	48963	49489	48841	49534	49140	49730	49088	49557
12 ^2A	49172	49599	49181	49562	49366	49986	49414	50021
				$6s^1$ level				
13 ^2A	61757	59127	59867	58564	58701	57143	57383	54545

Stokes shift 1 $^2A \rightarrow$ 8 ^2A

Relaxed:	CeO_8	CeO_8	$CeO_8Al_2O_4$	$CeO_8Al_2O_4$
Basis:	small[a]	large[b]	small	large
	530	550	566	562

[a] *small* basis set: Ce($14s10p10d8f$)/[$5s4p5d3f$], O($5s6p$)/[$2s3p$], Al($7s6p$)/[$2s3p$]

[b] *large* basis set: Ce ($14s10p10d8f3g$)/[$6s5p6d4f1g$], O ($5s6p1d$)/[$3s4p1d$], Al ($7s6p1d$)/[$2s3p1d$]

Table 11.13: Relative energies of the levels of main character Ce-$4f^1$, Ce-$5d^1$, and Ce-$6s^1$ of Ce,2AD:YAG as calculated with the $(CeO_8Al_2O_4)^{15-}$ cluster at the CASPT2 level using CASSCF geometries on Table 11.11 and the smaller basis set considered. Calculated Stokes shift. All numbers in cm^{-1}.

Material:	Ce,2AD:YAG	
State:	1-$4f^1$	1-$5d^1$
Relaxed:	CeO_8	CeO_8
Basis:	small[a]	small
	$4f^1$ levels	
1 ^2A	0	0
2 ^2A	35	28
3 ^2A	246	261
4 ^2A	443	497
5 ^2A	500	546
6 ^2A	617	646
7 ^2A	2409	2473
	$5d^1$ levels	
8 ^2A	23210	22772
9 ^2A	29159	29327
10 ^2A	45555	45885
11 ^2A	47478	47722
12 ^2A	52539	52625
	$6s^1$ level	
13 ^2A	64338	63820

Stokes shift 1 $^2A \rightarrow 8$ ^2A	
Relaxed:	CeO_8
Basis:	small[a]
	438

[a] *small* basis set: Ce($14s10p10d8f$)/[$5s4p5d3f$], O($5s6p$)/[$2s3p$], Al($7s6p$)/[$2s3p$]

Chapter 12

General conclusions

12.1 Conclusions

This chapter contains a brief summary of the main conclusions obtained in the present work:

- In this work, we tackle the study of Ce:YAG-based materials by means of a combined methodological approach. Our strategy starts by performing ground state PBC-DFT calculations in order to obtain reliable structural details of the solids of interest, focusing on the local geometries in the Ce^{3+} impurity surroundings, known to be responsible of the spectroscopic properties of these materials. Then, using these structures, we perform embedded cluster calculations using wave-function methods, in order to obtain the energy levels responsible of the $4f \rightarrow 5d$ spectroscopic transitions. For materials containing Ce and other defect (codopant ion or antisite defects), various calculations are performed on each considered cluster using different embeddings of increasing level of realism, accounting separately for short- and long- range distortions and electronic effects of the new atoms. Then, we can evaluate the role of each source of change in the total change of the spectra with respect to spectrum of parent Ce:YAG. Finally, we analyze transitions of interest in such spectra in terms of the variation of the difference between the centroids and the ligand field effects in the f and d states. Then, we can describe precisely the variation of each component of the spectra upon geometrical and electronic changes on double defect materials.

- We obtained pseudopotentials and basis sets for Y, Al, O, Ce, La and Ga atoms, which, used in PBC-DFT calculations, achieved a good agreement with experimental structures and previous calculations on various systems containing these atoms. Suitability of these basis and pseudopotentials for the problem of study the complex structural distortions experimented by Ce-doped YAG upon the presence of other defects has been confirmed afterwards, when such structures have been successfully used in wave-function based calculations to describe spectroscopic properties of Ce:YAG-based materials.

- We have performed for the first time a PBC-DFT first-principles calculation on pure and perfect YAG relaxing both lattice vectors and internal parameters of the lattice, matching accurately the experimental structural parameters. Calculated electronic structure, which slightly underestimates the gap, is coherent with the available experimental ELNES data for this system.

- We describe the local structure of Ce, La and Ga point defects in YAG using PBC-DFT methods. The flexibility presented by the covalent AlO_4 moieties upon the expansive distortions of the point defects show up the special behavior of the -Y-AlO_4-Y-AlO_4- structures that YAG presents all along the three crystallographic axes. Then, we state for the first time that YAG can be pictured as interleaving -Y-AlO_4-Y-AlO_4- *chains* linked by Al_{oct} atoms. Among all the studied point defects, only the presence of Ce alters the electronic structure of the host, α states of Ce-4f character appearing below the Fermi level.

- We use PBC-DFT techniques to describe for the first time, within a first-principles framework, the atomistic structure of intrinsic Y_{Al}-Al_Y antisite defects generated in bulk YAG during syntheses. From our calculations, the two exchanged cations prefer the closest positions in one antisite defect. This leads to a highly distorted structure, where Al_Y does not retain it new eightfold coordination, becoming off-center and leaving two oxygens unbound. Highest occupied states of these unbound oxygens rise in energy, diminishing the gap with respect to that of perfect YAG. We find a favorable interaction between two of these antisite defects in a YAG unit cell, in agreement with the experimental concentration found of two antisite defects per YAG unit cell. The two single antisite defects of this two-antisite defect structure are connected by an Al_{oct} as inversion center.

- Using PBC-DFT methods, we describe for the first time the atomistic structure of double Ce-La and Ce-Ga defects in YAG. In spite of both codopants cause a local expansion around Ce, our embedded cluster CASSCF/CASPT2 calculations show a remarkably different behavior of La and Ce shifting the first $4f \rightarrow 5d$ transition of Ce:YAG. La is found to red shift such transition, whereas Ga is found to blue shift it, both findings in agreement with experiments. Red shift associated to La appears as a result of (1) a decrease in the difference between the energy centroids of the $4f$ and $5d$ configurations and (2) an increase in the effective ligand field on the $5d$ shell associated to electronic effects of La and not compensated by a smaller blue shift associated to expansion around Ce. On the contrary, electronic effects of Ga appear to be negligible and the blue shift arises mainly from a decrease of the $5d$ shell splitting due to pure geometrical distortions around Ce. A reason behind such a different behavior could lie in the different relative positions of Ce-La and Ce-Ga, being Ce and La much closer in the double defect than Ce and Ga.

- By means of PBC-DFT methods, we describe for the first time the atomistic structure of Ce defect in YAG cells containing antisite defects. When Ce and one antisite

defect are taken into account, all the Y atoms appear to be substituted in the -Y-AlO_4-Y-AlO_4- *chain*, appearing -Ce-AlO_4- Al_Y -AlO_4- structures along the considered axis. On the contrary, if we consider Ce and two antisite defects, Ce is linked directly to the Y_{Al} of one of them. Calculations show that interaction between Ce and one or two antisite defects is favorable, though generating a second antisite defect requires more energy in Ce,1AD:YAG than in 1AD:YAG. The presence of antisite defects induces a blue shift of the first $4f \rightarrow 5d$ transition with respect to Ce:YAG, associated with strong distortions not only in Ce surroundings but also all over the cell.

- Embedded cluster CASSCF/CASPT2 calculations of Ce:YAG Stokes shift under the influence of one and two antisite defect have been performed. With respect to previous embedded cluster calculations on Ce:YAG considering a perfect host, no significant changes of the calculated Stokes shift are found, being the quantity still underestimated by our calculations. We do not find a role of intrinsic antisite defects on Ce:YAG Stokes shift within the approach followed in this work. The reasons behind the different experimental and theoretical values are still unknown.

The calculations performed in this work show up the convenience of using PBC-DFT methods to obtain relevant local and not so local structural features of systems made up by heavy metals in ionic solids. PBC-DFT methods provide structural data unknown experimentally, which is interesting by itself, widening the range of possible problems and systems to be studied by means of *ab initio* wave function based quantum mechanical methods, which offer reliable spectroscopic information of these systems. Our calculations, performed from scratch, reveal the synergy structure-spectroscopy in these systems, as well as the complementarity between the experimental information and the theoretically obtained information.

12.2 *Conclusiones*

Este capítulo contiene un breve resumen de las conclusiones principales obtenidas en este trabajo:

- En este trabajo, abordamos el estudio de Ce:YAG y derivados por medio de una ruta que combina varias metodologías. Nuestra estrategia comienza realizando cálculos de tipo PBC-DFT con objeto de obtener detalles estructurales fiables de los sólidos de interés, sobre todo de las geometrías locales alrededor de la impureza de Ce^{3+}, las cuales se sabe son responsables de las propiedades espectroscópicas de estos materiales. Despues, utilizando estas estructuras, realizamos cálculos de *cluster* embebido utilizando métodos de función de onda para obtener los niveles de energía responsables de las transiciones espectroscópicas $4f \rightarrow 5d$. En materiales que contienen Ce y otro defecto (codopante o defectos *antisite*), realizamos varios cálculos con cada *cluster* considerado utilizando diferentes *embedding* de creciente nivel de realismo, que tienen en cuenta separadamente las distorsiones de corto y largo alcance y los efectos electrónicos de los nuevos átomos. Así, podemos evaluar el papel que cada una de esas fuentes de cambio juega en la variación total del espectro de Ce:YAG. Finalmente, analizamos las transiciones de interés en cada uno de esos espectros en términos de la variación de la diferencia entre los centroides y de los efectos del campo ligando en los estados f y d. Así, podemos describir precisamente la variación de cada uno de estos componentes de los espectros de los materiale con defectos dobles respecto a cambios geométricos y efectos electrónicos.

- Hemos obtenido pseudopotenciales y conjuntos de base para Y, Al, O, Ce, La y Ga, los cuales, empleados en cálculos PBC-DFT, consiguen reproducir adecuadamente las estructuras experimentales y los resultados de cálculos previos en sistemas que contienen estos átomos. Lo apropiado de estas bases y pseudopotenciales en el estudio de de las complejas distorsiones estructurales experimentadas por el Ce:YAG en presencia de otros defectos se ha visto confirmado cuando tales estructuras han sido empleadas con éxito en cálculos con métodos basados en la función de onda para describir las propiedades espectroscópicas de materiales basados en Ce:YAG.

- Hemos realizado por primera vez un cálculo PBC-DFT en el cristal de YAG puro y perfecto con relajación de los parámetros internos de la celda y de los vectores de celda, reproduciendo fielmente los parámetros estructurales experimentales. La estructura electrónica calculada, si bien ligeramente subestima el valor del gap, es coherente con los datos ELNES disponibles para este sistema.

- Hemos descrito la estructura de los defectos puntuales de Ce, La y Ga en YAG utilizando métodos PBC-DFT. La flexibilidad que presentan las unidades covalentes de AlO_4 frente a distorsiones expansivas de los defectos muestra el comportamiento especial de unidades del tipo -Y-AlO_4-Y-AlO_4-, que el YAG presenta a lo largo de los tres ejes cristalográficos. Así pues, exponemos por primera vez un modelo para

el YAG consistente en cadenas -Y-AlO_4-Y-AlO_4- entrelazadas y unidas por átomos de Al_{oct}. De entre todos estos defectos puntuales estudiados, sólo la presencia de Ce altera la estreuctura electrónica del YAG, ya que aparecen estados α de carácter Ce-4f por debajo del nivel de Fermi.

- Usamos métodos PBC-DFT para describir por primera vez de un modo *ab initio* la estructura atomística de los defectos *antisite* Y_{Al}-AlinY que aparecen en el YAG durante la síntesis. Según nuestros cálculos, los dos cationes intercambiados prefieren las posiciones más cercanas en un antisite defect. Esto lleva a una estrucutura muy distorsionada donde el Al_Y no es capaz de mantener los ocho oxígenos de coordinación, quedando dos oxígenos no enlazados. Los estados más altos ocupados de estos dos oxígenos aumentan en energía, disminuyendo el gap con respecto al del YAG perfecto. Encontramos una interacción favorable entre dos de éstos defectos, en concordancia con la concentración hallada experimentalmente de dos defectos *antisite* por celda unidad de YAG. Los dos defectos *antisite* de esta estructura están conectados por un Al_{oct} que actúa de centro de inversión.

- Usando métodos PBC-DFT, hemos descrito por primera vez la estructura atomística de defectos dobles Ce-La y Ce-Ga en YAG. Pese a que ambos codopantes causan una expansión local alrededor del Ce, nuestros cálculos CASSCF/CASPT2 con el método de *cluster* embebido muestran un comportamiento marcadamente diferente de La y Ga desplazando la primera transición $4f \rightarrow 5d$ del Ce:YAG. Encontramos que La desplaza al rojo dicha transición, mientras que Ga la desplaza al azul, ambos resultados de acuerdo con los experimentos. El desplazamiento al rojo asociado a La se debe a (1) una disminución de la diferencia entre los centroides de las configuraciones $4f$ y $5d$ y (2) una disminución del campo ligando efectivo de la capa $5d$ asociada a efectos electrónicos de La no compensada por un menor desplazamiento al azul asociado a la expansión en el entoeno del Ce. Por el contrario, los efectos electrónicos de Ga son despreciables y el desplazamiento al azul se debe principalmente a una disminución de la dispersión de la capa $5d$ debido sólamente a distorsiones geométricas alrededor del Ce. Una razón para tan diferente comportamiento podía estar en la diferente posición relativa que adoptan los defectos Ce-La y Ce-Ga, estando Ce y La mucho más cercanos en el doble defecto que Ce y Ga.

- Describimos con métodos PBC-DFT por primera vez la estructura atomística del defecto de Ce en celdas de YAG que contienen defectos *antisite*. Cuando Ce y un defecto *antisite* se tienen en cuenta, todos los átomos de Y de una cadena -Y-AlO_4-Y-AlO_4- son sustituídos, apareciendo estructuras del tipo -Ce-AlO_4- Al_Y -AlO_4- a lo largo de todo un eje de la celda. Por el contrario, si se tienen en cuenta dos defectos *antisite*, el Ce se sitúa directamente unido a uno de los dos Y_{Al}. Los cálculos muestran que la interación de Ce con uno y dos defectos *antisite* es favorable, si bien generar un segundo defecto *antisite* en una celda que ya contiene uno requiere más energía en Ce,1AD:YAG que en 1AD:YAG. La presencia de defectos *antisite*

induce un desplazamiento al azul de la primera transición $4f \rightarrow 5d$ con respecto al Ce:YAG, asociado a fuertes distorsiones no sólo en las proximidades del Ce, sino en toda la celda

- Hemos realizado cálculos de *cluster* embebido a nivel CASSCF/CASPT2 del desplazamiento de Stokes de Ce:YAG bajo la influencia de uno o dos defectos *antisite*. Con respecto a cálculos de *cluster* embebido realizados anteriormente teniendo en cuenta el YAG perfecto, no obtenemos grandes diferencias en el resultado, de modo que nuestros cálculos siguen subestimando el valor experimental. No encontramos un papel de los defectos *antisite* intrínsecos en el desplazamiento Stokes del Ce:YAG dentro del enfoque usado en este trabajo para abordar el problema. Las razones de la gran diferencia entre el valor experimental y los teóricos son todavía desconocidas.

Los cálculos realizados en este trabajo muestran la conveniencia de usar métodos PBC-DFT en la obtención de propiedades locales y no tan locales de sistemas formados por metales pesados en sólidos iónicos. Éstos métodos proporcionan datos estructurales desconocidos experimentalmente, lo cual es interesante por sí mismo, ampliando el rango de problemas y sistemas que pueden estudiarse por medio de métodos *ab initio* basados en la función de onda, los cuales ofrecen información espectroscópica relevante de estos sistemas. Nuestros cálculos, realizados desde cero, revelan la sinergia entre estructura y espectroscopía en estos sistemas, así como la complementareidad entre la información experimental y la información obtenida teóricamente.

Bibliography

[1] F. Aragón de la Cruz, *Historia de la Química*. Ed. Síntesis, Madrid, 2004.

[2] R. Beatty, *The lanthanides (the elements)*. Marshall Cavendish, New York, 2007.

[3] F. A. Cotton and G. Wilkinson, *Advanced Inorganic Chemistry* (5th ed.), Wiley-Interscience, New York, 1988.

[4] V. M. Goldschmidt *Geochemische Verteilungsgesetze Der Elemente*, Part V *Isomorphie Und Polymorphie Der Sesquioxyde. Die Lanthaniden-Kontraktion Und Ihre Konsequenzen*, Oslo, 1925.

[5] Harvey, E. N. *A History of Luminescence. From the Earliest Times Until 1900.* American Philosophical Society, Philadelphia, (1957).

[6] Judd, B. R. *Phys. Rev. Lett.* **39**, 242 (1977).

[7] Morrison, C. A. *J. Chem. Phys.* **72**, 1001 (1980).

[8] Bettinelli, M. and Moncorgé, R. *J. Lumin.* **92**, 287–289 (2001).

[9] Dorenbos, P. *J. Lumin.* **87-89**, 970 (2000).

[10] Dorenbos, P. *J. Lumin.* **91**, 91 (2000).

[11] Dorenbos, P. *Phys. Rev. B* **62**, 15640 (2000).

[12] Dorenbos, P. *Phys. Rev. B* **62**, 15650 (2000).

[13] Dorenbos, P. *Phys. Rev. B* **64**, 125117 (2001).

[14] Seijo, L. and Barandiarán, Z. *J. Chem. Phys.* **118**, 1921 (2003).

[15] Tanner, P. A., Mak, C. S. K., Edelstein, N. M., Murdoch, K. M., Liu, G., Huang, J., Seijo, L., , and Barandiarán, Z. *J. Amer. Chem. Soc.* **125**, 13225 (2003).

[16] Ruipérez, F., Barandiarán, Z., and Seijo, L. *J. Chem. Phys.* **123**, 244703 (2005).

[17] Ordejón, B., Seijo, L., and Barandiarán, Z. *J. Chem. Phys.* **123**, 204502 (2005).

[18] Pascual, J. L., Schamps, J., Seijo, L., and Barandiarán, Z. *Phys. Rev. B* **74**, 104105 (2006).

[19] Eliseevaa, S. V. and Bünzli, J.-C. G. *Chem. Soc. Rev.* **39**, 189 (2010).

[20] Energy Savings Potential of Solid State Lighting in General Illumination Applications, Office of Energy Efficiency and Renewable Energy, US DOE, November 2003. Available on-line: http://www.netl.doe.gov/ssl.

[21] Gemological Institute of America, *GIA Gem Reference Guide*, 1995.

[22] Geusic, J. E., Marcos, H. M., and Uitert, L. G. V. *Appl. Phys. Lett.* **4**, 182 (1964).

[23] Moskalik, K., Kozlov, A., Demin, E., and Boiko, E. *Photomedical Laser Surgery* **27**, 345 (2009).

[24] Yang, J., Yin, T. L., Xu, W. M., Xia, L. B., Li, A. B., and Hu, J. *Photomedical Laser Surgery* **24**, 625 (2006).

[25] W. Koechner. *Solid-State Laser Engineering* (2^{nd} ed.). Springer-Verlag. 1988.

[26] Goss, L. P., Smith, A. A., and Post, M. E. *Review of Scientific Instruments* **60**, 3702 (1989).

[27] Welker, T. *J. Lumin.* **48**, 49 (1991).

[28] Blasse, G. and Bril, A. *J. Chem. Phys.* **47**, 5139 (1967).

[29] Mueller-Mach, R., Mueller, G., Krames, M., Höppe, H., Stadler, F., Schnick, W., Juestel, T., and P.Schmidt. *Phys. Status Solidi A* **202**, 1727 (2005).

[30] Krames, M. R., O.Shchekin, Mueller-Mach, R., Mueller, G., Zhou, L., Harbers, G., and Cradford, M. G. *J. Display. Techn.* **3**, 160 (2007).

[31] Brodrick, J. *J. Display. Techn.* **3**, 91 (2007).

[32] Pan, Y., Wu, M., and Su, Q. *J. Phys. Chem. Solids* **65**, 845 (2004).

[33] Lin, Y. S., Liu, R. S., and Cheng, B.-M. *J. Electrochem. Soc.* **152**, J41 (2005).

[34] Jang, H. S., Im, W. B., Lee, D. C., Jeon, D. Y., and Kim, S. S. *J. Lumin.* **126**, 371 (2007).

[35] amd W. Wang, Y. X. P., Liu, G., Skanthakumar, S., Rosenberg, R. A., Guo, X. Z., and Li, K. K. *J. All. Comp.* **488**, 638 (2009).

[36] Bachmann, V., Ronda, C., Meijerink, A., Oeckler, O., and Schnick, W. *Chemistry of Materials* **21**, 316 (2009).

[37] Justel, T., Nikol, H., and Ronda, C. *Angew. Chem. Int. Ed.* **37**, 3085 (1998).

[38] Holloway, W. W. and Kestigian, M. *J. Opt. Soc. Amer.* **59**, 60 (1969).

[39] Tien, T. Y., Gibbons, E. F., DeLosh, R. G., Zacmanidis, P. J., Smith, D. E., and Stadler, H. L. *J. Electrochem. Soc.* **120**, 278 (1973).

[40] Robertson, J. M., van Tol, M. W., Smits, W. H., and Heynen, J. P. H. *Philips J. Res.* **36**, 151 (1981).

[41] Gracia, J., Seijo, L., Barandiarán, Z., Curulla, D., Niemansverdriet, H., and van Gennip, W. *J. Lumin.* **128**, 1248 (2008).

[42] Bachmann, V., Ronda, C., and Meijerink, A. *Chemistry of Materials* **21**, 2077 (2009).

[43] Dong, J. and Lu, K. *Phys. Rev. B* **43**, 8808 (1991).

[44] Zorenko, Y. V., Voloshinovskii, A., Konstankevych, I., Kolobanov, V. N., Mikhailin, V. V., and Spassky, D. A. *Radiation Measurements* **38**, 677 (2004).

[45] Zorenko, Y., Gorbenko, V., Konstankevych, I., Voloshinovskii, A., Stryganyuk, G., Mikhailin, V., Kolobanov, V., and Spassky, D. *J. Lumin.* **114**, 85 (2005).

[46] Zorenko, Y., Voloshinovskii, A., V.Savchyn, Voznyak, T., Nikl, M., Nejezchleb, K., Mikhailin, V., Kolobanov, V., and Spassky, D. *Phys. Status Solidi B* **244**, 2180 (2007).

[47] Bohr, N. *Physica* **52**, 555 (1913).

[48] Schrödinger, E. *Ann. d. Physik* **79**, 361 (1926).

[49] Heitler, W. and London, F. *Physica* **44**, 455 (1927).

[50] Bloch, F. *Physica* **52**, 555 (1928).

[51] I. N. Levine. *Chemical Physics* (6^{th} ed.). McGraw-Hill. 2008.

[52] Bohr, M. and Oppenheimer, J. *Ann. d. Physik* **84**, 457 (1927).

[53] H. Jahn and E. Teller. *Stability of Polyatomic Molecules in Degenerate Electronic States. I. Orbital Degeneracy.* Proceedings of the Royal Society of London. Series A, Mathematical and Physical Sciences (1934-1990) 161 (905) 220Ű235, 1937.

[54] R. Renner Z. Phys. vol. 92, 172, 1934 (in German). English translation in H. Hettema, Quantum Chemistry, Classic Scientific Papers, World Scientific, Singapore (2000).

[55] Bernardi, F., Olivucci, M., and Robb, M. A. *Chem. Soc. Rev.* **25**, 321 (1996).

[56] G. Fischer. *Vibronic Coupling - The Interaction between the Electronic and Nuclear Motions*, Academic Press, New York, 1984.

[57] Hartree, D. R. *Proc. Cambridge Phil. Soc.* **24**, 89 (1928).

[58] Fock, V. *Z. Physik* **61**, 126 (1930).

[59] Slater, J. C. *Phys. Rev.* **35**, 210 (1930).

[60] Koopmans, T. A. *Physica* **1**, 104 (1933).

[61] Roothaan, C. C. J. *Rev. Mod. Phys.* **23**, 69 (1951).

[62] Pople, J. A. and Nesbet, R. K. *J. Chem. Phys.* **22**, 571 (1954).

[63] P-O. Lodwin. *Advances in chemical physics*, 2, Interscience, New York, p. 207 ed. 1. Prigogine, 1959.

[64] Sherrill, C. D. and Schaefer, H. F. *Adv. Quantum Chem.* **34**, 143 (1999).

[65] B.O. Roos. *Lecture notes in Quantum Chemistry*, Springer-Verlag, 1992.

[66] Schmidt, M. W. and Gordon, M. S. *Ann. Rev. Phys. Chem.* **49**, 233 (1998).

[67] Hylleraas, E. A. *Z. Phys.* **54**, 347 (1929).

[68] Foulkes, W. M., Mitas, L., Needs, R. J., and Rajagopal, G. *Rev. Mod. Phys.* **73**, 33 (2001).

[69] Mller, C. and Plesset, M. S. *Phys. Rev.* **46**, 618 (1934).

[70] K. Andersson, P.-Å. Malmqvist, B. O. Roos, A. J. Sadlej, and Wolinski, K. *J. Phys. Chem.* **94**, 5483 (1990).

[71] B. O. Roos, K. Andersson, M. P. Flscher, P. Markus P. åA. Malmqvist, L. Serrano-Andrés, K. Pierloot, M. Merchán. *Multiconfigurational Perturbation Theory: Applications in Electronic Spectroscopy* 93. pp. 219. 1996.

[72] Čižek, J. *J. Chem. Phys.* **45**, 4256 (1966).

[73] Čižek, J. and Paldus, J. *Int. J. Quantum Chem.* **5**, 359 (1971).

[74] Bartlett, R. J. *Ann. Rev. Phys. Chem.* **32**, 359 (1981).

[75] Bartlett, R. J. *J. Phys. Chem.* **93**, 1697 (1989).

[76] Hohenberg, P. and Kohn, W. *Phys. Rev. B* **136**, 864 (1964).

[77] R. G. Parr and W. Yang. *Density functional theory*. Oxford University Press, 1989.

[78] Furke, F. and Burke, K. *Ann. Rep. Comp. Chem.* **1**, 19 (2005).

[79] Mulliken, R. S. *Phys. Rev.* **74**, 736 (1948).

[80] Boys, S. F. *Proc. R. Soc. London, Ser. A* **200**, 542 (1950).

[81] Huzinaga, S. *J. Chem. Phys.* **42**, 1293 (1965).

[82] Taketa, H., Huzinaga, S., and O-ohata, K. **21**, 2313 (1966).

[83] Sankey, O. F. and Niklewski, D. J. *Phys. Rev. B* **40**, 3979–3995 (1989).

[84] Wigner, E. and Seitz, F. *Phys. Rev.* **43**, 804 (1933).

[85] Monkhorst, H. J. and Pack, J. D. *Phys. Rev. B* **13**, 5188 (1976).

[86] D.Vanderbilt. *Phys. Rev. B* **41**, 7892 (1990).

[87] Blöchl, P. *Phys. Rev. B* **50**, 17953 (1994).

[88] Slater, J. C. *Phys. Rev.* **45**, 794 (1937).

[89] Andersen, O. K. *Phys. Rev. B* **12**, 3060 (1975).

[90] Korringa, J. *Physica* **13**, 392 (1947).

[91] Kohn, W. and Rostoker, N. *Phys. Rev.* **94**, 1111 (1954).

[92] Koster, G. F. and Slater, J. C. *Phys. Rev.* **95**, 1167 (1954).

[93] Sugano, S. and Shulman, R. G. *Phys. Rev.* **130**, 517 (1963).

[94] Boys, S. F. *Rev. Mod. Phys.* **32**, 296 (1960).

[95] Pisani, C., Dovesi, R., Nada, R., and Kantorovich, L. N. *J. Chem. Phys.* **92**, 7448 (1990).

[96] Barandiarán, Z. and Seijo, L. *J. Chem. Phys.* **89**, 5739 (1988).

[97] Soler, J. M., Artacho, E., Gale, J. D., García, A., Junquera, J., Ordejón, P., and Sánchez-Portal, D. *J. Phys.: Cond. Mat.* **14**, 2745 (2002).

[98] Seijo, L. and Barandiarán, Z. *J. Chem. Phys.* **115**, 5554 (2001).

[99] Ordejón, B., Seijo, L., and Barandiarán, Z. *J. Chem. Phys.* **126**, 194712 (2007).

[100] Sánchez-Sanz, G., Seijo, L., and Barandiarán, Z. *J. Phys. Chem. A* **113**, 12591 (2009).

[101] G. Karlström, R. Lindh, P. A. Malmqvist, B. O. Roos, U. Ryde, V. Veryazov, P. O. Widmark, M. Cossi, B. Schimmelpfennig, P. Neogrady, and Seijo, L. *Comput. Mater. Sci.* **28**, 22 (2003).

[102] Fermi, E. *Physica* **48**, 73 (1928).

[103] Dirac, P. A. M. *Proc. Cambridge Phil. Soc.* **26**, 376 (1930).

[104] Kohn, W. and Sham, L. J. *Phys. Rev.* **140**, 1133 (1965).

[105] Ceperley, D. M. and Alder, B. J. *Phys. Rev. Lett.* **45**, 566 (1980).

[106] Perdew, J. and Zunger, A. *Phys. Rev. B* **23**, 5048 (1981).

[107] Vosko, S., Wilk, L., and Nusair, M. *Can. J. Phys.* **58**, 1200 (1980).

[108] Cole, L. A. and Perdew, J. P. *Phys. Rev. A* **25**, 1265 (1982).

[109] Perdew, J. P. and Wang, Y. *Phys. Rev. B* **45**, 13244 (1992).

[110] Langreth, D. C. and Mehl, M. J. *Phys. Rev. Lett.* **47**, 446 (1981).

[111] Bohm, D. and Pines, D. *Phys. Rev.* **92**, 609 (1953).

[112] Gell-Mann, M. and Brueckner, K. A. *Phys. Rev.* **106**, 364 (1957).

[113] Becke, A. D. *Phys. Rev. A* **38**, 3098 (1988).

[114] C. Lee, W. Y. and Parr, R. G. *Phys. Rev. B* **37**, 785 (1988).

[115] J.P. Perdew, K. B. and Ernzerhof, M. *Phys. Rev. Lett.* **77**, 3865 (1996).

[116] Lieb, E. H. and Oxford, S. *Int. J. Quantum Chem.* **19**, 427 (1981).

[117] J.P. Perdew, K. B. and Ernzerhof, M. *Phys. Rev. Lett.* **78**, 1396 (1997).

[118] Anisimov, V. I., Zaanen, J., and Andersen, O. K. *Phys. Rev. B* **44**, 943 (1991).

[119] Anisimov, V. I., Aryasetiawan, F., and Lichtenstein, A. *J. Phys.: Cond. Mat.* **9**, 767 (1997).

[120] Rohrbach, A., Hafner, J., and Kresse, G. *Phys. Rev. B* **70**, 125426 (2004).

[121] Mosey, N. J. and Carter, E. A. *Phys. Rev. B* **76**, 155123 (2007).

[122] Mosey, N. J., Liao, P., and Carter, E. A. *J. Chem. Phys.* **129**, 014103 (2008).

[123] Becke, A. D. *J. Chem. Phys.* **98**, 1372 (1993).

[124] Kleinman, L. and Bylander, D. M. *Phys. Rev. Lett.* **48**, 1425–1428 (1982).

[125] Feynman, R. P. *Phys. Rev.* **56**, 340 (1939).

[126] Troullier, N. and Martins, J. L. *Phys. Rev. B* **43**, 1993–2006 (1991).

[127] Phillips, J. C. and Kleinman, L. *Phys. Rev.* **116**, 287 (1959).

[128] Dolg, M., Stoll, H., and Preuss, H. *J. Chem. Phys.* **90**, 1730 (1989).

[129] W. Küchle, Dolg, M., Stoll, H., and Preuss, H. *Mol. Phys.* **74**, 1245 (1991).

[130] S.G. Louie, S. F. and Cohen, M. *Phys. Rev. B* **26**, 1738 (1982).

[131] Lorentz, H. A. *Proc. Ac. Sc. Amsterdam* **1**, 205 (1899).

[132] Lorentz, H. A. *Proc. Ac. Sc. Amsterdam* **4**, 669 (1904).

[133] Bachelet, G. B. and Schlüter, M. *Phys. Rev. B* **25**, 2103 (1982).

[134] Cowan, R. D. and Griffin, D. C. *J. Opt. Soc. Am.* **66**, 1010 (1976).

[135] Wood, J. H. and Boring, A. M. *Phys. Rev. B* **18**, 2701 (1978).

[136] Blöchl, P. *Phys. Rev. B* **41**, 5414 (1990).

[137] E. Anglada, J.M. Soler, J. and Artacho, E. *Phys. Rev. B* **66**, 205101 (2002).

[138] Mermin, N. D. *Phys. Rev. B* **137**, 1441 (1965).

[139] Methfessel, M. and Paxton, A. T. *Phys. Rev. B* **40**, 3616 (1989).

[140] Mulliken, R. S. *J. Chem. Phys.* **23**, 1933 (1955).

[141] Judd, B. R. *Operator Techniques in Atomic Spectroscopy.* Princeton University Press, Princeton, (1965).

[142] Wybourne, B. G. *Spectroscopic Properties of Rare Earths.* Interscience, New York, (1965).

[143] G. H. Dieke. *Spectra and energy levels of rare earth ions in crystals.* Interscience, New York, 1968.

[144] S. Hufner. *Optical spectra of transparent rare earth compounds.* Academic Press, London, 1978.

[145] B. R. Judd. *Handbook on the physics and chemistry of rare earths.* Edited by K. A. Geschneider Jr and L. Eyring. North-Holland, Amsterdam, 1988.

[146] Bethe, H. *Ann. Phys.* **3**, 133 (1929).

[147] Huzinaga, S. and Cantu, A. A. *J. Chem. Phys.* **55**, 5543 (1971).

[148] Huzinaga, S., McWilliams, D., and Cantu, A. A. *Adv. Quantum Chem.* **7**, 187 (1973).

[149] R. McWeeny, Proc. R. Soc. London, Ser. A **253**, 242 (1959); Rev. Mod. Phys. **32**, 335 (1960); M. Kleiner and R. McWeeny, Chem. Phys. Lett. **19**, 476 (1973).

[150] McWeeny, R. *Methods of molecular quantum mechanics.* Academic Press, London, second edition, (1989).

[151] Parr, R. G., Ellison, F. O., and Lykos, P. G. *J. Chem. Phys.* **24**, 1106 (1956).

[152] Barandiarán, Z. and Seijo, L. *Computational Chemistry: Structure, Interactions and Reactivity*, volume 77B of *Studies in Physical and Theoretical Chemistry*, 435–461. Elsevier, Amsterdam (1992).

[153] Evjen, H. M. *Phys. Rev.* **39**, 675 (1932).

[154] M. A. Nygren, L. G. M. Pettersson, A. Freitag, V. Staemmler, D. H. Gay and Rohl, A. L. *J. Phys. Chem.* **100**, 294 (1996).

[155] Pascual, J. L., Seijo, L., and Barandiarán, Z. *J. Chem. Phys.* **98**, 9715 (1993).

[156] Höjer, G. and Chung, J. *Int. J. Quantum Chem.* **14**, 623 (1978).

[157] Moss, R. E. *Advanced Molecular Quantum Mechanics*. Studies in Chemical Physics. Chapman and Hall, London, (1973).

[158] Barandiarán, Z., Seijo, L., and Huzinaga, S. *J. Chem. Phys.* **93**, 5843 (1990).

[159] Pitzer, R. M. and Winter, N. W. *J. Phys. Chem.* **92**, 3061 (1988).

[160] Roos, B. O., Taylor, P. R., and Siegbahn, P. E. M. *Chem. Phys.* **48**, 157 (1980).

[161] Siegbahn, P. E. M., Heiberg, A., Roos, B. O., and Levy, B. *Phys. Scr.* **21**, 323 (1980).

[162] Siegbahn, P. E. M., Heiberg, A., Almlöf, J., and Roos, B. O. *J. Chem. Phys.* **74**, 2384 (1981).

[163] Ruipérez, F., Roos, B. O., Barandiarán, Z., and Seijo, L. *Chem. Phys. Lett.* **434**, 1 (2007).

[164] B. Ordejón, M. Karbowiak, L. Seijo and Barandiarán, Z. *J. Chem. Phys.* **125**, 074511 (2006).

[165] Roos, B. O. and Andersson, K. *Chem. Phys. Lett.* **245**, 215 (1995).

[166] Geller, S. *Z. Krist.* **125**, 1 (1967).

[167] deWith, G. In *High Technology Ceramics,* Vincenzini, P., editor, 2063. Elsevier, Amsterdam (1987).

[168] Powell, R. C. *Physics of Solid State Laser Materials*. AIP, New York, (1998).

[169] Stoddart, P. R., Ngoepe, P., Mjwara, P. M., Comins, J. D., and Saunders, G. A. *J. Appl. Phys.* **73**, 7298 (1993).

[170] Hurrell, J. P., Porto, S. P. S., Chang, I. F., Mitra, S. M., and Bauman, R. P. *Phys. Rev.* **173**, 851 (1968).

[171] Xu, Y.-N. and Ching, W. Y. *Phys. Rev. B* **59**, 10530 (1999).

[172] Shelyapina, M. G., Kasperovich, V. S., and Wolfers, P. *J. Phys. Chem. Solids* **67**, 720 (2006).

[173] Pari, G., Mookerjee, A., and Bhattacharya, A. K. *Physica B* **365**, 163 (2005).

[174] Xu, Y.-N., Chen, Y., Mo, S.-D., and Ching, W. Y. *Phys. Rev. B* **65**, 235105 (2002).

[175] Wang, C. M., Cargill, G. S., Harmer, M. P., Chan, H. M., and Cho, J. *Acta Mater.* **47**, 3411 (1999).

[176] Freeman, C. L., Allan, N. L., and van Westrenen, W. *Phys. Rev. B* **74**, 134203 (2006).

[177] D'Arco, P., Fava, F. F., Dovesi, R., and Saunders, V. R. *J. Phys.: Cond. Mat.* **8**, 8815 (1996).

[178] Landron, C., Lefloch, S., Gervais, M., Coutures, J. P., and Bazin, D. *Phys. Status Solidi B* **196**, 25 (1996).

[179] Euler, F. and Bruce, J. A. *Acta Crystallogr.* **19**, 971 (1965).

[180] Fu, W. T. and Ijdo, D. J. W. *J. Solid State Chem.* **179**, 2732 (2006).

[181] Bouvier, P. and Kreisel, J. *J. Phys.: Cond. Mat.* **14**, 3981 (2002).

[182] Murnagan, F. D. *Proc. Nat. Acad. Sci.* **30**, 244 (1944).

[183] Slack, G. A., Oliver, D. W., Chrenko, R. M., and Roberts, S. *Phys. Rev.* **177**, 1308 (1969).

[184] Gülgün, M. A., Ching, W.-Y., Xu, Y.-N., and Rühle, M. *Phil. Mag. B* **79**, 921 (1999).

[185] Ching, W. Y. and Xu, Y. N. *Phys. Rev. B* **59**, 12815 (1999).

[186] Bhattacharyya, S. and Ghatak, S. *Trans. Ind. Ceram. Soc.* **66**, 77 (2007).

[187] Geller, S. and Wood, E. A. *Acta Crystallogr.* **9**, 563 (1956).

[188] Christensen, A. N. and Hazell, R. G. *Acta Chem. Scand.* **45**, 226 (1991).

[189] Ching, W. Y. and Xu, Y. N. *J. Amer. Chem. Soc.* **77**, 404 (1994).

[190] Mueller, D. R., Ederer, D. L., v. Ek, J., O'Brient, W. L., Dong, Q. Y., Jia, J., and Calcott, T. A. *Phys. Rev. B* **54**, 15034 (1996).

[191] Jollet, F., Noguera, C., Thromat, N., Gautier, M., and Duraud, J. P. *Phys. Rev. B* **42**, 7587 (1990).

[192] Ching, W. Y. and Xu, Y. N. *Phys. Rev. B* **56**, 14993 (1997).

[193] N.L. Ross, J. and Angel, R. *J. Solid State Chem.* **17**, 1276 (2004).

[194] Pari, G., Mookerjee, A., and Bhattacharya, A. K. *Physica B* **353**, 192 (2004).

[195] Wu, X., Qin, S., and Wu, Z. *J. Phys.: Cond. Mat.* **18**, 3907 (2006).

[196] Kuklja, M. *J. Phys.: Cond. Mat.* **12**, 2953 (2000).

[197] Kuklja, M. and Pandey, R. *J. Amer. Chem. Soc.* **82**, 2881 (1999).

[198] Bush, T. S., Gale, J. D., Richard, C., Catlow, A., and Battle, P. D. *J. Mater. Chem.* **4**, 831 (1994).

[199] Hofmeiser, A. M. and Campbell, K. R. *J. Appl. Phys.* **72**, 638 (1992).

[200] Djemia, P. *J. Europ. Ceram. Soc.* **27**, 4719 (2007).

[201] Yogurtcu, Y. K., Miller, A. J., and Saunders, G. A. *J. Phys. C* **13**, 6585 (1980).

[202] Diehl, R. and Brandt, G. *Mat. Res. Bull.* **10**, 85 (1975).

[203] Ross, N. *Phase Transitions.* **58**, 27 (1996).

[204] Faucher, M. and Pannetier, J. *Acta Crystallogr. B* **36**, 3209 (1980).

[205] Xu, Y.-N., Gu, Z., and Ching, W. Y. *Phys. Rev. B* **56**, 14993 (1997).

[206] W.R. Manning, O. H. and Powell, B. *J. Amer. Chem. Soc.* **52**, 436 (1969).

[207] Lewis, J., Schwarzenbach, D., and Flack, H. D. *Acta Crystallogr. A* **38**, 733 (1982).

[208] Boettger, J. C. *Phys. Rev. B* **55**, 750 (1996).

[209] Ossowwski, M. M., Boyer, L. L., and Mehl, M. J. *Phys. Rev. B* **66**, 224302 (2002).

[210] T. Goto, O.L. Anderson, I. O. and Yamamoto, S. *J. Geophys. Res.* **94**, 7588 (1989).

[211] d'Amour, H., Schiferl, D., Dernier, W., Shulz, H., and Holzapfel, W. P. *J. Appl. Phys.* **49**, 4411 (1978).

[212] Fu, W. T. and Ijdo, D. J. W. *J. Solid State Chem.* **177**, 2973 (2004).

[213] L. Schuh, R. M. and Catlow, C. *J. Europ. Ceram. Soc.* **7**, 67 (1991).

[214] Hayward, S. A., Morrison, F. D., Redfern, S. A. T., Salje, E. K. H., Scott, J. F., Knight, K. S., Tarantino, S., Glazer, A. M., Shuvaeva, V., Daniel, P., Zhang, M., and Carpenter, M. A. *Phys. Rev. B* **72**, 054110 (2005).

[215] Wu, B., Zinkevich, M., Aldinger, F., and Zhang, W. *J. Phys. Chem. Solids* **68**, 570 (2007).

[216] Wyckoff, R. W. G. *Crystal Structures.* Wiley, (1968).

[217] N. Hirosaki, S. O. and Kocer, C. *J. All. Comp.* **351**, 31 (2003).

[218] Dillon, J. *J. Appl. Phys.* **29**, 539 (1958).

[219] Dillon, J. *J. Appl. Phys.* **29**, 1286 (1958).

[220] J. Chenavas, J. C. and Marezio, M. *J. Less-Common Met.* **62**, 373 (1978).

[221] Milanese, C., Buscaglia, V., Maglia, F., and Anselmo-Tamburini, U. *Chem. Mater.* **16**, 1232 (2004).

[222] Babin, V., Blazek, K., Krasnikov, A., Nejezchleb, K., Nikl, M., Savikhina, T., and Zazubovich, S. *Phys. Status Solidi C* **2**, 97 (2005).

[223] Volzhenskaya, L., Zorenko, Y., Patsagani, N., and Pashkovsky, M. *Opt. Spectrosc.* **63**, 135 (1987).

[224] Pascale, F., Zicovich-Wilson, C. M., Orlando, R., Roetti, C., Ugliengo, P., and Dovesi, R. *J. Phys. Chem. B* **109**, 6146 (2005).

[225] Huzinaga, S., Seijo, L., Barandiarán, Z., and Klobukowski, M. *J. Chem. Phys.* **86**, 2132 (1987).

[226] Barandiarán, Z. and Seijo, L. *Can. J. Chem.* **70**, 409 (1992).

[227] Seijo, L., Barandiarán, Z., and Ordejón, B. *Mol. Phys.* **101**, 73 (2003).

[228] Dunning, T. H. and Hay, P. J. In *Modern Theoretical Chemistry,* Schaefer III, H. F., editor. Plenum, New York (1977).

[229] J. Andzelm, M. Klobukowski, E. Radzio-Andzelm, Y. Sakai, and H. Tatewaki, *Gaussian Basis Sets for Molecular Calculations*, edited by S. Huzinaga, (Elsevier, Amsterdam, 1984).

[230] Sadoc, A., Broer, R., and de Graaf, C. *J. Chem. Phys.* **126**, 134709 (2007).

[231] K. Andersson, P.-Å. Malmqvist and Roos, B. O. *J. Chem. Phys.* **96**, 1218 (1992).

[232] Zaitsevskii, A. and J. P. Malrieu. *Chem. Phys. Lett.* **233**, 597 (1995).

[233] J. Finley, P.-Å. Malmqvist, B. O. Roos and Serrano-Andrés, L. *Chem. Phys. Lett.* **288**, 299 (1998).

[234] Tomiki, T., Akamine, H., Gushiken, M., Kinjoh, Y., Miyazato, M., Miyazato, T., Toyokawa, N., Hiraoka, M., Hirata, N., Ganaha, Y., and Futemma, T. *J. Phys. Soc. Japan* **60**, 2437 (1991).

[235] Tanner, P. A., Fu, L., Ning, L., Cheng, B.-M., and Brik, M. G. *J. Phys.: Cond. Mat.* **19**, 216213 (2007).

[236] Zhao, G. J., Zeng, X. H., Xu, J., Zhou, S. M., and Zhou, Y. Z. *Phys. Status Solidi A* **199**, 355 (2003).

[237] Zorenko, Y. V., Konstankevych, I. V., Mikhailin, V. V., Kolobanov, V. N., and Spassky, D. A. *Opt. Spectrosc.* **96**, 390 (2004).

[238] Merenga, H., Andriessen, J., and Eijk, C. W. E. V. *Radiation Measurements* **24**, 343 (1995).

[239] Barandiarán, Z., Edelstein, N. M., Ordejón, B., Ruipérez, F., and Seijo, L. *J. Solid State Chem.* **178**, 464 (2005).

[240] Hooge, P. N. *J. Chem. Phys.* **45**, 4504 (1966).

[241] N. M. Sammes, A. Smirnova and O. Vasylyev. *Fuel cell technologies: state and perspectives*. NATO Science Series (Mathematics, Physics and Chemistry), Vol.202, 2005 .

[242] Steele, B. C. H. and Heinzel, A. *Nature* **414**, 345 (2001).

[243] Rose, L., Menon, M., Kammer, K., Kesler, O., and Larsen, P. H. *Adv. Materials Research* **15**, 293 (2007).

[244] Jiang, S. P. *J. Mater. Sci.* **43**, 6799 (2008).

[245] Adler, S. B. *Chem. Rev.* **104**, 4791 (2004).

[246] M. Godickermeier. *Mixed ionic electronic conductors for solid oxide fuel cells*. PhD Thesis, Swiss Federal Institute of Technology. Zurich, 1996.

[247] Jacobson, A. J. *Chemistry of Materials* **22**, 660 (2010).

[248] Aguadero, A., Alonso, J. A., Escudero, M. J., and Daza, L. *Solid State Ionics* **179**, 393 (2008).

[249] Mastrikov, Y. A., Kuklja, M. M., Kotomin, E. A., and Maier, J. *Energy and Environmental Science* **3**, 1544 (2010).

[250] Chen, F., Liu, Q., Xiao, G., and Zhao, F. *Advanced Materials* **1**, 1 (2010).

[251] Patterson, F. K., Moeller, C. W., and Ward, R. *Inorg. Chem.* **2**, 196 (1963).

[252] Jonker, G. and Santen, J. H. V. *Physica* **16**, 337 (1950).

[253] Longo, J. and Ward, R. *J. Amer. Chem. Soc.* **83**, 2816 (1961).

[254] Sleight, A. W. and Weither, J. F. *J. Phys. Chem. Solids* **33**, 679 (1972).

[255] Galasso, F. S., Douglas, F. C., and Casper, R. J. *J. Chem. Phys.* **44**, 1672 (1966).

[256] Nakawa, T. *J. Phys. Soc. Japan* **24**, 806 (1968).

[257] Kobayashi, K. I., Kimura, T., Sawada, H., Terakura, K., and Tokura, Y. *Nature* **395**, 677 (1998).

[258] Sarma, D. D., Mahadevan, P., Saha-Dasgupta, T., Ray, S., and Kumar, A. *Phys. Rev. Lett.* **85**, 2549 (2000).

[259] García-Landa, B., Ritter, C., Ibarra, M. R., Blasco, J., Algarabel, P. A., Mahendiran, R., and García, J. *Solid State Commun.* **110**, 435 (1999).

[260] Tomioka, Y., Okuda, T., Okimoto, Y., Kumai, R., and Kobayashi, K. I. *Phys. Rev. B* **61**, 422 (2000).

[261] G. Kresse and J. Furthmueller, VASP the guide. s.l.: Univ. Vienna, 2003.

[262] Linden, J., Yamamoto, T., Karppinen, M., and Yamauchi, H. *Appl. Phys. Lett.* **76**, 2925 (2000).

[263] Nakamura, S., Tanaka, M., Kato, H., and Tokura, Y. *J. Phys. Soc. Japan* **72**, 424 (2003).

[264] Kapusta, C., Zajac, D., Riedi, P. C., Sikora, M., Oates, C. J., Blasco, J., and Ibarra, M. R. *J. Phys.: Cond. Mat.* **12**, 272 (2004).

[265] Herrero-Martín, J., García, J., Subías, G., Blasco, J., and Sánchez, M. C. *J. Phys.: Cond. Mat.* **17**, 4863 (2005).

[266] Serrate, D., Teresa, J. M. D., and Ibarra, M. R. *J. Phys.: Cond. Mat.* **19**, 023201 (2007).

[267] Stoeffler, D. and Colis, S. *J. Phys.: Cond. Mat.* **17**, 6415 (2005).

[268] Wu, X. *Phys. Rev. B* **64**, 125126 (2001).

[269] Xiang, H. P., Wu, Z. J., and Meng, J. *Phys. Status Solidi B* **242**, 1414 (2005).

[270] Mandal, T. K., Felser, C., Greenblatt, M., and Kübler, J. *Phys. Rev. B* **78**, 134431 (2008).

[271] Balcells, L., Navarro, J., Bibes, M., Roig, A., .Martinez, B., and Fontcuberta, J. *Appl. Phys. Lett.* **78**, 2001 (781).

[272] Ogale, A. S., Ogale, S. B., Ramesh, R., and Venkatesan, T. *Appl. Phys. Lett.* **75**, 1999 (537).

[273] D. Stoeffler *Lect. Notes Phys.* **795**, 197-226 (2010).

[274] Solovyev, I. V. *Phys. Rev. B* **65**, 144446 (2002).

[275] R.F.W. Bader, *Atoms in Molecules - A quantum theory*, Oxford University Press, New York, 1990.

[276] W. Koch and M. C. Holthausen, *A chemist's guide to density functional theory*, 2^{nd} edition, Wiley, 2001.

[277] Carter, E. A. and Goddard-III, W. A. *J. Phys. Chem.* **92**, 2109 (1988).

[278] Chmaissem, O., R, R. K., Dabrowski, B., Brown, D. E., Xiong, X., Kolesnik, S., Jorgensen, J. D., and Kimball, C. W. *Phys. Rev. B* **62**, 14197 (2000).

[279] Zhao, P., Yu, R. C., Li, F. Y., Liu, Z. X., Jin, M. Z., and Jin, C. Q. *J. Appl. Phys.* **92**, 1942 (2002).

[280] Borges, R. P., Thomas, R. M., Cullinan, C., Coey, J. M. D., Suryanarayanan, R., Ben-Dor, L., Pinsard-Gaudart, L., and Revcolevschi, A. *J. Phys.: Cond. Mat.* **11** (1999).

[281] Moritomo, Y., Xu, S., Akimoto, T., Machida, A., Hamada, N., Ohoyama, K., Nishibori, E., Takata, M., and Sakata, M. *Phys. Rev. B* **62**, 14224 (2000).

[282] Saitoh, T., Nakatake, M., Kakizaki, A., Nakajima, H., Morimoto, O., Xu, S., Moritomo, Y., Hamada, N., and Aiura, Y. *Phys. Rev. B* **68**, 035112 (2002).

Part III

APPENDICES

Appendix A

Other topics tackled in this work

A.1 First-principles modeling of Sr_2FeMoO_6 (SFMO) as cathode material for solid oxide fuel cell application

This appendix reports the results obtained during a research stage at the Princeton University as *Visitor Student Research Collaborator* (VSRC) in the group of Prof. Emily A. Carter, from May 1^{st} to July 31^{st} and from November 12^{th} to December 6^{th}, 2010. This work, supervised by Prof. Carter and Dr. Michele Pavone, is part of an ongoing collaborative project for the development of new effective cathode materials for solid oxide fuel cells.

A.1.1 Solid oxide fuel cells

Recent worldwide interest in renewable energy has refocused attention on solid oxide fuel cells (SOFCs), thanks to their ability to produce energy in a environmental-friendly framework.

Fuel cells are devices able to convert to electricity the chemical energy of fuels, such as hydrogen or methane, through electrochemistry [241]. Usually, the nature of the electrolyte names the type of fuel cell. SOFCs are characterized by the use of solid oxide materials as the electrolyte, which conducts oxygen anions from the cathode to the anode. A SOFC is made of three main layers, anode (for fuel oxidation), cathode (for oxygen reduction) and electrolyte, as depicted by Fig. A.1, plus an interconnect material. A single cell consisting of these four layers stacked together is typically only a few millimeters thick. Hundreds of these cells are then connected in series to form what most people refer to as an "SOFC stack". The materials used in SOFCs are mostly ceramics that become electrically and ionically active only at high temperature, typically between 700 and 1000°C. At these temperatures, SOFCs can convert a wide variety of fuels with a very good resistance to poisoning. However, at the same time the high thermal stress results in premature aging of interconnect materials and an active research is devoted

to find new effective materials for intermediate temperature SOFCs, that can run more efficiently within the 500-800°C range.

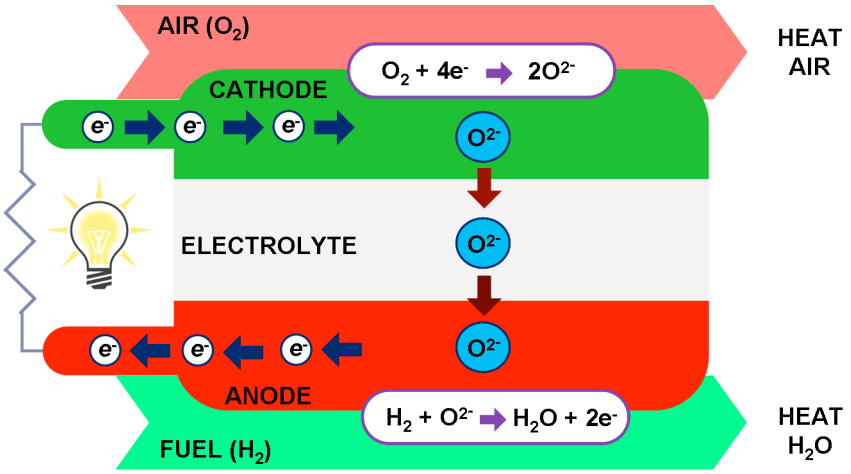

Figure A.1: Scheme of functioning of a Solid Oxide Fuel Cell.

In state-of-the-art SOFCs, the electrolyte is a dense layer of ceramic that conducts oxygen ions. Its electronic conductivity must be kept as low as possible to prevent losses from leakage currents. The most exploited electrolyte materials are yttria stabilized zirconia (YSZ) and gadolinium doped ceria (GDC) [241, 242, 243].

Anode and cathode materials must be very porous to allow easy diffusion of the fuel and must conduct both oxygen anion and electrons.

The anode is the thickest and strongest layer in an SOFC and it usually provides the mechanical support with very reduced polarization losses. The most common anode material is a composite made of Ni and YSZ.

The cathode, also known as an *air* electrode, is a thin porous layer on the electrolyte where the oxygen reduction reaction (ORR) takes place. Currently, lanthanum strontium manganite (LSM) is the cathode material of choice for commercial use because of its its compatibility with doped zirconia electrolytes, stability at high temperature, ability to catalyze the ORR, good enough electronic conductivity, adequate porosity and low cost [244]. However, LSM is not a good ionic conductor and so the electrochemically active ORR is thought to be limited to occur only at the triple phase boundary (TPB), where the electrolyte, air and cathode meet [245].

The aforementioned aimed reduction of the SOFC operating temperature affects the diffusion of O anions and increases the polarization resistance, with this effect more pronounced at the cathode where the ORR takes place. Therefore, great efforts have been devoted to find effective cathode materials that present the following properties: (1) good electrical conduction; (2) good ionic diffusion rate; (3) good catalytic activity for the ORR and (4) a thermal expansion coefficient compatible with the electrolyte. The ideal material should be then a mixed ionic electronic conductor (MIEC) [246].

Within this context, the development of innovative and efficient cathode materials

has been focused on strontium doped lanthanum transition-metal oxides ((La,Sr)MO_3, M=Mn,Co,Fe,Ni) [247, 248], that present complex perovskite structures. Other noteworthy promising materials are the $Ba_xSr_{1-x}Co_yFe_{1-y}O_3$ [249] and the $Sr_2Fe_{2-x}Mo_xO_6$ materials, the properties being very sensitive to the relative concentration of the transition metal ions.

Recently, a symmetric SOFC with both cathode and anode made of $Sr_2Fe_{2-x}Mo_xO_{6-\delta}$ achieved very promising results [250]. Further developments of this new type of material call for a deep understanding of their physico-chemical properties, and, in particular, and how these can be tuned by varying the Fe:Mo ratio.

To this purpose, in this work we report a first-principles study of the bulk properties of the double perovskite Sr_2FeMoO_6 the ratio of Fe:Mo being 1:1. In particular, we address the structural, electronic and magnetic features of this material in its equilibrium structure and in the presence of defects, namely anti-sites and oxygen vacancies, that are likely to form under SOFC operation.

This appendix contains two introductory sections to results obtained on SFMO: in Section A.1.2, we present a general overview on the SFMO material concerning its structure and properties and, in Section A.1.3, the computational details used in this work are described. Results on SFMO have been split in two main sections: one concerning stoichiometric SFMO (Section A.1.4), where the parent SFMO material and SFMO containing antisite defects are studied, and the other concerning SFMO containing oxygen vacancies, i.e., non-stoichiometric SFMO (Section A.1.5), where the study of vacancies is performed both in parent SFMO and in SFMO containing antisite defects.

A.1.2 SFMO: general considerations

The Sr_2FeMoO_6 (SFMO) structure was already studied in the 1960s [251], mostly because of its characteristic ferromagnetism, which persists above room temperature. High-temperature ferromagnetism was reported also for other perovskite-like compounds such as manganites ($AMnO_3$) [252] and Re-based double perovskites [253]. Unexpectedly, these A_2FeMoO_6 and A_2FeReO_6 compounds were also found to be highly conductive [254, 255, 256]. All these features suggested that the physics involved was much richer than expected. However, little further research on these compounds was carried out during the next three decades till Kobayashi *et al.* fully characterized in 1998 the half-metallic properties of SFMO [257]. This paper resulted in a new boost of interest in this material, within the context of potential applications in the field of spin electronics.

Stoichiometric ordered double perovskites ($A_2BB'O_6$) possess a modified perovskite structure (ABO_3) where the BO_6 and $B'O_6$ octahedra are alternately arranged in two interleaving fcc sublattices. The A sites are occupied by alkaline or rare earth ions, while the B and B' sites correspond to transition metal ions. This cubic structure can be well described within the $Fm3m$ space group. However, this structure is very often distorted as a consequence of steric pressure and temperature variations. In Sr_2FeMoO_6 because of the large size of Sr^{2+} ions, FeO_6 and MoO_6 octahedra undergo cooperative

tilting distortions towards the most energetically favorable structure, which brings about a symmetry reduction of the cubic cell to the tetragonal group $I4/m$ (Fig. A.2). Thus, the Sr_2FeMoO_6 crystal structure contains two formula units per unit cell, i.e., 20 atoms: two Fe atoms placed in the (a) Wyckoff positions of the $I4/m$ cell, two Mo atoms in (b) sites, four Sr atoms in (d) sites and 12 O atoms in both 4(e) and 8(h) symmetry sites.

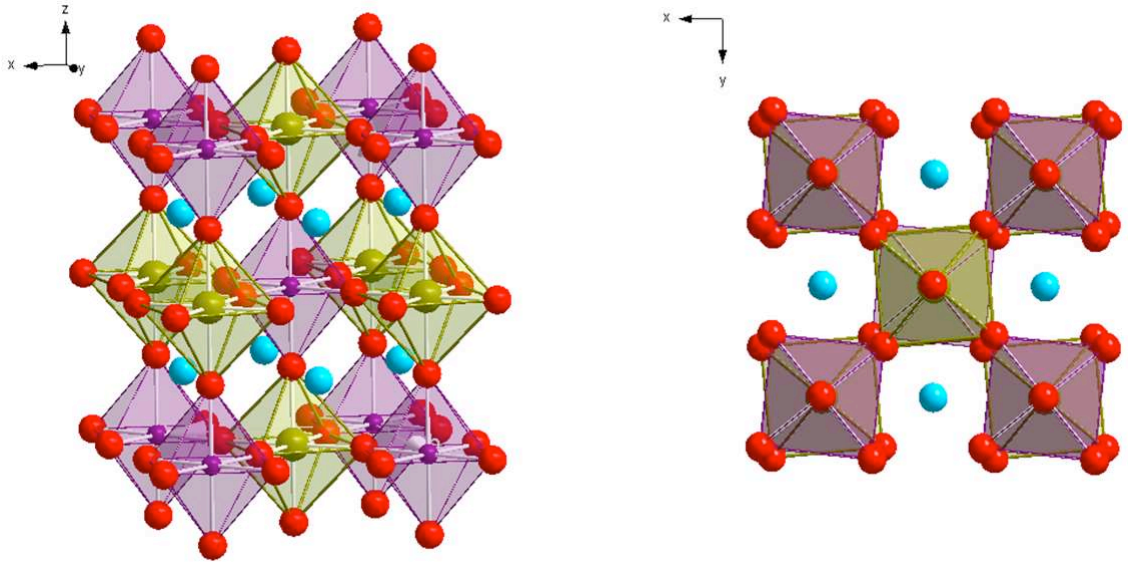

Figure A.2: Left: $I4/m$ unit cell of $Sr_2FeMoO_6\dot{F}eO_6$ octahedra in purple, MoO_6 octahedra in olive green, Sr^{2+} ions in blue and O^{2-} in red shown. Right: view along c axis, tilted octahedra shown.

In Sr_2FeMoO_6 ferromagnetism arises from spin properties at Fe and Mo sites. In the high spin configuration, Fe^{3+} (d^5) has an $S = 5/2$ spin moment, whereas Mo^{5+} (d^1) bears an $S = 1/2$ spin moment. Within this ionic picture, and in analogy with manganites, one can think about a bare antiferromagnetic interaction between neighboring Fe and Mo sites by means of their 5 μB/f.u. and -1 μB/f.u. respective spin moments. However, some SFMO properties cannot be explained by means of such simple model. Sarma *et al.* [258] proposed a model for magnetism in this compound arising from electron hopping interactions between Fe and Mo states with the same spin and orbital symmetry, which allows Fe(t_{2g})-O(2p)-Mo(t_{2g}) hybridization and, as a consequence, lowers the energy of the Mo spin down states, whereas the spin up states are pushed further up. This electron transfer results in a non-integer valence for both the cations, $Fe^{(3-\delta)+}/Mo^{(5+\delta)+}$, in agreement with Mössbauer and X-ray absorption experiments, as originally proposed by García-Landa *et al.* [259]. Additionally, this feature also explains the half-metallic nature of the compound, as reported in the pioneering calculations of Kobayasi *et al.* based on density functional theory [257]. In this compound, the Fermi level lies in between the Fe $3d_{eg}$/O 2p valence band and the Mo $4d_{t2g}$/O 2p conduction band.

One of the very important factors that affects the magnetic behavior of double per-

ovskites is the presence of antisite defects. In SFMO, although the total Fe and Mo atomic concentrations are well controlled, it is much more difficult to control the distribution of the Fe and Mo atoms in the two interleaving lattices during synthesis. Actually, in realistic compounds, there is always a certain amount of antisite defects (ADs), where some of the Fe atoms exchange their positions with the same number of Mo atoms. Typically these antisite defects are randomly distributed and their number is characterized by the degree of Fe/Mo ordering of the sample, which can be probed by X-ray diffraction. Due to the close atomic size of Fe and Mo, the degree of ordering in SFMO single crystals is not higher than 92% (ADs∼8%) [260]. The half-metallic character (and, then, the electronic transport properties) are quite sensitive to the presence of ADs, since they modify the Fe-O-Mo bonding network responsible for electron hopping.

Moreover, the introduction of oxygen vacancies (O*) in SFMO, which corresponds to removal of a neutral O atom from the lattice, should alter the amount of delocalized electrons and affect the magnitude of the magnetic moments of surrounding atoms. In defect-free SFMO (no antisite defects), oxygen vacancies involve only Fe-O-Mo-type bonds. However, in AD:SFMO, we can find also oxygen vacancies along Fe-O-Fe and Mo-O-Mo bonds. Insight into the likelihood of formation of these different types of vacancies and their role on tuning the magnetic and electronic properties of bulk SFMO is then of great interest in the context of SOFCs.

A.1.3 Method and computational details.

All the calculations reported in this work were carried out using the VASP code (5.2.2 version) [261]. We started from the characterization of defect-free Sr_2FeMoO_6 using methods based on density functional theory (DFT). Thanks to its effective balance of accuracy and feasibility, DFT has become the most common framework for studying the electronic structure of materials. However, the self-interaction error (SIE) that arises from the approximate forms of currently available exchange-correlation functionals produces especially large errors in mid-to-late first row transition metal oxides. To eliminate much of the SIE, we employ the DFT+U method [118, 119]. This approach consists of applying an on-site potential at atom positions and requires a parameter, U-J, which is the difference between the average Coulomb and exchange interactions felt by electrons localized on the same atom with the same angular momentum. While frequently effective, this method often retains some empiricism in the choice of the U-J parameter. Instead, we use a recently developed *ab initio* DFT+U method [121, 122] that has been successfully validated on chromium and iron oxides. In this work, because of the presence of d electrons in Fe and Mo atoms we tested not only DFT but also DFT+U approaches, with local (LDA) [106] and semi-local (PBE) [115] exchange-correlation density functionals.

For Sr_2FeMoO_6 a plane-wave basis set was used for the valence electrons, while core electrons have been taken into account according to the projector-augmented wave (PAW) method. Among the available PAW potentials supplied with the VASP code, we used the only one available for Sr, which leaves ten electrons in the valence ($4s^2$, $4p^6$ and

$5s^2$). For oxygen, there are three different potentials, all dealing the same number of valence electrons ($2s^2$ and $2p^4$), but with different core radii: a soft potential with a large core radius (O_s), an intermediate one (O), and an hard potential (O_h); we used the intermediate (O) as the best compromise between accuracy and cost. For Fe, we tested PAW potentials dealing with eight ($4s^2$ and $3d^6$) or fourteen ($3p^6$, $4s^2$ and $3d^6$) electrons in the valence and for Mo, we tested the six ($5s^2$ and $4d^4$) and twelve ($4p^6$, $5s^2$ and $4d^4$) valence electron PAW potentials. No significant differences on prediction of Sr_2FeMoO_6 properties were found with the more demanding Fe and Mo PAW potentials, so we used the *standard* potentials for Fe and Mo, with eight and six valence electrons, respectively.

All our calculations were carried out with a kinetic energy cut-off of 800 eV for planewaves and with a k-point sampling based on the Monkhorst-Pack [85] scheme (6x6x4 for the Sr_2FeMoO_6 tetragonal cell, 4x4x4 for the pseudocubic one). These parameters ensured convergence of the computed total energy within 1 meV per formula unit for SFMO.

Regarding the DFT+U approach used in this work, d shells on Fe and Mo have to be taken into account simultaneously and, thus, in principle, two U-J parameters should be chosen. In Fe, d electrons are strongly localized and give rise to the gap in the α spin-channel of this half-metallic compound. Then, apart from the standard DFT U-J_{Fe}=0 eV, we checked Sr_2FeMoO_6 bulk and magnetic properties for the following set of U-J_{Fe} values: 3.7 eV and 4.3 eV (corresponding to the *ab initio* values for Fe^{2+} and Fe^{3+}, respectively [122]) and the average between them (4.0 eV). Taking into account the intermediate $Fe^{(3-\delta)+}$ valence and the negligible variation of the Sr_2FeMoO_6 properties under study, the average value of U-J_{Fe}=4.0 eV is our choice all along this work. By contrast, according to former investigations on this material [259, 258, 262, 263, 264, 265], the metallic character of the *beta* spin-channel of this compound is mostly due to a delocalized d electron of Mo, which can be seen as $Mo^{(5+\delta)+}$. For this reason, Mo was expected to be accurately described within the DFT framework and no U-J_{Mo} is in principle needed. Actually, some calculations performed in SFMO browsing different values of U-J_{Mo} with fixed U-J_{Fe}=4 eV confirm that no U-J_{Mo} is needed and its use even worsens the good properties predicted with U-J_{Fe}=4 eV and U-J_{Mo}=0 eV values.

A.1.4 Results I: Stoichiometric SFMO

A.1.4.1 Defect-free Sr_2FeMoO_6

First, we discuss the magnetic arrangement of Fe and Mo within the tetragonal Sr_2FeMoO_6 unit cell. The experimental value of the total magnetic moment 3.5-4.0 μ_B and former investigations on this material [266, 257, 258] suggested the iron to be in a high spin configuration. Full relaxation of both lattice vectors and atomic positions were performed without any symmetry constraints and starting from different relative magnetic configurations between iron and molybdenum ions: (a) Fe^{3+} and Mo^{5+} species ($S = 5/2$ and $S = 1/2$, respectively) with spins anti-ferromagnetically aligned (AF), (b) all species with spins ferromagnetically aligned (FM) and (c) considering the limit of Fe^{2+} and Mo^{6+} ($S = 4/2$ and $S = 0$, respectively). From all these initial configurations, the LDA and

PBE density functionals predicted a non-magnetic solution. These results are in contrast with experimental observations and prove that pure DFT should not be used for describing SFMO. With DFT+U, all the initial magnetic configurations converged to the same AF state; the non-magnetic arrangement, obtained by pure DFT, was predicted to be higher in energy than the AF state by $\sim$ 1.0 and $\sim$ 1.6 eV, at the LDA+U and PBE+U levels of theory, respectively. Moreover, concerning only the iron lattice, the ferromagnetic alignment of Fe ions is found to be the most stable with respect to all the antiferromagnetic ones that we tested by more than $\sim$ 130 meV.

The most stable AF magnetic arrangement predicted by DFT+U is compatible with the model of Sarma *et al.* [258]. This model explained the electronic and magnetic properties of SFMO on the basis of electron hopping between Fe and Mo states with the same spin and orbital symmetry. In particular, the AF configuration is the only one that allows the down-spin Mo $d(t_2g)$ electron to delocalize onto the empty down-spin Fe $d(t_{2g})$ orbitals, consistent with the $Fe^{(3-\delta)+}$ / $Mo^{(5+\delta)+}$ valence.

Table A.1 lists calculated Sr_2FeMoO_6 bulk properties in comparison to experimental values. From these data, we observe very different behavior of DFT and DFT+U approaches, regardless of the exchange-correlation flavor. Despite a good matching of structural properties of Sr_2FeMoO_6 DFT completely fails in the description of the magnetic properties, as discussed above, and the electronic structure. Actually, DFT predicts a non-magnetic ground state and a symmetric electronic structure for the α and β spin-channels, leading to a description of Sr_2FeMoO_6 as a semi-conducting material, in contrast with its half-metallic nature (Fig. A.3, top). Consequently, no further calculations were carried out at the pure DFT level of theory. LDA+U and PBE+U, with the *ab initio* derived U-J value for Fe, predicted accurately the SFMO structural parameters, within a range of 1% for the lattice constants. Despite a little overestimate of the α-gap value, DFT+U provides a good description of the half-metallic character (Fig. A.3, bottom) as well as the total magnetization and the magnetization on iron and molybdenum compared to experimental data and to previous calculations [257, 258, 267, 268, 269, 270]. The Fermi level in SFMO was predicted by DFT+U to be at the band formed exclusively by the Fe($t_{2g}\downarrow$)-O($2p$)-Mo($t_{2g}\downarrow$) sub-band, responsible for the electron hopping. In the spin up band, the top of the valence band has a Fe($e_g\uparrow$)-O($2p$) mixed character, whereas the bottom of the conduction band is dominated by Mo($t_{2g}\uparrow$) states, with a small O($2p$) contribution.

A.1.4.2 SFMO with antisite defects (AD:SFMO)

When SFMO contains antisite defects, some Fe occupy Mo sites (Fe_{Mo}) and the same number of Mo atoms occupy Fe sites (Mo_{Fe}), which appear as new Fe_{Mo}-O-Fe and Mo_{Fe}-O-Mo bonds. Regarding the spin arrangement of Fe_{Mo} and regular Fe in AD:SFMO, the experimentally observed total saturation magnetization of SFMO was interpreted as being due to the presence of ADs and an antiferromagnetic alignment between the two now neighboring Fe_{Mo} and Fe [271, 272]. However, recent reliable *ab initio* calculations have clearly

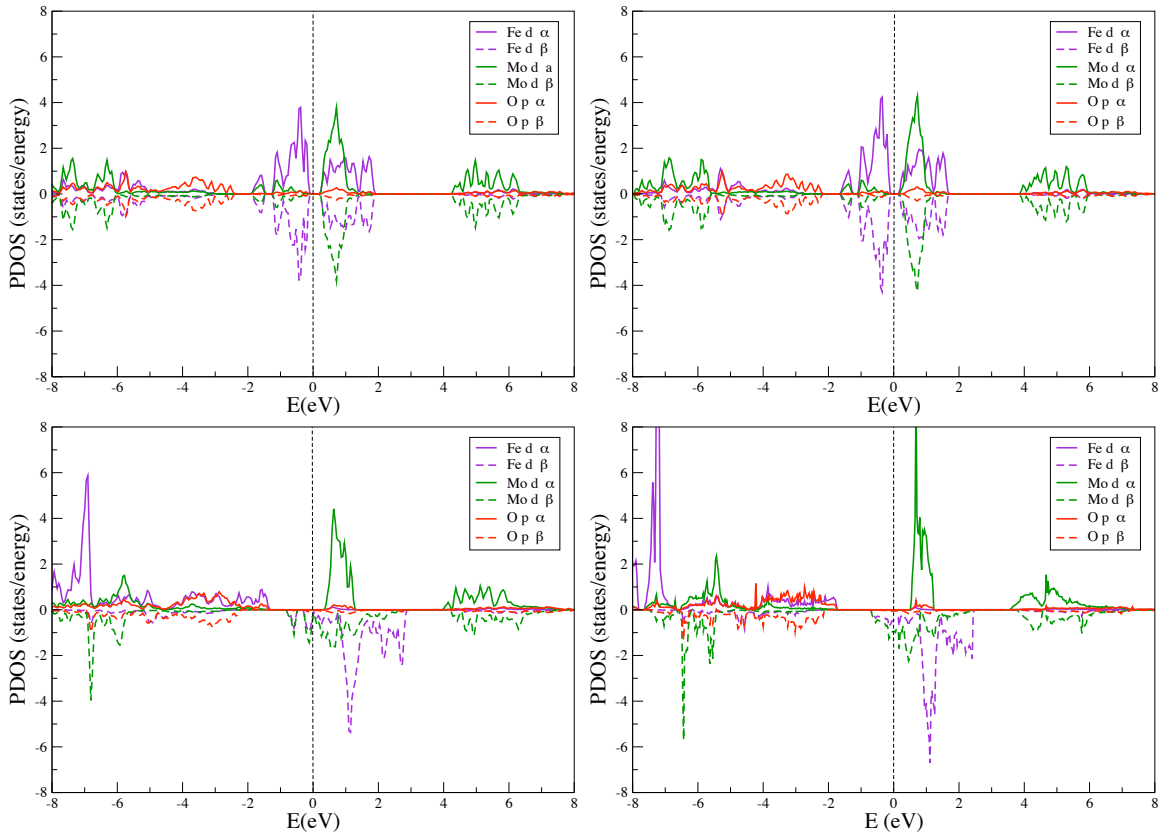

Figure A.3: Top: LDA (left) and PBE (right) calculated projected density of states (PDOS) of Sr_2FeMoO_6Ḃottom: LDA+U (left) and PBE+U (right) calculated projected density of states (PDOS) of Sr_2FeMoO_6 for $(U\text{-}J)_{Fe} = 4$ eV. PDOS on Fe(d), Mo(d) and O(p) orbitals shown.

shown that Fe_{Mo} and regular Fe are ferromagnetically coupled [273, 258, 274]. Therefore, in this work, we follow the approach of parallel alignment of their spin moments.

In order to study SFMO with antisite defects, we analyzed a hypothetical model in which the antisite defects are ordered in a $\sqrt{2} \times \sqrt{2} \times 1$ pseudocubic SFMO supercell, that contains four Sr_2FeMoO_6 formula units and fulfills $a = b < c$ (Fig. A.4, top). The pseudocubic supercell vectors and atomic positions were generated from optimized parameters of tetragonal SFMO calculated at the LDA+U and PBE+U levels of theory. Only one pair of Fe and Mo have been exchanged at once, leading to an ordering degree of 75% (ADs∼25%), lower than the maximum ordering observed experimentally. Nevertheless, our calculations provided useful information about the local properties around the defects, as well as setting a reference for the study of SFMO with both antisite defects and oxygen vacancies, discussed below in section A.1.5.

Three different antisite defects Fe_{Mo}-Mo_{Fe} have been taken into account, due to the pseudocubic character of the considered supercell. They are shown in Fig. A.4 and correspond to Fe_{Mo} and Mo_{Fe} exchanged along the diagonal of the cube formed by the four Fe and four Mo atoms (antisite (a)), exchanged in the x (or the equivalent y) direction of

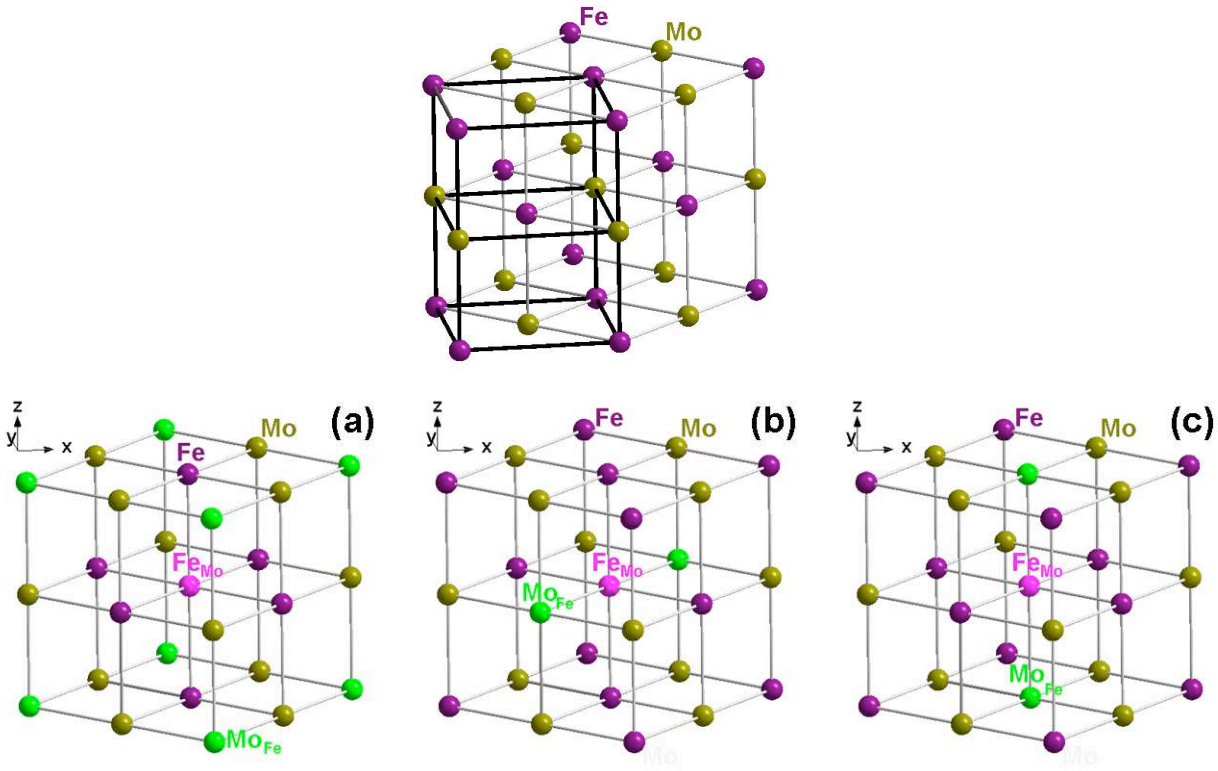

Figure A.4: Top: Representation of interleaving Fe (purple) and Mo (olive green) sublattices of the tetragonal unit cell of SFMO (black thick lines, 2 Sr_2FeMoO_6 f.u.) and the corresponding $\sqrt{2} \times \sqrt{2} \times 1$ pseudocubic SFMO supercell (grey lines, 4 Sr_2FeMoO_6 f.u.). Bottom: Representation of the three different Fe_{Mo}(pink)-Mo_{Fe}(green) antisite defects (AD) in pseudocubic SFMO: (a) AD on the diagonal of the pseudocubic sublattice. (b) AD in the xy plane. (c) AD on the z axis.

the xy plane (antisite (b)), and along the z axis (antisite (c)).

AD formation energies were calculated according to

$$Sr_8Fe_4Mo_4O_{24} \rightarrow \text{AD:}Sr_8Fe_4Mo_4O_{24}$$

Full relaxation of all the internal positions within the unit cell was accounted for. Table A.2 lists some of the results on the different ADs.

The computed energies of formation of the ADs are not very high ($\sim$ 1 eV), as expected considering the similar size of Mo and Fe ions. From our results, the diagonal AD is the most unfavorable. The ADs along the xy plane and z directions are very similar, in accordance with the fact that in the pseudocubic cell $a \sim c$. The AD along xy is slightly lower in energy.

Distances between Fe_{Mo} and Mo_{Fe} do not substantially change compared to defect-free SFMO Fe-Mo distances. In addition, structural parameters within the new $Fe_{Mo}O_6$ and $Mo_{Fe}O_6$ moieties do not change with respect to their defect-free SFMO counterparts.

The total magnetic moment of the ADs are slightly higher than for the structure

without ADs. Regarding the magnetic moment of ions at the AD sites, calculations provide a range of values for Fe: among the different ADs, LDA+U results are very similar, around 4.1-4.2 μ_B; with PBE+U we found more variability, the values being within the range of 3.8-4.3 μ_B. Regarding the magnetic moment of Mo ions at the ADs sites, LDA+U predicted absolute values within the 0.1-0.5 μ_B range, while higher values were predicted with PBE+U, going from 0.3 to 0.8 μ_B. No trend can be highlighted from these results, however it clearly appears that a significant rearrangement of the electronic degrees of freedom takes place at the AD sites.

As a matter of fact, the electronic structures of AD:SFMO compounds appear to be quite different to the parent SFMO. Both LDA+U and PBE+U predict very low pseudo-gaps, from zero to a maximum of 0.28 eV. Such different behavior is consistent with the fact that the Fe-O-Mo network is strongly modified by the presence of antisite defects, new Fe_{Mo}-O-Fe and Mo_{Fe}-O-Mo bonds structures appear and the Fe-O-Mo ones decrease in number.

A.1.5 Results II: Non-stoichiometric SFMO: $Sr_2FeMoO_{6-\delta}$

Diffusion of oxygen anions is a mandatory capability for effective SOFC cathode materials. Oxygen vacancies are required for diffusion of such anions so that they may hop between empty sites. A first estimate of how good SFMO-based materials are as ionic conductors could be drawn by computing the energy of formation of oxygen vacancies.

In this work, we modeled $Sr_2FeMoO_{6-\delta}$ materials with δ =0.25, by removing one oxygen atom from the $Sr_8Fe_4Mo_4O_{24}$ pseudocubic supercells represented in Fig. A.4, both defect-free and containing antisite defects. From defect-free SFMO, we created oxygen vacancies along the Fe-O-Mo bonds on the xy plane and along the z axis. For SFMO with antisite defects, we have studied all the possible Fe-O*-Fe and Mo-O*-Mo vacancies. Fig. A.5 depicts schematically all of the accounted for oxygen vacancies.

After removal of a neutral O atom the electronic density was optimized according to the self-consistent procedure, in order to get the minimum of the total energy, without imposing any constraints. The lattice parameters of the cell were fixed as optimized for the SFMO perfect structure, whereas all atomic positions were allowed to relax to the minimum of the total energy.

The first effect after removal of a neutral oxygen atom is a reorganization of the electronic structure. A first, qualitatively useful insight on this process was obtained by computing Bader charges.

The Bader model [275] uses the total charge density of a molecule or solid to determine its topology. The charge density is a scalar field, $\rho(r)$, which possesses a unique topology, characterized in terms of its critical points. These are points in the space where the gradient of the scalar field is zero, and they can be minima, maxima or saddle points, which are the zeros of the gradient of the scalar field. According to the Bader model, the chemical bonds in a molecule can be seen in terms of the topology of $\rho(r)$: a bond path connecting two nuclei (two maxima of the density) through a minimum critical point, such

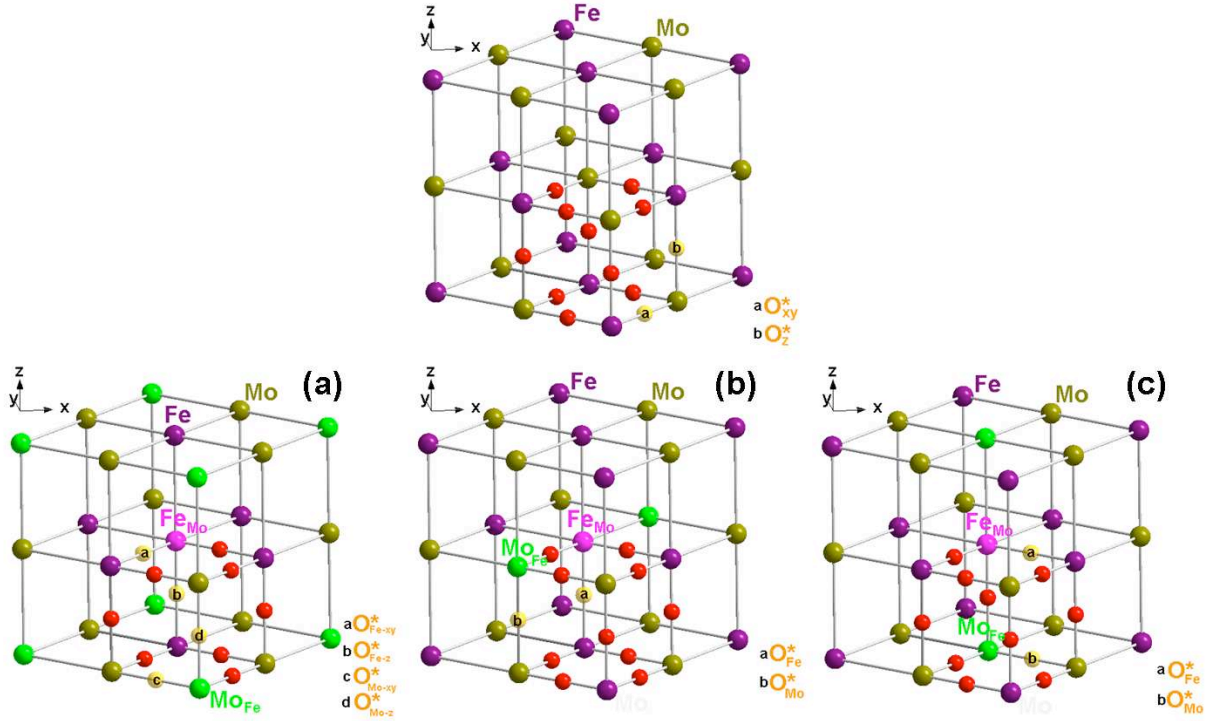

Figure A.5: Top: Representation of the two different oxygen vacancies (O*) in SFMO: Fe-O*-Mo in the xy plane (O^*_{xy}) and Fe-O*-Mo along the z axis (O^*_z) Bottom: Representation of the Fe-O*-Fe and Mo-O*-Mo oxygen vacancies studied for the three (a), (b) and (c) AD:SFMO of Fig. A.4: (a) : Fe-O*-Fe in the xy plane (O^*_{Fe-xy}), Fe-O*-Fe on the z axis (O^*_{Fe-z}), Mo-O*-Mo in the xy plane (O^*_{Mo-xy}) and Mo-O*-Mo on the z axis (O^*_{Mo-z}). (b): Fe-O*-Fe (O^*_{Fe}) and Mo-O*-Mo (O^*_{Mo}). (c): Fe-O*-Fe (O^*_{Fe}) and Mo-O*-Mo (O^*_{Mo}). Oxygen atoms in red, oxygen vacancies in light orange.

that the charge density at nuclei are always a maximum with respect to any neighboring path. In Bader analysis, the whole 3D space is divided into subsystems, each usually containing one nucleus (but sometimes none, i.e., pseudoatoms: maxima of the density without nuclei). The subsystems are delimited by "zero-flux" surfaces, where

$$\nabla\rho(r) \bullet \vec{n}(r) = 0 \ (\vec{n}(r) \text{ is a vector normal to the surface})$$

Within the Bader theory, an atom is defined as a region of real space bounded by the surfaces where the flux in the gradient vector field of $\rho(r)$ is null, without resorting to the concept of atomic orbitals. Then, the Bader charge associated with an atom is the total charge density within the volume delimited by these surfaces.

Table A.3 lists Bader charges of Fe and Mo in the defect-free SFMO, together with the ones at Fe and Mo AD sites in the three AD:SFMO s, before and after the formation of the oxygen vacancy (O*).

The absolute values of Bader charges are lower than expected by considering standard ion valencies. This is consistent with the fact that the bonds in perovskite transition

metal oxides are not purely ionic. As a matter of fact, the analysis of Bader charges can be safely used to quantify the amount of covalency involved in the chemical bond under investigation.

For defect-free SFMO at the PBE+U level of theory, the Bader charges are 1.61e for Sr, -1.15e and -1.17e for the two types of oxygen atoms, and 1.65e and 2.22e for Fe and Mo, respectively.

The Sr cation has the most ionic character, and upon removal of a neutral oxygen atom, its Bader charge does not change. The effective charges of Fe and Mo, much lower than +3 and +5 respectively, indicate a considerable amount of covalency exists in the Fe-O and Mo-O bonds. Such picture is consistent with the features of computed PDOS (Fig. A.3) and with the aforementioned hopping model proposed for understanding the half metallic nature of this material. The formation of an oxygen vacancy calls for compensation of an effective negative charge of $\sim$1.16e.

For O*:SFMO, the computed Bader charges provide similar pictures for the two vacancies O$_x$$y$ and O$_z$: $\sim$0.3e were donated to the Fe closest to the O vacancy, $\sim$0.5-0.7e were distributed among the other iron ions, with the Mo closest to the vacancy and the other ions playing a very marginal role. Overall, the iron atoms received most of the charge left behind by the neutral oxygen. Form another perspective, the formation of an oxygen vacancy implies a reduction of other remaining species. Our results suggest that within the SFMO environment, the iron is the most likely to reduce its valence.

The presence of antisite defects in stoichiometric SFMO results in effective charges that are essentially consistent with the case of defect-free SFMO. The presence of AD allowed us to study O vacancy formation along the Mo-O-Mo and Fe-O-Fe bonds, as listed in Table A.3 (AD,O*:SFMO). Overall, we found as a general trend that the two closest ions to the O vacancy take the most of the charge left behind, with the second closest transition metal ions being involved in a less relevant way.

Comparing SFMO and AD:SFMO oxygen vacancy formation energies, as well as structural and electronic features in these reduced materials could be of extreme interest from the perspective of using SFMO-based materiasl as cathode for SOFCs. Table A.4 lists our results obtained using both LDA+U and PBE+U. We report the data obtained with LDA+U for completeness, however we discuss here only the results with PBE+U because in our opinion LDA is less accurate in describing bond breaking and the triplet state of molecular oxygen [276].

In all the O*:SFMO and AD,O*:SFMO cases, the closest ions to the O vacancy moved slightly outward; this behavior has been also observed in other perovskite-based materials.

In O*:SFMO, the presence of the vacancy did not alter significantly the electronic features of the bulk: the system retained its half-metallic nature. The iron closest to the vacancy presented a lowering of magnetic moment values (from 4.1 to 3.7μ_B), as expected upon reduction. For molybdenum, the magnetic moment changed from -0.5 to -0.1$\sim$-0.2μ_B. We can rationalize these results considering that in high spin Fe^{3+}($d5$) all the electrons have, e.g., α spin. Therefore, in order to preserve the magnetic balance of the system, the two formal electrons left by the oxygen vacancy can only occupy the β

spin-orbitals on iron (the only ones available) and an α spin-orbital on molybdenum.

Also in the case of AD,O*:SFMO the resulting eigenvalue gaps are not qualitatively different from the cases of vacancy-free systems. The magnetic moments of the ions closest to the vacancy have a complex behavior, in general compatible with a splitting of the α and β electrons between the two ions. However these data should not be overinterpreted, because analysis of magnetic moments can only provide a qualitative description of such subtle electronic features.

The most interesting results by far are the energies of formation. The O vacancy formation energy was computed in the standard way, with respect to a free oxygen molecule in its triplet state, according to the processes:

$$Sr_8Fe_4Mo_4O_{24} \rightarrow Sr_8Fe_4Mo_4O_{23} + \tfrac{1}{2}O_2$$

and

$$AD{:}Sr_8Fe_4Mo_4O_{24} \rightarrow AD{:}Sr_8Fe_4Mo_4O_{23} + \tfrac{1}{2}O_2$$

for the parent SFMO and SFMO with antisite defects, respectively.

From our calculations, oxygen vacancies in defect-free SFMO costs ∼4.0 eV to form. Comparing this result to other consistently predicted values for MIEC cathode materials, this energy of formation is quite high, compared to, for example, 1-2 eV in $Ba_{(1-x)}Sr_xCo_{(1-y)}Fe_yO_3$ [249]. However, beside the absolute value it is important to address how the oxygen vacancy formation energy changes as a function of the local surroundings, for example by looking at the antisite SFMO.

In the case of AD,O*:SFMO we predict very interesting behavior. Formation energies of oxygen vacancies along Fe-O-Fe bonds are within the range of ∼3.0-3.2 eV. Along Mo-O-Mo bonds they are much higher, at 4.57 and 4.89 eV. It appears clear from our results that the formation of O vacancies is significantly more favorable near iron ions rather than near molybdenum. Consistent with this finding is the fact that the Fe-O*-Fe formation energy is predicted to be ∼1 eV lower in energy than the Fe-O-Mo one in defect-free SFMO. Such results are also consistent with our analysis of Bader charges where we find the iron to be better disposed to reduction. Accordingly, the probability of formation of an oxygen vacancy follows the trend Fe-O*-Fe > Fe-O*-Mo > Mo-O*-Mo.

One reason behind this trend can be found considering that the creation of an oxygen vacancy implies the breaking of metal-oxygen bonds and it is well known that early transition metals, such as Mo, make much stronger metal-oxide bonds than late transition metals do, such as Fe [277].

A.1.6 Conclusions

In the present work, we studied Sr_2FeMoO_6 (SFMO) bulk properties, by considering the cases of the perfect crystal and the combined presence of defects like anti-site defects (AD) and oxygen vacancies (O*). First, we found that use of the DFT+U method was mandatory to obtain a reliable description of this material: using the *ab initio* derived

U-J value for iron we are able to predict structural, electronic, and magnetic properties in close agreement with measurements. Pure DFT was not successful in doing so.

After validation of our theoretical approach, we explored properties of AD:SFMO, O*:SFMO and AD,O*:SFMO. Structural features were not affected by antisite defects, while the presence of an oxygen vacancy led to a more pronounced relaxation of its closest ions. Oxygen vacancies did not affect qualitatively the electronic structure of defect-free SFMO, while the presence of ADs affected the electronic properties in a more pronounced way.

Formation of antisite defects has a low cost, with the highest computed AD energy of formation being ∼1 eV. By contrast, the formation energy of an oxygen vacancy was predicted to be ∼4 eV in defect-free SFMO. However, this energy is significantly reduced when AD and O* defects are present simultaneously. We predict that the energy of formation of an oxygen vacancy along Fe-O-Fe bonds is lower than the one along Fe-O-Mo bonds, which is itself lower than the one in the case of an Mo-O-Mo bond.

These predictions suggest that an excess of iron over molybdenum should provide an SFMO-based material with a higher concentration of oxygen vacancies than Sr_2FeMoO_6 and therefore be a better material for application as a SOFC cathode. Indeed, this has been recently proven by measurements of the performance of SOFCs made with $Sr_2Fe_{2-x}Mo_xO_{6-\delta}$ [250].

Finally, following the approach and the method validated in this work, we are performing calculations on SFMO-based materials with higher Fe:Mo ratio, $Sr_2Fe_{1.5}Mo_{0.5}O_{6-\delta}$, focusing on formation and diffusion of oxygen vacancies in the bulk and at the most stable surfaces.

A.1.7 *Conclusiones*

En el presente trabajo estudiamos las propiedades del material Sr_2FeMoO_6 (SFMO), considerando tanto el cristal puro como la presencia de defectos *antisite* (AD) o/y vacantes de oxígeno (O*). Como primer resultado, encontramos que el uso del método DFT+U es obligatorio para obtener una descripción fiable de este material: usanndo el valor obtenido en modo *ab initio* para el término U-J del átomo de hierro, somos capaces de predecir la propiedades estructurales, electrónicas y magnéticas en gran concordancia con las observaciones experimentales. La teoría DFT convencional falla en esta descripción.

Después de la validación del método teórico elegido en Sr_2FeMoO_6, exploramos los resultados obtenidos en AD:SFMO, O*:SFMO y AD,O*:SFMO. Las características estructurales no se ven afectadas por la presencia de defectos *antisite*, mientras que la presencia de una vacante de oxígeno lleva a una relajación más pronunciada de los cationes más cercanos. La vacante de oxígeno no afecta cualitativamente la estrucura electrónica semi-metálica del SFMO sin defectos, mientras que la presencia de defectos *antisite* afecta a la estructura electrónica de un modo más relevante.

La formación de defectos *antisite* tiene un bajo coste energético, siendo la energía de formación más alta calculada de ∼1 eV. Sin embargo, las energías de formación de vacantes

de oxígenos son más altas, del orden de ∼4 eV en SFMO sin defectos. Sin embargo, éstas energías disminuyen significativamente cuando defectos *antisite* y vacantes de oxígeno están presentes simultáneamente. Segun nuestros resultados, la energía de formación de una vacante de oxígeno en un enlace Fe-O-Fe es menor que en un enlace Fe-O-Mo, y ésta es a su vez menor que la energía de formación de una vacante en un enlace Mo-O-Mo.

Esta predicción sugiere que un material con exceso de hierro respecto a molibdeno contendría una concentración más alta de vacantes de oxígeno y, por tanto, sería un mejor material para su uso en el cátodo de las SOFCs. De hecho, esto ha sido recientemente probado a través de medidas realizadas en el comportamiento de SOFCs hechas con $Sr_2Fe_{2-x}Mo_xO_{6-\delta}$ [250].

Finalmente, siguiendo el enfoque y el método validado en este trabajo, estamos realizando cálculos en materiales basados en SFMO con una mayor proporción Fe:Mo, $Sr_2Fe_{1.5}Mo_{0.5}O_{6-\delta}$, focalizando nuestro trabajo en la formación y difusión de vacantes de oxígeno en el sólido y en sus superficies más estables.

A.1.8 Data tables

Table A.1: Calculated structural, magnetic and electronic properties of bulk Sr_2FeMoO_6 ($I4/m$ space group). Fe/Mo AF alignment considered. References of experimental values: a [278], b [279], c [280] , d [259], e [281], f [260], g [282].

	Exp.	LDA+U		PBE+U	
		$(U\text{-}J)_{Fe}$=0 eV	$(U\text{-}J)_{Fe}$=4 eV	$(U\text{-}J)_{Fe}$=0 eV	$(U\text{-}J)_{Fe}$=4 eV
a=b (Å)	5.55215[a]	5.39	5.48	5.52	5.61
c (Å)	7.90134[a]	7.63	7.87	7.81	8.03
V_{cell} (Å^3)	243.570[a]	221.95	236.04	237.79	252.44
$z(O_I)$	0.2542[a]	0.2465	0.2531	0.2488	0.2544
$x(O_{II})$	0.2767[a]	0.2560	0.2892	0.2589	0.2882
$y(O_{II})$	0.2266[a]	0.2370	0.2160	0.2387	0.2201
$d(Fe\text{-}Mo)_{xy}$(Å)	3.926	3.81	3.87	3.90	3.96
$d(Fe\text{-}Mo)_z$(Å)	3.951	3.81	3.93	3.90	4.01
$d(Fe\text{-}Mo)_d$(Å)	6.814	6.60	6.74	6.76	6.89
d(Fe-O)(Å)	2.009(x2), 1.986(x4)[a]	1.88(x6)	1.99(x2) 1.98(x4)	1.94(x6)	2.04(x2) 2.03(x4)
d(Mo-O)(Å)	1.942(x2), 1.960(x4)[a]	1.93(x6)	1.94(x6)	1.96(x6)	1.97(x6)
α $(Fe\text{-}O\text{-}Mo)_{xy}$ (°)	169[a]	176	163	175	164
α $(Fe\text{-}O\text{-}Mo)_z$ (°)	180[a]	180	180	180	180
B (GPa)	266[b]	218	183	170	153
M_{Fe} (μ_B)	4.0 - 4.1[c,d,e]	0.0	4.0	0.0	4.1
M_{Mo} (μ_B)	-0.2 - -0.5[c,d,e]	0.0	-0.4	0.0	-0.5
M_s/f.u (μ_B)	3.5-4.0[c,d,e]	0.0	3.8	0.0	3.9
gap (α)	0.5[f],1.3[g]	0.48	1.84	0.43	2.24
gap (β)	0.0[f,g]	0.48	0.00	0.43	0.00

Table A.2: LDA+U and PBE+U calculated formation energies of antisite defects in SFMO (Fig. A.4). Structural parameters and magnetic properties concerning the Fe_{Mo} and Mo_{Fe} atoms involded in the AD and electronic properties also shown. $(U\text{-}J)_{Fe}$=4 eV used. Fe/Mo AF alignment considered. Labels according to Fig. A.4.

	AD:SFMO, AD:$Sr_8Fe_4Mo_4O_{24}$					
	LDA+U $(U\text{-}J)_{Fe}$=4 eV			PBE+U $(U\text{-}J)_{Fe}$=4 eV		
	(a)	(b)	(c)	(a)	(b)	(c)
E_f (eV)	1.10	1.00	1.09	1.00	0.835	0.933
d(Fe_{Mo}-Mo_{Fe})(Å)	6.74	3.87	3.93	6.90	3.96	4.01
d(Fe_{Mo}-O)(Å)	2.00(× 2)	2.00(× 2)	2.02(× 2)	2.04(× 2)	2.06(× 2)	2.07(× 2)
	1.96(× 4)	1.98(× 2)	1.96(× 4)	2.02(× 4)	2.03(× 2)	2.01(× 4)
		1.97(× 2)			2.01(× 2)	
d(Mo_{Fe}-O)(Å)	1.97(× 4)	1.97(× 2)	1.97(× 4)	2.01(× 4)	2.01(× 2)	2.00(× 4)
	1.96(× 2)	1.96(× 2)	1.91(× 2)	2.00(× 2)	2.00(× 2)	1.94(× 2)
		1.90(× 2)			1.94(× 2)	
α (Fe-O-Fe_{Mo})$_{xy}$(°)	171	165	168	170	166	168
α (Fe-O-Fe_{Mo})$_z$(°)	180	180	-	180	180	-
α (Mo-O-Mo_{Fe})$_{xy}$(°)	161	165	161	164	165	164
α (Mo-O-Mo_{Fe})$_z$(°)	180	180	-	180	180	-
$M_{Fe_{Mo}}$ (μ_B)	4.27	4.18	4.20	4.31	3.84	4.14
$M_{Mo_{Fe}}$ (μ_B)	–0.15	–0.27	–0.51	–0.55	–0.83	–0.33
M_s/f.u (μ_B)	4.70	4.35	4.20	4.46	4.07	4.11
gap (α)	0.00	0.25	0.18	0.19	0.25	0.28
gap (β)	0.00	0.00	0.00	0.19	0.00	0.00

Table A.3: LDA+U and PBE+U ($(U\text{-}J)_{Fe}$=4 eV) calculated Bader charges in SFMO, AD:SFMO, O*:SFMO and AD,O*:SFMO.

		LDA+U	PBE+U
	SFMO, $Sr_8Fe_4Mo_4O_{24}$		
	Fe	1.58	1.65
	Mo	2.23	2.22
	AD:SFMO, AD:$Sr_8Fe_4Mo_4O_{24}$		
(a)	Fe_{Mo}	1.63	1.69
	Mo_{Fe}	2.04	2.03
	3 × Fe (aver.)	1.60	1.67
	3 × Mo (aver.)	2.20	2.19
(b)	Fe_{Mo}	1.58	1.69
	Mo_{Fe}	2.08	2.05
	3 × Fe (aver.)	1.61	1.62
	3 × Mo (aver.)	2.22	2.24
(c)	Fe_{Mo}	1.58	1.67
	Mo_{Fe}	2.11	2.10
	3 × Fe (aver.)	1.58	1.66
	3 × Mo (aver.)	2.24	2.22
	O*:SFMO, $Sr_8Fe_4Mo_4O_{23}$		
O^*_{xy}	Fe(-O*)	1.25	1.32
	Mo(-O*)	1.95	2.20
	3 × Fe (aver.)	1.52	1.41
	3 × Mo (aver.)	2.17	2.19
O^*_z	Fe(-O*)	1.24	1.28
	Mo(-O*)	1.92	2.11
	3 × Fe (aver.)	1.53	1.46
	3 × Mo (aver.)	2.17	2.17

		LDA+U	PBE+U
	AD,O*:SFMO, AD:$Sr_8Fe_4Mo_4O_{23}$		
(a)	O^*_{Fe-xy}	Fe_{Mo}(-O*)	1.43	1.32
		Fe(-O*)	1.30	1.48
		2 × Fe (aver.)	1.60	1.52
		4 × Mo (aver.)	2.18	2.16
	O^*_{Fe-z}	Fe_{Mo}(-O*)	1.93	1.54
		Fe(-O*)	1.31	1.33
		2 × Fe (aver.)	1.60	1.55
		4 × Mo (aver.)	2.11	2.12
	O^*_{Mo-xy}	Mo_{Fe}(-O*)	1.60	1.65
		Mo(-O*)	1.91	1.97
		2 × Mo (aver.)	2.14	2.15
		4 × Fe (aver.)	1.60	1.67
	O^*_{Mo-z}	Mo_{Fe}(-O*)	1.62	1.69
		Mo(-O*)	1.89	1.96
		2 × Mo (aver.)	2.15	2.24
		4 × Fe (aver.)	1.60	1.59
(b)	O^*_{Fe}	Fe_{Mo}(-O*)	1.41	1.46
		Fe(-O*)	1.37	1.30
		2 × Fe (aver.)	1.58	1.51
		4 × Mo (aver.)	2.10	2.17
	O^*_{Mo}	Mo_{Mo}(-O*)	1.64	1.62
		Mo(-O*)	1.84	1.91
		2 × Mo (aver.)	2.20	2.24
		4 × Fe (aver.)	1.59	1.62
(c)	O^*_{Fe}	Fe_{Mo}(-O*)	1.39	1.46
		Fe(-O*)	1.32	1.37
		2 × Fe (aver.)	1.57	1.56
		4 × Mo (aver.)	2.13	2.16
	O^*_{Mo}	Mo_{Mo}(-O*)	1.68	1.63
		Mo(-O*)	1.85	1.92
		2 × Mo (aver.)	2.20	2.11
		4 × Fe (aver.)	1.58	1.61

Table A.4: LDA+U and PBE+U ((U-J)$_{Fe}$=4 eV) calculated formation energies of oxygen vacancies (O*) in SFMO and AD:SFMO Some structural, magnetic and electronic features of the O*:SFMO and AD,O*:SFMO species also included. Labels according to Fig. A.5.

O*:SFMO, $Sr_8Fe_4Mo_4O_{23}$

	LDA+U		PBE+U	
	O^*_{xy}	O^*_z	O^*_{xy}	O^*_z
E_f (meV)	5.11	5.17	3.94	4.01
d(B-O*-B')(Å)	3.93	3.98	4.03	4.08
M_{Fe-O*} (μ_B)	3.72	3.71	3.71	3.72
M_{Mo-O*} (μ_B)	-0.57	-0.56	-0.10	-0.18
M_s/f.u (μ_B)	3.61	3.61	3.51	3.54
gap (α)	1.62	1.54	1.82	1.79
gap (β)	0.00	0.00	0.00	0.00

AD,O*:SFMO, AD:$Sr_8Fe_4Mo_4O_{23}$

LDA+U

	(a)				(b)		(c)	
	O^*_{Fe-xy}	O^*_{Fe-z}	O^*_{Mo-xy}	O^*_{Mo-z}	O^*_{Fe}	O^*_{Mo}	O^*_{Fe}	O^*_{Mo}
E_f (meV)	3.95	4.03	5.57	5.71	3.94	5.81	3.89	5.74
d(B-O*-B')(Å)	3.91	3.88	3.95	4.01	3.94	3.91	3.98	3.94
M_{Fe-O*} (μ_B)	4.07, 3.80	4.07, 3.83	- -	- -	3.91, 3.86	- -	3.96, 3.80	- -
M_{Mo-O*} (μ_B)	- -	- -	0.1, -0.08	0.04, -0.08	- -	-0.14, -0.34	- -	-0.42, -0.39
M_s/f.u (μ_B)	4.53	4.56	4.68	4.64	3.91	4.26	3.74	4.12
gap (α)	0.00	0.19	0.00	0.00	0.26	0.19	0.26	0.14
gap (β)	0.00	0.00	0.00	0.00	0.00	0.00	0.00	0.00

PBE+U

	(a)				(b)		(c)	
	O^*_{Fe-xy}	O^*_{Fe-z}	O^*_{Mo-xy}	O^*_{Mo-z}	O^*_{Fe}	O^*_{Mo}	O^*_{Fe}	O^*_{Mo}
E_f (meV)	3.18	3.23	4.57	4.76	3.02	4.89	3.14	4.79
d(B-O*-B')(Å)	4.04	4.07	4.06	4.11	4.12	4.00	4.04	4.02
M_{Fe-O*} (μ_B)	4.15, 3.80	4.17, 3.83	- -	- -	4.13, 3.81	- -	3.85, 3.80	- -
M_{Mo-O*} (μ_B)	- -	- -	0.53, 0.02	0.80, 0.07	- -	-0.87, -0.45	- -	-1.00, -0.45
M_s/f.u (μ_B)	4.60	4.76	4.68	4.71	3.65	3.98	3.58	3.89
gap (α)	0.00	0.00	0.00	0.07	0.22	0.30	0.95	0.07
gap (β)	0.25	0.00	0.12	0.37	0.16	0.00	0.00	0.00

Appendix B

Scientific publications related to this work

- First-Principles Study of the Structure and the Electronic structure of Yttrium Aluminum Garnet
  A. B. Muñoz García, E. Anglada and L. Seijo
  Int. J. Quantum Chem. **109**, 1991 (2009)

- Atomistic and electronic structure of antisite defects in yttrium aluminum garnet: Density-functional study
  A. B. Muñoz García, E. Artacho and L. Seijo
  Phys. Rev. B **80**, 014105 (2009)

- Structural effects and $4f - 5d$ transition shifts induced by La codoping in Ce-doped yttrium aluminum garnet: First-principles study
  A. B. Muñoz García, J. L. Pascual, Z. Barandiarán and L. Seijo
  Phys. Rev. B **82**, 064114 (2010)

- Structural, electronic, and spectroscopic effects of Ga codoping on Ce-doped yttrium aluminum garnet: First-principles study
  A. B. Muñoz García and L. Seijo
  Phys. Rev. B **82**, 184118 (2010)

- Ce and La Single- and Double-Substitutional Defects in Yttrium Aluminum Garnet
  A. B. Muñoz García and L. Seijo
  J. Phys. Chem. A **115**, 815 (2011).